NOVEL ACOUSTO-OPTIC SYSTEMS FOR SPECTRUM ANALYSIS AND PHASED ARRAY RADAR SIGNAL PROCESSING

Thesis by

Nabeel Agha Riza

In Partial Fulfillment of the Requirements

for the Degree of

Doctor of Philosophy

California Institute of Technology

Pasadena, California

1990

(Submitted October 30, 1989)

To my parents

Agha Ghulam Riza and Sakina Sultan

ACKNOWLEDGEMENTS

First and foremost, I am deeply indebted to my parents Agha Ghulam Riza and Sakina Sultan, my brother Farzan, and my sister Shehla, for their unwavering love, support, and encouragement throughout my graduate studies at Caltech. I would like to thank my research advisor Professor Demetri Psaltis for his deep technical insights and consistent encouragement throughout my studies. In particular, I greatly enjoyed and gained from the intellectual freedom given to me, thus allowing me to experience research in a wide variety of areas. I am also grateful for the optics laboratory allocated for me, as I greatly enjoyed the physical aspect of scientific research.

I would like to thank Dr. Kelvin Wagner for his numerous discussions on the subject of acousto-optic spectrum analysis, and his work on the additive Mach-Zehnder spectrum analyzer discussed in chapter 3. In addition, I greatly benefited from the numerous technical discussions with members of the multi-talented optical information processing group. In particular, I would like to thank Scott Hudson, Claire Gu, Dr. Ken Hsu, Dr. Jeff Yu, Alan Yamamura, and Mark Neifeld. I would like to express my appreciation to Seiji Kobayashi and Tetsuya Furuse of Sony Corporation, Japan, and Dr. Eung Gi Paek of Bellcore, for their technical expertise in electronics. In addition, I greatly enjoyed the social and world affairs discussions with many of my colleagues, especially Dr. Robert Snapp, Charlie Stirk, David Brady, Amir Atiya, Ruth Erlanson and Sidney Li. I thank all the present and past members of the optical information processing group for their friendship and entertaining presence. The administrative help and assistance in Caltech affairs by Mrs. Su McKinley, Mrs. Linda Dozsa, Mrs. Helen Carrier, and Mrs. Paula Samazan are greatly appreciated.

I sincerely thank my undergraduate advisor Professor Seemyon Meerkov for his kind advice, and consistent encouragement for pursuing a Ph.D. I also thank my high school mathematics mentor, Mr. Hafeez Farouqi for making mathematics and science a curious and interesting learning experience. I thank Dr. Azhar A. Rizvi and Frank Perez for their great friendship. Thanks to F. P. Duck for introducing me to soccer. I also would like to thank all the members of the Kaos soccer team

for a memorable captaining experience.

I would like to thank Caltech, and various funding organizations for providing financial support during my five years of graduate study. Finally, I thank the California Institute of Technology and its community for providing me with an environment for pursuing scientific excellence, thus making the most challenging part of my educational life also the most gratifying.

ABSTRACT

Novel acousto-optic systems for spectrum analysis and phased array radar signal processing are proposed. The pulsed source 2-D multiplicative time and space integrating spectrum analyzer is proposed and experimentally demonstrated. This architecture is simpler, physically smaller, and less sensitive to mechanical vibrations than the pulsed source 2-D additive Mach-Zehnder interferometer based spectrum analyzer. Simple and compact optical disk based systems for 1-D and 2-D spectrum analysis are presented. The high data packing density, angular motion, and parallel read out capability of optical disks is uniquely exploited to generate the very high time bandwidth product reference signals required for temporal spectrum analysis, that are otherwise difficult to generate using electronics. A continuous wave 1-D time integrating disk spectrum analyzer is successfully demonstrated in the laboratory. The limited dynamic range due to huge bias levels in interferometric time integrating processors is alleviated by using photorefractive crystals as real time bias removers. Continuous wave 1-D and 2-D bias free acousto-optic architectures for spectrum analysis are theoretically and experimentally investigated from a systems viewpoint.

Simple, compact, and powerful acousto-optic systems for control and signal processing in phased array radars are proposed that eliminate many system components like phase shifters, mixers, power dividers, and complex antenna feed networks, that are encountered in typical electronically controlled phased array radars. Via a single control parameter, namely frequency, the optical technique provides appropriately phased signals for transmission and reception in phased array antennas. The system is capable of continuous beam scanning, simultaneous multiple beam formation, and multi-target tracking, and can be integrated on a substrate to provide smaller and lighter phased array radars. Also, the system is resistant to electromagnetic interference (EMI), and signal phase shifts are independent of the radar carrier frequency employed. A 1-D linear phased array radar acousto-optic beam steerer is successfully demonstrated in the laboratory, and performance issues such as detector phase sampling error and phase linearity are highlighted. The linear array design is extended to planar and multiple linear arrays.

Table of Contents

CHAPTER 1

INTRODUCTION

Acousto-optic devices are high resolution, large bandwidth, one dimensional electrical to optical transducers, suited for the optical implementation of certain specific signal processing transformations. The current high level of maturity of acousto-optic technology has prompted its use in various applications, and many national and commercial laboratories are building prototype systems [1]. This thesis is a theoretical and experimental investigation of novel acousto-optic system concepts for spectrum analysis of signals and images, and phased array radar optical control and signal processing.

We begin in Chapter 2 with the basic principles of acousto-optic systems, including an acousto-optic device model, the time and space integrating technique for two dimensional (2-D) optical processing using one dimensional (1-D) input devices, and a description of other optical and electronic components used in a typical acousto-optic system. As an application, a multichannel acousto-optic device based coherent image correlator is introduced, along with time and space multiplexing techniques for implementing large filter functions. This processor is fully programmable, and allows bias removal via interferometric detection and electronic carrier demodulation.

In Chapter 3, we review the past history of acousto-optic spectrum analyzers, and address some of their problems. In particular, we look at the recent additive pulsed source 2-D Mach-Zehnder discrete Fourier transform based spectrum processor, and the inherent mechanical instability present in its additive architecture [2]. We introduce the **multiplicative** pulsed source 2-D time and space integrating discrete Fourier transform based folded spectrum processor that is highly insensitive to mechanical instabilities [3]. Unlike the additive design that requires two spatially separate optical beams, the multiplicative technique uses the multiple Bragg diffraction of a single laser beam to generate the desired 2-D spectrum. In addition,

the multiplicative processor has a simpler optical design, although it is less light efficient. The principle of time and space integrating folded spectrum processing in the multiplicative processor are introduced for applications in signal and video processing. The need for an electronic reference signal for interferometric detection in the processor is explained. The 1-D space integrating and 1-D time integrating subsystems of the 2-D multiplicative processor are introduced, and experimental results are given, including a description of the optical implementation of the discrete Fourier transform algorithm. The 2-D Mach-Zehnder spectrum analyzer is reviewed. Next, the theory and design of the multiplicative processor are presented in detail, and experimental results are analyzed. The additive and multiplicative architectures are compared from a systems viewpoint, and performance tradeoffs are highlighted.

One limitation associated with 2-D time and space integrating folded spectrum processors is that they require extremely high time bandwidth product (10^6) reference signals for performing the time based acousto-optic spectrum analysis. These reference signals are hard to generate using commercially available electronic hardware. In Chapter 4, a simple, compact, and economical solution to this problem is proposed by the use of **optical disks**. Recently, parallel access optical disks were proposed for optical information processing in general [4–5]. Here, we exploit the extremely high data packing density, parallel access, and angular motion of optical disks to generate these reference signals [6]. A serial read-out optical disk electronic signal generator system is presented. This system can be used to generate discrete Fourier transform and chirp reference signals required in coherent spectrum processors. In addition, a 2-D time and space integrating spectrum analyzer is introduced that employs a 1-D space integrating acousto-optic spectrum processor, coupled with a 1-D sampling disk based time integrating spectrum processor. Here, the spinning disk acts as a light sampler, providing the effect of a pulsed light source. The two 1-D systems are combined in an orthogonal format in space to provide a 2-D folded spectrum at the output. Next, a continuous wave 1-D time integrating disk spectrum analyzer is introduced, which generates a spatially multiplexed bank

of temporal frequency oscillators (also called distributed local oscillators) that are used for time based signal spectrum analysis. This system is successfully demonstrated in the laboratory, and various system issues are discussed.

Another problem associated with interferometric time and space integrating acousto-optic processors is the gradual build up of unwanted bias terms in time integrating detectors. This high bias level leads to saturation of the electronic time integrating detector, giving a limited dynamic range for the processor output. Past approaches for bias removal involving electronic bias subtraction and electronic carrier demodulation do not solve the problem of limited dynamic range, as the bias removal is done after optical detection. Recently, the ability of a photorefractive crystal to record and erase temporally varying light intensity patterns in real time has been used for real time bias removal in a 1-D correlator [7]. In Chapter 5, we investigate, from a systems viewpoint, the application of **photorefractive crystals** as bias removers in continuous wave 1-D and 2-D architectures for spectrum analysis [8]. The basic concept for bias removal involves recording the desired spectrum term on a spatial carrier, while leaving the bias terms as spatially unmodulated light levels. As the holographic recording process in the crystal reacts only to spatially modulated incident light, we can approximately time integrate the spectrum term in the crystal. The resulting time integrated charge pattern on the crystal is read out using an external beam that is Bragg matched to the spatial carrier on the crystal. First, the 1-D time integrating and 1-D space integrating interferometric subsystems of a 2-D continuous wave acousto-optic spectrum analyzer are experimentally tested. Then, a bias-free crystal based 1-D time integrating spectrum analyzer/correlator is demonstrated in the laboratory, and results are compared with the earlier bias infested outputs. Next, a 2-D bias free time and space integrating crystal based architecture for spectrum analysis is introduced. The experimental results from this system are described, and processor performance issues and limitations are discussed.

Chapter 6 introduces novel acousto-optic systems for control and signal processing in phased array radars. We begin with an introduction to the theory of

phased array radars, and look at the current phased array radar technology. In particular, we investigate the phase shifting device technology, and note that in the lower half of the microwave frequency spectrum ($\leq 10GHz$), current radars mainly employ digital phase shifters based on a hybrid microwave integrated circuit (HMIC) technology consisting of discrete and integrated components. Although this hybrid technology is robust, it leads to certain undesired features such as large system size, non-adaptability to changes in radar carrier frequency, multiple control signals, multiple phase shifting devices, higher design complexity of antenna feed networks, and high susceptibility to electromagnetic interference (EMI) problems. In effect, these hybrid technology based phased array radars are very hardware intensive, and thus are extremely expensive. In this thesis, we introduce **acousto-optic radar signal processors** that eliminate all problems associated with the hybrid phase shifter technology based radars [9,10]. The basic acousto-optic radar processor consists of two acousto-optic beam deflectors that map frequency deviations of the driving electronic signals to angular deflections of the two Bragg diffracted, doppler shifted beams in space, with the beams interfering at the output plane of the processor. An array of detectors samples the desired phase pattern, and is used to drive the phased array radar. Thus, this optical system produces global phase changes via a single control parameter, namely, the frequency of the control signal. Other features of the system include no phase shifters, adaptability to changes in radar carrier frequency, and EMI immunity. These features and others are discussed in the Chapter. We analyze a 1-D linear phased array antenna acousto-optic beam steerer, and present the basic design rules for the processor. The experimental results from the processor are presented, and processor performance issues such as phase linearity, detector phase sampling, and beam scan angle behavior, are analyzed. The impulse response of the radar processor is derived, and its antenna beam switching speed discussed. Capabilities of the optical processor are highlighted, including continuous beam scanning, simultaneous multiple beam formation, and coexistent multiple multifrequency beams. A multichannel AOD architecture is presented that produces simultaneous multiple beams. In addition,

transceiver systems based on the acousto-optic radar system are presented, including an all optical processing system. Various applications are introduced including a multitarget tracking and detection system. This processor can be built in either bulk or integrated forms, and the system architectures are proposed. Finally, the 1-D linear phased array radar processor is extended to multiple linear arrays, non-uniform phase sampling arrays, and planar arrays using fiber optic technology for sampling and antenna feed networks.

References:

[1] A. P. Goutzoulis and I. J. Abramovitz, "Digital electronics meets its match," *IEEE Spectrum* Cover Issue on Acousto-optics, 21, August, 1988.

[2] K. Wagner and D. Psaltis, "Time and Space Integrating Acousto-optic Folded Spectrum Processing for SETI," *Proc SPIE*, Vol. 564-31, 1985.

[3] N. A. Riza and D. Psaltis,"Multiplicative Time and Space Integrating Acousto-optic Architectures for Real-Time Spectrum Processing,"*Proc. SPIE*, Vol. 827-34, 1987.

[4] Y. S. Abu-Mostafa and D. Psaltis, "Optical Neural Computers," *Scientific American*, March 1987.

[5] D. Psaltis, M. A. Neifeld, A. Yamamura, and S. Kobayashi "Optical Memory Disks in Optical Information Processing," submitted to *Applied Optics.*

[6] "Optical disk based spectrum analysis," to be published with D. Psaltis.

[7] D. Psaltis, J. Yu, and J. Hong, "Bias free time integrating optical correlator using a photorefractive crystal," *Applied Optics*, Vol. 24, No.22, 15 November, 1985.

[8] "Performance and limitations of photorefractive crystal based bias free continuous wave architectures for spectrum analysis ," to be published with D. Psaltis.

[9] N. A. Riza and D. Psaltis, "An acousto-optic technique for beam scanning and beam formation in phased array radars," *OSA Annual Conf. Digest*, No. 0127, Oct-Nov., Santa Clara, CA, 1988.

[10] "Acousto-optic signal processors for transmission and reception of phased array radar signals," to be published with D. Psaltis.

CHAPTER 2

ACOUSTO-OPTICAL COMPUTING SYSTEMS

2.1 Introduction

Acousto-optic interaction, or the interaction between sound and light was first predicted by Brillouin in 1922 [1]. Almost sixty years have past since the first experimental verification of the acousto-optic effect by Debye and Sears in the United States and Lucas and Biquard in France. Today, acousto-optic technology has developed to the extent that it is the most mature electrical to optical transducer technology available [2,3]. Furthermore, there has been rapid development in other optical component technologies such as lasers, detectors, integrated optics, fibers, and passive optics. This simultaneous maturing of optical technologies has led to realizing practical and powerful analog signal processing systems for implementing certain computationally intensive operations that are otherwise difficult to achieve using alternative hardware technologies. For example, applications include spread spectrum communications, radar, and electronic warfare surveillance [4].

Fig. 2.1.1 shows the block diagram of a general acousto-optical computing system. This system consists of four basic components, i.e., light sources, light modulation devices, passive optics, and light detection devices. The goal of the system designer is to combine the best features of the available optical components to realize a compact, robust, high speed computing system that implements the desired signal processing operation. In this thesis, we will describe novel acousto-optical systems for spectrum analysis and phased array radar signal processing. This Chapter describes the underlying principles and techniques that are used to construct these acousto-optical systems. First, we shall introduce the simple acousto-optic device model that is used in system analysis thoughout this thesis. Next, other sys-

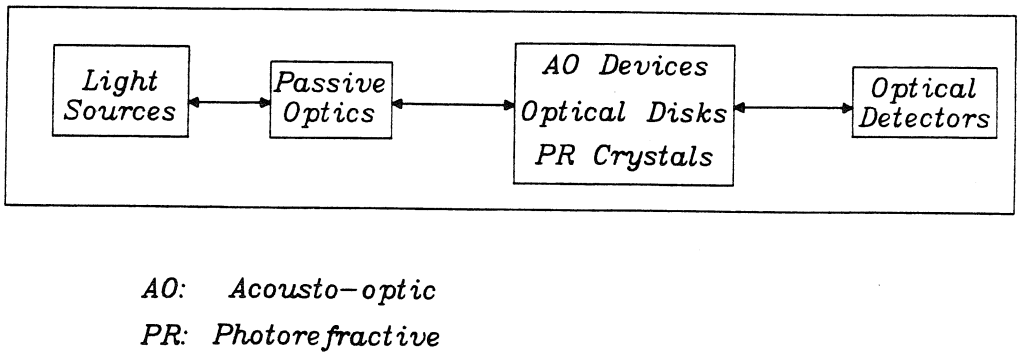

Fig.2.1.1 General acousto-optical computing system.

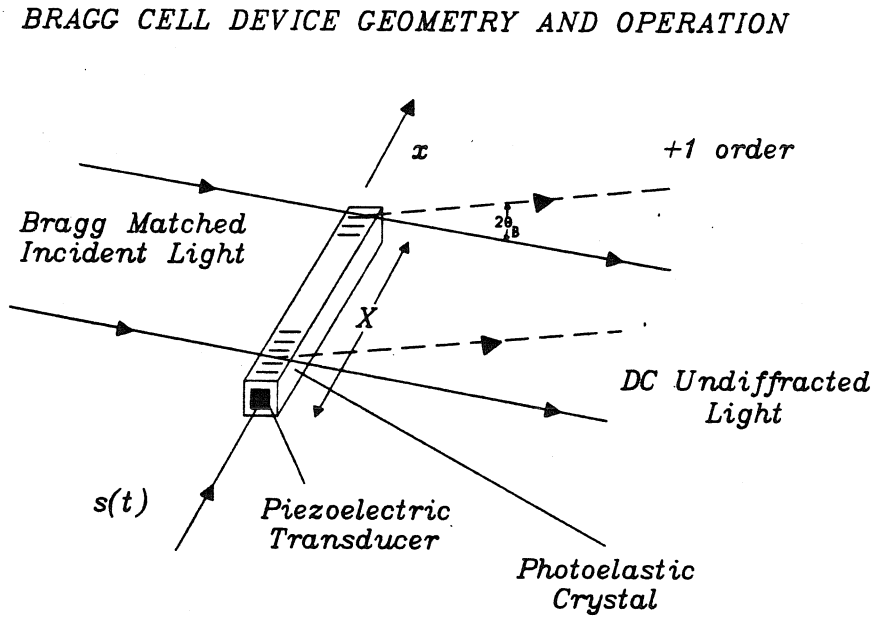

Fig.2.2.1 Device geometry of a Bragg cell.

tem components are described, and important performance issues are highlighted from a designer's point of view. In addition, optical processing techniques are introduced that are used to perform the desired signal processing transformations. In particular, we describe a multichannel AOD, programmable image correlator architecture.

2.2 The Acousto-optic Device Model

Basic acousto-optic devices exist in three different interaction geometries defined by the value of the parameter $a = (\delta\theta_o/\delta\theta_a)$, the ratio of divergence angles of the optical beam θ_o, and the acoustic beam θ_a. In the limit $a \ll 1$, the device acts as a optical beam deflector, while with $a \approx 1$, the device functions as a modulator. Furthermore, for the limit $a \gg 1$, the device performs as an optical filter. In this thesis, the acousto-optic deflector (AOD), or Bragg cell, will be used in the optical processing systems to be described later. The name Bragg cell derives from the particular Bragg angle incidence operation of the acousto-optic device, where the long interaction length between the acoustic and optical waves produces a volume diffraction effect allowing only one sideband of the diffracted beam to be produced. The analysis to follow gives a simple device model for the Bragg cell. This model is adequate for initial system analysis when designing acousto-optic systems. For a more in-depth study of the acousto-optic interaction and devices, the reader is referred to papers in the optics literature [5–9].

Fig. 2.2.1 shows the typical device geometry of a Bragg cell. The device consists of a transparent photoelastic crystal whose one end is bonded to a piezoelectric transducer. A bandlimited RF electronic signal $s(t)$ centered at frequency f_0 is applied to the transducer of the cell. In order to avoid non-linear, second harmonic intermodulation terms, the bandwidth of the signal must be less than $B \leq 2f_0/3$, corresponding to an octave bandwidth centered at f_0. The transducer is typically

designed to have a resonant octave bandwidth centered at f_0. The RF signal applied to the transducer launches an acoustic wave replica of the signal $s(t)$ that lies within the transducer's octave bandwidth. The acoustic wave travels with a velocity v_a along the crystal length X, and it is represented along the x direction by the expression:

$$u(x,t) = s(t - x/v_a)\text{rect}\left[\frac{x - X/2}{X}\right], \tag{2.2.1}$$

where

$$\text{rect}\left(\frac{x}{X}\right) = \begin{cases} 1, & \text{if } |x| \leq X/2; \\ 0, & \text{otherwise.} \end{cases} \tag{2.2.2}$$

An important device parameter is the acoustic delay time T_a that corresponds to the acoustic signal travel time across the finite window of the crystal. The product of the device delay T_a with the device bandwidth B gives the maximum number of resolvable analog samples that can be stored at any instant in the device. This product T_aB, also called the time bandwidth product of the Bragg cell, is an important system design parameter.

The acoustic signal induces a travelling wave volume index perturbation via the photoelastic effect in the crystal, causing a phase modulation along the crystal length that can be approximately represented as an optical transmittance function given by:

$$\begin{aligned} t(x,t) &= e^{j\epsilon s(t-x/v_a)} \quad \text{rect}\left[\frac{x - X/2}{X}\right] \\ &\approx [1 + j\epsilon s(t - x/v_a) + \ldots]\text{rect}\left[\frac{x - X/2}{X}\right], \end{aligned} \tag{2.2.3}$$

where ϵ is the modulation index that depends on the acoustic signal amplitude and the photoelastic interaction efficiency. For small diffraction efficiencies, the higher order terms of the phase modulation expansion can be neglected, giving only the first order travelling wave acoustic signal term $s(t - x/v_a)$. The real signal $s(t)$ can be expressed as its upper and lower sideband complex conjugate terms, as the analytic signal expansion gives $s(t) = [\tilde{s}(t) + \tilde{s}^*(t)]/2$. The transmittance of the

Bragg cell can be rewritten as:

$$t(x,t) = \left[1 \quad + \frac{j\epsilon}{2}\tilde{s}(t - x/v_a) + \frac{j\epsilon}{2}\tilde{s}^*(t - x/v_a)\right]\mathrm{rect}\left[\frac{x - X/2}{X}\right]. \qquad (2.2.4)$$

Similarly, the signal spectrum can be written as a purely negative frequency sideband $\tilde{S}(f) = \int_{-\infty}^{0} s(t)e^{-j2\pi ft}dt$, and a purely positive frequency sideband given by $\tilde{S}^*(f) = \int_{0}^{\infty} s(t)e^{-j2\pi ft}dt$. When collimated light from a coherent source such as a laser operating at a wavelength λ and temporal frequency $\nu = c/\lambda$ is incident as a tilted plane wave at the negative midband Bragg angle $\theta = -|\theta_B|$, where $|\theta_B| = \sin^{-1}(\lambda/2\Lambda_0) \approx \lambda/2\Lambda_0$ with respect to the acoustic propagation direction x, with the incident optical field expressed as:

$$a(x,z,t) = \mathrm{Re}[Ae^{-j2\pi[\nu t - \sin\theta_B x/\lambda + \cos\theta_B z/\lambda]}], \qquad (2.2.5)$$

the incident light is efficiently coupled into the upshifted single sideband of the first order diffracted wave. In other words, when the optical field is incident at the negative Bragg angle on the thick index perturbation, with the x component of optical field counterpropagating with respect to the acoustic wave direction, the last term in Eqn. 2.2.4 produces negligible diffraction, and the optical field is said to undergo $+1$ order diffraction represented by the purely negative sideband of the signal. This purely negative frequency sideband is responsible for a doppler upshifting of the optical carrier, as the analytic representation of the optical carrier is chosen as a negative temporal frequency. When the incident optical field is incident at the positive Bragg angle, the first signal term in Eqn. 2.2.4 gives negligible diffraction, and the diffracted optical field from the last term in Eqn. 2.2.4 is downshifted. Thus, the light modulated by the Bragg cell can be approximately expressed as the product of the incident optical field with the appropriate single sideband transmittance of the Bragg cell. For a $+1$ order upshifted Bragg geometry, the emerging optical

field is given by:

$$b(x,z,t) = a(x,z,t)t_+(x,t)$$
$$\approx Ae^{-j2\pi[\nu t - \sin\theta_B x/\lambda + \cos\theta_B z/\lambda]}\left[1 \quad + \frac{j\epsilon}{2}\tilde{s}(t-x/v_a)\right]\mathrm{rect}\left[\frac{x-X/2}{X}\right], \tag{2.2.6}$$

where the explicit notation of the real part of the coherent optical field has been dropped for analysis purposes in this thesis. The expression in Eqn.2.2.6 consists of an undiffracted term that propagates along the input angle $-\theta_B$, and a doppler upshifted first order diffracted term centered around the midband angle $+\theta_B$. Here the midband acoustic wavelength $\Lambda_0 = v_a/f_0$, where f_0 is the midband frequency of the Bragg cell. To see the effect of doppler upshifting, as well as beam deflection, let's consider a single tone input signal at the frequency f. For $s(t) = \cos(2\pi ft) = [e^{j2\pi ft} + e^{-j2\pi ft}]/2$, the diffracted field is given by:

$$\begin{aligned} d_f(x,z,t) &= Ae^{-j2\pi[\nu t - \sin\theta_B x/\lambda + \cos\theta_B z/\lambda]}\frac{j\epsilon}{2}e^{-j2\pi f(t-x/v_a)}\mathrm{rect}\left[\frac{x-X/2}{X}\right] \\ &= A\frac{j\epsilon}{2}e^{-j2\pi[(\nu+f)t + (f-f_0/2)x/v_a + \cos\theta_B z/\lambda]}\mathrm{rect}\left[\frac{x-X/2}{X}\right], \end{aligned} \tag{2.2.7}$$

where the device has been Bragg matched for the midband frequency f_0 with the $+\theta_B = \sin^{-1}(\lambda f_0/2v_a) \approx (\lambda f_0/2v_a)$. Note that the temporal frequency of the field has increased by an amount equal to the input temporal frequency, resulting in a positive doppler shift. Also, the angular spatial frequency of diffraction is linearly related to the input signal frequency. Thus, the diffracted optical field emerging from the Bragg cell has been temporally and spatially modulated by the input signal $s(t)$. Dropping the z propagation term for simplicity, the diffracted optical field for an input signal $s(t)$ at midband frequency f_0 can be expressed as:

$$d(x,t) = A\frac{j\epsilon}{2}e^{-j2\pi[\nu t - f_0 x/2v_a]}\tilde{s}(t-x/v_a)\mathrm{rect}\left[\frac{x-X/2}{X}\right]. \tag{2.2.8}$$

This is the basic modulation introduced by a Bragg cell, where the diffracted optical field is a windowed travelling wave replica of the single sideband of the octave

bandwidth input signal $s(t)$. This diffracted field experiences a temporal frequency shift equal to the signal frequency, and is spatially deflected by an angle proportional to the signal frequency. These two properties of the Bragg cell form the basic optical modulation techniques that are used to accomplish various signal processing tasks throughout this thesis. A simpler model of the Bragg cell drops the optical carrier term, along with the multiplicative constants, and the optical axis is aligned with the input signal drirection. This gives the diffracted field from the Bragg cell to be:

$$d(x,t) = \tilde{s}(t - x/v_a)\text{rect}\left[\frac{x - X/2}{X}\right]. \tag{2.2.9}$$

In general, this expression will be used in the analysis of acousto-optic systems to be described in this thesis. Sometimes, it is convenient to reference the window function at the center of the AOD. In this case, the diffracted field is expressed as:

$$d(x,t) = \tilde{s}(t - x/v_a - T_a/2)\text{rect}\left[\frac{x}{X}\right], \tag{2.2.10}$$

where $T_a/2$ is the acoustic time delay from the transducer end of the device to the center of the cell.

From the coupled mode theory of the Bragg interaction in the thick acousto-optic medium, we can express the diffracted field amplitude $A_d(v)$ normalized by the incident field amplitude A_i as:

$$\frac{A_d(v)}{A_i} = -j\frac{cv}{|cv|}\sin(|cv|L), \tag{2.2.11}$$

where v is the applied acoustic signal voltage, L is the interaction length in the crystal, or the transducer width, and c is the coupling constant per unit applied voltage, that depends on paramters such as crystal photoelastic constant, and piezoelectric coupling efficiency [5,10]. Fig.2.2.2(a)shows the behavior of the normalized diffracted field amplitude with applied acoustic voltage as expressed in Eqn. 2.2.11. Note that for small diffraction efficiencies ($\leq 10\%$), the optical field amplitude varies linearly

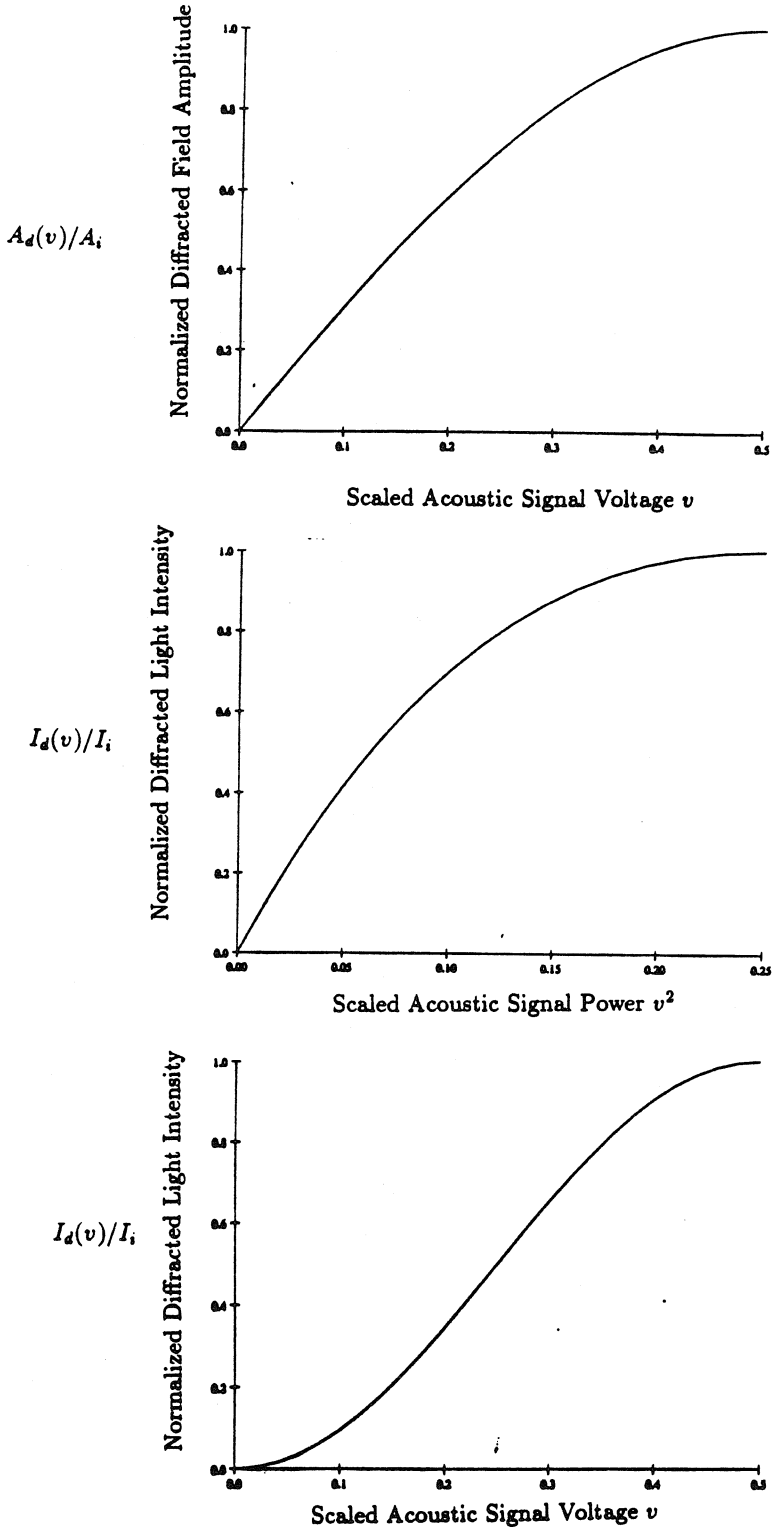

Fig.2.2.2 Plots show different AOD response curves: (a) Behavior of the normalized diffracted field amplitude with applied voltage, (b) Behavior of the normalized diffracted light intensity with applied acoustic power, and (c) Behavior of the normalized diffracted light intensity with applied acoustic voltage.

with the applied acoustic signal amplitude. This property of the device permits its use in implementing linear electrical to optical signal transformations. The diffraction efficiency based on the ratio of the diffracted light intensity to the incident light intensity is given by:

$$\frac{I_d(v)}{I_i} = \sin^2(|cv|L) \approx (|cv|L)^2, \tag{2.2.12}$$

and is plotted against applied acoustic power in Fig.2.2.2(b). Here, the diffracted light intensity varies linearly with acoustic power for small diffraction efficiencies corresponding to small arguments of the sine function. Another approach to obtaining linear intensity modulation is shown by the curve in Fig.2.2.2(c), where the desired modulating signal amplitude is biased around the linear region of this diffracted intensity versus acoustic amplitude curve [11]. Certain drawbacks of this bias dependent intensity modulation scheme include small modulation depth, large bias signal requirements, and large acoustic power related problems such as nonlinear acoustic effects in the crystals.

In summary, some of the key features of the acousto-optic deflector (AOD) or Bragg cell include (a) temporal modulation through the doppler effect, (b) amplitude, phase and intensity modulation, (c) storage/time delay capability, (d) beam deflection capability, and (e) one dimensional (1-D) spatial light modulation. In this thesis, the mentioned AOD features will be combined in one dimensional (1-D) and two dimensional (2-D) optical systems to perform specific processing operations. For instance, the AOD beam deflection and doppler properties will be used in the optical phased array radar signal processors that are introduced later in the thesis.

Commercially available Bragg cells come in a variety of specifications. Typical materials used for the crystals include fused silica, Tellurium dioxide, Gallium Phosphide, and Lithium Niobate. Devices exist in large aperture, high resolution, high diffraction efficiency designs, as well as in wide bandwidth designs [12–14]. For

example, devices exist with bandwidths ranging from 30 MHz @f_0 = 50 MHz to 2 GHz @f_0 = 3 GHz. Typical device storage capability or space bandwidth product is around 2000 for large aperture cells. Apart from single channel cells, certain companies are providing multichannel Bragg cells. For instance, a 32 channel, 200 MHz bandwidth, f_0 = 400 MHz multichannel device is available [15]. Recently, a two dimensional, single element, acousto-optic beam deflector has been introduced [16,17]. Unlike 1-D acousto-optic deflectors, this 2-D acousto-optic deflector is capable of deflecting laser beams in 2-D space. As described later in the thesis, this particular device can be used for phased array radar beam azimuth/height control. The acousto-optic devices described to this point have been bulk devices, as an unguided acoustic wave travels though a thick crystal. Another sister technology, called the surface acoustic wave (SAW) device technology exists along side the bulk technology. The basic principles of the SAW technology are similar to the bulk technology. In SAW devices, the acousto-optic interaction is in a 2-D planar geometry, and not in a 3-D volume. This results in miniaturization of the acousto-optic device. Today, many robust, vibration resistant integrated optic SAW based signal processors have been demonstrated [18–20].

2.3 Optical System Components and Issues

The previous section featured the acoustic optic device model. In this section, we will briefly describe other optical system components that compose an acousto-optical computing system. The optical source is not only the power supply of an optical system, but also acts as the information carrier for communication and distribution of data throughout the optical system. In addition, the light source can be directly modulated to provide an additionnal port of signal entry into the optical system. Typical sources used in optical information processing systems include semiconductor laser diodes, gas lasers, and semiconductor light emitting diodes

(LED's). Depending on a system's power and size constraints, along with specific design requirements, a different type of light source may be optimum. Semiconductor laser diodes are highly efficient, compact, robust, highly coherent, infrared (800-1600 nm) light sources with $10 - 200$ mW continuous wave light power. Recently, relatively low power (4 mW), highly reliable, visible (670nm) laser diodes have been introduced into the market [21]. Small physical size ($300\ \mu m \times 10\ \mu m \times 50\ \mu m$), direct pumping by low power electric currents (15 ma at 2 volts), high electrical to optical conversion efficiency ($\geq 20\%$), direct light modulation capability exceeding 10 GHz rates, and monolithic integration with other III-V semiconductor optical and electronic devices to form optoelectronic circuits, make semiconductor laser diodes the most attractive light source for practical optical computing systems [22]. Compared to LED's that have a large light emitting area ($\approx 1\ mm^2$), and a broad spectral width (≈ 50 nm), laser diodes typically have $1 - 5$ nm spectral widths, with a higher light directivity, allowing for applications in coherent optical processing, where temporal and spatial coherence of the light source plays an important role in system performance [23–25]. Nevertheless, LED's are very inexpensive, highly reliable, visible/infrared, incoherent light sources that are used in incoherent, intensity based optical processing [26,27].

The laser diode can also be used in a pulsed mode, where an appropriately biased narrow pulse signal drives the diode junction. This approach is used in the spectrum analysis experiments described in Chapter 3, where the pulsing action of the laser diode is used to freeze the travelling acoustic signal in the AOD, and simultaneously heterodyne signal frequency components to baseband. Unfortunately, the pulsing action adversely efffects the temporal coherence of the laser diode. This problem is mainly due to interpulse modal hopping and frequency drifting, and can be reduced by biasing the laser just below threshold, with the drive signal rise time and pulse amplitude carefully adjusted [28]. This system issue is particularly

important while designing interferometric optical processors. Finally, continuous wave gas lasers are excellent sources of highly coherent, high power laser energy. Unfortunately, because of their large cavity size and bulky and power consuming electronics, they are limited mainly to laboratory and ground based systems. In this thesis, both laser diodes and gas lasers have been used in the experiments. In particular, they include the Hitachi HLP 1600 laser diode, the Laser Diode Incorporated LA-65 pulsed laser diode, 10 mW Helium-Neon lasers, and a 2.5 Watt single line Argon ion laser.

Optical detection in acousto-optic systems is typically achieved by semiconductor high speed point detectors, and 1-D/2-D charge coupled devices (CCD's). Various high bandwidth ($\geq$ 1 GHz) point detectors are commercially available, such as PIN photo-diodes, avalanche photo-diodes, and photo-transistors [29,30]. These devices are also manufactured in linear array formats, and are particularly suited for high speed parallel readout of spatially multiplexed channels. In this thesis, 3 nsec rise time silicon PIN photodiodes are used to detect the 120 MHz phased array radar antenna drive signals that are generated by an acousto-optic processor. Similarly, photo-transistors connected to electronic charge integrators (OP amps) are used to detect charge in spatially multiplexed frequency channels in an optical disk based spectrum analyzer. 1-D and 2-D CCD's are used as detection and time processing devices in the acousto-optic systems. In the time integration mode, the CCD collects spatially processed light signals over a coherent processing frame time. In the time delay and integrate mode (TDI), the CCD acts as a time integrating signal processor capable of implementing the correlation operation. Present CCD technology is mature, with devices like the Tektronix CCD, with 2048 $\times$ 2048 pixels [31–33]. The experiments described in this thesis employ the XC-37 Sony black and white 2-D CCD array with 384 $\times$ 491 pixels, using the time integrate/staring mode [34]. Important system issues associated with optical detection devices include

optical signal-to-noise ratio of the detected image, noise from driving electronics, spectral responsivity, rise time/bandwidth, pixel size, and photo response linearity.

The link between the light sources and optical detectors in an acousto-optic system is established via various passive optical components. These optical components spatially transform and distribute the optical wavefronts to other active and passive devices in the system. For instance, lenses can be used for light collimation, spatial Fourier transforming, imaging, and focussing operations, where spherical and cylindrical lenses perform 2-D and 1-D spatial transformations, respectively [35]. Similarly, beam splitters can be used as three port optical devices that add and split optical beams. The light from the processing components in the optical computing system is recollected on the optical detectors by additional passive optics, thus completing the communication link between sources, processing elements, and detectors. Today, many companies manufacture high quality, passive optical components for scientific and commercial applications [36]. Typical component parameters that affect system performance include component aperture size, surface flatness, polarization dependence, and presence of antireflection coatings.

Apart from using acousto-optic devices as spatial and temporal light modulators in optical processing systems, other device technologies are also being incorporated into various processing architectures [37,38]. In this thesis, we will introduce the application of optical disk and photorefractive technologies in acousto-optic spectrum analysis. Chapter 4 describes how the high storage density and angular motion of the optical disk can be used for reference signal generation in optical spectrum analysis. In addition, Chapter 5 deals with the application of photorefractive crystals as time integrating bias removers in interferometric acousto-optic spectrum analyzers.

2.4 Optical Processing Techniques

Optical processing techniques can be divided into three main categories. These techniques are: space processing, time processing, and hybrid time and space processing, respectively. In this thesis, a combination of these processing techniques will be incorporated into new signal processing architectures. The following sections briefly describe the concepts of these optical processing methods.

2.4.1 Space Processing

Space processing shown in Fig.2.4.1.1 involves the mapping of light from one spatial region A at $z = z_0$ along the optic axis z, to another spatial region B at $z = z_0'$. Typical mappings include spatial Fourier transforming, imaging, and free space Fresnel transformations. The classic space processing element is the space integrating spherical lens [39]. When used in the appropriate configuration, the spherical thin lens can be used as a powerful two dimensional spatial Fourier transformer, as shown in Fig.2.4.1.2, or as an imaging/interconnection device, as displayed in Fig.2.4.1.3. The architecture in Fig.2.4.1.2 forms the basic building block of two dimensional space integrating spectrum analysis [39]. When an input with amplitude transmittance $f(x, y)$ is placed at the front focal plane of a spherical lens of focal length F, the back focal plane produces the coherent 2-D spatial Fourier transform of $f(x, y)$. In other words, the lens implements the linear transformation:

$$F(u,v) = \int_{-\infty}^{+\infty}\int_{-\infty}^{+\infty} f(x,y)e^{-j\frac{2\pi}{\lambda F}(xx'+yy')}dxdy, \qquad (2.4.1.1)$$

where λ is the wavelength of the coherent light, x, y are the spatial coordinates of the input plane, and $u = x'/\lambda F$, $v = y'/\lambda F$ are the output plane spatial frequency coordinates. The ability of a lens to map spatial frequency components at the input Fourier plane to spatially separated frequency components at the output

SPACE PROCESSING

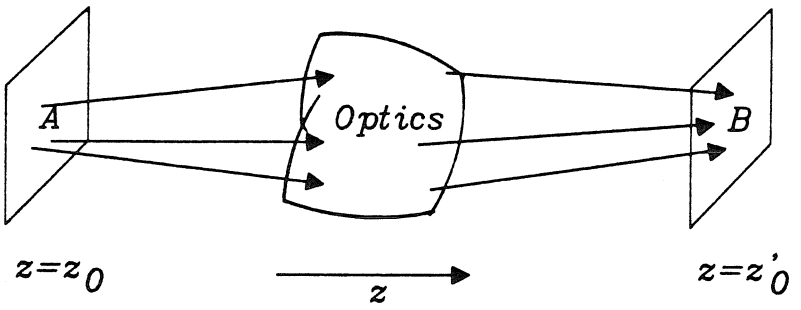

Fig.2.4.1.1 Optical space processing.

FOURIER TRANSFORM SPHERICAL LENS

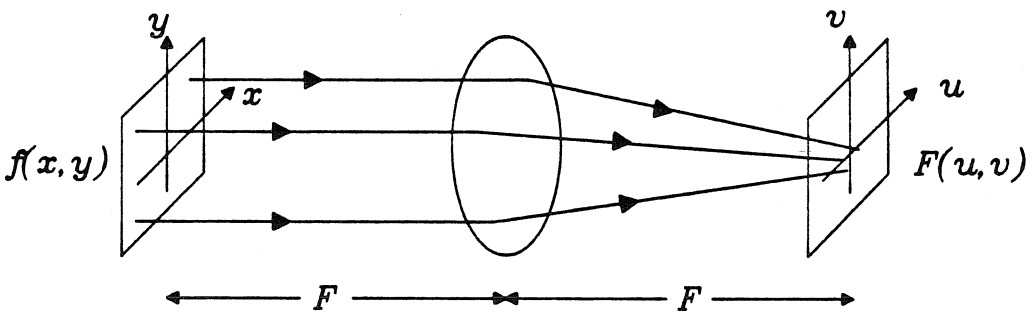

Fig.2.4.1.2 Spherical lens as a two dimensional spatial Fourier transformer.

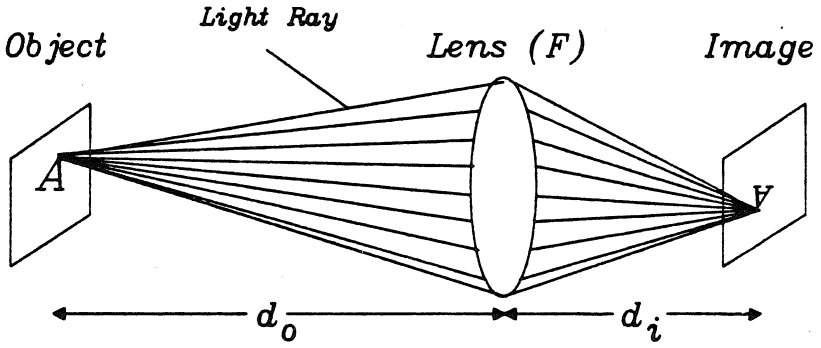

Fig.2.4.1.3 Lens as an imaging/interconnection device.

Fourier plane makes possible certain spatial operations. For example, input spatial data can be spatially separated into parallel output plane channels by using spatial frequency multiplexing of the input Fourier plane data [40]. In addition, Fourier plane spatial filtering can be accomplished to alter or remove certain input signal spatial features [41]. Fig.2.4.1.3 shows the imaging operation, another powerful linear 2-D spatial transformation by a spherical lens [35]. Here, with the imaging condition, $1/d_i + 1/d_0 = 1/F$, satisfied, the output plane contains an inverted, scaled, diffraction limited replica of the input image. This operation is readily used to schlieren image the acoustic travelling waves in a Bragg cell to other processing planes. In addition, the imaging operation is also used for interconnecting points in the input image plane to certain points in the output image plane. The lens has been used extensively in numerous optical space processing architectures for signal and image processing, and recently in neural network processors [42–44].

From the linearity of the free space wave equation, light propagation in a coherent optical system can be modelled as a linear system represented by the superposition integral,

$$E(x',y') = \int_{-\infty}^{+\infty}\int_{-\infty}^{+\infty} h(x',y';x,y)E(x,y)dxdy, \qquad (2.4.1.2)$$

where $E(x,y)$ is the input plane optical field, $h(x',y';x,y)$ is the free space impulse response for optical propagation, and $E(x',y')$ is the output plane optical field after light propagates a distance z in the optical system. For the special Fresnel diffraction case,

$$h(x',y';x,y) = \frac{e^{jkz}}{j\lambda z} exp\left[j\frac{k}{2z}[(x'-x)^2 + (y'-y)^2]\right], \qquad (2.4.1.3)$$

where $h(x',y';x,y) = h(x'-x, y'-y)$ is a linear, shift-invariant impulse response, and the wave number $k = 2\pi/\lambda$. This linear shift-invariant property of the Fresnel propagation allows the optical system designer to use Fourier domain frequency

analysis techniques associated with linear time invariant systems theory [35]. In this thesis, a variety of different space processing techniques will be used to accomplish the desired linear transformations.

2.4.2 Time Processing

Apart from the two dimensional coordinate space that is available to an optical system designer, time provides another important degree of freedom to the system architect. **Time** can be used to optically process information in discretized steps or continuously. Over the years, a variety of temporal processing schemes have been devised [45]. Here, we will briefly highlight some of the time processing techniques used in this thesis. For instance, repetitive pulsing of a light source can be used to divide a long time signal into smaller duration signals, that can be represented in the finite window of an optical system. Thus, this repetitive pulsing technique converts an otherwise large time bandwidth product signal into a smaller space bandwidth product signal that exists as a space-time rastered signal in the optical system. Pulsing can also be used to heterodyne temporal signal spectrums to baseband via the Nyquist limited aliasing phenomenon. In addition, pulsing is used to freeze acoustic signals in Bragg cells for schlieren imaging. This repetitive signal freezing and imaging results in a temporally modulated spatial light distribution. In Chapter 3, this technique is used to implement the discrete Fourier transform algorithm (DFT) using spatial optics and time. As Bragg cells represent continuously travelling acoustic waves in time, continuous time processing plays an important role in a certain class of processors. For example, in time integrating acousto-optic correlators, the continuous nature of the operation allows for an almost unlimited correlation time window, finally limited by the dynamic range of the time integrating detector [46].

Optical detectors play an important role in time processing, and can be utilized

in a variety of modes. An optical detector can be used to continuously collect spatially processed light for further temporal integration over a desired coherent frame time. For instance, in Chapter 3, a time integrating 2-D CCD array is used to implement the DFT algorithm to complete the 2-D space-time Fourier transform operation. The CCD can also be used in a special time-delay and integrate (TDI) or scrolling mode where integrated charge is sequentially shifted and added to previously accumulated charge along a CCD dimension [47]. This type of TDI CCD photo detector has been used to implement incoherent correlation operations [48]. Another light detecting element is the high speed photodetector that produces an electric current that is modulated by the intensity modulated signal incident on the detector photo-sensitive surface. This type of high speed optical detection is used in the acousto-optic phased array radar processor experiments discussed in this thesis. Also, the current generated from these high speed point detectors can be collected in an external charging circuit to implement longer signal processing frame times. This approach was used in the continuous wave optical disk based spectrum analyzer experiments described later in the thesis.

Although time processing offers the system designer with another important variable for implementing multidimensional linear transformations, it leaves an undesired gradual build up of DC and signal dependent bias light in the time integrating optical detectors, which finally limits the processor dynamic range and performance, respectively. Unfortunately, optical detectors react to light intensity, which is a positive quantity. This makes it necessary to represent biploar signals with a bias term, making the DC bias an unwanted, yet necessary, term in time integrating processors. In the past, two electronic techniques have been employed for bias removal [10]. They involve two CCD or computer bias substraction, and electronic carrier demodulation, respectively. The experimental results in Chapter 3 use computer bias substraction. Later, in this thesis, we will describe how pho-

torefractive crystals can be used for bias removal in interferometric optical spectrum analyzers.

2.4.3 Time and Space Processing

The unavailability of high quality, fast, two dimensional spatial light modulators, along with the presence of the highly mature, one dimensional, real-time, acousto-optic spatial light modulator technology, has led to the concept of two dimensional optical processing using one dimensional devices [49]. The spatial dimension of the acousto-optic device coupled with time as the other orthogonal dimension, are used to transduce very large time bandwidth product signals such as images and long 1-D signals into the optical processing system. This real-time, simultaneous, time and space processing technique allows for multidimensional optical computing. In particular, Chapter 3 of this thesis shows how time and space integrating (TSI) optical architectures are combined to provide wideband, high resolution, 2-D optical spectrum analysis of large time bandwidth product signals. The hybrid time and space processing approach combines some of the best features of both space processing and time processing, respectively. For example, space processing provides an extremely high instantaneous data throughput, while time processing allows for very large processing windows. These attributes of time and space processing allow for wide bandwidth, high resolution, optical spectrum analysis.

2.5 An Application: Multichannel AOD Programmable Image Correlator

The 2-D correlation operation is an important image processing operation with applications in pattern recognition, image restoration and enhancement, and video compression. The basic 2-D correlation operation between a signal image $f(x, y)$

and a reference image $h(x,y)$ can be expressed as:

$$g(x',y') = \int\int f(x,y)h^*(x+x',y+y')dxdy. \tag{2.5.1}$$

Past acousto-optic approaches for image correlation have used time and space integrating, and 2-D time integrating optical processing techniques [48,50–52]. One approach uses a Fourier transform hologram for storing the reference image, and a time integrating, shift and add (TDI) mode CCD detector array to perform the time integrating 1-D correlation [50]. As this system uses a hologram to store the reference image, it is not fully programmable for real time operation, and changing the reference image requires the fabrication of another hologram, which has to be critically reinserted into the optical system. An alternate version of this system uses a magneto-optic device to store a computer generated Fourier transform hologram, thus making the correlator programmable. Nevertheless, due to the relatively small space bandwidth product of the magneto-optic device, this system is limited to processing small reference images. Another approach proposed is the incoherent electro-optic image correlator which solves the programmability problem, nevertheless, introduces such problems as incoherent bias build-up, and correlations limited to small (100×100) reference images.

The architecture shown in Fig. 2.5.1 is a coherent, interferometric, fully programmable, acousto-optic image correlator, where the multichannel AOD is used to input the reference image into the optical system. This architecture is based on the frequency plane correlation technique, where the correlation is accomplished by multiplying the Fourier transforms of the signal and reference images, respectively. In other words, the correlation expression in Eqn. 2.5.1 can be written as:

$$g(x',y') = FT^{-1}\{F\,H^*\}, \tag{2.5.2}$$

where F is the spatial Fourier transform of the input image $f(x,y)$, H^* is the complex conjugate spatial Fourier transform of the reference function $h(x,y)$, and

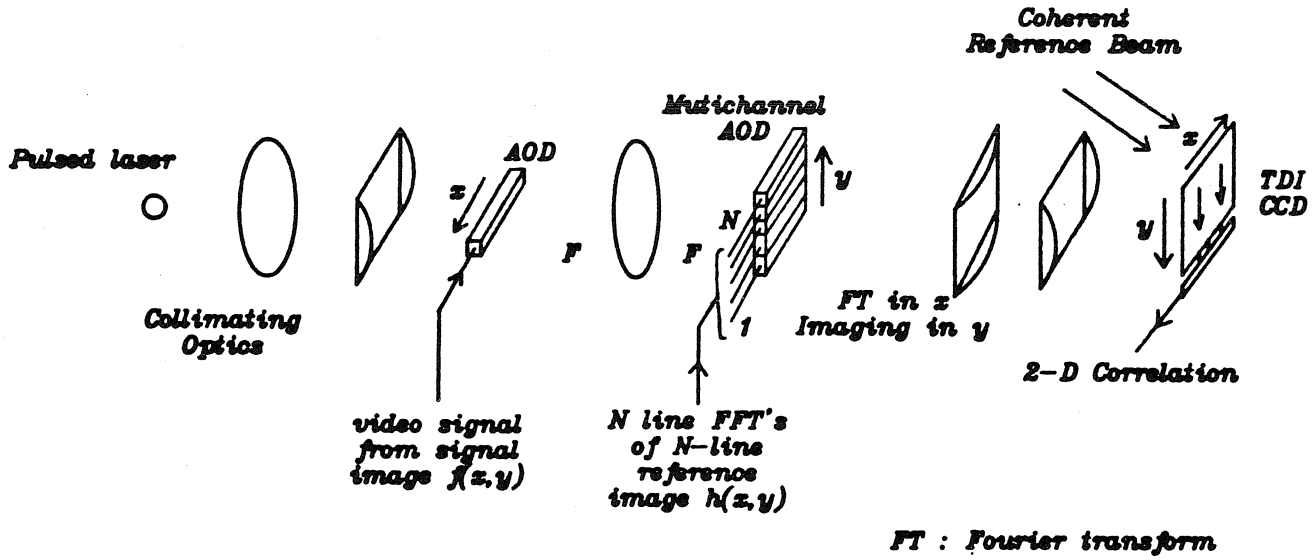

Fig.2.5.1 Multichannel AOD programmable coherent image correlator.

FT^{-1} represents the inverse Fourier transform operation. The basic operation of this processor is very similar to the holographic correlator that implements the 2-D spatial correlation as a space-time 2-D correlation with orthogonally oriented space and time integrating systems, respectively [48,50]. This space-time 2-D correlation can be expressed as:

$$g(x', y') = \sum_n \int f(x, nd) h^*(x + x', nd + y') dx, \tag{2.5.3}$$

where n is the light pulse number corresponding to the n^{th} video line in the signal image, and d is the spatial shift of the charge pattern on the TDI CCD for every light pulse. The signal image is introduced into the system through the single channel AOD, on a video line by line basis. The spherical lens takes the Fourier transform of the Bragg diffracted video line, giving a 1-D spatial Fourier spectrum at the multichannel AOD plane. The reference image is scanned by a video camera, and the video signal is fed to a frame grabber that snaps one frame in order to generate N line Fast Fourier transforms (FFT) corresponding to the N lines in the reference function. These line FFT's are stored in a computer memory, and read out simultaneously to drive the N acoustic columns in the multichannel AOD. The read out rate is synchronous with the signal video line rate that also triggers the light pulses, giving the effect of a standing 1-D Fourier transform phase hologram. After N light pulses, and some delay time, the desired 2-D correlation scrolls out of the TDI CCD. Because of interferometric detection, the correlation output is generated on a spatial carrier along the non-scrolling x' direction of the CCD. This feature allows for bias removal in the processor.

Currently available multichannel AOD's have a maximum of 32 channels, implying a reference function size of $N = 32$ in the scrolling y' direction of the processor. In order to process larger filter functions, we can employ **space and frequency multiplexing** to simultaneously input all the reference image line Fourier trans-

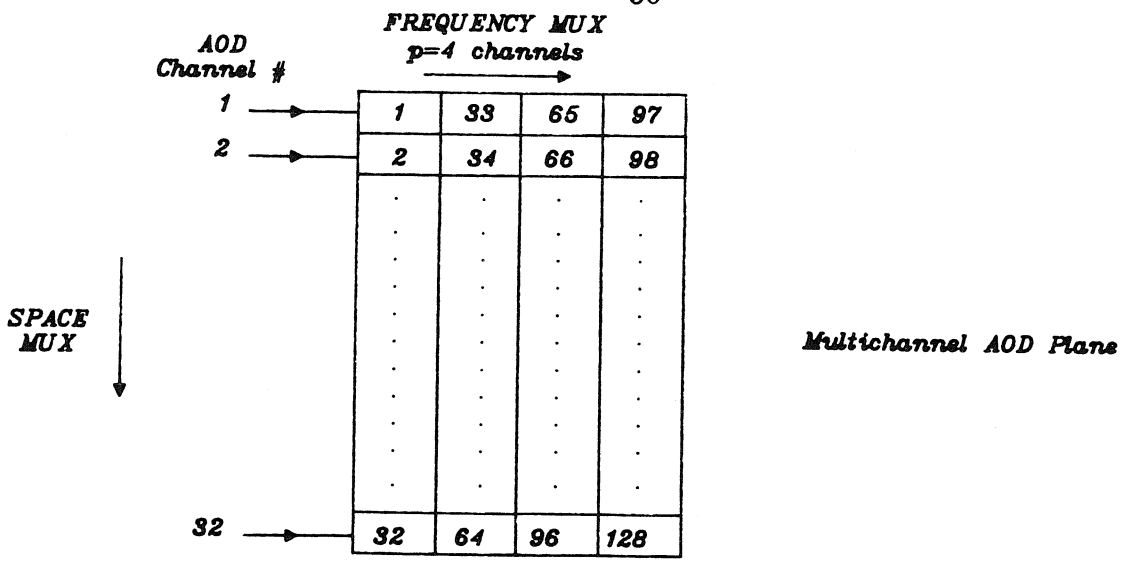

Fig.2.5.2 Frequency and space multiplexing of reference image line Fourier transform data in the multichannel AOD.

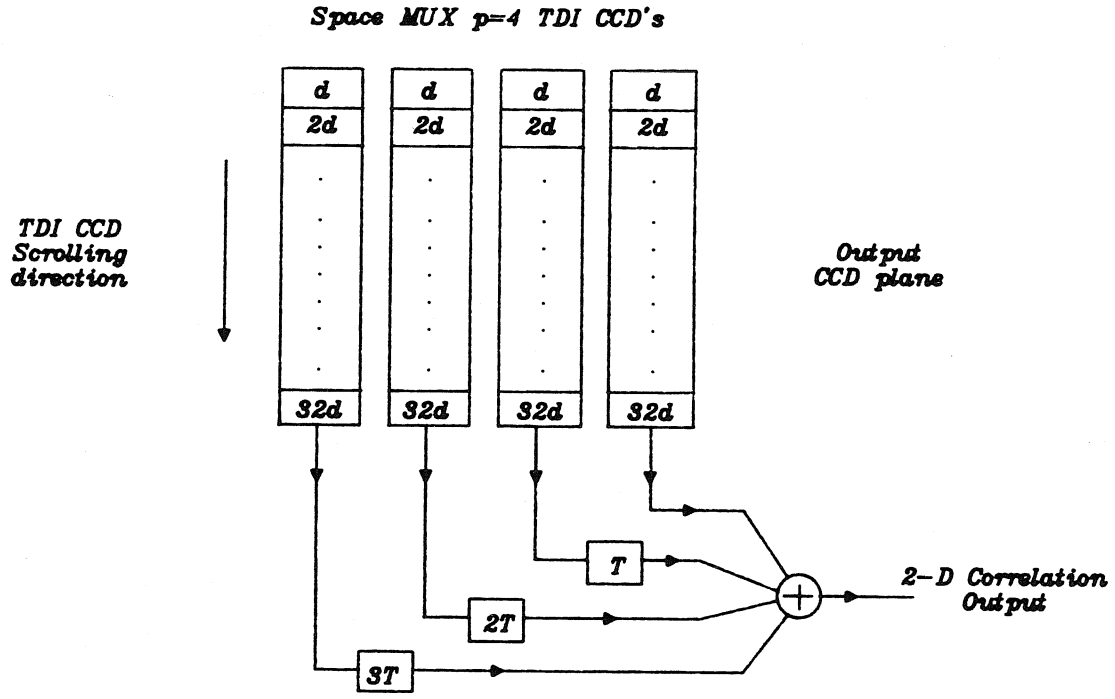

d = unit spatial shift along scrolling direction of TDI CCD

T = 32d/v time delay ; v = CCD scroll velocity in mm/sec

Fig.2.5.3 Delay lines associated with the space multiplexed TDI CCD's to generate the 2-D correlation.

forms into the multichannel AOD [40,53]. One multiplexing approach is shown in Fig. 2.5.2 for $N = 32p$, where $p = 4$. Each number in the AOD grid represents the line Fourier transform of the respective line in the reference function. In this case, each AOD channel is fed by $p = 4$ frequency multiplexed signals that are detected by $p = 4$ spatially multiplexed TDI CCD's at the output correlation plane of the processor. The outputs of these TDI CCD's are further time delayed by certain values before being summed in an electronic adder to give the desired 2-D correlation (See Fig. 2.5.3). The time delay step between the adjacent CCD's corresponds to 32 time scrolling intervals of the TDI CCD. For standard TV rate processing, the scroll interval is the video line time of $63.6\mu sec$, giving an external time delay step of $2.03msec$. Thus, in order to process larger ($N \geq 32$) filter functions along the scrolling direction of the CCD, additional electronics has to be added to the processor. For the non-scrolling direction, the AOD's provide a very large space bandwidth product (≈ 2000), enabling filter functions of large size. Moreover, recall that this processor is programmable, and allows real time bias removal.

2.6 Conclusion

In this Chapter, we have discussed the basic building blocks of an acousto-optical computing system. A simple model for the acousto-optic deflector (AOD) or Bragg cell was presented, and other system components such as light sources, detectors, and passive optics were introduced. Moreover, time, space, and the hybrid time and space optical processing techniques available to the optical system designer were highlighted. In addition, a programmable, multichannel AOD image correlator architecture is described from a system's point of view. In conclusion, this Chapter has set the stage for further exploring the various acousto-optic systems and concepts that are introduced in this thesis.

References:

[1] L. Brillouin, "Diffusion de la lumière et des rayons X par un corps transparent homogène," *Ann Phys. (Paris)*, Vol. 17, 88-122, 1922.

[2] P. Debye and F. W. Sears, "On the scattering of light by supersonic waves," *Proc. Nat. Acad. Sci (U.S.)*, Vol. 18, 409-414, June, 1932.

[3] R. Lucas and P. Biquard, "Propriètès optiques des milieux solides et liquides soumis aux vibration èlastiques ultra sonores," *J. Phys. Rad.*, Vol. 3, 464-477, 1932.

[4] A. P. Goutzoulis and I. J. Abramovitz, "Digital electronics meets its match," IEEE Spectrum Cover Issue on Acousto-optics, 21, August, 1988.

[5] I. C. Chang, "Acousto-optic interactions - a review: I. Acousto-optic devices and applications," *IEEE Trans. Sonics & Ultrasonics*, Vol. SU-23(1), 2, 1976.

[6] B. A. Auld, *Acoustic Fields and Waves in Solids*, John Wiley & Sons, New York, 1973.

[7] J. Sapriel, *Acousto-optics*, John Wiley & Sons, New York, 1979.

[8] A. Yariv and P. Yeh, *Optical Waves in Crystals*, John Wiley & Sons, New York, 1984.

[9] A. Korpel, Acousto-optics, in Applied Solid State Science, Vol. 3, R. Wolfe, Ed, Academic Press, New York, Ch. 2, 73, 1972.

[10] K. Wagner, Time and space integrating acousto-optic signal processing, Ph.D. Thesis, Chapter 4, Caltech, 1987.

[11] R. A. Sprague and C. L. Koliopoulos, "Time integrating acousto-optic correlator," *Applied Optics*, Vol. 15(1), 89, 1976.

[12] Crystal Technology Data Sheets (1988), Model 4075-4, TeO_2 slow shear AOD, B=50 MHz @f_0=75 MHz, T_a=100 μsec, T_aB=5000, 200%/RF Watt efficiency, 30 dB contrast ratio, Palo Alto, CA.

[13] Crystal Technology Mini Catalog (1988), Model 41000S-GP, GaP shear AOD, B=0.5 GHz @f_0=1 GHz, T_a=1 μsec, T_aB=500, 10%/RF Watt efficiency; Model 42000L-LN, $LiNbO_3$ Longitudinal AOD, B=1 GHz @f_0=2 GHz, T_a=1 μsec, T_aB=1000, 1.5%/RF Watt efficiency, Palo Alto, CA.

[14] Brimose Corp. Specification Sheet (1988), RAST-1 GaP Longitudinal AOD, B=1 GHz @f_0=1.5 GHz, T_a= 0.5 μsec, T_aB= 500, 20%/RF Watt efficiency; LINS-3 $LiNbO_3$ Shear AOD, B= 2.5 GHz @f_0= 2.5 GHz, T_a= 0.3 μsec, T_aB= 750, 2%/RF Watt efficiency, Baltimore, MD.

[15] Crystal Technology Mini Catalog (1988), Model MC400-1, TeO_2 Longitudinal 32 Channel AOD, B=200 MHz @f_0=400 MHz, T_a=5 μsec, T_aB=1000, 30%/RF Watt efficiency, Channel Isolation$\geq$ 30 dB, Palo Alto, CA.

[16] R. G. Rosemeier, J. I. Soos, and J. Rosenbaum, "A single element 2-D acousto-optic GaP laser beam steerer," *SPIE Proc.*, No. 89807, Los Angeles, CA, Jan., 1988.

[17] Brimose Corp. Specification Sheet (1989), 2DL-475 GaP Longitudinal 2-D AOD, B=150 MHz @f_0=475 MHz, T_a=0.16 μsec, T_aB=24, 80%/RF Watt efficiency, Baltimore, MD.

[18] Crystal Technology Inc. Mini Catalog of SAW Devices (1989), Model B0294, $LiNbO_3$ SAW non-dispersive delay line, B= 400 MHz @f_0= 700 MHz, T_a= 9.6 μsec, T_aB= 384; plus SAW bandpass filters, resonators, and SAW monolithic signal processors such as pulse compressors and convolvers, Palo Alto, CA.

[19] R. L. Davis (Northrop Corporation), "Integrated optic interferometric spectrum analyzer," *SPIE Proc.*, 1988.

[20] R. G. Hunsperger, *Integrated Optics: Theory and Technology*, Chapter 16, Springer Series in Optical Sciences, Vol. 33, Springer-Verlag, 2nd Ed., New York, 1985.

[21] Visible CW laser diodes: NEC Model NDL3200, 3mW power, 680nm @100ma,

newer model is 4mW @ 670nm, 85ma, life of 250,000 hrs; Toshiba America Inc. Model TOLD9200, 3mW power, 670nm @85ma, life $\geq$ 10,000 hrs, 58 & 199, Photonics Spectra, April, 1989.

[22] J. Shibata and T. Kajiwara, "Optics and electronics are living together," IEEE Spectrum, 34, February, 1989.

[23] A. Yariv, *Optical Electronics*, Chapter 15, Holt, Rinehart and Winston, 3nd Ed., New York, 1985.

[24] J. Gowar, *Optical Communication Systems*, Prentice Hall International Series in Optoelectronics, Series Editor: P. J. Dean, London, 1984.

[25] Laser Diode Inc. Catalog (1988), Components: CW laser diodes, LED's, pulsed laser diodes and arrays, fiber optic data links and systems, New Brunswick, NJ; Spectra Diode Labs DDL-2420 200 mW CW laser diode, Optics News, 24, December (1985).

[26] D. Psaltis and N. Farhat, "Optical information processing based on an associative memory model of neural nets with thresholding and feedback," *Optics Letters*, Vol. 10, No.2, February, 1985.

[27] D. Psaltis, E. G. Paek, and J. Hong, "Acousto-optic implementation of the Hopfield model," *JOSA*, 2, No.13, 48, December, 1985.

[28] M. Haney and D. Psaltis, "Measurement of the temporal coherence properties of pulsed single mode laser diodes," *Applied Optics* , Vol. 24(13), 1926, 1985.

[29] Telefunken Infrared Detectors, Emitters, and Laser Devices Data Book(1986), Heibronn, West Germany.

[30] United Detector Technology Data Sheets (1988), Hawthorne, CA.

[31] Tektronix CCD Model TK2048M, 2048 $\times$ 2048, $27\mu m \times 27\mu m$ pixel size, 10 MHz output bandwidth (C amplifier), 10 nA/cm^2 dark current, Tektronix, Beaverton, Oregon.

[32] EG & G Reticon Model RA1200J CCD, 400 $\times$ 1200 pixels, 140,000:1 dynamic

range @ 120°K, noise floor 3.5 noise electrons per pixel @120°K, Sunnyvale, CA; Konan Model L4000 linear CCD, 4096 pixels, 1024 pixels × 4 channel output data @10 MHz per channel, Chronix Inc., Tokyo, Japan; 184 & 214, Photonics Spectra, April, 1989.

[33] J. R. Janesick et.al., "Scientific charge coupled devices," *Optical Engineering*, Vol.26, No.8, August, 1987.

[34] XC-37 SONY CCD Manual, 384 × 491, $23\mu m \times 13.4\mu m$ pixel size, 7.16 MHz clock frequency, S/N≥ 46 dB, Standard video output, 1985.

[35] J. W. Goodman, *Introduction to Fourier Optics*, McGraw-Hill Inc., 1968.

[36] Spindler & Hoyer Precision Optics Guide 1989, Gottingen, West Germany; Melles Griot Optics Guide 1989, Irvine, CA.

[37] D. Psaltis, M. A. Neifeld, and A. A. Yamamura, "Optical disk based correlation architectures," OSA Topical Meeting, Salt Lake City, Utah, Feb.- March, 1989.

[38] D. Psaltis, J. Yu, and J. Hong, "Bias free time integrating optical correlator using a photorefractive crystal," *Applied Optics*, Vol. 24, No.22, 15 November, 1985.

[39] K. Preston, "Use of the Fourier transforming properties of lenses for signal spectrum analysis," in *Optical and Electrooptical Information Processing*, J. T. Tippet *et al.* Eds. MIT Press, Cambridge, MA, 1965.

[40] D. Casasent, "Frequency multiplexed acousto-optic architectures and applications," *Applied Optics*, Vol.24(6), 856, 1985.

[41] A. Vander Lugt, "Signal detection by complex spatial filtering ," *IEEE Trans. Info. Theory*, IT-10, 139, 1964.

[42] *Optical Data Processing: Applications*, edited by D. Casacent, Topics in Applied Physics, Vol.23, Springer-Verlag, New York, 1977.

[43] *Optical Information Processing: Fundamentals*, edited by S. H. Lee, Springer-Verlag, New York, 1981.

[44] Y. S. Abu-Mostafa and D. Psaltis, "Optical Neural Computers" , Scientific American, March, 1987.

[45] P. Kellman, "Time integrating optical signal processing," *Optical Engineering.*, Vol.19(3), 370, 1980.

[46] R. A. Sprague and C. L. Koliopoulos, "Time integrating acousto-optic correlator," *Applied Optics*, Vol.15(1), 89, 1976.

[47] D. F. Barbe, "Imaging devices using the charge coupled concept ," *Proc. IEEE*, Vol.63, 38-67, Jan., 1975.

[48] E. G. Paek *et. al.*, "Acousto-optic image correlators," *Proc. SPIE*, Vol.638-05, 1986.

[49] D. Psaltis, "Two dimensional optical processing using one dimensional input devices ," *Proc. IEEE*, Vol.72(7), 962, 1984.

[50] D. Psaltis, "Optical Image Correlation using Acouto-optic and Charge-coupled Devices,"*Applied Optics*, Vol. 21, 491, 1982.

[51] D. Psaltis, "Incoherent Electro-optic Image Correlator," *Optical Engineering*, Vol.23, No.1, Jan.-Feb., 1984.

[52] T. Turpin, "Time Integrating Optical Processing," *Proc SPIE*, Vol 154, 196, 1978.

[53] D. Casasent, "General Time, Space and Frequency Multiplexed Acousto-optic Correlator," *Applied Optics*, Vol. 24, No 17, 1985.

CHAPTER 3

PULSED SOURCE TWO DIMENSIONAL SPECTRUM ANALYSIS

3.1 History and Background

Spectrum analysis is a basic tool in science and engineering, with past and present applications in a wide variety of disciplines such as medicine, astronomy, geology, radar signal analysis, etc. The processing power and natural simplicity of optical spectrum analysis was realized a long time ago, when it was discovered that a simple spherical lens can produce at its back focal plane, the two dimensional (2-D) spatial Fourier transform of an image at the front focal plane. This meant that an image of at least 1000 × 1000 points could be transformed into a million or more parallel spatial frequency channels in the amount of time it takes the light to travel between the two focal planes. This almost instantaneous spectrum processing power led to many successful film based two dimensional optical spectrum analyzers for image analysis. Later, Thomas [1–4] invented a wideband, high resolution, signal spectrum analysis scheme using the same basic lens optical system. This technique, called folded spectrum analysis, is shown in Fig.3.1.1. It requires the long (10^6 points) one dimensional time signal to be written as a two dimensional raster signal on a two dimensional spatial light modulator such as film. The lens takes the two dimensional spatial Fourier transform of the raster, giving a wideband, high resolution signal Fourier transform written in a two dimensional raster format of mutually orthogonal wideband (coarse) and high resolution (fine) spatial frequency axes, respectively. When unrastered, this coarse/fine 2-D spatial raster produces the wideband, high resolution, one dimensional (1-D) spectrum of the signal.

The ideal optical spectrum analyzer needs a 2-D spatial light modulator with dynamic range and resolution properties comparable to film, and high temporal bandwidth capabilities to permit real-time spectrum analysis. Unfortunately, present-day programmable 2-D spatial light modulators lack these required specifications. Nevertheless, for the past ten years, there have been high quality, 1-D programmable,

PRINCIPLE OF FOLDED SPECTRUM SYSTEMS

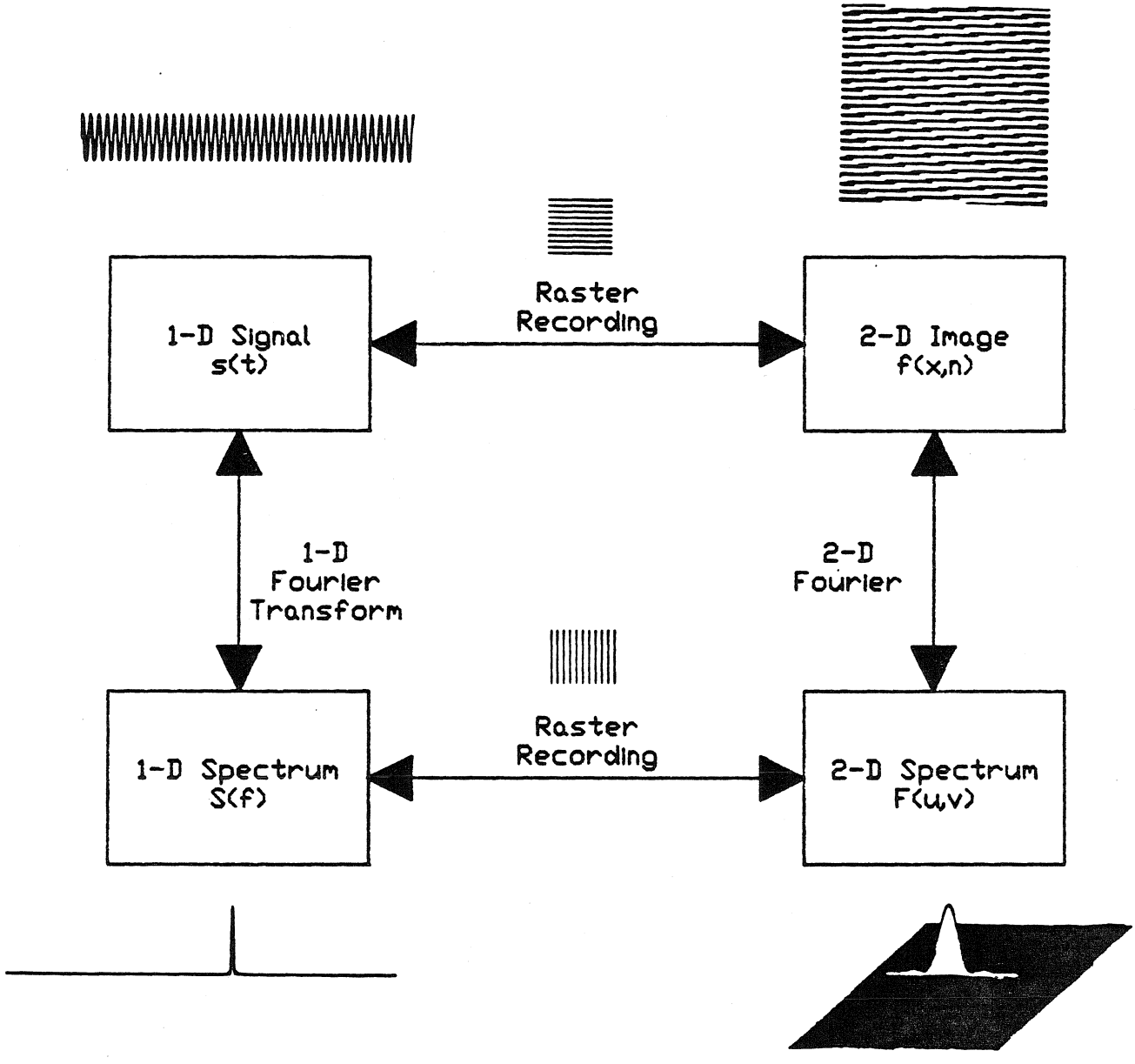

Fig.3.1.1 Principle of folded spectrum processing.

acousto-optic spatial light modulators available. It is for this reason that researchers have explored these 1-D programmable acousto-optic devices for real-time 1-D and 2-D spectrum analysis.

3.2 Introduction

So far, various approaches to building 2-D optical folded spectrum systems have been considered, such as 2-D space integrating techniques employing 2-D spatial light modulators (SLM's) [4,5], 2-D time integrating methods using 1-D acousto-optic devices and electronic reference signals [6–8], and a combination of time and space integrating (TSI) techniques employing acousto-optic devices and charge coupled device (CCD) detector arrays, respectively [9–14]. The motivation to explore optical TSI techniques to build spectrum analyzers was partly generated by the Search for Extra-Terrestrial Intelligence (SETI) program, which requires a wideband, multichannel, high resolution, high sensitivity spectrum processor to detect narrowband highly coherent beacon signals buried in a sea of broadband white noise coming from outerspace [12]. With the present state of the art in optical transducer and detector technology, the TSI approach to spectrum processing provides some of the best features desired in an optical spectrum analyzer [15], i.e., high system bandwidth provided by the high bandwidth AOD's, and excellent frequency resolution controlled by the detector integration time, although obtaining both high bandwidth and high resolution simultaneously is difficult [14]. In this chapter, the additive and multiplicative time and space integrating acousto-optic pulsed source architectures for two dimensional spectrum analysis are presented and experimental results are shown. The additive design uses the Mach-Zehnder interferometer, where two separate optical beams corresponding to the signal and reference signals are added on a 2-D time integrating detector. In the multiplicative design, a single optical beam is modulated in succession by separate signal and reference acousto-optic modulators, respectively. In both systems, a 1-D space integrating acousto-optic spectrum analyzer is used to provide the signal coarse frequency components, while a 1-D time integrating acousto-optic processor implements the Discrete Fourier Transform (DFT) algorithm to provide the

signal fine frequency components [16].

3.3 Pulsed Source TSI Processing Principles

In this and the following Sections, two possible implementations of a time and space integrating (TSI) crossed Bragg cell folded spectrum processor that utilizes a pulsed laser diode as the optical source will be considered [12–14]. Here, the pulsed laser is used as an alternate approach to using the reference distributed local oscillator (DLO) in Bader's continuous light time and space integrating spectrum analyzer [10,11]. The DLO is defined as a uniform array of evenly spaced blur spots in the Fourier plane of the reference AOD, each with a field oscillating at one distinct well defined temporal frequency, which linearly increases as a function of space. Any broadband signal having uniform power over the desired analysis bandwidth can be used to generate a reference DLO by repetitively applying it to the reference AOD in a space integrating spectrum analyzer. The reference DLO is used to interferometrically beat the output of a space integrating acousto-optic spectrum analyzer to baseband [10]. In this pulsed source method, the sampling action of the pulsed laser effectively aliases interferometrically detected tones to baseband, thereby removing the coarse frequency content, leaving only the fine frequency for subsequent time integrating processing. Fine frequency analysis of each coarse frequency bin can be performed with a number of possible techniques. We use a multichannel DFT implemented on a starring CCD array as a spatially multiplexed bank of time integrating matrix vector multiplication modules. Let us now look at how time and space integrating processing principles are applied to signal and video spectrum analysis, respectively.

3.3.1 Signal Processing Principles

Fig.3.3.1.1 shows the general architecture for a pulsed source acousto-optic TSI folded spectrum processor. Since the limited time bandwidth product of the AOD will not allow the entire signal to be within the aperture simultaneously, successive overlapping portions of the long signal will slide into the AOD and the acoustic motion

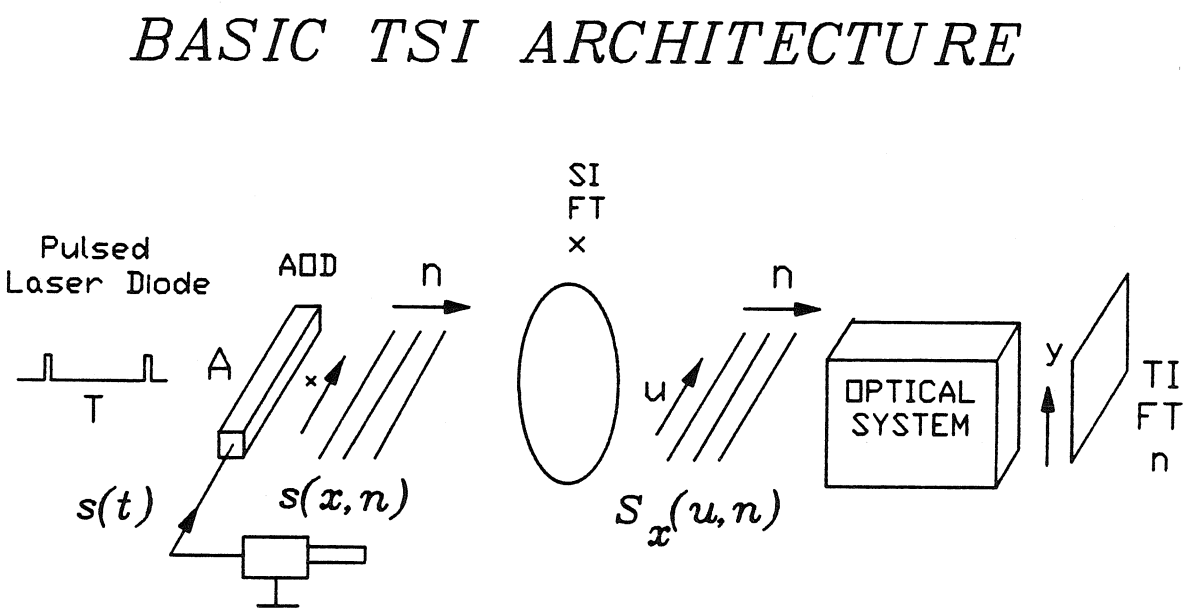

Fig.3.3.1.1 General pulsed source time and space integrating architecture for folded spectrum processing.

will be frozen by pulsing the laser with a very narrow pulse. This laser pulse train can be approximately written as:

$$p(t) = \sum_{n=0}^{N-1} \delta(t - nT - t_0), \tag{3.3.1.1}$$

where t_0 is a fixed time delay used to accommodate the signal in the illuminated AOD aperture. For each laser pulse the AOD converts part of the input signal into a 1-D spatial modulation of a coherent optical wave front, and on successive pulses it will convert succeeding portions of the input signal into the optical system. Thus, the long 1-D signal has been transformed into a 2-D raster of space x, and discrete time or pulse number n. The transformation performed by the AOD illuminated with a repetitively pulsed laser produces a raster of space and time, where the spatial dimension is continuous, and time is discrete. The pulsing effect of the laser on the signal $s(t)$ fed to the AOD can be approximately expressed as:

$$s(x, nT) \approx \int s\Big(t - \frac{x - X/2}{v_a}\Big) \mathrm{rect}\Big[\frac{x}{X}\Big] \delta(t - nT - t_0)\, dt \tag{3.3.1.2}$$

$$s(x, nT) = s\Big(nT + t_0 - \frac{x - X/2}{v_a}\Big) \mathrm{rect}\Big[\frac{x}{X}\Big], \tag{3.3.1.3}$$

where the integration is over the time variable t in the CCD detector. In this expression X is the AOD aperture, T is the laser pulse repetition interval, and n indexes the pulse number. If the AOD temporal window is greater than the laser pulse repetition interval $T_a = \frac{X}{v_a} \geq T$, then the raster is oversampled, which means that successive raster lines contain overlapping portions of the signal. The desired 1-D Fourier transform can be performed on the input signal $s(t)$ with a 2-D transform on its oversampled space-time raster representation $s(x, n)$. Because of the separability of the multidimensional Fourier kernel,

$$e^{-j2\pi(ux+vy)} = e^{-j2\pi ux} e^{-j2\pi vy}, \tag{3.3.1.4}$$

a 2-D transformation can be performed as N_y 1-D transforms along the x axis followed by N_x 1-D transforms along the orthogonal y axis, resulting in a transform with $N_x N_y$

independent spectral measurements. This cascaded system can be implemented by performing a spatial Fourier transform in x with a lens on the diffracted wave front for each of the N_y laser diode pulses, producing an intermediate data set, $S_x(u,n)$, which is also a space-time raster. This is followed by an array of N_x parallel time integrating narrowband Fourier transform modules multiplexed in the spatial frequency variable u, which utilize the second spatial dimension y to perform the desired accumulation of partial products, thereby Fourier transforming $S_x(u,n)$ across n. After a succession of N_y laser diode pulses the full folded spectrum is produced in a 2-D format on a time integrating CCD detector array. The rastered 1-D signal produced at the output from the 2-D detector array gives the wideband, high resolution, 1-D spectrum of the input signal $s(t)$. This is the principle of pulsed source time and space integrating (TSI) spectrum processing, and it is schematically shown in Fig.3.3.1.1.

A simple analytical representation of the idealized action of this system is a cascade of a 1-D continuous Fourier transformation, and a 1-D discrete Fourier transform.

$$S(u,m) = \sum_{n=0}^{N-1} [\int_X s(x,n) e^{-j2\pi ux} dx]\, e^{-j2\pi \frac{mn}{N}}. \qquad (3.3.1.5)$$

The spatial integral is performed across the aperture X of the AOD and produces a space integrating output spectrum with normalized spatial frequency variable $u = \frac{x'}{\lambda F}$ with a corresponding temporal frequency $f = uv_a$. The N laser diode pulses are multiplied by a vertical linear phase factor and coherently summed to produce a bank of time integrating DFT processors to complete the folded spectrum operation.

3.3.2 Video Processing Principles

The concept of folded spectrum processing can easily be applied to real-time image spectrum analysis. In fact, the natural raster scanning mechanism of a real-time imaging device such as a television (TV) camera adapts very well to the time and space integrating acousto-optic technique for spectrum analysis. For instance, a typical 512 × 512 pixel video image $f(x,y)$ is 1:1 imaged on to a 2-D sensor, such as a CCD. The video rastering mechanism of the CCD camera converts the 2-D spatial

intensity distribution to a long serial waveform $s(t)$ consisting of 512 image line time Sections, each line being separated by some synchronizing signal information. This signal $s(t)$ is called the baseband video signal, and can be written as:

$$s(t) = \sum_{n=0}^{N-1} f[v_r(t - nT), n\Delta y]\text{rect}(\frac{t - nT - T_l/2}{T_l}) \qquad (3.3.2.1)$$

Here, every n^{th} image line is scanned over its physical size A in a time $t = nT$ to $t = nT + T_l$ seconds, at a scan velocity of $v_r = A/T_l$. The spatial separation between successive image lines is Δy. This sequential line by line scanning is done for all N (e.g. 512) lines. For a typical video signal, $T_l \approx 52\mu sec$, and $T \approx 63\mu sec$, with almost $11\mu sec$ of signal synchronizing (non-image) information between lines . For our image analysis purposes, this synchronizing information is not required during optical processing. The typical Tellurium dioxide slow shear wave AOD has a time aperture of $70\mu sec$, with a time bandwidth product of more than 1000. These AOD specifications are more than adequate to transduce $52\mu sec$ duration, 512 point video line signals into a diffracted optical field. This baseband video signal is introduced into the optical system by mixing it to the Bragg cell transducer center frequency ω_0, giving an amplitude modulated (AM) signal with a double sideband (DSB) spectrum. At a time $t = nT + t_0$, a complete video line fills the illuminated aperture of the Bragg cell, where t_0 is the fixed time delay used for centering the video line in the defined AOD coordinates. At this instant, the laser is pulsed in synchronism with the camera raster scanning rate $1/T$, resulting in the spatial modulation of the optical wave front by a video line of the image. The light source is triggered by a very narrow train of pulses, with each pulse instantly freezing a video line that falls within the illuminated aperture of the Bragg cell. This successive pulsing of the light source in synchronism with the video camera line rate converts the serial video signal into a light modulated space-time raster of successive video image lines, where the n^{th} image line +1 order

optical wave front is approximately represented by:

$$\begin{aligned} s(x,nT) &\approx \int s(t-\frac{x-X/2}{v_a})e^{-j\omega_0(t-\frac{x-X/2}{v_a})}\delta(t-nT-t_0)dt \\ &= f[k_1(x-X/2),n\Delta y]e^{-j\omega_0 nT}\mathrm{rect}(\frac{x}{X})e^{j\frac{\omega_0}{v_a}[x-X/2]} \\ &\approx f[k_1(x-X/2),n\Delta y]e^{-j\omega_0 nT}\mathrm{rect}(\frac{x}{X}), \end{aligned} \tag{3.3.2.2}$$

where the amplitude term is a spatially scaled version of the n^{th} image line, with the scaling constant $k_1 = -\frac{v_r}{v_a}$, $X = v_a T_l$, and $t_0 = T_l$. The carrier spatial phase or light deflection $e^{j\frac{\omega_0}{v_a}[x-X/2]}$, has been dropped by aligning the space integrating lens in the time and space integrating processor with the diffracted wave front, while the temporal pulse to pulse variation term can be cancelled by either ensuring that the carrier frequency is an integer multiple of the video line rate, or by interfering the wave front with an identical frequency carrier wave front from the signal or reference AOD.

The formation of this video image space-time raster implies that in order to obtain an image spectrum with a time and space integrating processor, each spatially modulated image line is Fourier transformed by a lens to produce the image spatial frequency components along the x or temporally fast direction of the image, while the successive spatial transforms over all the N pulses are processed in a time integrating spectrum analyzer to resolve the image spatial frequency components along the orthogonal y (n) or temporally slow dimension of the image. The charge integrated on the 2-D optical sensor gives the desired 2-D Fourier spectrum of the image in a (u,v) spatial frequency coordinate space corresponding to the orthogonal spatial frequencies in the image. Because of the standard video rastering format of both the input video image camera, and the output 2-D optical sensor (CCD), real-time operation of the time and space integrating processor is natural to image analysis, providing image spectrum outputs after every video frame time (typically 1/30 sec).

For a TV camera looking at a tilted grating image with a spatial frequency u_0 in the x coordinate (fast temporal variation), frequency v_0 in the y (slow) direction of successive raster lines, and image line spatial resolution Δy, the image is represented

as:

$$f(x, n\Delta y) = \cos[2\pi(u_0 x + v_0 n\Delta y)]. \tag{3.3.2.3}$$

This expression is employed in Section 3.7 to find the image impulse response of the multiplicative time and space integrating processor. Next, we discuss the 1-D space integrating spectrum analyzer using a pulsed light source.

3.4 Space Integrating Interferometric Pulsed Source Spectrum Analyzers

Theory and Experiment:

The space integrating part of the 2-D time and space integrating spectrum processor can be implemented by two different optical architectures. The generic Mach-Zehnder interferometric architecture is shown in Fig.3.4.1, while an in-line additive architecture is shown in Fig.3.4.2. Both systems employ the 1-D space integrating pulsed source acousto-optic spectrum analyzer using a Fourier transform lens to obtain the input signal spectrum coarse frequency components as spatially resolved spectral bins. The +1 order Bragg diffracted field amplitude at the detector plane is given by:

$$\begin{aligned} E(x', t) &= \int \tilde{s}(t - \frac{x - X/2}{v_a}) \text{rect}(\frac{x}{X}) e^{-j2\pi x \frac{x'}{\lambda F}} dx \; e^{-j2\pi\nu t} \\ &= \int c\, \tilde{S}(f) e^{j2\pi f t} B(u + \frac{f}{v_a}) df \; e^{-j2\pi\nu t}, \end{aligned} \tag{3.4.1}$$

In the Eqn. 3.4.1, F is the Fourier transform lens focal length, $\tilde{S}(f)$ is the temporal Fourier spectrum of the analytic signal $\tilde{s}(t)$, and $B(u)$ is the blur spot taking into account the finite aperture of the Bragg cell and additional apodization effects [17]. Also, x and x' are coordinates on the AOD and detector planes, respectively, with $u = \frac{x'}{\lambda F}$, $e^{-j2\pi\nu t}$, the optical carrier, and $c = e^{j\pi f \frac{X}{v_a}}$, a signal frequency dependent phase term. In futher analysis, we drop the optical oscillation term for simplicity. Thus, on the n^{th} laser pulse at time $t = nT + t_0$, the optical field is given by:

$$E(u, n) = \int c\, \tilde{S}(f) e^{j2\pi f(nT + t_0)} B(u + \frac{f}{v_a})\, df, \tag{3.4.2}$$

where $t_0 = X/v_a$. In order to retain the phase information of the signal spectrum given in Eqn. 3.4.2, we have to perform interferometric detection using a reference

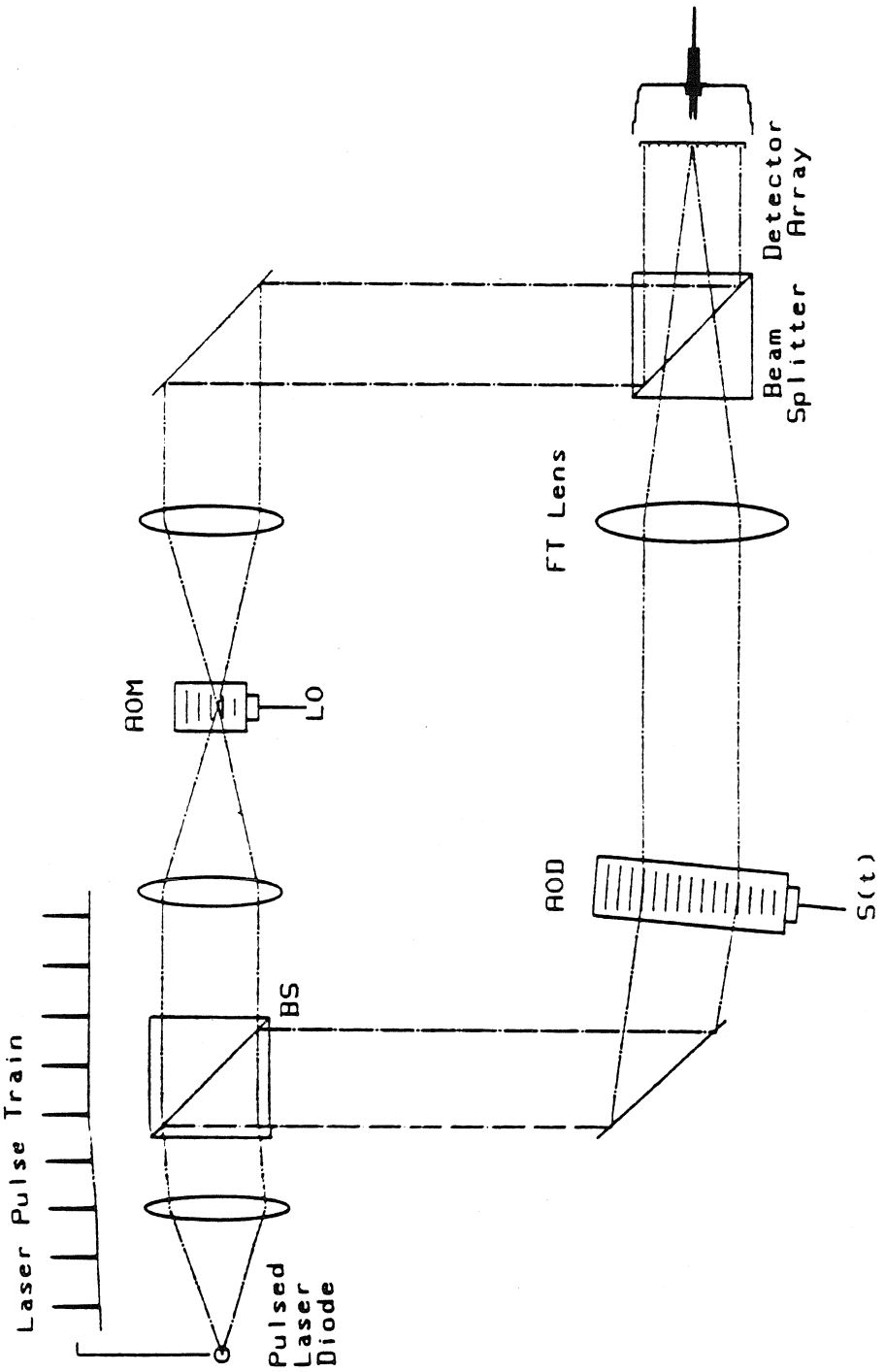

Fig.3.4.1 The 1-D acousto-optic pulsed source space integrating Mach-Zehnder spectrum analyzer.

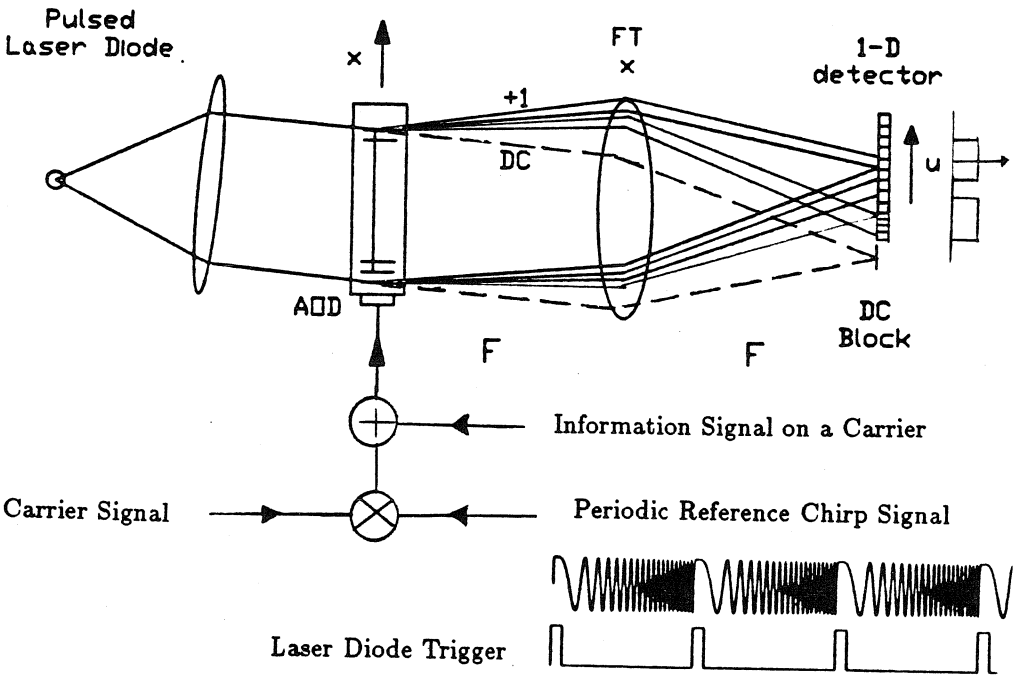

Fig.3.4.2 The 1-D acousto-optic pulsed source space integrating in-line additive spectrum analyzer.

signal $r(x',t)$. In this case, the intensity at the detector plane on the n^{th} pulse is given by:

$$I(u,n) = \left| \int c\, \tilde{S}(f) e^{j2\pi f(nT+t_0)} B(u + \frac{f}{v_a})\, df + r(x',t) \right|^2. \tag{3.4.3}$$

Both the Mach-Zehnder and in-line additive systems use a pulsed laser diode with a pulse repetition period of T seconds and a narrow pulse with a width of τ seconds. The interferometrically detected signal is aliased down to baseband by using the periodic nature of the pulse train as long as the pulse width is less than the inverse of the bandwidth of the signal $s(t)$, and much greater than the optical period of oscillation. The reference signal $r(x',t)$ can be introduced by either electronic or optical means.

In the **Mach-Zehnder** configuration, the reference signal is introduced via the acousto-optic modulator (AOM) as an optical plane wave front of spatial width X', doppler frequency f_0, and spatial frequency α_0 with respect to the undiffracted signal beam. The reference +1 diffracted optical field in the reference arm is given as:

$$r(x',t) = r_0 e^{-j2\pi f_0 t}\, e^{j2\pi\alpha_0 x'} \mathrm{rect}(\frac{x'}{X'}), \tag{3.4.4}$$

where r_0 is the amplitude term. For a single tone input signal with the +1 diffracted order $\tilde{s}(t) = a e^{-j2\pi(f_0+f')t}$ with spectrum $\tilde{S}(f) = a\,\delta(f + f_0 + f')$, and the pulsing action every T seconds of the laser diode taken into account with the trigger pulse train approximated in the limit as an impulse train, the detected light field on the n^{th} pulse in the Mach-Zehnder system is given by:

$$\begin{aligned} E(u,n) &= a e^{-j\pi(f_0+f')\frac{X}{v_a}} e^{-j2\pi(f_0+f')nT} B[u - \frac{(f_0+f')}{v_a}] \\ &\qquad + r_0 e^{-j2\pi f_0 nT} e^{j2\pi\alpha_0 x'} \mathrm{rect}(\frac{x'}{X'}) \\ &= e^{-j2\pi f_0 nT} \left\{ c'\, a e^{-j2\pi(f_c+\delta_f)nT} B[u - \frac{(f_c+\delta_f)}{v_a}] + r_0 e^{j2\pi\alpha_0 x'} \mathrm{rect}(\frac{x'}{X'}) \right\}, \end{aligned} \tag{3.4.5}$$

where the signal frequency $f' = f_c + \delta_f$, with f_c and δ_f being defined as the signal coarse and fine frequencies, respectively, and f_c defined as the maximum integer multiple of the laser PRF frequency, such that $\delta_f \leq \frac{1}{T}$, where $f_c = \frac{k}{T}$. $c' = e^{-j\pi f' \frac{X}{v_a}}$, and we have dropped the signal AOD carrier spatial frequency term $e^{-j\frac{\omega_0}{v_a}[x - X/2]}$ by

aligning the diffracted signal wave front with the space integrating lens. This allows the output frequency coordinate axis to be centered around the $u = 0$ position that corresponds to the input signal DC ($f' = 0$) position. Note that the light intensity detection will remove the AOD sampled carrier from both the signal and reference terms, while the laser pulsing will alias the signal frequency to the baseband fine frequency. The intensity detected on the n^{th} pulse is given by:

$$\begin{aligned} I(u,n) &= \left| c'ae^{-j2\pi\delta_f nT} B[u - \frac{(f_c + \delta_f)}{v_a}] + r_0 e^{j2\pi\alpha_0 x'} \text{rect}(\frac{x'}{X'}) \right|^2 \\ &\approx |a|^2 B^2(u - \frac{f_c}{v_a}) + |r_0|^2 \text{rect}(\frac{x'}{X'}) \\ &\qquad + 2|a||r_0| B(u - \frac{f_c}{v_a}) \cos(2\pi\delta_f nT + \Omega' + 2\pi\alpha u), \end{aligned} \tag{3.4.6}$$

where $\alpha = \alpha_0 \lambda F$, $a = |a|e^{-j\Omega}$, and $\Omega' = \Omega + \pi f' \frac{X}{v_a}$. We have used the fact that the fine frequency component δ_f will not move the blur spot $B(u)$ significantly and can be dropped from within the blur spot argument. Eqn.3.4.6 shows that for a single tone input, the output of the processor consists of a constant bias that is due to the reference beam, a signal dependent bias term positioned according to the signal coarse frequency, f_c, and a sampled temporal modulation at the signal fine frequency on a spatial carrier that can be set to zero, if desired, or used to demodulate the desired interferometric term. Note that the third term has an amplitude proportional to the amplitude of the input tone, its position is proportional to the nput coarse frequency, and the fine frequency and phase of the input remain as residual oscillations of the temporally sampled output, except that it has been aliased to baseband by the pulsing action of the laser diode. It is this sampled, low frequency, temporal modulation that allows us to use baseband time domain spectral analysis schemes, such as the DFT algorithm, to resolve the signal into higher resolution spectral components. In order to avoid aliasing effects between the bandlimited signals in each coarse frequency blur spot, we need to satisfy the Nyquist criteria [16], i.e., $\frac{1}{T} > \frac{2}{T_a}$, where T is the sampling time of the laser diode and T_a is the aperture of the Bragg cell, which implies that the space-time raster should be oversampled.

For an amplitude modulated video signal input with the pulsing action of the

laser diode every T seconds taken into account, the spatial Fourier transform of the n^{th} image line is expressed as:

$$\begin{aligned} E(u,n) &\approx \int f[k_1(x-X/2), n\Delta y) e^{-j\omega_0 nT} \mathrm{rect}(\frac{x}{X})\, e^{-j2\pi ux}\, dx \\ &= e^{-j\omega_0 nT} \left\{ \left[\frac{1}{|k_1|} F(\frac{u}{k_1}, n\Delta y) e^{-j\pi X u} \right] * B(u) \right\}, \end{aligned} \tag{3.4.7}$$

where $*$ represents the convolution operation, $F(\frac{u}{k_1}, n\Delta y)$ is the double sided real Fourier spectrum of the n^{th} scaled video image line, and $e^{-j\omega_0 nT}$ is the sampled AOD carrier as shown in Eqn.3.2.2. To illustrate how the spatial variations of an image are resolved in the Fourier domain by an acousto-optic spectrum analyzer, consider two types of input images. First, for an image consisting of a grating with spatial variation of frequency u_0 in the x direction, and $v_0 = 0$, we have $f(x, n\Delta y) = \cos(2\pi u_0 x)$. In this case,

$$F(u, n\Delta y) = \delta(u - u_0) + \delta(u + u_0), \tag{3.4.8}$$

and Eqn.3.4.7 can be written as:

$$E(u,n) = e^{-j\omega_0 nT} \left\{ e^{-j\pi k_1 u_0 X} B(u - k_1 u_0) + e^{j\pi k_1 u_0 X} B(u + k_1 u_0) \right\}, \tag{3.4.9}$$

where the location $u = \pm k_1 u_0$ of the two blur spots on the 2-D sensor array are proportional to the scaled image spatial frequency in the x direction. For an image with spatial frequency v_0 in the y direction, and $u_0 = 0$, the image $f(x, \Delta y) = \cos(2\pi v_0 n\Delta y)$ is independent of the spatial variable x, and we get:

$$E(u,n) = e^{-j\omega_0 nT}\, B(u) \cos(2\pi v_o n\Delta y). \tag{3.4.10}$$

From Eqn 3.4.9 it is clear that the spatial frequencies along the x direction of an image can be resolved in the Fourier plane by using an AOD as an input transducer and a Fourier transforming lens to spatially channelize these frequencies into coarse frequency bins as long as $B(u)$ is narrow enough, implying that the AOD is wide enough to contain a full video line. Eqn.3.4.10 tells us that spatial variations of frequency v_0 along the y direction in the image are converted to a sampled temporal

variation of the same frequency. This temporal variation can then be channelized into its frequency components along the y direction by using time integrating spectrum analysis schemes to be described in the next Section. As spatial frequencies along any arbitrary direction in an image can be expressed as a linear combination of frequency components along the orthogonal x and y image directions, we can employ time and space integrating spectrum analysis to obtain 2-D spectra of images.

Fig.3.4.2 shows the **in-line additive spectrum analyzer** that employs an electronic reference signal for interferometric detection. In particular, this electronic reference is a repetitive high time bandwidth product chirp signal $c(t)$ that linearly sweeps in frequency from the AOD center frequency f_0 to $f_0 + B$ MHz, where B is the chirp bandwidth. This signal is electronically added to the input signal $s(t)$ before being input to the Bragg cell. The reference chirp $c(t)$ is given by the expression:

$$c(t) = \sum_{n=0}^{N-1} \cos[2\pi f_0 t + \pi b(t - nT)^2] \, \mathrm{rect}[\frac{t - nT - T_1/2}{T_1}], \tag{3.4.11}$$

where b is the chirp rate in $MHz/\mu sec$, $B = bT_1$ is the bandwidth of the chirp, T is the laser pulse repetition period, and T_1 is the chirp duration between each pulse. In the experiments to follow, we use $T_1 = T_l$, where T_l is the video line duration, with $T_l \leq T$. Note that in order to maximize the signal analysis bandwidth, we need to maximize the chirp bandwidth. For any fixed chirp rate b, this is possible when $T_1 = T$. Also, note that this chirp signal is phase coherent over its repetition periods. In this system, the optical pulse width τ is given by the expression $\tau \leq \frac{1}{B}$. During each light pulse, the chirp signal appears frozen in the acoustic column of the Bragg cell, and the lens takes the Fourier transfom of the Bragg diffracted chirp spatial modulation giving the wideband chirp spectrum on the detector plane. Thus, in the detector plane, the signal and chirp spectra add together optically and hence retain the phase information in the input signal. The +1 Bragg diffracted single-sideband spatial chirp modulation is approximately given by:

$$\begin{aligned} \tilde{c}(x,n) &\approx \tilde{c}(nT + t_0 - \frac{x - X/2}{v_a}) \\ &= e^{-j2\pi f_0 nT} \, e^{-j\frac{\pi b}{v_a{}^2}(x - X/2)^2} \, \mathrm{rect}[\frac{x}{X}] \, e^{j2\pi \frac{f_0}{v_a}(x - X/2)}, \end{aligned} \tag{3.4.12}$$

where $e^{-j2\pi f_0 nT}$ represents the sampled AOD temporal carrier, $X = v_a T_1$, $t_0 = T_1$, and $e^{j2\pi \frac{f_0}{v_a}(x-X/2)}$ is the spatial deflection term that can be dropped by aligning the Fourier transform lens with the diffracted wave front. The diffracted chirp modulation becomes:

$$\tilde{c}(x,n) = e^{-j2\pi f_0 nT}\, e^{-j\frac{\pi b}{{v_a}^2}(x-X/2)^2} \mathrm{rect}[\frac{x}{X}]. \tag{3.4.13}$$

The Fourier transform lens in this space integrating acousto-optic spectrum analyzer takes the spatial Fourier transform of the single sideband diffracted chirp modulation, giving the chirp spectrum on the n^{th} laser pulse to be:

$$\begin{aligned}
\tilde{C}(x,n) &= \int \tilde{c}(x,n)\, e^{-j2\pi ux}\, dx \\
&= e^{-j\omega_0 nT} \int e^{-j\frac{\pi b}{{v_a}^2}(x-X/2)^2} \mathrm{rect}[\frac{x}{X}] e^{-j2\pi ux}\, dx \\
&= \sqrt{\frac{j}{b}} e^{-j\omega_0 nT}\, e^{j\pi[\frac{(uv_a)^2}{b} - uX]} * X\mathrm{sinc}(Xu) \\
&= \sqrt{\frac{j}{b}} e^{-j\omega_0 nT} \int e^{-j\pi\left\{(u-u')X - \frac{[(u-u')v_a]^2}{b}\right\}} X\mathrm{sinc}(Xu')du',
\end{aligned} \tag{3.4.14}$$

where $*$ represents the convolution operation. In order to further simplify the expression in Eqn.3.4.14, the quadratic term ${u'}^2$ in the convolution integral can be ignored because its contribution over the main lobe of the sinc function is negligible. This is because $\frac{\pi(uv_a)^2}{b} = \frac{\pi {v_a}^2}{bX^2} = \frac{\pi}{BT_1} \ll 1$, as the time bandwidth BT_1 of the chirp is large. Thus, we can approximate the chirp spectrum as:

$$\begin{aligned}
\tilde{C}(x,n) &\approx \sqrt{\frac{j}{b}} e^{-j\omega_0 nT} e^{-j\pi[uX - \frac{(uv_a)^2}{b}]} \int X\mathrm{sinc}(Xu') e^{j2\pi[X/2 - \frac{{v_a}^2}{b}u]u'}\, du' \\
&= \sqrt{\frac{j}{b}} e^{-j\omega_0 nT} e^{-j\pi[uX - \frac{(uv_a)^2}{b}]} \mathrm{rect}\left[\frac{uv_a - B/2}{B}\right] \\
&= C_0 e^{-j\omega_0 nT} e^{-j\pi uX} e^{j\phi_c} \mathrm{rect}\left[\frac{uv_a - B/2}{B}\right],
\end{aligned} \tag{3.4.15}$$

where C_0 is a uniform amplitude term centered at the frequency $B/2$, having a spread B, with a quadratic spatial phase curvature term given by $\phi_c = \frac{\pi(uv_a)^2}{b}$. Substituting this electronic reference spectrum term in Eqn.3.4.3 with the laser pulsing taken into account, we get the interferometrically generated intensity at the Fourier plane of the

in-line additive spectrum analyzer to be:

$$I(u,n) = \left| \int c\ \tilde{S}(f) e^{j2\pi f(nT+t_0)} B(u + \frac{f}{v_a}) df \right. \\ \left. + C_0 e^{-j\omega_0 nT} e^{-j\pi u X} e^{j\phi_c} \text{rect}\left[\frac{uv_a - B/2}{B}\right] \right|^2 . \tag{3.4.16}$$

Using the expression for the signal Fourier spectrum in Eqn.3.4.5, with the single tone input signal frequency $f_0 + f'$, where $f' \leq B$, the intensity on the n^{th} pulse at the detector plane of this in-line additive spectrum analyzer is given by:

$$I(u,n) = \left| a e^{-j2\pi f_0 nT} e^{-j\pi \frac{f'}{v_a} X} e^{-j2\pi(f_c+\delta_f)nT} B[u - \frac{(f_c + \delta_f)}{v_a}] \right. \\ \left. + C_0 e^{-j2\pi f_0 nT} e^{-j\pi u X} e^{j\phi_c} \text{rect}\left[\frac{uv_a - B/2}{B}\right] \right|^2 . \tag{3.4.17}$$

This expression can be further written as:

$$I(u,n) \approx |a|^2 B^2(u - \frac{f_c}{v_a}) + |C_0|^2 \text{rect}\left[\frac{uv_a - B/2}{B}\right] \\ + 2|a||C_0| B(u - \frac{f_c}{v_a}) \cos(2\pi\delta_f nT + \Omega + \phi_c), \tag{3.4.18}$$

where the first and second terms give the signal and reference chirp dependent bias terms, respectively. The third interferometric term is the desired term, where the input signal coarse frequency f_c is related to the position of the spatially integrated blur spot $B(u)$, and the signal fine frequency δ_f is represented as a sampled temporal modulation. Note that the temporal fine frequency of the input signal is not affected by the phase term ϕ_c. Again, it is this sampled fine frequency temporal modulation term that allows the use of time integrating spectrum analysis methods for further resolving the fine frequency into high resolution spectral bins. For video image inputs, we need to use the expression in Eqn. 3.4.7 along with the appropriate interferometric optical or electronic reference terms, respectively, to arrive at a similar result for the video image 2-D spectrum output. In conclusion, both the Mach-Zehnder architecture using the optical reference and the in-line additive architecture using the electronic

chirp reference produce the required signal coarse and fine frequency components. The signal coarse frequency is resolved in space, while the fine frequency is represented as a sampled, low frequency, temporal carrier, that subsequently can be spectrally resolved using a baseband time integrating spectral analysis scheme.

To demonstrate the in-line additive space integrating acousto-optic spectrum analyzer, the system shown in Fig.3.4.2 was set up in the laboratory. A $70\mu sec$ aperture TeO_2 AOD is used with a $60MHz$ carrier signal. A $30cm$ focal length spherical lens performs the space integrating Fourier transform, and the 1-D spectra are detected by a 2-D time integrating CCD detector array that acts as a 1-D detector along one of its sides. The reference chirp is generated digitally using a PROM memory chip and a digital to analog converter. The chirp signal data samples are stored in the memory, and read out using the CCD pixel clock, with the read-out triggering controlled by the CCD $15.734KHz$ horizontal drive or scanning signal. This circuit produces a $3.5MHz$ bandwidth, $52.84\mu sec$ duration, $15.734KHz$ PRF chirp signal. Fig.3.4.3 shows an oscilloscope trace of the coherent reference chirp and its trigger signal. As the chirp is digitally generated, it is perfectly coherent over successive trigger pulses. The light source is also triggered by the CCD line scanning signal, with the repetition period $T \approx 63\mu sec$. This baseband chirp is mixed with the AOD carrier frequency f_0 before being introduced into the Bragg cell, giving an amplitude modulated (AM) signal with a double sided spectrum of bandwidth $2B$, where the AM chirp signal is:

$$c_{AM}(t) = \sum_{n=0}^{N-1} \cos(2\pi f_0 t)\cos[\pi b(t-nT)^2]\,\mathrm{rect}[\frac{t-nT-T_1/2}{T_1}], \tag{3.4.19}$$

and its Fourier spectrum on the n^{th} light pulse is expressed as:

$$\begin{aligned} C(u,n) &= \tilde{C}(u,n) + \tilde{C}'(u,n) \\ &= e^{-j\omega_0 nT} e^{-j\pi uX} \left\{ C_0 e^{j\phi_c} \mathrm{rect}\left[\frac{uv_a - B/2}{B}\right] + {C_0}^* e^{-j\phi_c} \mathrm{rect}\left[\frac{uv_a + B/2}{B}\right] \right\}, \end{aligned} \tag{3.4.20}$$

where the spectrum consists of two spatially separate sidebands of width $\frac{B}{v_a}$, and centered at $\frac{B}{2v_a}$ and $\frac{-B}{2v_a}$, respectively. As defined earlier, C_0 and ϕ_c are the single sided

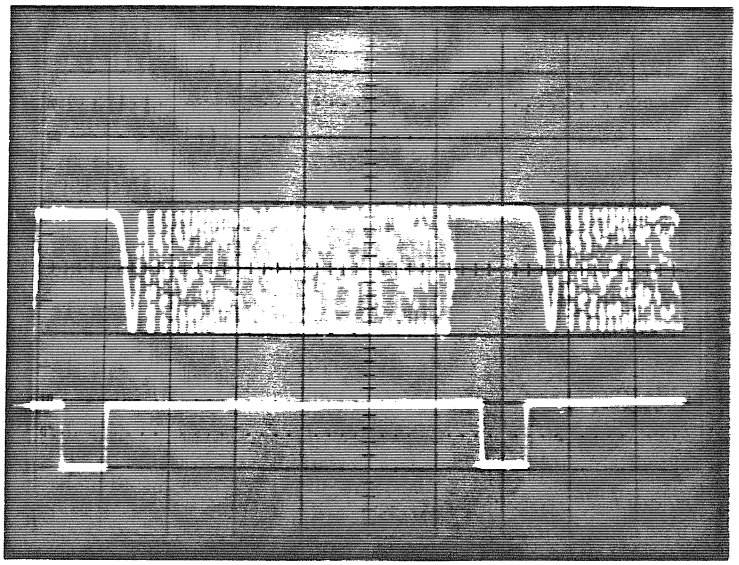

Fig.3.4.3 PROM generated repetitive 3.5 MHz bandwidth reference chirp signal (upper trace) and its 15.734 KHz trigger signal.

chirp amplitude and quadratic phase terms, respectively. Note that the single sided chirp introduced earlier in Eqn.3.4.11 produces only one Fourier spectrum sideband at the detector plane. Thus, depending on whether we are performing double or single sided spectrum analysis, the amplitude modulated (AM) or single sideband chirp are respectively employed in the system. In our case, due to hardware constraints, we used the AM chirp signal in the experiments. The input test signal used in the experiment is already on the carrier f_0, and thus produces a single sided spectrum. Fig.3.4.4 is the $\frac{1}{30}sec$ time integrated CCD output over N laser pulses, showing the expected single sided signal spectra for $f' = 1, 2,$ and $3MHz$ input test signals, with the spectra spatially overlapping with the doubled sided 3.5 MHz AM chirp spectrum centered around the AOD carrier frequency position $u = 0$. The interferometric signal peak oscillates over successive CCD frames, and is shown at its high point, with a modulation depth of around 30%, and a coarse frequency resolution around 80 KHz. The system is operated for test signals ranging over the AM chirp bandwidth. Next, we look at the time integrating optical processors used for fine frequency spectrum analysis.

3.5 Time Integrating Pulsed Source Interferometric DFT Processors

Theory and Experiment:

In the previous section, we presented two pulsed source space integrating interferometric spectrum analyzers that spectrally resolve a signal into its spatial coarse frequency bins, each bin oscillating in discrete time with its characteristic fine frequency. In order to complete the 2-D folded spectrum operation, we need to perform a baseband time integrating DFT transformation on each coarse frequency bin. This narrowband spectrum analysis will be performed by one of two possible optical architectures shown in Fig.3.5.1 and 3.5.2. The time integrating DFT system needs to be a baseband processor with an analysis bandwidth of at least the blur spot width, $\frac{2}{T_a}$, and it should process the full Nyquist limited bandwidth of half the laser pulsing frequency. The resolution of the time integrating fine frequency processor should ideally be equal to the inverse of the total processing time, i.e. $\frac{1}{NT}$. The DFT of a sequence

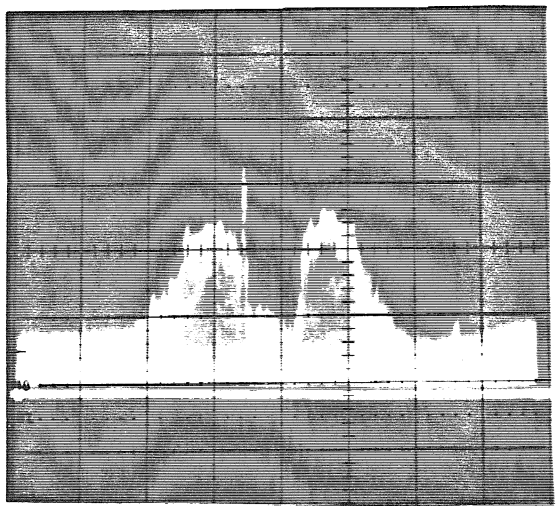

$f' = 1$ MHz

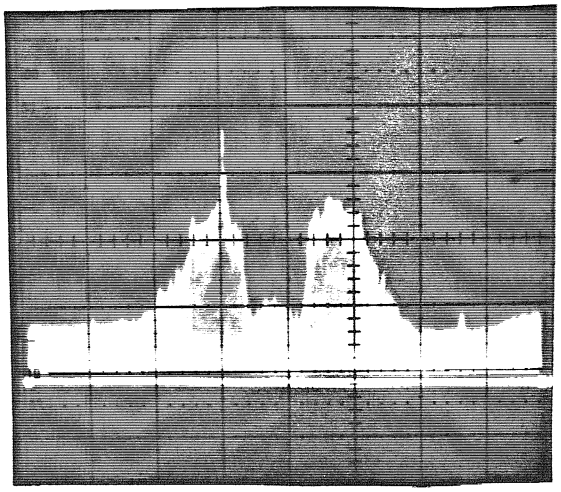

$f' = 2$ MHz

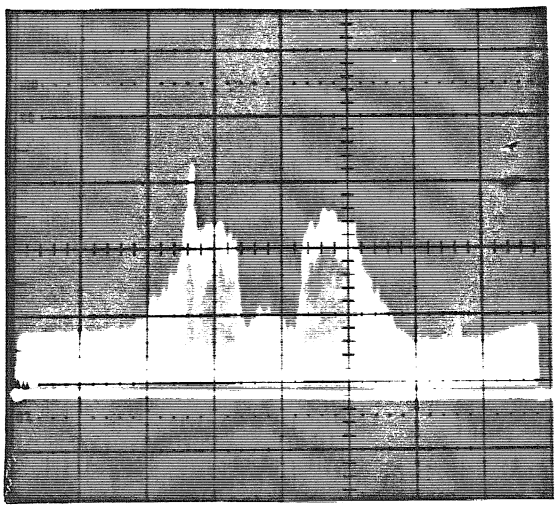

$f' = 3$ MHz

Fig.3.4.4 In-line additive space integrating processor output using the 3.5 MHz bandwidth AM reference chirp signal with the input signal frequency being equal to 1, 2, and 3 MHz respectively.

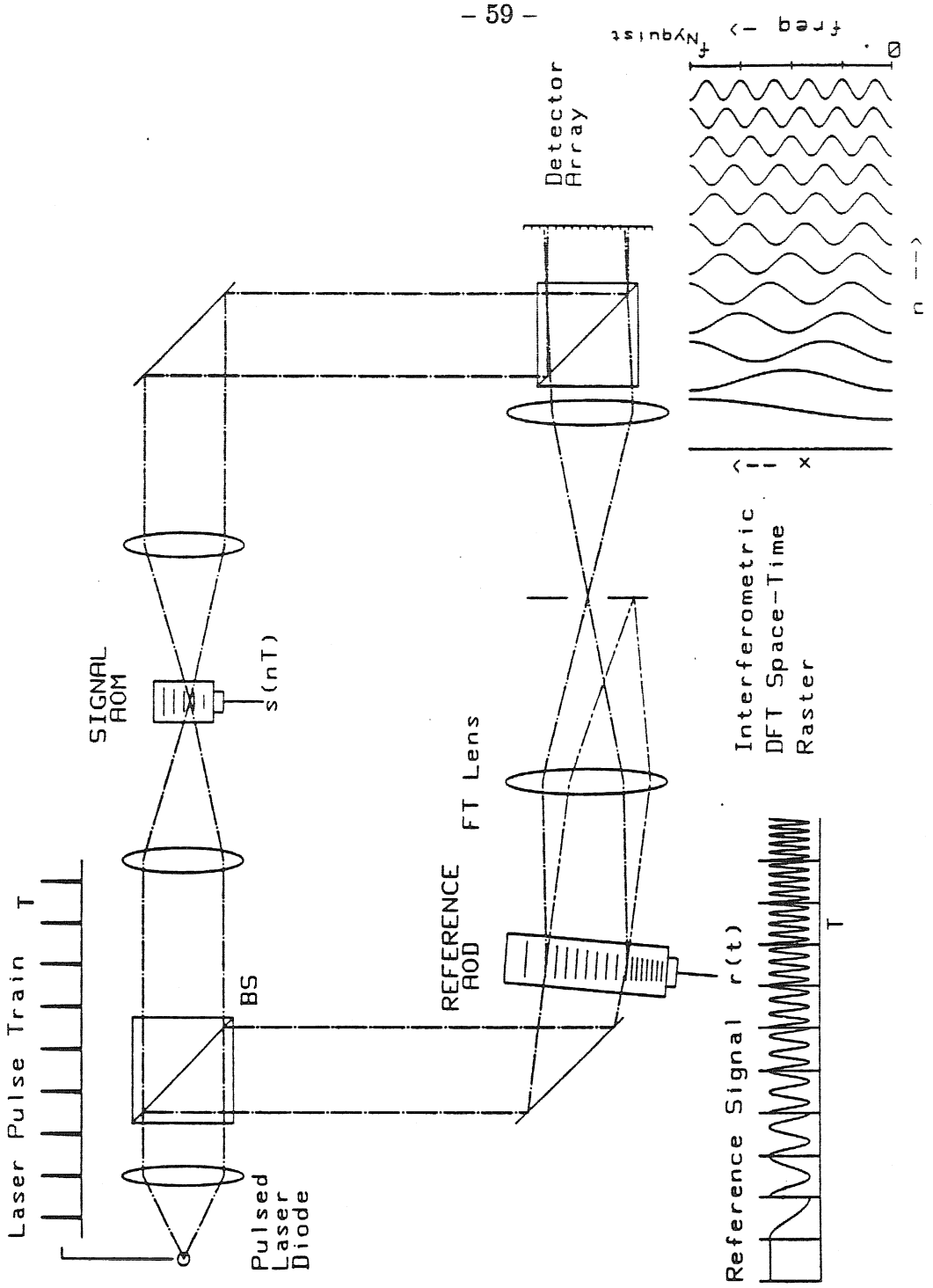

Fig.3.5.1 The 1-D acousto-optic pulsed source time integrating Mach-Zehnder DFT processor.

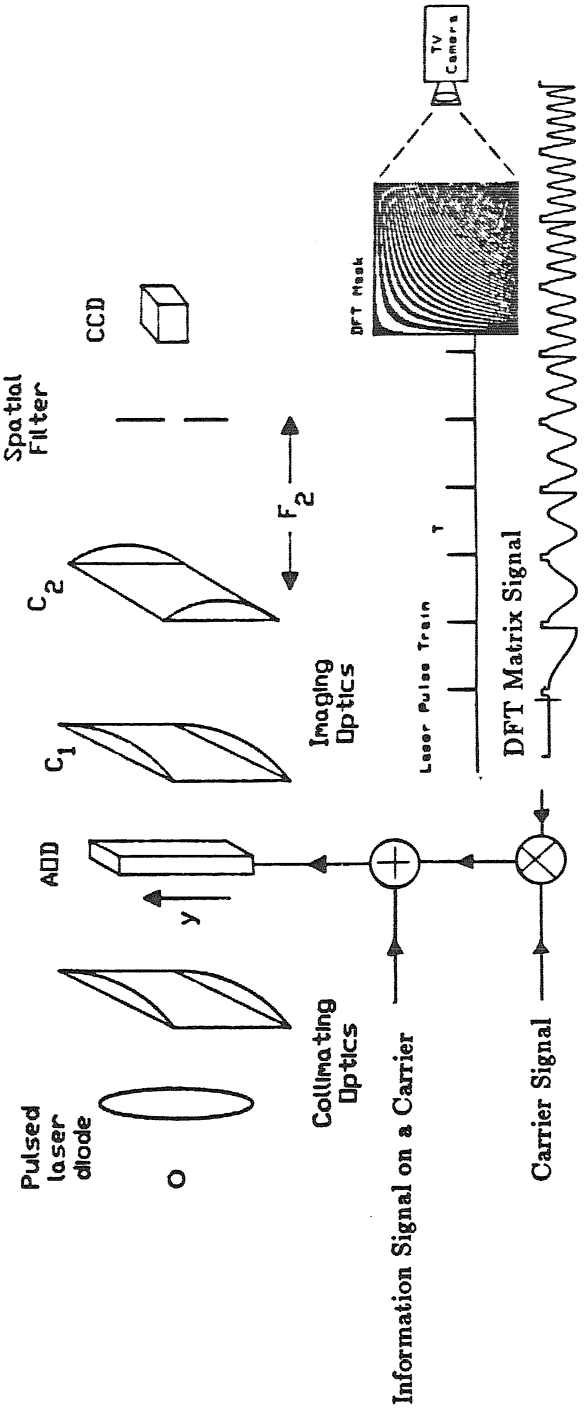

Fig.3.5.2 The 1-D acousto-optic pulsed source time integrating in-line additive DFT processor.

$s(n)$ is described by [16]

$$S(k) = \sum_{n=0}^{N-1} s(n) {W_N}^{nk} \tag{3.5.1}$$

$$W_N = e^{-j\frac{2\pi}{N}} . \tag{3.5.2}$$

The successive columns of the DFT matrix, ${W_N}^{nk}$, represent complex sinusoids of successively higher frequencies, with all columns aligning to zero phase in the first row of the matrix . Thus, the waveform $d(t)$ that is input to the AOD to introduce the DFT kernel is a stepped frequency chirp, with each new frequency phase reset to zero phase. In other words, this signal consists of successively higher frequency signal segments that represent the successive columns of the DFT matrix. This DFT signal is written as:

$$d(t) = \sum_{n=0}^{N-1} \cos[2\pi n \Delta f(t - nT)] \mathrm{rect}[\frac{t - nT - T_1/2}{T_1}] \tag{3.5.3}$$

In our experiments, the large time bandwidth waveform $d(t)$ is generated by a personal computer and video frame buffer, and stored in a 2-D raster format in the computer memory, which is output as a serial video signal. Fig.3.5.3 shows one such DFT raster stored in the personal computer with T_1 equal to the video line duration and $\frac{1}{T}$ equal to the video line rate. The lower trace in Fig.3.5.3 shows the first, second, and third DFT column signals, respectively. Both the Mach-Zehnder DFT processor of Fig.3.5.1 and the in-line additive DFT processor in Fig.3.5.2 use the time between the laser pulses to slide new columns of the DFT matrix into an AOD. At the instant $t = nT + t_0$ of the n^{th} light pulse, the acoustic motion is frozen in the cell, thereby schlieren imaging that column on to the spatially discrete CCD pixel structure, which samples the DFT column. Successive imaging of the DFT matrix columns on to the CCD generates a distributed local oscillator (DLO), where on a pulse to pulse basis, one end of the schlieren imaged column on the CCD corresponds to DC or no temporal variation, and the other end oscillates at a maximum possible Nyquist limited rate of half the laser pulse repetition frequency, i.e. $\frac{1}{2T}$. The maximum DLO frequency is achieved when an additional half cycle of the stepped frequency reference

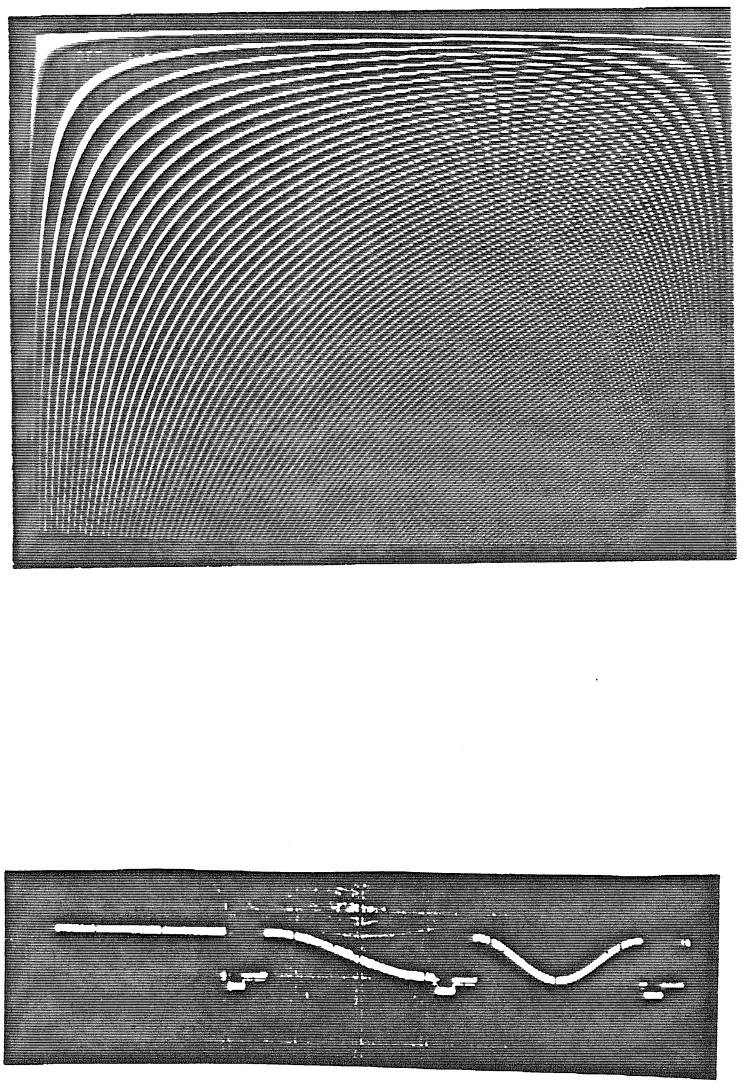

Fig.3.5.3 Single sided DFT matrix stored in a TV raster format (upper trace) with its video signal output showing the first three DFT column signals.

is added with each frequency step, i.e., $\Delta f = \frac{1}{2T_1}$. The sampled temporal DLO frequency increases linearly along the CCD in the y direction. When a narrowband signal with a temporal variation within the DLO bandwidth is incident on the CCD, the component of the DLO that best matches the signal frequency beats to baseband and produces an interferometric spatial peak by time integration over the N laser pulses. The location of the peak along the detector array gives the frequency of the narrowband signal. The systems shown in Fig.3.5.1 and Fig. 3.5.2 employ this principle for narrowband spectrum processing.

Note that these DFT based systems differ in two respects. First, they differ in how they introduce the narrowband signal $s(t)$ into the optical system, and second, they use different techniques to accomplish the interference between the signal and the DFT columns. In the **Mach-Zehnder system**, the narrowband signal is fed to an acousto-optic point modulator (AOM) positioned in one arm of the interferometer, while the stepped frequency reference is applied to an AOD in the other arm. The +1 Bragg diffracted light from the AOM and the AOD in the two respective arms of the interferometer are recombined and interfered on the CCD plane. The narrowband signal is on a carrier frequency f_0, while the DFT chirp signal is also mixed up to the AOD center frequency f_0 before being input into the device. In order to accomplish single sided processing, we must spatially filter out one of the sidebands of the amplitude modulated (AM) DFT chirp signal in the Fourier plane of the AOD. The signal beam is given an offset angle θ_y with respect to the starting frequency of the DFT chirp by rotating the output stage beam splitter, which results in an additional spatial carrier of spatial frequency $\alpha_y = \frac{sin(\theta_y)}{\lambda}$. The +1 order diffracted signal term at time $t = nT + t_0$ of the n^{th} laser pulse is given by:

$$E_s(y,n) = a_1\, \tilde{s}(nT + t_0) e^{j2\pi(\frac{f_0}{v_a} - \alpha_y)y} e^{-j2\pi f_0(nT+t_0)} \text{rect}\left[\frac{y - Y/2}{Y}\right], \qquad (3.5.4)$$

where a_1 is the amplitude of the diffracted field, and we have included the spatial frequency term that is due to the beam splitter and acoustic Bragg deflection, respectively. Once again, $e^{-j2\pi f_0(nT+t_0)}$ represents the AOM sampled carrier frequency that is removed by the intensity detection with the reference AOD sampled carrier.

$\tilde{s}(nT+t_0)$ is the temporally sampled single sided (+1 order) complex input signal. For the DFT reference AOD, the n^{th} light pulse Bragg diffracted field after Fourier plane single sideband spatial filtering of the DFT chirp lower sideband, is approximately given by:

$$\begin{aligned} E_d(y,n) &\approx a_2\,\tilde{d}(nT+t_0-\frac{y}{v_a})e^{j2\pi(\frac{f_0}{v_a})y}e^{-j2\pi f_0(nT+t_0)} \\ &= e^{j2\pi(\frac{f_0}{v_a})y}\,e^{-j2\pi f_0(nT+t_0)}e^{-j2\pi n\frac{\Delta f}{v_a}(Y-y)}\,\mathrm{rect}\big[\frac{y-Y/2}{Y}\big], \end{aligned} \tag{3.5.5}$$

where a_2 is the amplitude of the diffracted field, $\tilde{d}$ is the Fourier plane filtered DFT signal upper sideband, and $t_0 = T_1 = \frac{Y}{v_a}$, with t_0 being equal to the DFT column signal duration corresponding to the illuminated Bragg cell aperture Y that is imaged on to the CCD. The $y = 0$ position corresponds to the transducer end of the AOD. The interferometrically detected intensity pattern on the n^{th} laser pulse is formed by combining the phase modulated diffracted signal plane wave and the DFT column generated angularly stepped plane wave at the detector plane, giving an intensity distribution expressed as:

$$\begin{aligned} I(y,n) &= \Big|E_s(y,n)+E_d(y,n)\Big|^2 \\ &= \Big|e^{-j2\pi f_0(nT+t_0)}e^{j2\pi(\frac{f_0}{v_a})}\Big\{a_1\,\tilde{s}(nT+t_0)e^{-j2\pi\alpha_y y}+a_2e^{-j2\pi n\frac{\Delta f}{v_a}(Y-y)}\Big\}\Big|^2 \\ &\qquad\qquad \mathrm{rect}\big[\frac{y-Y/2}{Y}\big] \\ &= \Big|a_1\,\tilde{s}(nT+T_1)e^{-j2\pi\alpha_y y}+a_2e^{-j2\pi n\frac{\Delta f}{v_a}(Y-y)}\Big|^2\mathrm{rect}\big[\frac{y-Y/2}{Y}\big]. \end{aligned} \tag{3.5.6}$$

On expanding Eqn. 3.5.6, we get the intensity on the n^{th} pulse as:

$$\begin{aligned} I(y,n) = \Big\{ &|a_1\tilde{s}(nT+T_1)|^2+|a_2|^2 \\ &+2|a_1|\,|a_2|\,|\tilde{s}(nT+T_1)|\cos\big[2\pi[n\frac{\Delta f}{v_a}(Y-y)-\alpha_y y] \\ &+\Omega(nT+t_0)\big]\Big\}\mathrm{rect}\big[\frac{y-Y/2}{Y}\big], \end{aligned} \tag{3.5.7}$$

where $|\tilde{s}(nT)|$ and $\Omega(nT)$ are the respective amplitude and phase terms of the complex signal sequence $\tilde{s}(nT)$. The total integrated charge over the N laser pulses is given

by:

$$I(y) = \Bigg\{ N|a_2|^2 + \sum_{n=0}^{N-1} |a_1 \tilde{s}(nT+T_1)|^2 + 2|a_1|\,|a_2| \sum_{n=0}^{N-1} |\tilde{s}(nT+T_1)| \cos\Big[2\pi\Big[n\frac{\Delta f}{v_a}(Y-y) - \alpha_y y\Big] + \Omega(nT+t_0)\Big] \Bigg\} \mathrm{rect}\Big[\frac{y-Y/2}{Y}\Big], \tag{3.5.8}$$

where the first two terms are the reference and signal dependent bias terms, and the third term is recognized as the discrete cosine transform of the complex sequence $\tilde{s}(nT+T_1)$, on a spatial carrier at the midband spatial frequency γ. The carrier allows the utilization of a bandpass filter operation on the detector output which removes the bias terms, and the full complex DFT can be reconstructed by measuring the amplitude and phase of the modulated carrier. For a narrowband signal of frequency δ_f, $\tilde{s}(t) = ae^{-j2\pi\delta_f t}$, the integrated charge in the CCD is given by:

$$\begin{aligned} I(y,n) &= \Big\{ C_1 + C_2 \sum_{n=0}^{N-1} \cos\Big\{2\pi n\Big[\frac{\Delta f}{v_a}(y-Y) + \delta_f T\Big] + 2\pi(\alpha_y y + \delta_f T_1)\Big\}\Big\} \mathrm{rect}\Big[\frac{y-Y/2}{Y}\Big] \\ &= \Big\{ C_1 + C_2 \cos(2\pi\gamma y + \beta) \frac{\sin(N\pi\alpha)}{\sin\pi\alpha} \Big\} \mathrm{rect}\Big[\frac{y-Y/2}{Y}\Big], \end{aligned} \tag{3.5.9}$$

where

$$\gamma = \alpha_y + (N-1)\frac{\Delta f}{2v_a} \tag{3.5.10}$$

$$\beta = \pi\delta_f[(3-N)T_1 + (N-1)T] \tag{3.5.11}$$

$$\alpha = \frac{\Delta f}{v_a}(y-Y) + \delta_f T\,, \tag{3.5.12}$$

and C_1 and C_2 are real constants. The expression in Eqn.3.5.9 can further be approximated as:

$$I(y) \approx \Big[C_1 + C_2 \cos(2\pi\gamma y + \beta) N \mathrm{sinc}\Big\{NT\Big[\delta_f + \frac{\Delta f}{v_a T}(y-Y)\Big]\Big\}\Big] \mathrm{rect}\Big[\frac{y-Y/2}{Y}\Big], \tag{3.5.13}$$

where we use the approximation $\frac{\sin N\pi\alpha}{\sin\pi\alpha} \rightarrow N\mathrm{sinc}(N\alpha)$ [18]. This approximation has been used in further analysis in this chapter. Note that the location of the sinc

function maximum peak at $y = Y - \frac{\delta_f}{\Delta f} v_a T$ is proportional to the signal fine frequency δ_f. As the narrowband frequency δ_f is increased from DC ($\delta_f = 0$) to the Nyquist limit $\delta_f = \frac{1}{2T}$, the integrated peak on the CCD moves linearly along the imaged DFT column ridge from the $y = Y$ position to the $y = 0$ position, respectively. Note that the y coordinate has been inverted because of the imaging from the AOD plane to the CCD plane. Thus, the Mach-Zehnder DFT processor can be used to temporally resolve narrowband frequency signals using an optical discrete Fourier transform implementation with a pulsed light source.

The **in-line additive DFT processor** shown in Fig.3.5.2 works in a similar fashion to the Mach-Zehnder DFT processor. Here, the narrowband signal and the DFT reference chirp signal, both centered at the Bragg cell center frequency f_0, are electronically summed in a RF adder circuit before being fed into the AOD. Note that the DFT reference signal $d'(t)$ is on an extra offset carrier frequency f_s. This offset carrier generates a spatial carrier on the CCD that is used for bias removal via carrier demodulation. The signal driving the Bragg cell is given by:

$$s'(t) = a_1 \cos[2\pi(f_0 + \delta_f)t] \; + \; a_2 d'(t) \cos(2\pi f_0 t), \tag{3.5.14}$$

where a_2 is an amplitude term, and

$$d'(t) = \sum_{n=0}^{N-1} \cos[2\pi(f_s + n\Delta f)(t - nT)] \mathrm{rect}[\frac{t - nT - T_1/2}{T_1}]. \tag{3.5.15}$$

The Bragg diffracted light, modulated by the narrowband signal and the DFT column, respectively, is imaged on-to the CCD after appropriate single sideband (SSB) Fourier plane filtering of the amplitude modulated (AM) DFT signal. As before, for a narrowband input signal with frequency δ_f, the light integrated on the CCD after N laser pulses can be expressed as:

$$\begin{aligned} I(y) &= \sum_{n=0}^{N-1} \left| \tilde{s}'(nT + T_1 - \frac{y}{v_a}) \right|^2 \\ &= \sum_{n=0}^{N-1} \left| a_1 e^{-j2\pi\delta_f(nT + T_1 - \frac{y}{v_a})} + a_2 e^{-j2\pi(f_s + n\Delta f)(T_1 - \frac{y}{v_a})} \right|^2 \mathrm{rect}[\frac{y - Y/2}{Y}], \end{aligned} \tag{3.5.16}$$

where $\tilde{s}'$ is the single sided +1 order diffracted signal, and the carrier spatial deflection term has been absorbed by the intensity detection operation in the analysis. Combining the terms in this expression, the integrated intensity on the CCD is given by:

$$I(y) = \sum_{n=0}^{N-1} \Bigg\{ |a_1|^2 + |a_2|^2 + 2|a_1||a_2| \cos\Big[2\pi n[\frac{\Delta f}{v_a}(y - Y) + \delta_f T] + 2\pi \frac{y}{v_a}(f_s - \delta_f) + 2\pi T_1(\delta_f - f_s)\Big]\Bigg\} \text{rect}[\frac{y - Y/2}{Y}]. \tag{3.5.17}$$

Completing the summation over N laser pulses, we can write the intensity distribution at the CCD as:

$$I(y) = \Big\{C_1 + C_2 \cos(2\pi\gamma' y + \beta') \frac{\sin(N\pi\alpha)}{\sin\pi\alpha}\Big\} \text{rect}[\frac{y - Y/2}{Y}] \approx \Big[C_1 + C_2 \cos(2\pi\gamma' y + \beta') N \text{sinc}\left\{NT[\delta_f + \frac{\Delta f}{v_a T}(y - Y)]\right\}\Big] \text{rect}[\frac{y - Y/2}{Y}], \tag{3.5.18}$$

where C_1, C_2 are real constants, and γ' is the midband spatial carrier frequency of the interferometric term. The other parameters are given by:

$$\gamma' = \frac{1}{v_a}[f_s - \delta_f + (N-1)\frac{\Delta f}{2}] \tag{3.5.19}$$

$$\beta' = \pi\delta_f[(3 - N)T_1 + (N-1)T] - 2\pi f_s T_1 \tag{3.5.20}$$

$$\alpha = \frac{\Delta f}{v_a}(y - Y) + \delta_f T\,, \tag{3.5.21}$$

where α is the same as in the Mach-Zehnder case, while γ' and β' are very similar to γ and β introduced earlier. Note that the spatial carrier γ' of the desired spectrum term is controlled by the offset frequency f_s of the DFT reference signal. As $\delta_f \ll f_s$, we can approximate $\gamma' \approx \frac{1}{v_a}[f_s + (N-1)\frac{\Delta f}{2}]$. Once again, note that in Eqn.3.5.18, the position of the time integrated Blur spot is proportional to the narrowband input frequency δ_f, and its resolution is given by $\frac{2v_a}{N\Delta f}$. Thus, by comparing Eqns. 3.5.13 and 3.5.18, we see that both the Mach-Zehnder and in-line additive DFT processors resolve the fine frequency of a narrowband signal in a similar way.

The in-line additive DFT system was set up in the laboratory using a $70\mu sec$ TeO_2 AOD, a 2-D Sony CCD sensor, and a pair of $10cm$ and $15cm$ focal length cylindrical imaging lenses, respectively. The cylindrical lens C_1 ($15cm$) images the narrow (x) direction of the acoustic column on to the CCD, while the cylinder C_2 ($10cm$) images the length Y of the acoustic column on to the optical sensor. In addition, the Fourier plane of lens C_2 provides the necessary single sideband spatial filtering of the reference DFT signal. As mentioned earlier, the DFT matrix columns are stored as video lines in a video frame buffer. Each DFT video line consists of 525, 8 bit DFT points, with each point (pixel) read with a $10MHz$ system clock, giving a video line time of $T_1 = 52.5\mu sec$. The line rate is the standard video rate of $15.734KHz$, that gives a DFT column repetition period of $T = 63.6\mu sec$. The video image is stored as $\frac{1}{60}sec$ duration odd and even TV fields, respectively, with each field consisting of 240 lines, with interleaving between lines of odd and even fields. Fig.3.5.3 shows the DFT columns displayed in this standard interleaved video image format. Here, we stored identical DFT data on the separate odd and even fields, with each successive DFT line having a frequency increase $\Delta f = \frac{1}{2T_1}$. Using this DFT signal generation scheme, we can get a Nyquist limited narrowband processor bandwidth of $\frac{1}{2T} = 7.86KHz$, and a fine frequency resolution of $\frac{1}{NT} = 60Hz$. This processor fine bandwidth corresponds to the maximum temporal variation along the slow (y) direction of a video image. In other words, this DFT signal is suited for single sided spectrum analysis of standard video images along the image slow (y) direction. In the laboratory system, the CCD sensor and the video frame buffer are phase locked, thus providing the necessary synchronization between the CCD charge integration window, and the DFT video signal frame time. The laser diode is pulsed with the CCD $15.734KHz$ line rate signal. The processor was successfully tested over its $7.86KHz$ bandwidth, with the time integrated spectral peak moving along the imaged DFT column ridge, with a frequency resolution of $\approx 100Hz$. Fig.3.5.4 shows the CCD video outputs for fine frequency $\delta_f = 5.157KHz$ and $7.054KHz$, respectively. No offset carrier f_s was used in this experiment.

Next, we shall discuss how the pulsed source 1-D space integrating spectrum

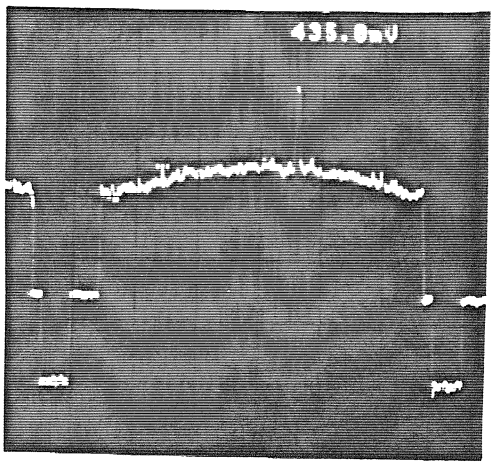

$\delta_f = 5.157$ KHz

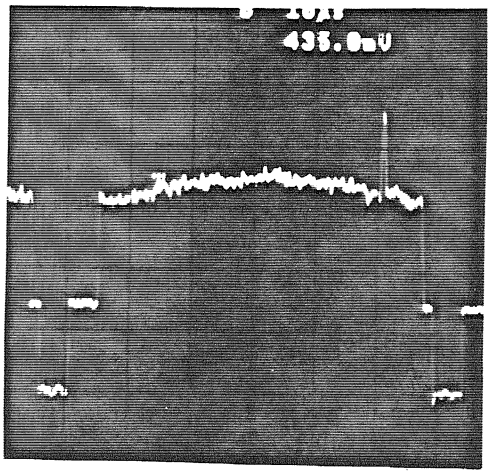

$\delta_f = 7.054$ KHz

Fig.3.5.4 Fine frequency peaks from the time integrating in-line additive DFT processor for input signal fine frequency of $\delta_f = 5.157$ KHz and $\delta_f = 7.054$ KHz respectively.

analyzers and the 1-D DFT based time integrating processors can be combined to form two dimensional crossed Bragg cell time and space integrating (TSI) DFT based spectrum analyzers.

3.6 Additive Mach-Zehnder 2-D Folded Spectrum Processor

In this section, we present an additive pulsed source Mach-Zehnder architecture for 2-D folded spectrum processing. This system combines the wideband Mach-Zehnder space integrating spectrum processor in Fig.3.4.1 with an array of narrowband Mach-Zehnder time integrating DFT processors shown in Fig.3.5.1. The architecture of this Mach-Zehnder system is shown in Fig.3.6.1. The signal $s(t)$ centered at the AOD center frequency f_0 is fed to the Bragg cell. The +1 order diffracted light is Fourier transformed by a spherical lens in the x direction, which collimates in y, and the space integrated spectrum is detected on the CCD array. This spectrum was derived earlier in Eqn.3.4.2, and is expressed as:

$$E_s(u,y,n) = a_1 e^{-j2\pi\alpha_y y} \int c\,\tilde{S}(f) e^{j2\pi f(nT+T_1)} B(u+\frac{f}{v_a})\,df\,\mathrm{rect}[\frac{y-Y/2}{Y}], \quad (3.6.1)$$

where α_y is a spatial frequency in the y direction caused by rotating the output beam splitter. The DFT reference signal $d(t)$ is heterodyned to frequency f_0, and is fed into the orthogonal AOD in the other arm of the interferometer. The +1 diffracted DFT signal is single sideband filtered in the Fourier plane of the orthogonal reference Bragg cell. A spherical and cylindrical lens combination is used to image the filtered DFT column along the y direction on the CCD, with the light being collimated in the x direction. This imaged DFT reference signal on the CCD was also derived earlier in Eqn.3.5.5, and it is expressed as:

$$E_d(x',y,n) = a_2 e^{j2\pi(\frac{f_0}{v_a})y}\, e^{-j2\pi f_0(nT+T_1)} e^{-j2\pi n\frac{\Delta f}{v_a}(Y-y)}\,\mathrm{rect}[\frac{y-Y/2}{Y}], \mathrm{rect}[\frac{x'}{X'}]. \quad (3.6.2)$$

The interferometrically detected intensity integrated over N light pulses is the mag-

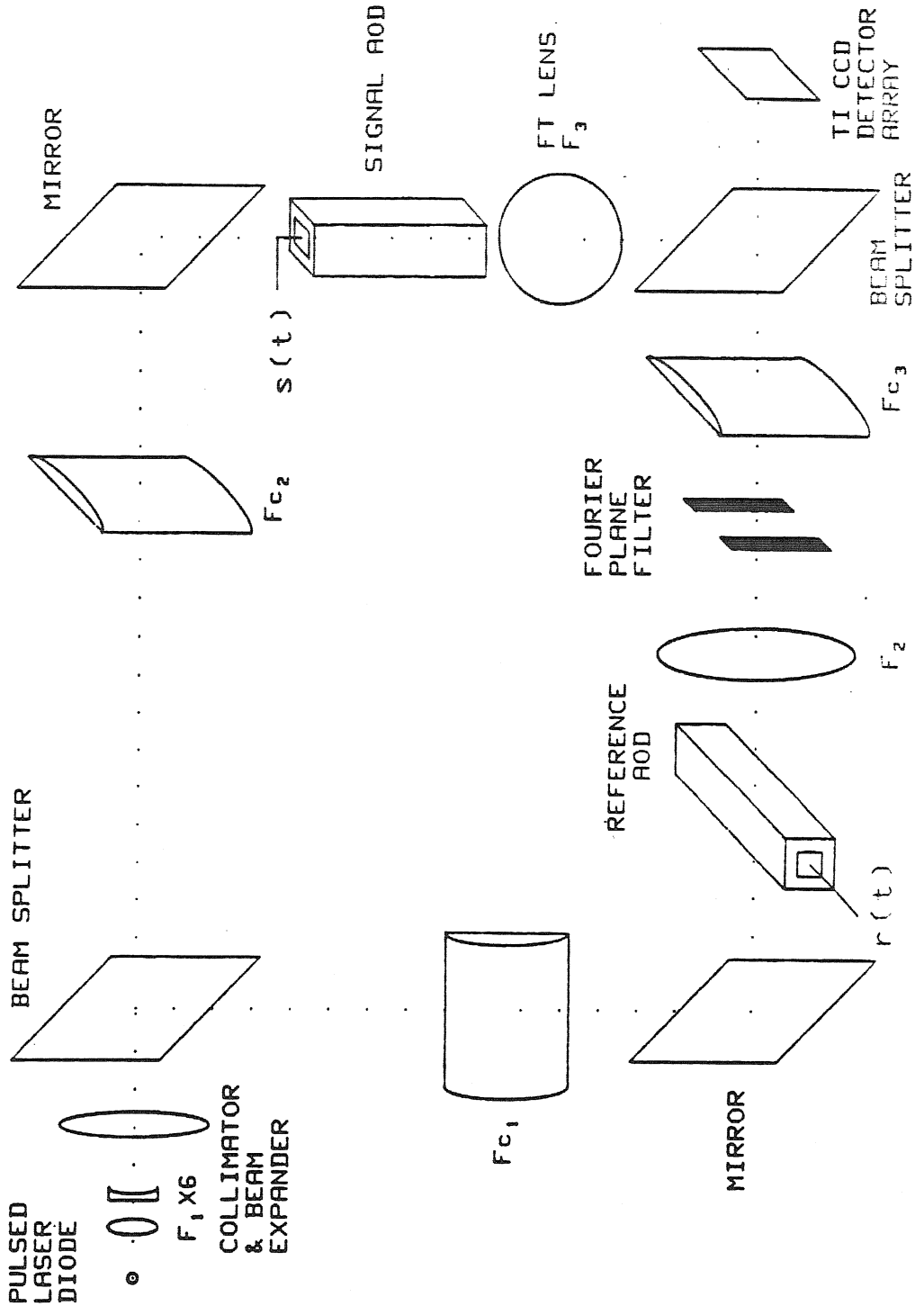

Fig.3.6.1 2-D pulsed source time and space integrating acousto-optic Mach-Zehnder folded spectrum processor.

nitude squared of the sum of the signal and reference waves:

$$
\begin{aligned}
I(u,y,n) &= \sum_{n=0}^{N-1} \Big| E_s(u,y,n) + E_d(x',y,n) \Big|^2 \\
&= |a_1|^2 \sum_{n=0}^{N-1} \Big| \int c\,\tilde{S}(f) e^{j2\pi f(nT+T_1)} B(u+\frac{f}{v_a})\,df \Big|^2 \mathrm{rect}[\frac{y-Y/2}{Y}] \\
&+ |a_2|^2 N \mathrm{rect}[\frac{x'}{X'}]\mathrm{rect}[\frac{y-Y/2}{Y}] \\
&+ 2|a_1|\,|a_2| \sum_{n=0}^{N-1} Re\Big\{ [\int c\,\tilde{S}(f) e^{j2\pi f(nT+T_1)} B(u+\frac{f}{v_a})df] \\
&\qquad\qquad e^{j2\pi\left\{[\frac{\Delta f}{v_a}(Y-y)]n-\alpha'_y y\right\}} \Big\} \mathrm{rect}[\frac{x'}{X'}]\mathrm{rect}[\frac{y-Y/2}{Y}],
\end{aligned}
\tag{3.6.3}
$$

where $\alpha'_y = \alpha_y + f_0/v_a$, and a_1, a_2 are the signal and reference beam amplitudes, respectively. The first and second terms in Eqn.3.6.3 are the signal dependent and constant bias terms, respectively, and the third interferometric term is the 2-D folded spectrum of the signal $s(t)$. For a single tone input signal $s(t)$ centered at the AOD frequency f_0, and having a signal offset frequency $f' = f_c + \delta_f$, we can write $\tilde{S}(f) = \delta(f + f_c + \delta_f)$. Recall from Sections 3.4 and 3.5 that f_c and δ_f are the input signal coarse and fine frequencies, respectively, where the coarse frequency is a multiple of the laser pulsing frequency. Substituting the value of $\tilde{S}(f)$ in Eqn.3.6.3, the impulse response of the system is given by:

$$
\begin{aligned}
I(u,y) \approx\; & C_1 B^2(u-\frac{f_c}{v_a})\mathrm{rect}[\frac{y-Y/2}{Y}] + C_2 \mathrm{rect}[\frac{x'}{X'}]\mathrm{rect}[\frac{y-Y/2}{Y}] \\
& + C_3 B(u-\frac{f_c}{v_a}) N \mathrm{sinc}\left\{NT[\delta_f + \frac{\Delta f}{v_a T}(y-Y)]\right\} \cos(2\pi\gamma y + \beta),
\end{aligned}
\tag{3.6.4}
$$

where C_1, C_2, C_3 are real constants, and γ and β are defined as:

$$
\gamma = \alpha'_y + (N-1)\frac{\Delta f}{2v_a} \tag{3.6.5}
$$

$$
\beta = \pi f' T_1 - (N-1)\pi\delta_f(T_1 - T). \tag{3.6.6}
$$

This single tone impulse response consists of a uniform bias, a space integrated coarse frequency bias ridge located at $u = \frac{f_c}{v}$, and the folded spectrum impulse of amplitude

C_3 riding on top of the coarse ridge at a fine frequency position of $y = Y - \frac{\delta_f}{\Delta f} v_a T$. This impulse or spectral peak is on a spatial carrier of frequency γ along the y dimension, where β is the carrier phase angle. The resolution of this spectral peak along the y dimension is given by the width of the sinc function, and is limited by the integration time to $\frac{1}{NT}$; however, numerous system parameters such as the CCD spatial frequency response, the Bragg cell band shape and the laser pulse width, will apodize the DFT and decrease the achievable resolution [17,19,20]. The processor fine frequency analysis bandwidth is $\frac{1}{2T}$, as y is varied over the CCD height Y, while the coarse frequency bandwidth is limited by the width X' of the reference optical wave front, although eventually by the signal Bragg cell device bandwidth.

This Mach-Zehnder TSI spectrum processor was set up in the Caltech laboratory [12,14]. Fig. 3.6.2 shows the laboratory system, while Fig. 3.6.3 shows the system design for the processor. A Hitachi HLP-1600 single mode laser diode with $20mW$ continuous wave power is used to produce $50nsec$ duration light pulses at a $15.734KHz$ video line rate provided by the composite blanking signal of the CCD sensor. A $15mm$ focal length collimator was combined with a 6 times beam expander to produce a collimated elliptical Gaussian output beam with half power points given by $D_x = 48mm$ and $D_y = 15mm$. The long axis of the beam profile is oriented along the x direction in the space integrating AOD1 aperture. The AOD's used in this experiment are slow shear mode TeO_2 devices with an aperture of $70\mu sec$ and bandwidths of $40MHz$. The signal $s(t)$ centered at $60MHz$ is applied to AOD1, and the diffracted component is Fourier transformed in x by the following $250mm$ focal length spherical lens. This diffracted light is reflected off the beam splitter on to the CCD detector. In the time integrating arm of the interferometer, an $8.4\mu sec$ portion of the orthogonal AOD2 aligned along the y direction is illuminated by a focussed beam. This light is Bragg diffracted and Fourier transformed along the y direction by a $120mm$ reference transform spherical lens, which allows single sideband filtering in the Fourier plane. The filtered light is retransformed in y by the following $150mm$ focal length cylinder, producing an appropriately scaled image of the reference signal in AOD2. This results in the $8.4\mu sec$ DFT sinusoid filling the entire CCD aperture in the y dimension, where

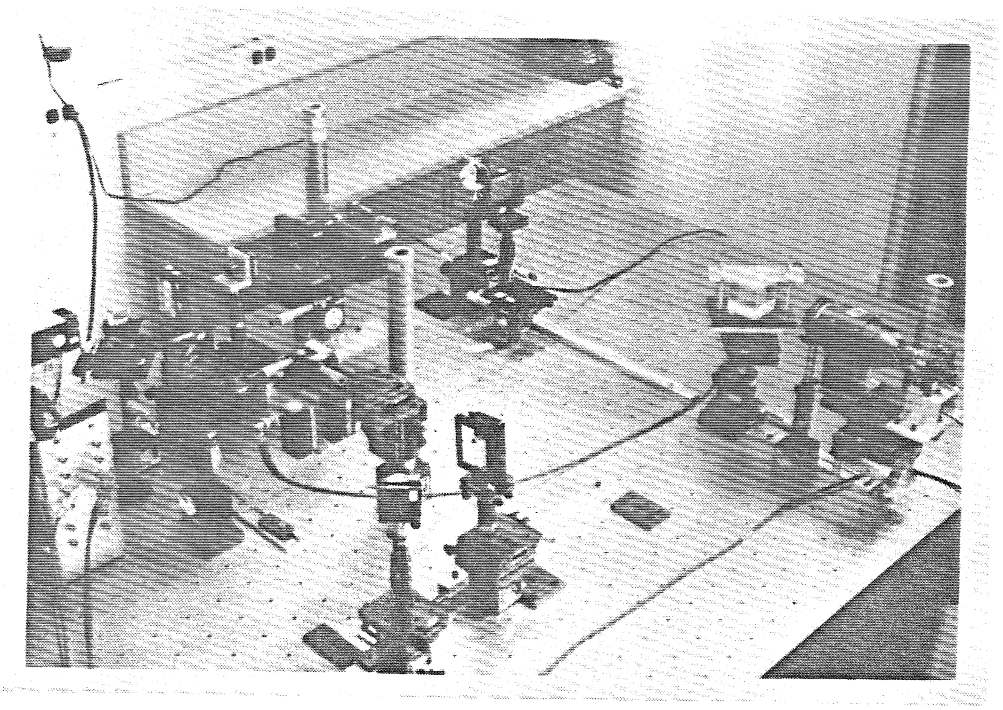

Fig.3.6.2 Laboratory set-up of the Caltech Mach-Zehnder time and space integrating folded spectrum processor.

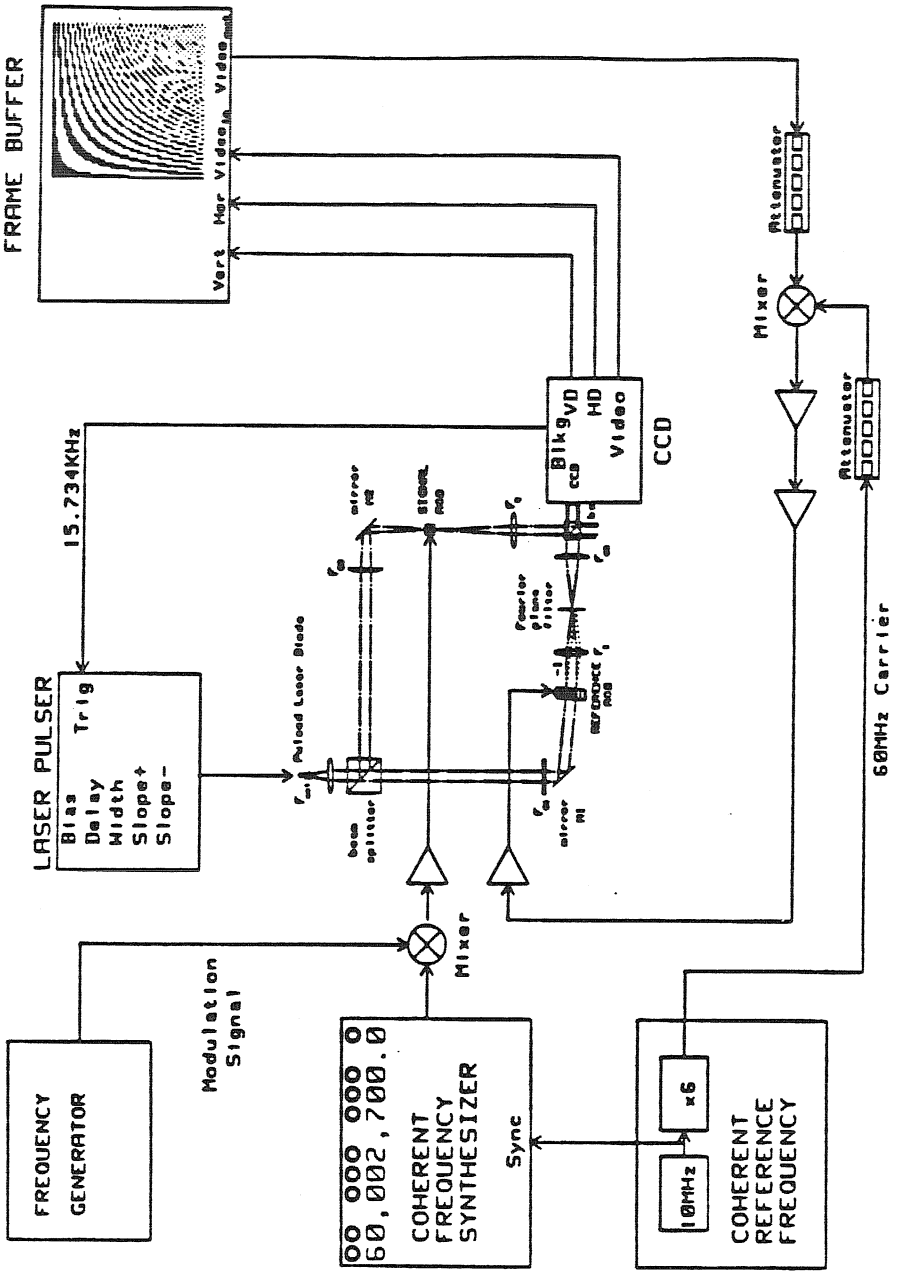

Fig.3.6.3 System diagram for the Mach-Zehnder TSI spectrum processor.

the light is uniformly spread and collimated in the x dimension. The DFT reference signal is mixed with a $60MHz$ carrier signal before being input into the system. The generation of the DFT matrix signal is achieved using a personal computer and a video frame buffer. Fig.3.6.4 shows the $8.4\mu sec$ CCD imaged space-time raster of the DFT matrix stored in a standard video format. This signal is compensated for effects such as interleaved fields and vertical blanking dead time. The laser diode is pulsed in synchronism with the video line rate. Also, the time integrating CCD is synchronized with the video frame buffer as shown in Fig.3.6.3, which displays the system timing signals. The limited $5MHz$ bandwidth of the frame buffer along with its video line rate format restricts the analysis bandwidth of the fine frequency DFT processor, although improvements can be made using a larger CCD area and different magnification imaging optics. As fine frequency bandwidths equal to the Bragg cell space integrating coarse frequency resolution are hard to achieve using the video buffer, we have a system designed for smaller fine frequency bandwidth, thus giving part of the full folded spectrum output, nevertheless, allowing us to demonstrate the TSI DFT processing principle.

Fig.3.6.5 shows the 2-D folded spectrum output data for the Caltech processor using a double sided DFT reference signal that sweeps down in frequency during one video field while sweeping up in frequency over the next field. The video outputs are displayed after bias subtraction using the personal computer to store successive constructive and destructive frames generated by rotating the beam splitter to eliminate the spatial carrier. The fine frequency resolution of the processor is about $120Hz$ with a system fine frequency bandwidth of $5.4KHz$. Fig. 3.6.5(a) shows a single coarse frequency spectral peak produced by a $56,003,211Hz$ input tone signal. The fine frequency resolving power of the processor is shown in Fig. 3.6.5(b), where two spectral peaks are positioned according to the coarse and fine frequency content of the $56,004,709.3Hz$ input signal tone. Two peaks occur along the fine frequency because a double sided DFT signal is used for the baseband processing. Fig. 3.6.5(c,d) shows the processor coarse frequency bandwidth to be better than $\pm 10MHz$. The carrier demodulation approach for bias removal was tested using external filtering

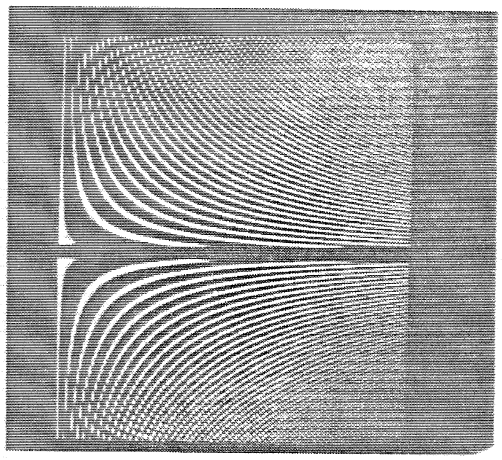

Fig.3.6.4 8.4μsec CCD imaged space-time raster of the double sided DFT reference signal.

electronics. Fig. 3.6.5(e,f) show carrier demodulated processor outputs for $60MHz$ and $60,000,900Hz$ suppressed $959.2KHz$ AM signal inputs, respectively. The coarse frequency achieved is $68KHz$ per pixel, and the number of coarse and fine frequency resolution bins is 384 and 50, respectively. A spectral sensitivity of $-40dB$ was obtained, with a 0.4 single tone signal to bias ratio. Successive frame averaging was used to get better output signal-to-noise ratio. A frequency measurement linearity plot of the processor is shown in Fig. 3.6.6, demonstrating the linear relationship between the spectral peak position on the CCD and the input frequency value.

Thus, the 2-D additive Mach-Zehnder interferometer based folded spectrum processor provides large bandwidth, high resolution, signal spectral outputs on a 2-D coarse/fine frequency raster coordinate frame. Nevertheless, this optical architecture is based on the Mach-Zehnder interferometer that is unstable due to mechanical vibrations, thus making the processor difficult to operate in uncontrolled environments, such as on board space applications. It is for this reason that we investigated an alternate optical architecture for 2-D folded spectrum processing. This in-line multiplicative design is a more stable optical architecture, and is discussed in detail in the next section.

3.7 Multiplicative TSI 2-D Folded Spectrum Processor

Theory and Experimental Results:

An alternate way to perform 2-D folded spectrum processing is the multiplicative pulsed source time and space integrating (TSI) spectrum processor. This architecture is a cascaded combination of the in-line, additive, electronic reference, space integrating broadband acousto-optic spectrum analyzer shown in Fig.3.4.2, and the in-line, additive, time integrating DFT narrowband processor of Fig.3.5.2. The multiplicative nature of the TSI processor comes about because the Bragg diffracted light from the first AOD is rediffracted by the second AOD in the system. This causes the diffracted signal and reference modulations from the first AOD to be multiplied by the appropriately biased DFT column modulation introduced by the second AOD.

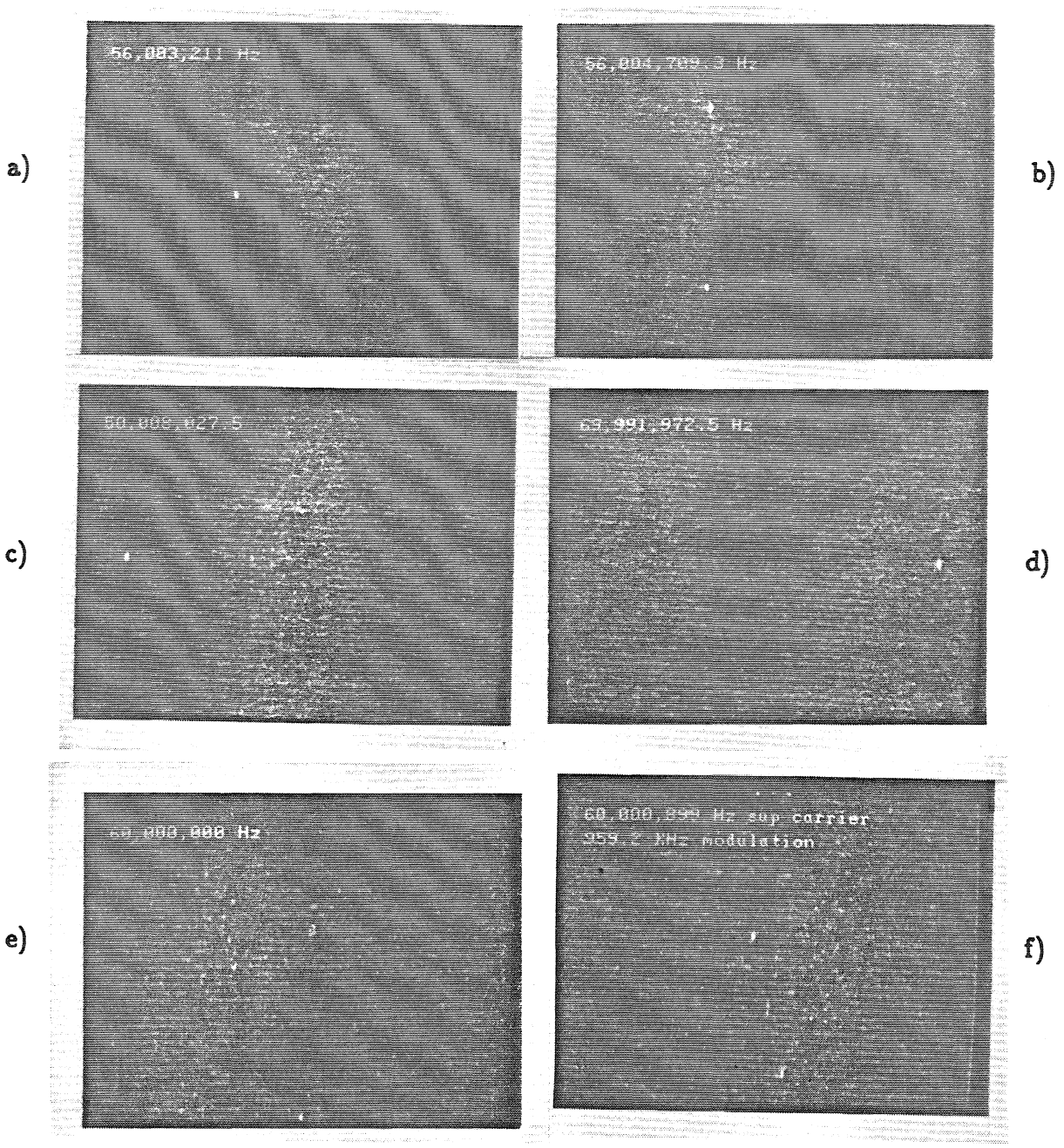

Fig.3.6.5 Double sided bias free folded spectrum 2-D outputs from the Mach-Zehnder TSI processor for input frequencies (a) $56,003,211Hz$, (b) $56,004,709.3Hz$, (c) $50,008,027.5Hz$, (d) $69,991,972.5Hz$ via computer bias subtraction, and (e) $60MHz$, (f) $60,000,900Hz$ *suppressed* $959.2KHz$ AM via carrier demodulation.

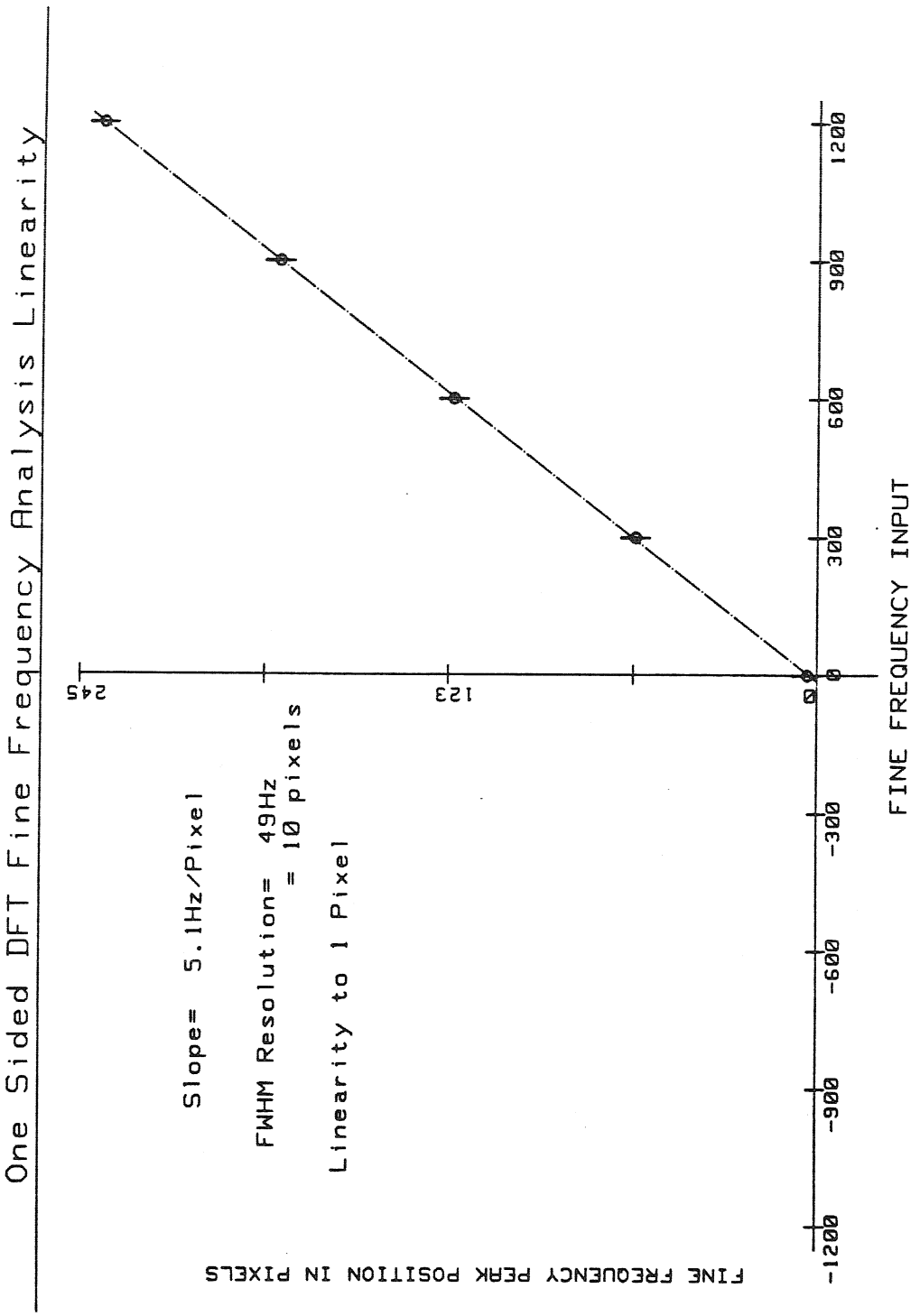

Fig.3.6.6 Fine frequency linearity plot for the Mach-Zehnder TSI spectrum processor.

Fig. 3.7.1 shows this TSI multiplicative architecture for 2-D folded spectrum analysis using crossed Bragg cells, anamorphic imaging and Fourier transforming optics, a high power pulsing laser diode, a CCD detector array, and supplementary electronics. The signal chain for the system is as follows. The information signal $s(t)$ is electronically added to the reference chirp $c(t)$, both signals being driven at the AOD center frequency f_0. This composite signal, $s_1(t)$, is fed to AOD1. The +1 diffracted light from AOD1 is Fourier transformed along x while being collimated in y by a spherical lens, thus giving a slit of light of length Y, incident at the Bragg angle in the orthogonal AOD2 acoustic column. The position of this slit of light along the x direction in AOD2 depends on the frequency of the input signal.The DFT reference signal $d'(t)$ on an offset carrier f_s is electronically added to a DC bias level d_0 before being heterodyned to the center frequency f_0, giving the composite signal $s_2(t)$, which drives AOD2. The +1 Bragg diffracted light from AOD1 is rediffracted by AOD2, giving light that is modulated by the product of the spatial Fourier transform of $\tilde{s}_1(t - \frac{x-X/2}{v_a})$ and the modulation $\tilde{s}_2(t - \frac{y}{v_a})$. This doubly diffracted signal is imaged by a pair of cylindrical lenses on to the CCD array, after appropriate single sideband DFT signal filtering in the Fourier plane of the cylindrical lens C_2. Thus, the electric field incident on the CCD detector plane on the n_{th} light pulse is given by:

$$E(u, y, n) = E_{aod1}(u, n)\, E_{aod2}(y, n), \tag{3.7.1}$$

where

$$E_{aod1}(u, n) = \int_X \tilde{s}_1\Big(nT + T_1 - \frac{x}{v_a}\Big) e^{-j2\pi ux}\, dx \tag{3.7.2}$$

$$E_{aod2}(y, n) = \tilde{s}_2\Big(t - \frac{y}{v_a}\Big), \tag{3.7.3}$$

and

$$s_1(t) = s(t) + c(t) \qquad\qquad s_2(t) = [d_0 + d'(t)]\cos(2\pi f_0 t), \tag{3.7.4a, b}$$

where $s(t)$, $c(t)$, and $d'(t)$ were defined in Sections 3.4 and 3.5. The intensity integrated

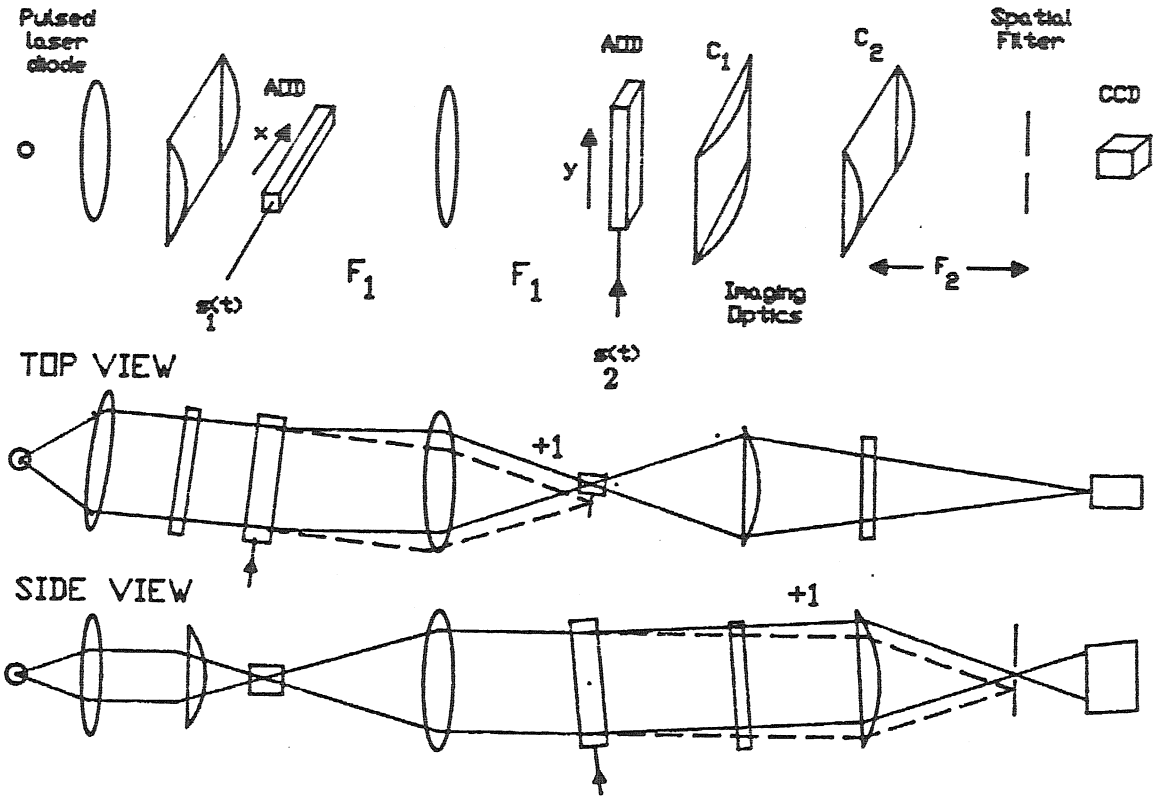

Fig.3.7.1 2-D pulsed source time and space integrating acousto-optic multiplicative folded spectrum processor.

on the CCD over N light pulses is given by:

$$\begin{aligned} I(u,y) &= \sum_{n=0}^{N-1} \left| E_{aod1}(u,n)\, E_{aod2}(y,n) \right|^2 \\ &= \sum_{n=0}^{N-1} \left| E_{aod1}(u,n) \right|^2 \left| E_{aod2}(y,n) \right|^2 \end{aligned} \tag{3.7.5}$$

where $|E_{aod1}(u,n)|^2$ is the intensity detected in the in-line additive electronic reference space integrating spectrum analyzer discussed in Section 3.4, while $|E_{aod2}(u,n)|^2$ is proportional to the intensity output of the in-line DFT based time integrating spectrum analyzer introduced in Section 3.5. In essence, the AOD's act as intensity modulators when the signal term in each AOD is biased by its reference signal. In this TSI processor, the reference signals correspond to a DC bias level associated with the DFT signal, and the repetitive chirp signal $c(t)$ is added to the input signal $s(t)$.

Using Eqn.3.4.16, we can write the +1 order diffracted electric field from the first Bragg cell ($AOD1$) as:

$$E_{aod1}(u,n) = S + C\,, \tag{3.7.6}$$

where

$$S = c' \int \tilde{S}(f) e^{j2\pi f(nT+T_1)} B(u + \frac{f}{v_a}) df \tag{3.7.7}$$

$$C = C_0 e^{-j\pi u X} e^{j\phi_c} \mathrm{rect}\left[\frac{uv_a - B/2}{B}\right], \tag{3.7.8}$$

where S and C are the single sideband space integrated signal and reference chirp spectrums, respectively, and f is the input signal coarse plus fine frequency component. Similarly, using Eqn.3.5.16, we can write:

$$E_{aod2}(u,n) = b + d\,, \tag{3.7.9}$$

where

$$b = d_0\, \mathrm{rect}[\frac{y - Y/2}{Y}] \tag{3.7.10}$$

$$d = d_1 e^{-j2\pi(f_s + n\Delta f)(T_1 - \frac{y}{v_a})} \mathrm{rect}[\frac{y - Y/2}{Y}], \tag{3.7.11}$$

where d is the spatially filtered single sideband DFT signal with amplitude d_1, and d_0 is a constant bias term. Note that in the terms S, C, b, and d, the AOD sampled

temporal carrier term has been removed by the intensity detection operation, as was earlier shown in Sections 3.4 and 3.5. Simply put, the intensity detected by the CCD in this multiplicative processor is given by:

$$\begin{aligned} I(u,y) &= \sum_{n=0}^{N-1} \left|E_{aod1}(u,n)\right|^2 \left|E_{aod2}(y,n)\right|^2 \\ &= \sum_{n=0}^{N-1} \Big[4\mathrm{Re}(SC^*)\,\mathrm{Re}(db^*) + \left|C\right|^2 \left|b+d\right|^2 \\ &\qquad + 2[\left|b\right|^2 + \left|d\right|^2]\,\mathrm{Re}(SC^*) + \left|S\right|^2 \left|b+d\right|^2 \Big] \end{aligned} \tag{3.7.12}$$

where the first term in the expansion gives the desired interferometric 2-D folded spectrum term, while the second term gives the constant bias term. The last two terms contribute to the signal dependent bias. Substituting the values for the signal and reference terms, we can express the 2-D folded spectrum as:

$$\begin{aligned} I_f(u,y) &= \sum_{n=0}^{N-1} 4\mathrm{Re}(SC^*)\,\mathrm{Re}(db^*) \\ &= 4\sum_{n=0}^{N-1} \mathrm{Re}\Big[\Big\{ \int c\,\tilde{S}(f) e^{j2\pi f(nT+T_1)} B(u+\frac{f}{v_a}) df \Big\} \\ &\quad \times \Big\{ C_0^* e^{j\pi u X} e^{-j\phi_c} \mathrm{rect}\big[\frac{uv_a - B/2}{B}\big] \Big\} \Big] \\ &\quad \times d_0 d_1 \cos\big[2\pi(\frac{n\Delta f + f_s}{v_a})(y-Y)\big] \mathrm{rect}\big[\frac{y-Y/2}{Y}\big], \end{aligned} \tag{3.7.13}$$

where c was earlier defined as $c = e^{-j\pi f \frac{X}{v_a}}$. For a single tone input signal $s(t)$ with frequency $f' = f_c + \delta_f$, where $\tilde{S}(f) = \delta(f+f')$, the system impulse response is approximately given by:

$$\begin{aligned} I_f(u,y) \approx 4C_0^* d_0 d_1\, B\big(u - \frac{f_c}{v_a}\big) \sum_{n=0}^{N-1} &\cos\big[2\pi\Delta f nT + \phi_c(f')\big] \\ &\times \cos\big[2\pi(\frac{n\Delta f + f_s}{v_a})(y-Y)\big] \mathrm{rect}\big[\frac{y-Y/2}{Y}\big]. \end{aligned} \tag{3.7.14}$$

On completing the summation over N light pulses accumulated in the finite CCD window of height Y, the system impulse response can be expressed as:

$$I_f(u,y) \approx K_1\, B\big(u - \frac{f_c}{v_a}\big) N \mathrm{sinc}\left\{NT[\delta_f + \frac{\Delta f}{v_a T}(y-Y)]\right\} \cos(2\pi\gamma' y + \beta') \tag{3.7.15}$$

where $K_1 = 2C_0^* d_0 d_1$ is a real constant proportional to the signal and reference amplitude terms. The folded spectrum is generated on a spatial carrier along the y direction, where the carrier frequency γ' and phase β' are given by:

$$\gamma' = \frac{1}{v_a}[f_s + (N-1)\frac{\Delta f}{2}] \tag{3.7.16}$$

$$\beta' = \phi_c(f') + \pi(N-1)[\delta_f T - \frac{1}{2}] - 2\pi f_s T_1 \tag{3.7.17}$$

where $\phi_c(f') = \frac{\pi f'^2}{b}$. Thus, the 2-D folded spectrum output consists of a spectral peak positioned at the CCD u, y coordinates of $u = \frac{f_c}{v_a}$, $y = Y - \frac{\delta_f}{\Delta f} v_a T$, corresponding to the input signal coarse and fine frequency components, respectively. Recall that the Mach-Zehnder additive processor desribed in Section 3.6 had a similar impulse response expressed in Eqn.3.6.4. The constant bias contribution is calculated from the second term in Eqn.3.7.12, giving the expression:

$$\begin{aligned} K_2 &= \sum_{n=0}^{N-1} |C|^2 \, |b+d|^2 \\ &= NC_0(d_0^2 + d_1^2)\mathrm{rect}[\frac{uv_a - B/2}{B}]\mathrm{rect}[\frac{y - Y/2}{Y}] \\ &\quad + 2d_0 d_1 N \mathrm{sinc}\left\{NT\frac{\Delta f}{v_a T}(y-Y)\right\}\mathrm{rect}[\frac{uv_a - B/2}{B}]\cos(2\pi\gamma' y + \eta), \end{aligned} \tag{3.7.18}$$

where $\eta = -[\frac{\pi(N-1)}{2} + 2\pi f_s T_1]$. Here, the first term corresponds to a uniform bias generated over the CCD surface by the chirp spectrum, while the second term gives a constant bias slit along the $y = Y$ ($\delta_f = 0$) fine frequency position, that rides on a spatial carrier γ' along the y direction.

The single tone signal dependent bias term is given by:

$$\begin{aligned} K_2 &= \sum_{n=0}^{N-1} \left\{ 2[|b|^2 + |d|^2]\,\mathrm{Re}(SC^*) + |S|^2 \, |b+d|^2 \right\} \\ &\approx NC_0(d_0^2 + d_1^2)B(u + \frac{f_c}{v_a})\mathrm{rect}[\frac{y - Y/2}{Y}] \\ &\quad + 2d_0 d_1 N \mathrm{sinc}\left\{NT\frac{\Delta f}{v_a T}(y-Y)\right\}B(u + \frac{f_c}{v_a})\cos(2\pi\gamma' y + \eta), \end{aligned} \tag{3.7.19}$$

where the first summation is negligible for $\delta_f \geq \frac{1}{NT}$, and the second summation gives the signal coarse frequency dependent bias terms. The first signal dependent bias term

is the coarse frequency bias ridge along the y direction of the CCD, centered at $u = \frac{f_c}{v_a}$, while the second term is a bias blur spot positioned at $u = \frac{f_c}{v_a}$, $y = Y$ that is riding on a spatial carrier γ'. Note that the major bias contribution is not modulated by the spatial carrier, and can be removed via electronic carrier demodulation and filtering. The additional small bias contribution can be removed by electronic thresholding.

The multiplicative TSI processor was set up in the laboratory, and is shown in Fig. 3.7.2. Fig. 3.7.3 shows the overall optical and electronic system design for the processor. A high power laser diode with an $8W$ peak radiant flux at its maximum drive current and .05% duty factor is used in the experiment with the Power Technology Inc. IL30C laser diode pulser circuit. The light from the laser diode is collimated by a $20cm$ focal length spherical lens, while a $9cm$ focal length cylindrical lens focusses the collimated light along the y direction in AOD1. An $F_1 = 20cm$ spherical lens Fourier transforms the diffracted AOD modulation along the x direction. The undiffracted light from AOD1 is blocked in the AOD2 plane. The AOD's used in this experiment are also slow shear mode Tellurium dioxide devices with an aperture time of 70 μsec and bandwidth of 40 MHz. A 60 MHz center frequency is used for the AOD's. Crossed cylinders C_1 and C_2 with $15cm$ and $10cm$ focal lengths, respectively, were used for imaging the diffracted light along the y direction. Unlike a telescopic $4F$ imaging system based architecture (see Fig.3.7.4) that uses the Fourier transform spherical lens (F_1) and another spherical lens for imaging, this crossed cylinder imaging design provides overall short system length and desired demagnifications for compatibility with the CCD detector specifications. In addition, the DFT signal single sideband filtering and AOD2 DC light removal are easily accomplished in the Fourier plane of cylinder C_2. In contrast, the $4F$ imaging system has the spatial filtering plane in the signal AOD crystal, thus preventing exact Fourier plane free space spatial filtering of the DFT signal and AOD DC light. The crossed cylinder imaging combination provides a 4 times demagnification along the y direction, with a 1.5 times magnification along the x direction. In essence, the 35.4 mm ($52.84\mu sec$) DFT video line is imaged on to the 8.8 mm horizontal side of the Sony black and white 2-D CCD sensor.

The processor timing is controlled by the CCD detector 7.16 MHz internal oscil-

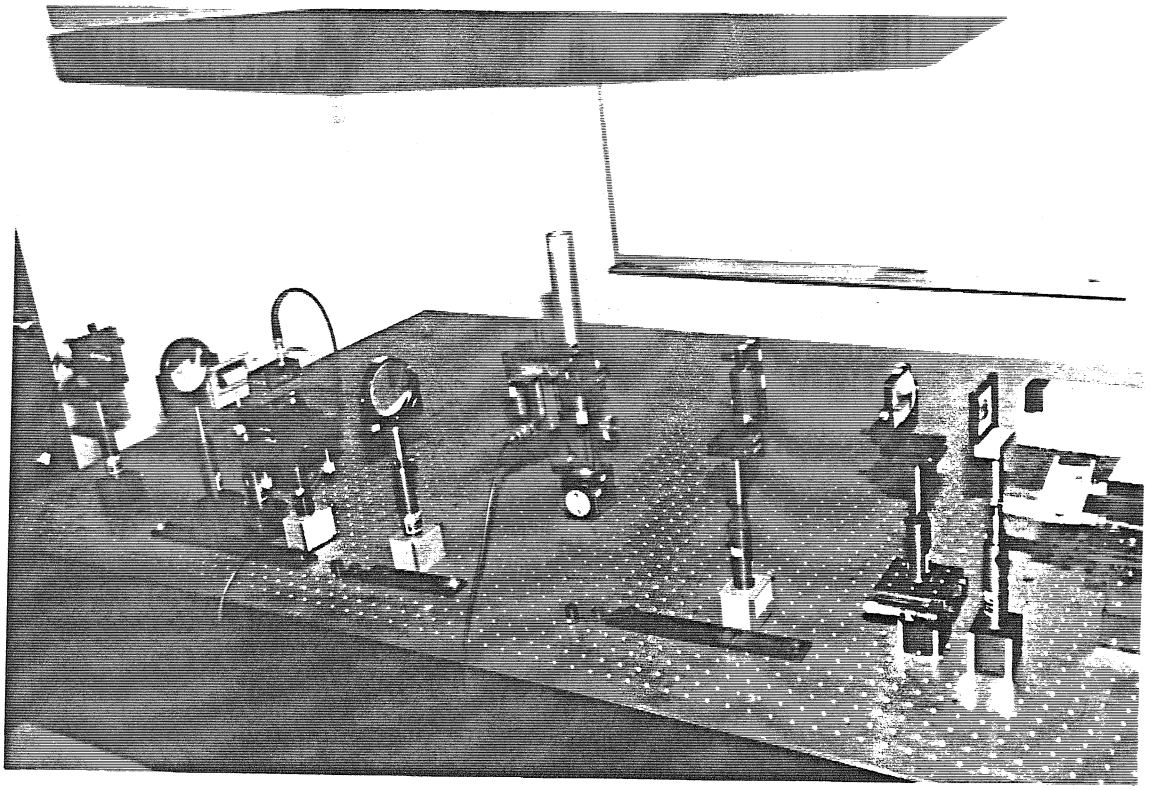

Fig.3.7.2 Laboratory set-up of the Caltech multiplicative time and space integrating folded spectrum processor.

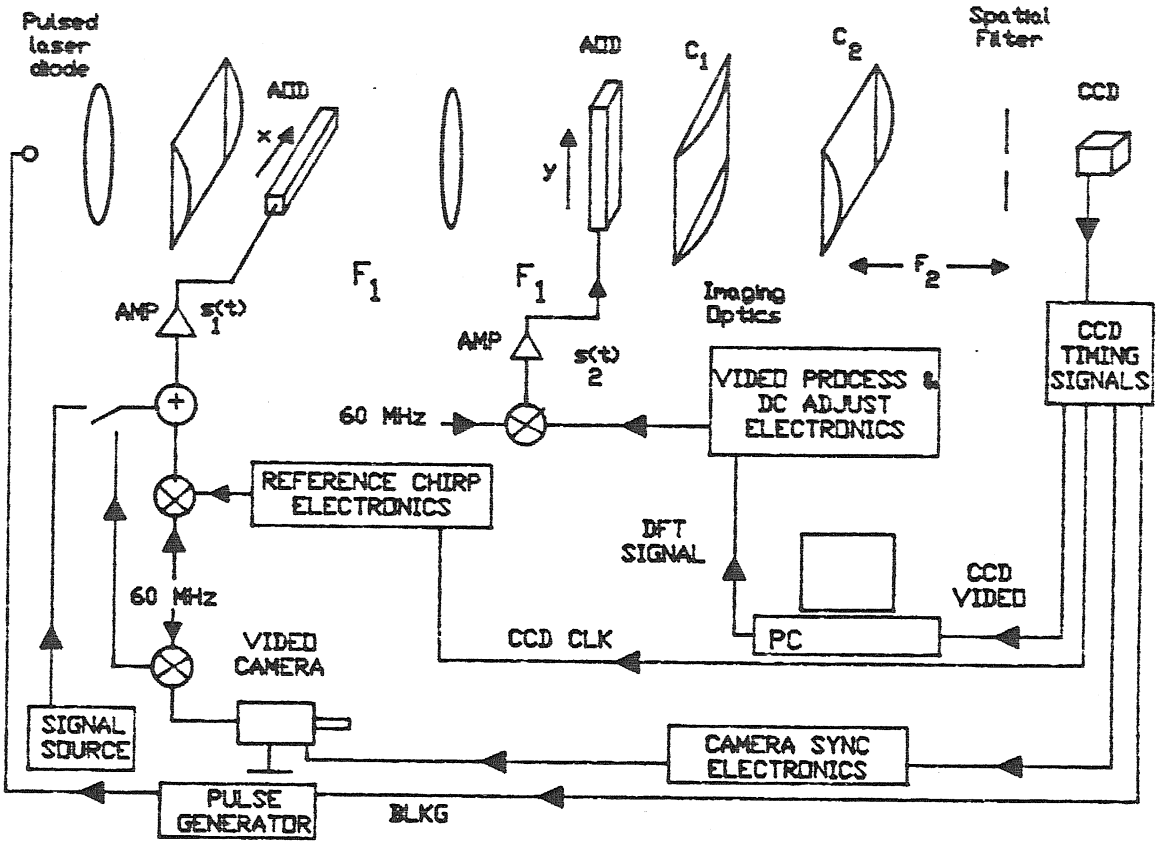

Fig.3.7.3 System diagram for the multiplicative TSI spectrum processor.

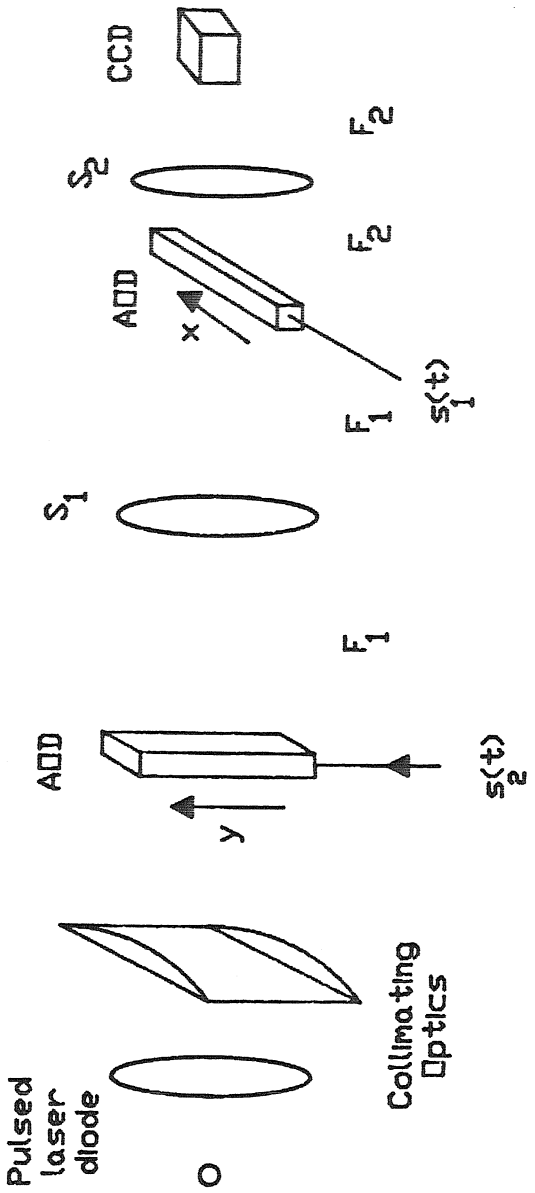

Fig.3.7.4 Multiplicative TSI folded spectrum processor based on the $4F$ imaging system.

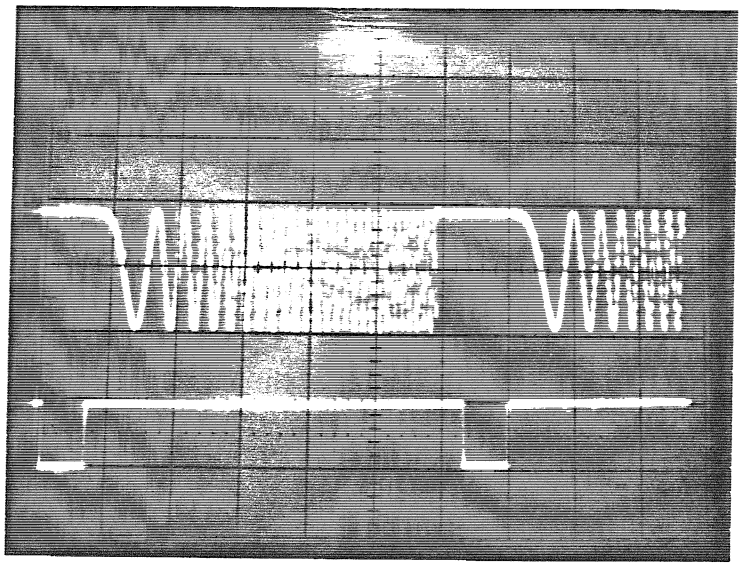

Fig.3.7.5 PROM generated repetitive 1 MHz bandwidth reference chirp signal (upper trace) and its 15.734 KHz CCD composite blanking trigger signal.

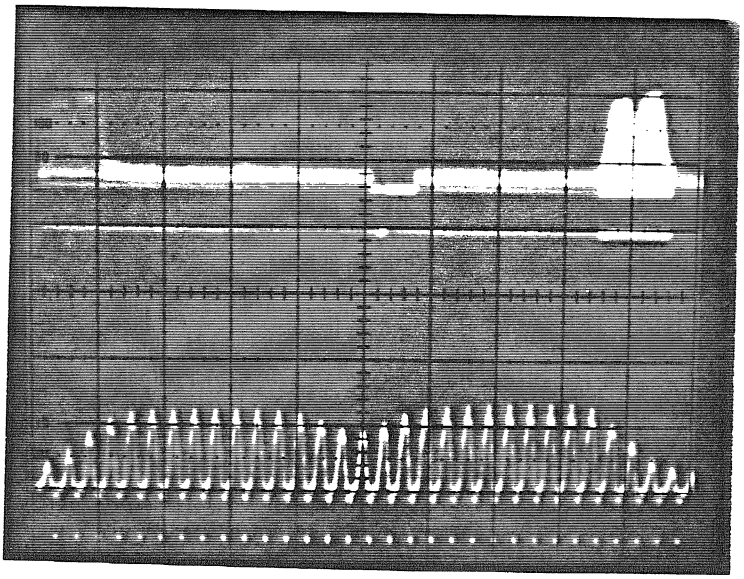

Fig.3.7.6 1 MHz reference chirp Fourier plane optical spectrum along the vertical (y) direction of the 2-D CCD. Lower trace shows a magnified view of the double sided chirp spectrum.

lator. The CCD composite blanking signal is used to generate the 15.734 KHz laser diode trigger signal with a pulse width of 100 nsec. This corresponds to a light flash for every video line. This is in contrast to the folded spectrum processing of tones, where the laser diode trigger frequency is adjusted according to the desired Nyquist limited bandwidth. As described in Section 3.4, the reference chirp is stored in a digitally programmable read only memory (PROM) and read-out each laser diode trigger pulse using the CCD pixel clock and a digital-to-analog converter. Fig. 3.7.5 shows a $1MHz$ bandwidth reference chirp signal that was used in one of the experiments with this TSI processor. Fig. 3.7.6 gives the Fourier plane optical spectrum of this chirp, with spatial sampling along the y (vertical) direction of the CCD. The lower trace in the picture gives a magnified view of the chirp spectrum across the vertical pixels of the CCD. The chirp, being digitally generated is highly coherent with the laser pulsing. The DFT signal is generated by the personal computer and video frame buffer system, as mentioned in Section 3.5. For video signal inputs, the CCD camera is locked to the CCD detector array by special synchronizing circuitry called Genlock (Sony). This assures that the input image and DFT reference video lines are synchronized in their signal and reference AOD's, respectively (see Fig.3.7.7).

Experimental results from this processor are shown in Fig. 3.7.8 and Fig. 3.7.13 for a fine frequency analysis bandwidth of $7.86KHz$ using the zero offset frequency single sided DFT reference signal shown in Fig. 3.5.3. Data in Fig. 3.7.8 correspond to a fine frequency variation from DC to 7.8 KHz. We see the interference peak move from left(DC) to right(7.86 KHz) along the respective coarse frequency bin. On further increasing the input tone fine frequency from $7.86KHz$ to $15.734KHz$, the peak moves back along the coarse frequency ridge from the right ($7.86KHz$) position to the left (DC) position. This effect is introduced through the aliasing phenomena in Nyquist limited sampling, and can be avoided by using a $\pm 7.86KHz$ double sided DFT signal, similar to the one used in the additive Mach-Zehnder TSI processor in Section 3.6. These single tone experiments are carried out using a signal generator whose frequency is varied around 60 MHz.

The 2-D results correspond to spectrums after electronic bias subtraction using

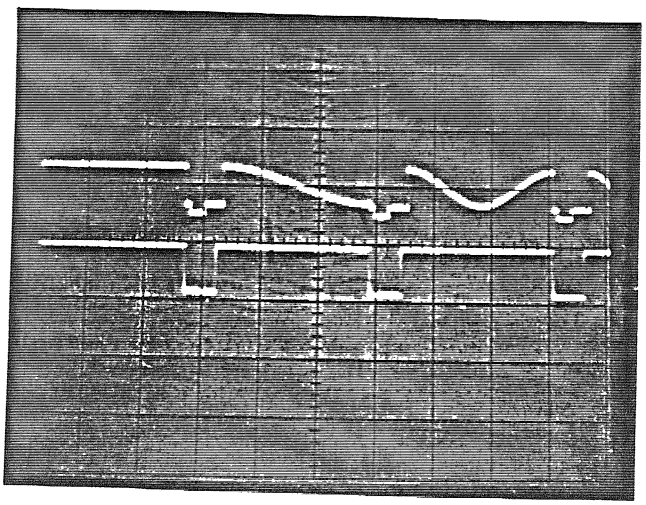

Fig.3.7.7 Oscilloscope trace shows the DFT video lines (upper trace) and the genlocked CCD camera horizontal drive signals (lower trace) are synchronized.

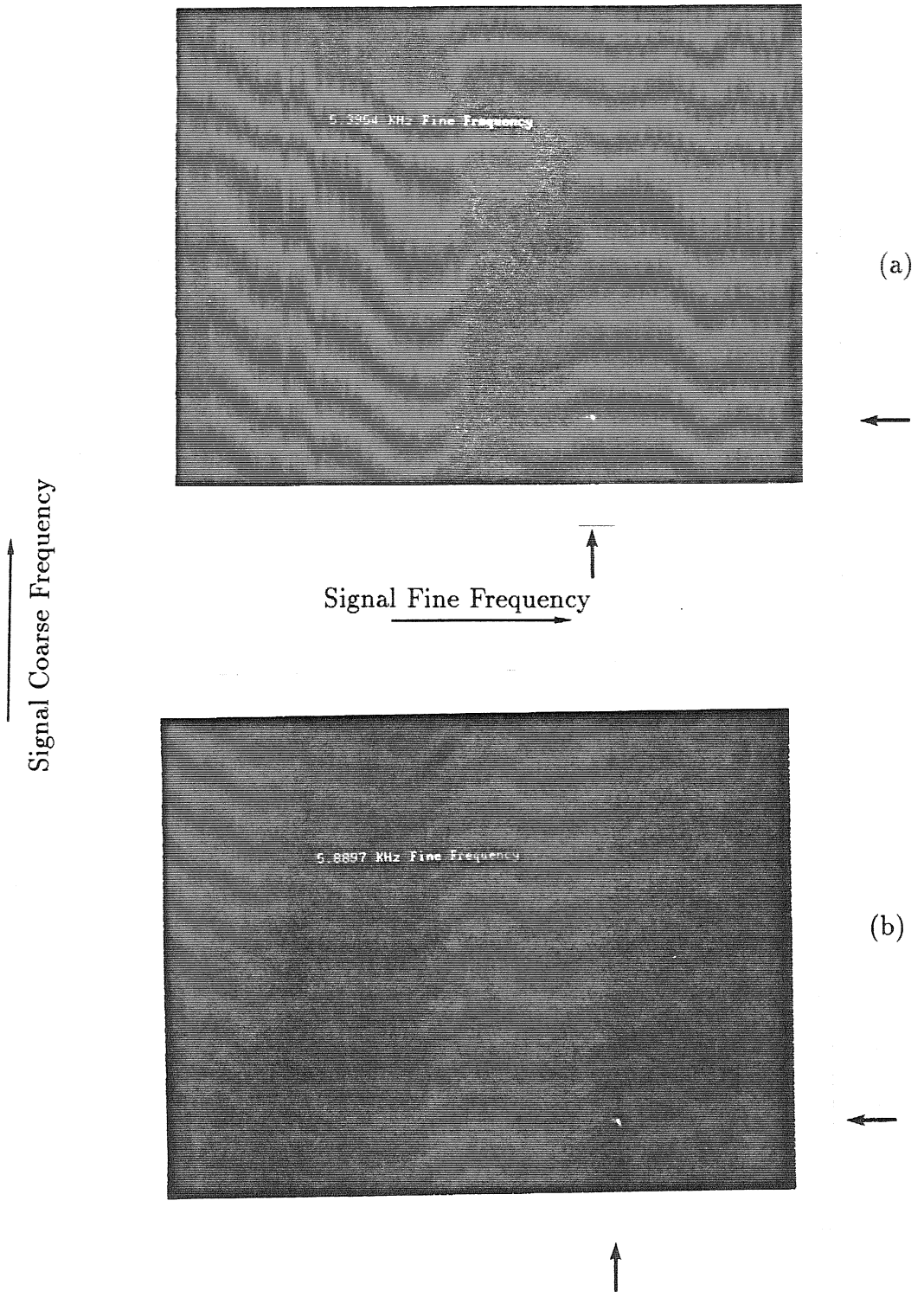

Fig.3.7.8 Single sided bias free folded spectrum 2-D outputs from the multiplicative TSI processor using a 1 MHz reference chirp for input signal frequencies (a) $60,005,395.0Hz$, (b) $60,005,889.0Hz$.

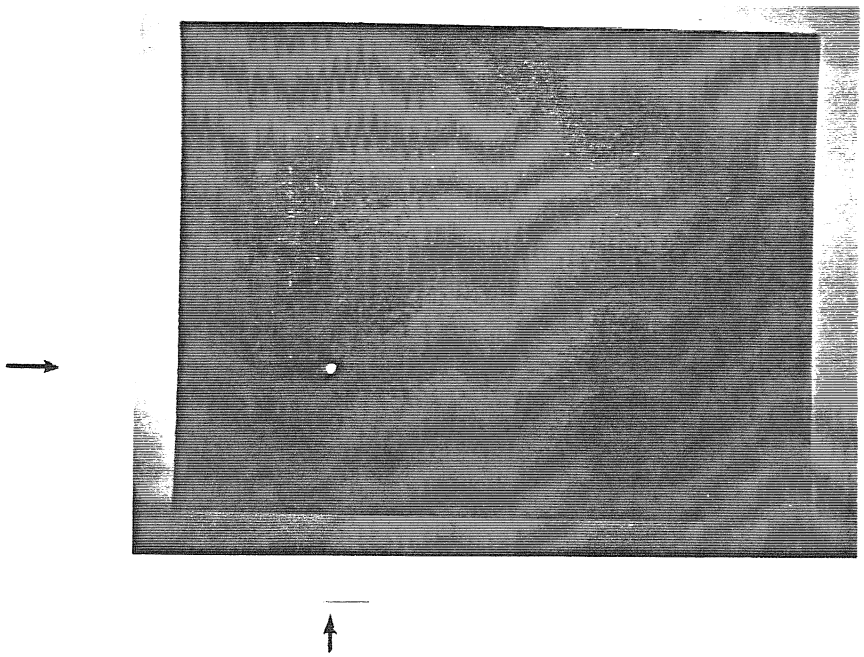

(c)

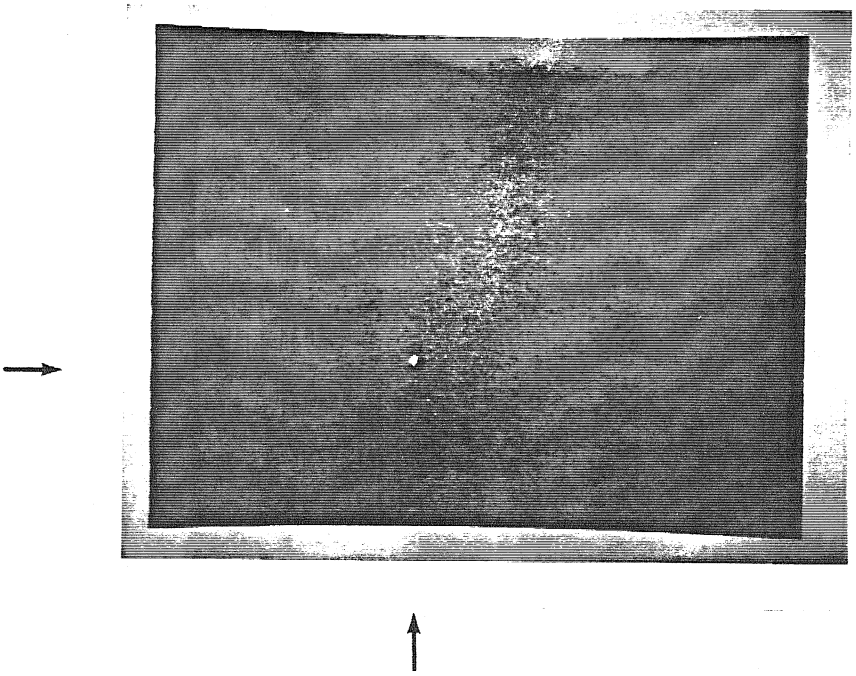

(d)

Fig.3.7.8 Single sided bias free folded spectrum 2-D outputs from the multiplicative TSI processor using a 3.5 MHz reference chirp for input frequencies (c) $62,377,934.0Hz$, (d) $62,945,658.0Hz$.

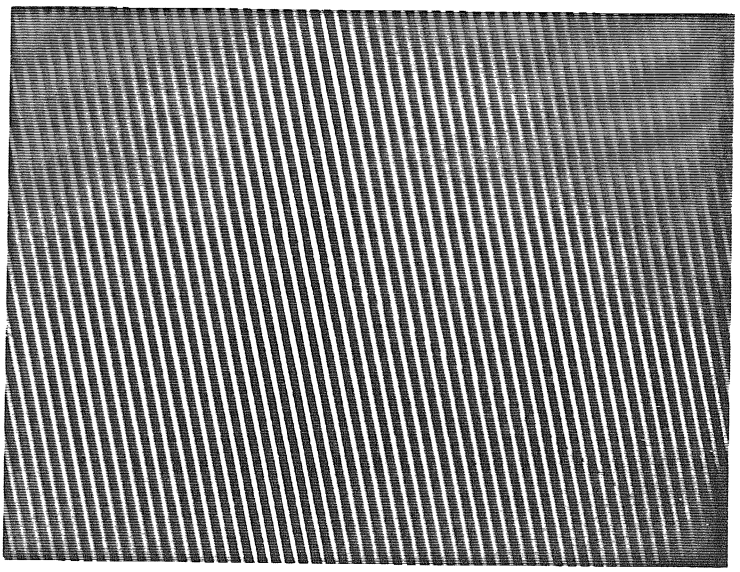

Fig.3.7.9 $\frac{1}{2}$ cycle/mm grating video image with a tilt angle $\theta \approx 14°$.

the IBM personal computer and video frame grabber configuration. The video frame grabber is used to acquire and store constructive and destructive spectral peaks over successive CCD frames, while the computer is used for pixel by pixel bias subtraction of these frames. Note that the experimental results from the single tone tests give the desired system signal impulse response expressed earlier in Eqn.3.7.15. Similar tests are carried out using the genlocked CCD video camera looking at simple grating images. Fig.3.7.9 shows a $\frac{1}{2}$ cycle/mm grating image with a tilt angle of approximately 14°. The camera is rotated to generate different tilt angles of the grating image, while a lens demagnifies and images the grating on to the $8.8 \times 6.6mm$ CCD sensor. The CCD pixel structure samples the grating light distribution using a $7.16MHz$ pixel clock along each horizontal line element of size $23\mu m$. This electronic scanning produces a temporally modulated video signal that consists of successive horizontal line scans of the input image. Fig.3.7.10 shows successive video lines from a grating image input. This signal is fed into an electronic circuit that removes the video synchronization pulses along with any DC bias level (see Fig.3.7.11). In addition, the circuit also amplifies and thresholds the signal to generate an amplified square wave signal that is mixed with the $60MHz$ AOD carrier frequency before being introduced into the optical processor (see Fig. 3.7.12). Fig. 3.7.13 shows the 2-D video spectrum of the tilted grating video image shown earlier in Fig. 3.7.9, using an imaging demagnification of ≈ 8. This input image corresponds to a $633KHz$ coarse frequency temporal variation along the x direction, with a $0.41KHz$ fine frequency variation along the vertical (y) direction. In the CCD two dimensional output signal, the DC of the fast (coarse) variation along the x direction of the image corresponds to the central bin between the two peaks in the picture. The slow (fine) variation along the y direction of the image corresponds to the left to right movement of the peak along each fast frequency bin. The positions of these spectral peaks are closely related to the expected result. Note that this 2- D spectrum gives the desired image impulse response of the processor expressed in Eqn. 3.7.26. Again, the frame grabber/computer system is used for bias removal in the image spectrum.

The processor yielded a coarse frequency resolution of 80 KHz corresponding to

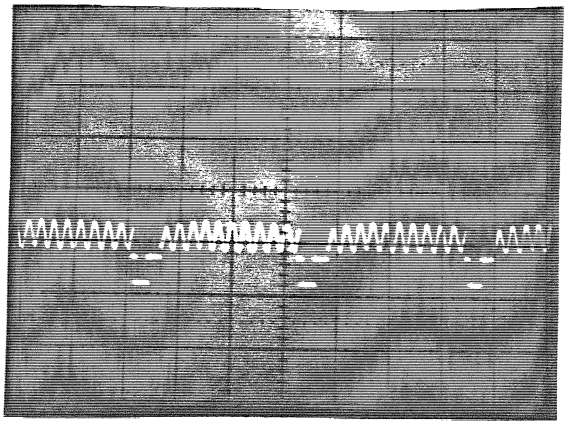

Fig.3.7.10 Video lines from the image input CCD camera.

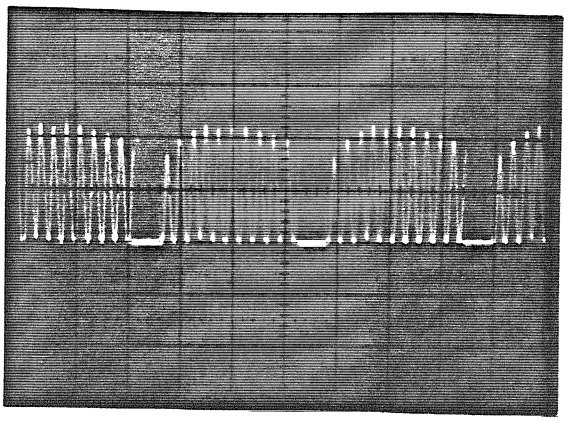

Fig.3.7.11 Video lines from the image input CCD camera after removing the video synchronization pulses and removing any DC level (DC=0).

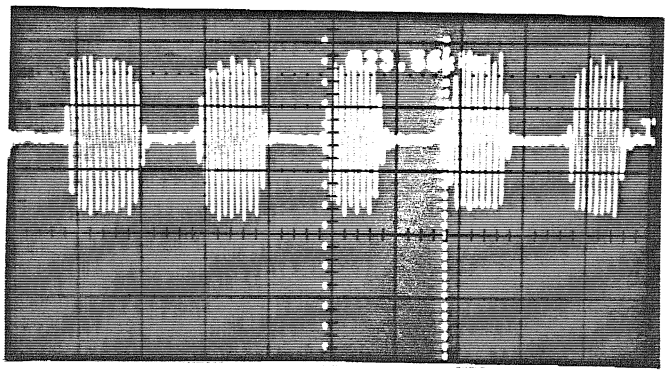

Fig.3.7.12 Amplitude modulated (AM) grating video signal that drives the signal Bragg cell. A 60 MHz carrier is used.

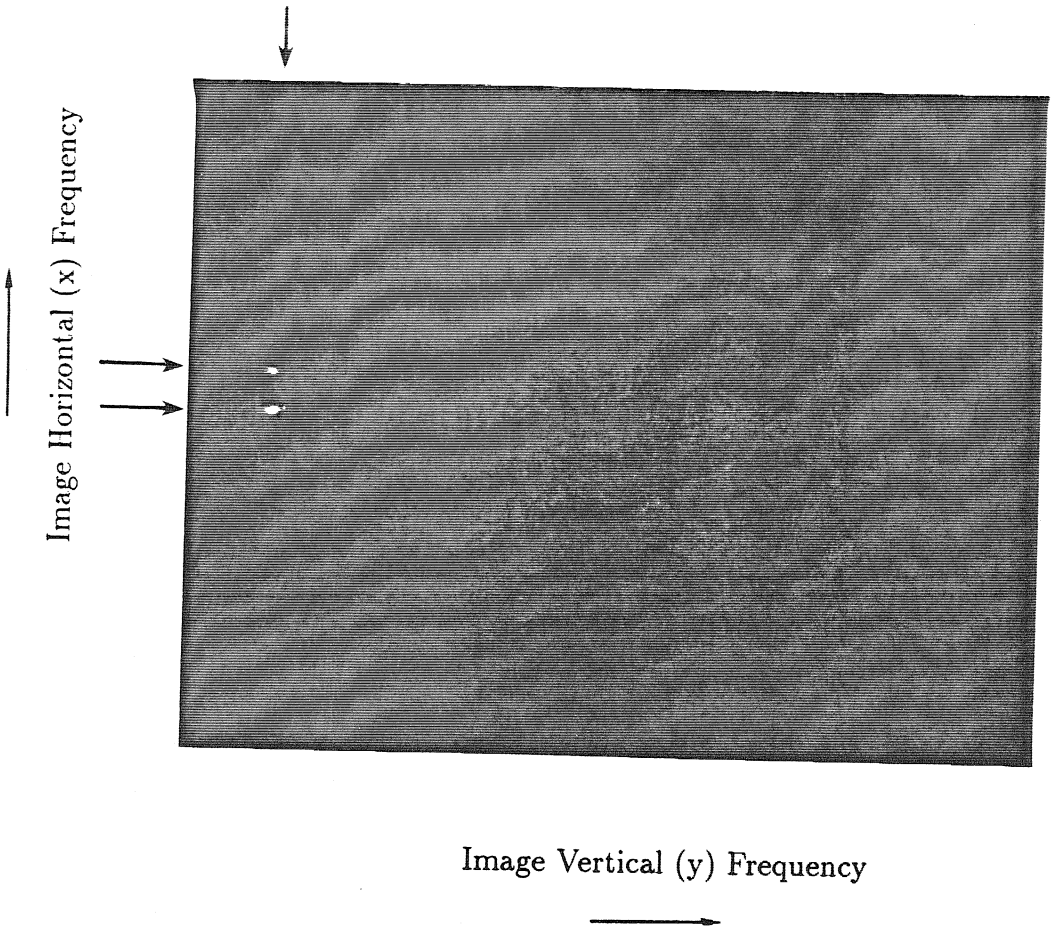

Fig.3.7.13 Double sided bias free 2-D image spectrum output from the multiplicative TSI processor using the tilted grating image in Fig.3.7.9. The spectrum corresponds to a 623 KHz horizontal (coarse) frequency with a 0.41 KHz vertical (fine) frequency.

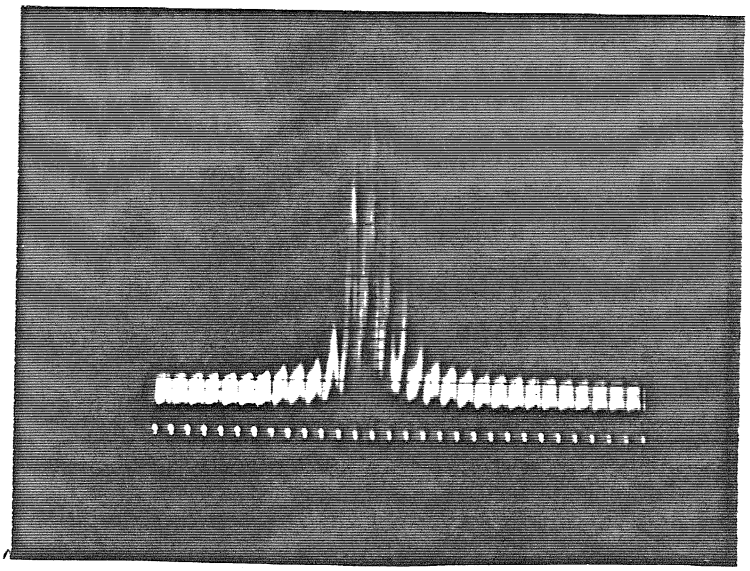

Fig.3.7.14 Multiplicative TSI processor coarse frequency resolution of 80 KHz corresponding to 5 interleaved vertical pixels of the 2-D CCD sensor.

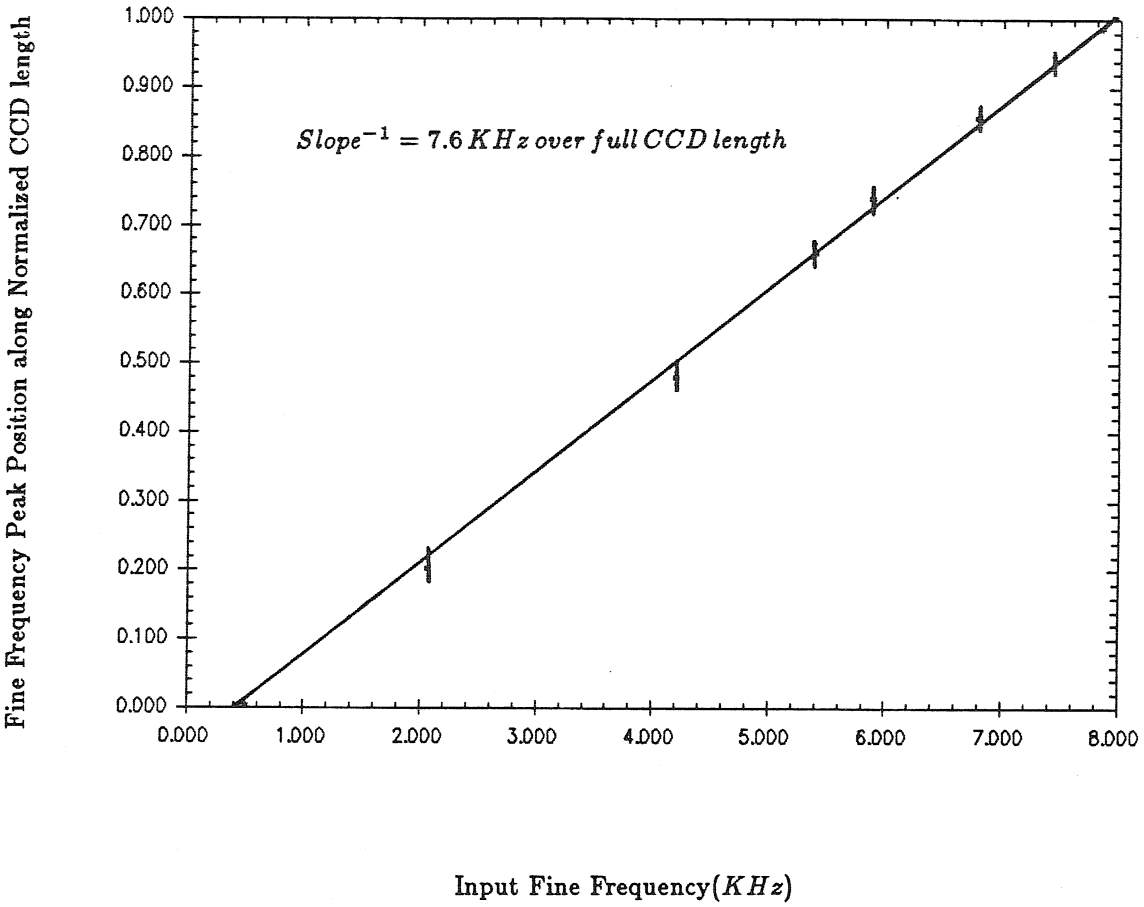

Fig.3.7.15 Fine frequency linearity plot for the multiplicative TSI spectrum processor.

5 interleaved vertical pixels shown in Fig. 3.7.14. Using the $3.5MHz$ bandwidth reference chirp, there are approximately 44 spatially multiplexed coarse frequency bins along the CCD vertical direction. The processor provided a fine frequency analysis bandwidth of $7.86KHz$, with a fine frequency resolution of $100Hz$, giving approximately 78 fine frequency bins along the horizontal direction of the CCD. The processor gave a single tone signal to bias ratio of 0.3 with a spectral sensitivity of $-26dB$. Fig. 3.7.15 gives the frequency measurement linearity plot for the processor over its fine frequency processing bandwidth, showing a high degree of linearity. Next, we shall discuss the system issues related to the additive and multiplicative TSI processors, respectively.

3.8. System Issues for the 2-D Folded Spectrum Processors

The Caltech prototype additive and multiplicative processors illustrate the application of time and space integrating acousto-optic pulsed laser systems for spectrum analysis of large time bandwidth product signals. The performance of these prototype systems is limited by a combination of inherent architecture limitations and deficiencies in the commercially available hardware employed in the systems. These TSI systems demonstrate the tradeoff principle, where the inherent architecture limitations in one system become the system advantages in the other system, and vice versa. For instance, starting with the additive architecture, its inherent system limitations include a reasonably high coherence length requirement for the pulsed laser emission to obtain optimum optical interference in the Mach-Zehnder interferometer [20], a coarse frequency analysis bandwidth limited by the light pulse width, interferometer precision alignment, and a high degree of sensitivity to mechanical instabilities and component vibrations at frequencies higher than $30Hz$. These limitations of the additive processor are turned around to inherent system advantages in the multiplicative processor. In particular, because of the common path nature of the light propagation, the laser light coherence requirements are less severe. In addition, the system becomes virtually insensitive to air currents and component vibrations, and the optical alignment procedure becomes much simpler. Also, the narrow laser pulse

width condition can be relaxed somewhat if the pulse width remains less than the inverse of the reference chirp bandwidth. The chirp bandwidth is determined by the maximum signal frequency to be processed by the spectrum analyzer. Nevertheless, compared to its additive counterpart, the multiplicative design suffers from other problems. For instance, the multiplicative system is light inefficient because of the multiple diffraction in the signal and reference AOD's, although this problem can be somewhat compensated for by using longer laser pulses. For a typical AOD intensity diffraction efficiency of $\epsilon \approx 0.1$, the multiplicative processor gives an overall light efficiency of $\epsilon_1 \epsilon_2 \approx 0.01$, while the additive design gives a light efficiency of $\frac{1}{2}(\epsilon_1 + \epsilon_2) \approx 0.1$. Thus, the additive design has a considerably higher light throughput than the multiplicative design. Also, the maximum signal bandwidth is limited by the physical width of the reference AOD crystal, as the position of the focussed slit of light in the reference AOD depends on the signal frequency driving the signal AOD. In addition, there is the extra signal dependent quadratic phase term ϕ_c in the processor output that is due to the reference DLO chirp spectrum. As mentioned earlier, the multiplicative approach is essentially an intensity modulated system that introduces an additional conjugate sideband contribution that produces additional signal and bias terms. In a multitone environment, these additional signal and bias terms can produce strong undesirable sidelobes, thus deteriorating the processor performance. Again, the additive architecture does not suffer from these problems of light efficiency, strong sidelobes, etc.

Apart from the inherent architecture limitations associated with each system, the Caltech prototype systems suffered from the non-optimized peripheral electronic hardware utilized for reference signal generation and optical detection. We used a Sony XC-37 industrial black and white video camera as the 2-D optical detector. This CCD has 384 horizontal pixels with a $23\mu m$ pixel separation, and 491 interlaced pixels with $13.4\mu m$ separation in the vertical direction. System performance parameters that were adversely affected by the non-optimized CCD specifications include processor coarse and fine frequency resolution, number of coarse and fine frequency bins, spectrum dynamic range, maximum detectable carrier spatial frequency, and

amplitude linearity of system response. The CCD specifications that are critical to the design of the processor include pixel size, number of pixels, read-out rate, dynamic range, modulation transfer function (MTF) at the near infrared wavelength of the laser diode, and CCD integration time. The additive and multiplicative processors achieved spectral sensitivities of $-40dB$ and $-26dB$, respectively. Both processors achieved a high degree of frequency linearity over their fine frequency processing bandwidths as shown in Figures 3.6.7 and 3.7.15, respectively. For ideal fine frequency processing, the optimum DFT reference waveform should have a bandwidth that fully utilizes the AOD bandwidth, a temporal duration that is N times each DFT column segment duration, thus giving a very high time bandwidth ($TB = N^2 \approx 10^6$) signal. In our experiments, we used a video bandwidth ($5MHz$) frame buffer with a $15.735KHz$ video line read-out rate to generate a lower than optimum time bandwidth product DFT matrix signal, thus resulting in a processor output that corresponds to only a part of the complete folded spectrum. Note that the coarse frequency resolution of the space integrating acousto-optic processor depends on various factors such as the illuminated AOD aperture, acoustic apodization effects, beam profile and CCD pixel size [17,21]. In addition, excessive degradation of the blur spot is caused by optical aberrations, as well as photo generated charge diffusion that is due to deep penetration of the infrared photons in the CCD detector, thereby degrading the MTF [19]. Thus, we expect that by employing higher quality optics, a high performance CCD detector optimized for scientific application, along with state of the art customized electronics for generation of the high time bandwidth product DFT matrix and DLO reference chirp signals, we can realize a practical 2-D folded spectrum pulsed laser processor, which is limited only by its inherent architectural constraints. Later in the thesis, we will see how optical disk technology can be incorporated in TSI acousto-optic spectrum analyzers to generate the extremely high time bandwidth product reference signals to produce complete folded spectrum outputs.

An issue that cannot be neglected in all time integrating processors is the removal of the interferometrically generated bias from the desired signal information. In the TSI processors introduced earlier, we note that the useful 2-D folded spectrum can be

generated on a spatial carrier in the x or y direction on the CCD surface, allowing the natural read-out mechanism of the CCD to convert a spatial variation to a temporal variation that is bandpass filtered and rectified to give the desired signal term without bias. This method is called bias removal via carrier demodulation, and was tested in the additive processor where the rotation in the output beam splitter produced the spatial carrier. Data in Fig. 3.6.5(e,f) show carrier demodulated bias-free folded spectrum outputs.

Another approach to bias removal applicable to the additive processor employs two synchronous CCD detector arrays exactly aligned in both the output ports of the recombining dielectric beam splitter cube positioned near the output plane of the processor [22]. The phase shift upon reflection from the multilayer dielectric surface is such that the two separately detected interferometrically generated modulations differ in phase by 180 degrees, thus allowing electronic subtraction of the two video signals, giving a bias free modulating signal. This type of two CCD approach for real-time bias removal was simulated in the Caltech processors by using a successive frame bias subtraction technique using a personal computer and video frame grabber.

These carrier demodulation and bias subtraction methods for bias removal do not solve the problem of limited system dynamic range, since processing is performed after the detection of the signal. The effective system dynamic range at the output is:

$$DR_s = DR_{CCD}[\frac{S}{(S+B)}],$$

where DR_{CCD} is the dynamic range of the output CCD detector and S and B are the signal and bias power levels on the detector, respectively. In most time integrating systems, the signal to bias power ratio is much less than one. One approach to real-time bias removal in spectrum analyzers is the use of a photorefractive crystal as a time integrating detector [23]. The idea is to generate the desired spectrum term on a fast spatial carrier on the crystal surface using an additive optical architecture. The spectrum is read by illuminating the crystal by a Bragg matched read-out beam, thus leaving the bias behind on the crystal. The physical properties of photorefractive crystals such as bismuth silicon oxide (BSO) offer other system advantages such as

high resolution detection, an increased space bandwidth product, leading to a large number of coarse and fine frequency bins in the spectrum analyzer. Later in the thesis, we address this photorefractive approach to bias removal in time integrating processors.

3.9 Conclusion

We have investigated pulsed source time and space integrating acousto-optic techniques for spectrum analysis of large time bandwidth signals, exploiting the inherent 2-D nature of optical systems. In particular, we presented two alternate approaches for realizing TSI 2-D spectrum analyzers; namely, the additive and multiplicative optical architectures, respectively. It was shown that both these architectures possess their distinct advantages and limitations (see Table 3.9.1). Thus, depending on the particular application, its environment, and desired special features, one of the systems could be chosen, given the engineering tradeoffs. For example, the additive design would not be appropriate in a mechanically unstable environment, whereas the multiplicative architecture will give a much better performance in a similar uncontrolled setting. On the other hand, an application where little optical power is available, the additive design would prevail over the multiplicative system. The pulsed source was uniquely exploited in these systems to provide the necessary aliasing to baseband of the high frequency input signals, as well as to implement the freezing action of the Bragg cell acoustic signals for periodic imaging to generate spatially distributed local oscillators. The Discrete Fourier transform algorithm for spectrum processing adapted well to the pulsed source nature of these systems, unlike the Chirp-Z algorithm implementation [24], which introduces unwanted triangular apodization in gain and resolution across the frequency bins. We built both these systems in the laboratory using available optics and electronics. The systems were successfully tested using 1-D and 2-D inputs. The two key limitations to these prototype systems were the inadequate quality of the CCD detector array, and the DFT matrix signal generation electronics used in the experiments. Using dedicated high speed DFT matrix generation hardware along with a state of the art scientific detector array, a high performance spectrum

COMPARISON OF THE TSI MACH-ZEHNDER & MULTIPLICATIVE ARCHITECTURES FOR SPECTRUM ANALYSIS

	Mach-Zehnder Additive	In-line Multiplicative
Mechanical Stability	Relatively Unstable	Better Stability
Light Efficiency	Higher	Low due to Multiple AOD Diffraction
Temporal Coherence of Light Source	High due to Interferometer	Not as Critical; Intensity Modulation
Processing Bandwidth	Good; Limited by AOD Bandwidth	Limited by AOD & Reference Chirp Bandwidth
Signal to Bias ratio	Higher	Limited by Greater Bias Contribution

analyzer can be realized that has a system bandwidth near the $100MHz$ range, and a spectral resolution approaching a $100Hz$. With respect to limitations inherent in the particular TSI optical architecture, such as unwanted bias accumulation in time integrating processors, we have proposed various bias removal techniques, including a real-time approach using a photorefractive crystal as a bias eliminator. Given the current optical transducer and detector technology available for optical computing, these pulsed source acousto-optic TSI 2-D spectrum analyzers combine the features of the mature 1-D acousto-optic spatial light modulator technology and the 2-D CCD detector technology. The space-time raster format to input, process and output long 1-D signals allows the spectrum processing of very large time-bandwidth product signals such as video images, very long 1-D signals, and high time-bandwidth product radar returns. Nevertheless, it is important to point out that unlike their continuous wave counterparts, these extremely low duty factor pulsed wave systems suffer from low optical efficiency related problems.

References:

[1] C. E. Thomas,"Optical Spectrum Analysis of Large Space Bandwidth Signals," *Applied Optics*, Vol.5, 1782, 1986.

[2] G. Lebreton,"Power Spectrum of Rastered Scanned Signals," Optica Acta, Vol. 29(4), 413, 1982.

[3] W. T. Rhodes,"The Falling Raster in Optical Signal Processing," *Proc. SPIE*, Vol. 373, 1981.

[4] J. L. Anderson, H.B. Brown, and B. V. Markevitch,"Wideband Real-Time Fourier Analyzer using Folded Spectrum Techniques,"*Proc SPIE*, Vol 373, 1981.

[5] L. N. Flores and D. L. Hecht, "Acousto-optic Signal Processors," *Proc SPIE*, Vol 128, 118, 1977.

[6] T. M. Turpin, "Spectrum Analysis using Optical Processing," *Proc IEEE*, Vol 69-1, 79, 1982.

[7] P. Kellman,"Time Integrating Optical Signal Processing,"*Ph.D Thesis*, Stanford Univ, Stanford, CA, 1979.

[8] P. Kellman,"Time Integrating Optical Signal Processing,"*Opt. Engg.*, Vol. 19(3), 370, 1980.

[9] D. Psaltis and D. Casasent, "Time and Space Integrating Spectrum Analyzer," *Applied Optics*, Vol. 18, 3203, 1979.

[10] T. R. Bader, "Acoustooptic Spectrum Analysis: a high performance hybrid technique,"*Applied Optics*, Vol. 18,No.10, May 1979.

[11] T. R. Bader,"Coherent hybrid Optical Processors," *Proc. SPIE*, Vol. 232, 1980.

[12] K. Wagner and D. Psaltis, "Time and Space Integrating Acousto-optic Folded Spectrum Processing for SETI,"*Proc SPIE*, Vol. 564-31, 1985.

[13] N. A. Riza and D. Psaltis,"Multiplicative Time and Space Integrating Acousto-optic Architectures for Real-Time Spectrum Processing,"*Proc. SPIE*, Vol. 827-34, 1987.

[14] K. Wagner, "Time and Space Integrating Acousto-optic Signal Processing," Ph.D Thesis, California Institute of Technology, May 1987.

[15] D. Psaltis, "Two Dimensional Optical Processing using One Dimensional Input Devices," *Proc. IEEE*, Vol. 72(7), 292, 1984.

[16] A. V. Oppenheim and R. W. Schafer, *Digital Signal Processing*, Prentice-Hall, 1975.

[17] I. C. Chang and D. L. Hecht, "Characteristics of Acousto-Optic Devices for Signal Processors," *Optical Eng.*, Vol.21, 76, 1982.

[18] M. Abramowitz and L. Stegun, Handbook of Mathematical Functions, NBS, 1970.

[19] D. H. Seib, "Carrier Diffusion Degradation of Modulation Transfer Function in Charge Coupled Imagers," IEEE Trans.,ED-21(3), 210, 1974.

[20] M. Haney and D. Psaltis, "Measurement of the Temporal Coherence properties of pulsed single mode Laser Diodes,"*Applied Optics*, Vol. 24, 1926, 1985.

[21] D. L. Hecht, "Three Dimensional Acousto-Optic Dispersion effects in acousto-optic devices for optical information processing," IEEE Ultrasonics Symp., 463, 1983.

[22] M. W. Haney, "Acousto-optical Time and Space Integrating Processors for real-time Synthetic Aperture Radar Imaging," Ph.D. Thesis, Caltech, 1986.

[23] D. Psaltis, J. Yu and J. Hong, "Bias-free Time Integrating Optical Correlator using a Photorefractive Crystal," *Applied Optics*, Vol. 24, No.22, Nov. 1985.

[24] L. R. Rabiner *et at.*, "The Chirp-Z Algorithm," IEEE Trans. on Audio and Electroacoustics, Vol. AU-17(2), 86, 1969.

CHAPTER 4

OPTICAL DISK BASED ACOUSTO-OPTIC SPECTRUM ANALYSIS

4.1 Introduction

Recently, there has been interest in the application of optical disks in optical computing systems [1–5]. This chapter introduces the application of optical disks in acousto-optic spectrum analyzers. The disk is used as an electronic signal generator, a 1-D optical spatial light modulator, and an optical distributed local oscillator generator. Various disk based optical spectrum analyzer designs are introduced along with an engineering analysis of the capability of currently available optical disk systems. Experimental results relating to a continuous wave optical disk spectrum analyzer are presented. The experiments conducted demonstrate the principle of the optical disk based distributed local oscillator (DLO) and its application to acousto-optic spectrum analysis. The various DLO reference data disk formats are presented and experimentally tested. The optical DLO system is described and the output signals are analyzed. Next, the system for the acousto-optic disk spectrum analyzer is described and the test results are analyzed. Finally, the practical limitations of this disk system are studied and system issues are discussed.

The question arises, "Why use optical disks in acousto-optic spectrum analyzers?". Recall from Chapter 3 that in 2-D time and space integrating acousto-optic folded spectrum analyzers, such as the additive and multiplicative DFT algorithm based processors, and the additive Chirp-Z 2-D folded spectrum processor, the reference signals used in the temporal spectral processing necessary for generating the complete folded spectrums are of extremely high time bandwidth product ($\geq 10^6$ data points) [6–8]. So far it has been very difficult to generate these signals using commercially available electronics, and only incomplete folded spectrums have

been experimentally demonstrated [7,9]. One way of addressing this signal generation problem is by exploring the angular motion and the extremely high data storage potential in optical disk technology. In other words, the high data packing density and storage capacity, along with the angular motion of the optical disk can be combined to generate the extremely high time bandwidth product signals used for temporal frequency processing in acousto-optic spectrum analyzers, thus giving the desired complete folded spectrums.

The following calculation for a practical 2-D acousto-optic spectrum analyzer illustrates the high data generation requirement. Take a typical large aperture, high resolution acousto-optic deflector (AOD) with a time aperture of $40\mu sec$ and a bandwidth of $50MHz$ giving a maximum storage capacity of 2000 analog data samples [10]. This AOD is used as the input signal transducer in the space integrating arm of a 2-D TSI acousto-optic spectrum analyzer, generating a maximum of 2000 resolvable signal coarse frequency space multiplexed channels along one spatial dimension. The maximum number of spatial coarse frequency channels is equal to the space bandwidth product of the acousto-optic device. Along the orthogonal spatial direction in each coarse frequency channel, another AOD is used to form an acousto-optic time integrating spectrum analyzer that can generate 2000 fine frequency space multiplexed bins along the orthogonal direction. This gives a total of 4 million frequency channels in a two dimensional coarse-fine frequency format on a 2-D time integrating CCD. In order to achieve this massive processing power from the AOD's, the reference DFT signal used in the time integrating processor should have 2000 constant frequency segments, each segment having 2000 data samples corresponding to the maximum storage capacity of the AOD. For the AOD bandwidth of $50MHz$, the DFT signal has to be serially read-out at the minimum Nyquist limited rate of $100MHz$, corresponding to twice the maximum signal bandwidth. Assuming an 8-bit (256 level) digital quantization of the 4 million analog

DFT signal samples, we require a 4 megabyte digital memory with an 8 channel bus, and a 100 MHz digital to analog converter. Typically, in practical digital to analog systems, sampling is performed at a rate that is higher than the Nyquist rate. This implies that in order to generate a high quality DFT signal, we would require a 100-400 MHz digital to analog converter chip. Although the 4 megabyte DFT signal memory is not a critical limitation, the unusually high digital to analog conversion rate imposes a severe limitation for present-day signal generation electronics. An elegant solution to this problem is the parallel access of data through optics and spinning disks. Thus, we introduce the application of optical disk technology in acousto-optic spectrum analyzers to cope with the reference signal high data rate and large storage requirements. The next section deals with a brief look at optical disk technology.

4.2 Optical Disk Technology

The impact of optical disk technology has come from three main applications. These applications include the digital audio compact disk (CD), the video disk, and digital data storage disk systems [11]. All three applications have emerged from innovations and consistent developments in three areas, namely, materials for data storage, laser based data writing systems, and optical read-out systems [12–14]. The current data storage capacity of a $5.25in$ double sided magneto-optic disk is 650 Mbytes, and typical bit size corresponds to $1\mu m$, with a $1.5\mu m$ track pitch [15].

Initial development was in the write once read many (WORM) disks. Here the digital bit streams corresponded to depressions (pits) or burnt out holes (dots) along spiral tracks on the disk surface. The data are read by scanning these pits and dots with a focussed laser beam and detecting the interference between the wave fronts of multiple beams diffracted by the pits and dots. Disks can be used in either light reflection or transmission modes, although present systems mainly employ reflection

type devices. Currently, the WORM disk technology is well developed, and both accurate write and read systems exist in the market. Present research efforts are mainly directed at improving the erasable magneto-optic disk technology [16–17]. In this case the data is stored by a thermal process in each pixel of the magneto-optical material, and read-out by either the reflective magneto-optic Kerr effect or the transmissive Faraday effect. So far, disk data have been recorded serially pixel by pixel and also by parallel techniques such as contact printing, and magneto-optic disk systems for data storage have been demonstrated [18].

In addition, film based optical absorption disks have been proposed that can use the standard holographic high resolution films with 10,000 line pairs per mm and a track density of 500 tracks per mm [11]. These film based disks promise applications in coherent optical processing with multilevel signal storage capability. First, let's look at how existing optical disk systems can be employed as opto-electronic signal generators.

4.3 Optical Disks as Discrete Fourier Transform Signal Generators

The extremely high data storage density of optical disks along with their angular motion allows the optical disk to be used as a programmable high time bandwidth product electronic signal generator. For the DFT signal case with 4 million data samples, the signal data values can be generated by a computer and then stored along the spiral tracks of an optical disk. The writing process is similar to the one used in recording audio, video, and digital data bit streams, and a standard disk writing system can be employed. The read-out process is also the standard serial pixel by pixel laser scanning approach, and many such drives exist today. The coherent electronic DFT signal generated by the disk reading system can be fed to the orthogonal AOD in the time integrating spectrum analyzer to perform the coherent optical processing that results in the complete 2-D folded spectrum output

(See Fig. 4.3.1). The actual analog data values of the DFT signal can be stored as a digital pulse width modulation encoded signal with appropriate error correction schemes. Current write sytems have demonstrated high quality signal reproduction using various data recording and correction techniques.

Recall from the ideal processor designs in Chapter 3 that the typical DFT signal should have 2100 time segments, each of $70\mu sec$ duration, giving an overall signal time of 147 msec with around 4 million analog data samples. Using a standard video disk with a 15 cm radius and constant angular rotation of 1800 rpm (NTSC TV standard), these data can be written as $1\mu m$ pits in approximately 4.4 revolutions along the outer tracks (radius $\approx 15cm$) of the disk. Note that read systems have been developed that provide stable disk rotation of 1800 rpm, using sophisticated servo systems. If data samples using N-bit quantization are used, the data read-out rate and storage area increases by N times. Nevertheless, the disk has more than adequate storage capacity for these DFT signals and a much smaller size disk could be employed, allowing even higher angular velocity as inertial effects are reduced. An added feature of this optical disk based signal generator is that the frequency resolution of the spectrum analyzer can be controlled by the rotation speed of the disk, thus allowing high speed frequency resolution control.

In short, currently existing optical disk systems can be incorporated to provide high time bandwidth product signal generation systems for driving high space bandwidth product AOD's used in 2-D acousto-optic signal processors. Some advantages of this disk opto-electronic signal generation approach include programmablity, potential for storing extremely large time bandwidth signals, applicability to coherent optical processing, and compactness. The next section deals with the application of parallel read-out optical disks in time and space integrating optical spectrum analysis.

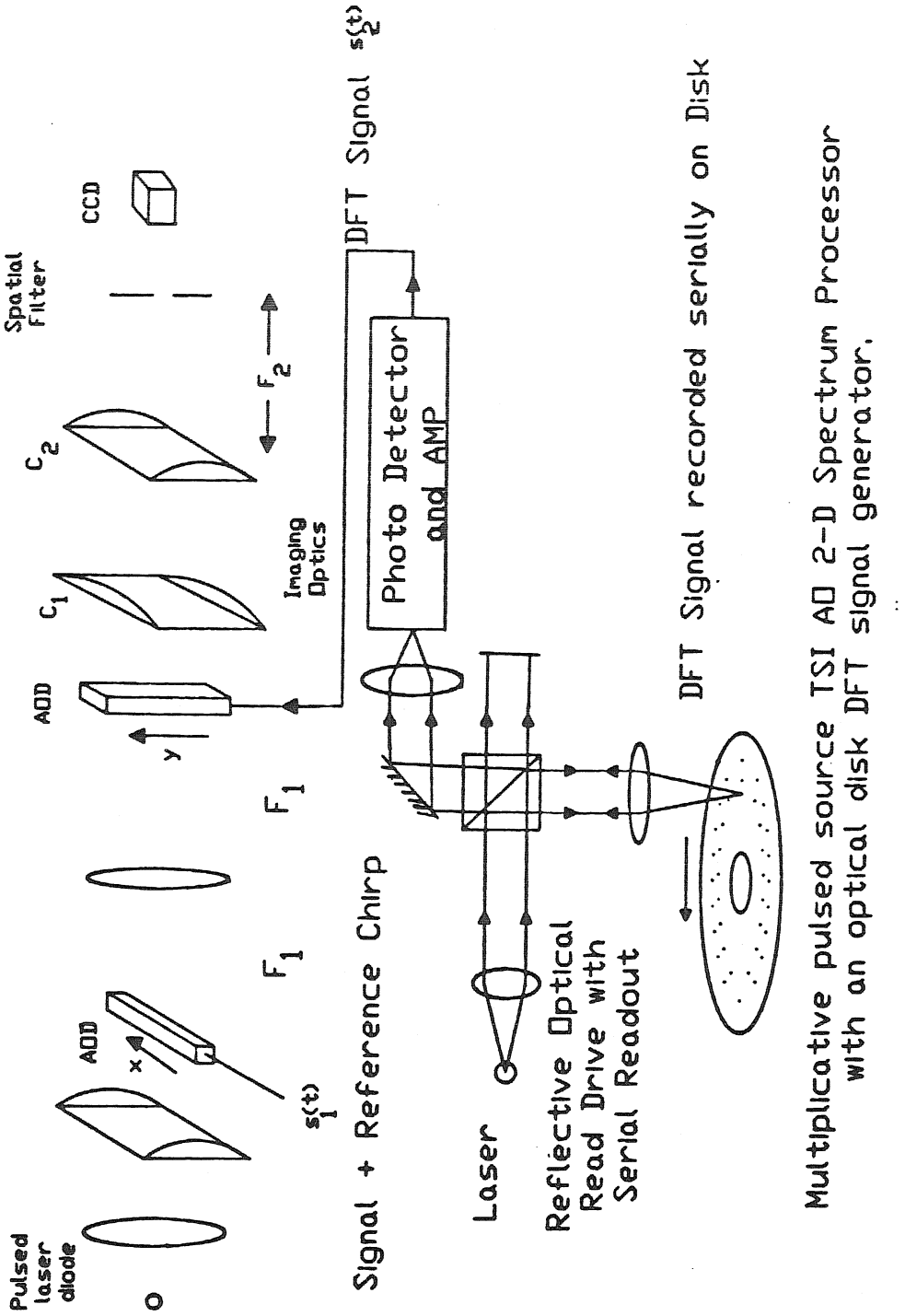

Fig. 4.3.1 The application of the opto-electronic disk signal generator to DFT based 2-D acousto-optic spectrum analysis.

4.4 Pulsed Mode TSI DFT based Disk Spectrum Processor

In this section, the optical disk is introduced as a 1-D time dependent spatial light modulator. The reference signals required for optical processing in acousto-optic spectrum analyzers are stored on the 2-D surface of the disk and read-out optically, using the disk's angular motion. The angular motion allows the selective sampling of the disk data, creating the effect of a pulsed light source. Thus, the two dimensional nature of the data storage area combined with the rotation ability of the disk (CAV: constant angular velocity; CLV: constant linear velocity modes) allows the disk to act as a 1-D spatial light modulator with the temporal modulation controlled by the disk rotation speed. Depending on the type of optical disk we are using, that is, transmissive, reflective, absorptive, or having magneto-optic, film, or pit(spot) based storage, the disk can act as an incoherent or coherent spatial light modulator.

For DFT signal generation, the DFT signal is stored in the format shown in Fig. 4.4.1 where the disk has been divided into N sectors. The number N depends on the disk rotation speed, the desired light source pulse repetition frequency, and the total number of DFT columns in the DFT matrix. The DFT signal columns are stored along radial lines bounding the sectors. Light is focussed as a narrow slit along the radial direction of the disk running from near the disk center to the disk boundary. When the disk spins at a constant angular velocity, each DFT data segment positioned on the different radial lines passes by the focussed light slit, thus impressing the segment disk data on to the light. The net result is that the light slit behaves as a distributed local oscillator (DLO), where the outward radial direction corresponds to optical oscillators with increasing frequency .i.e. DC to half the Nyquist sampling frequency.

Fig. 4.4.2 shows a multiplicative 2-D acousto-optic folded spectrum processor

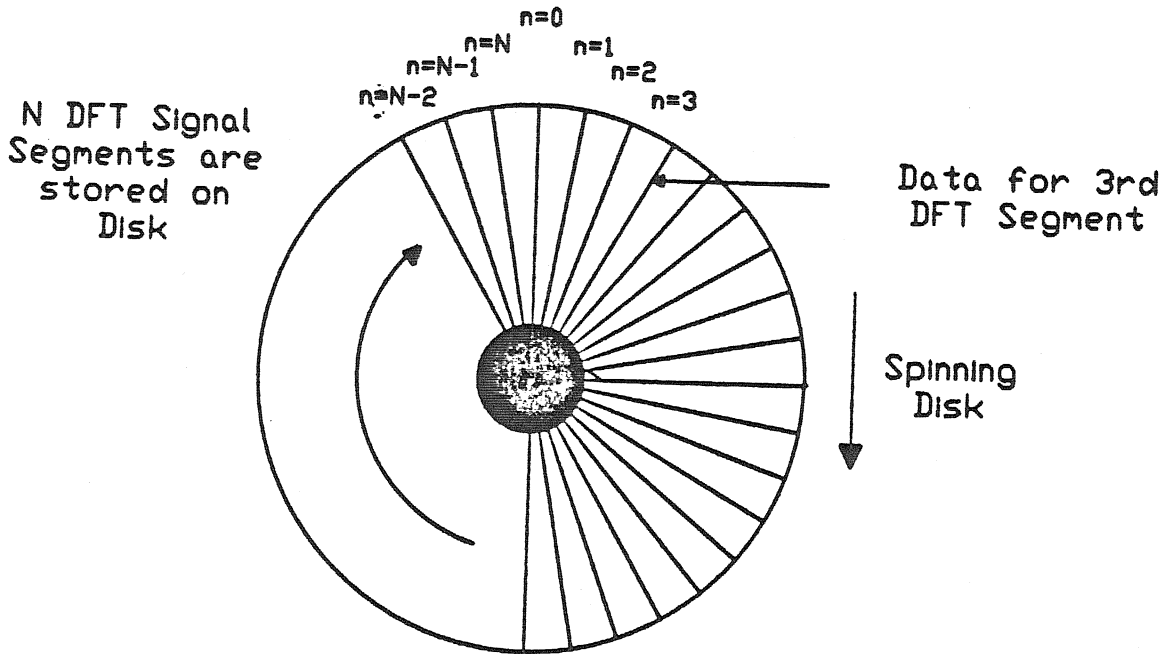

Fig. 4.4.1 DFT signal data storage format on an optical disk.

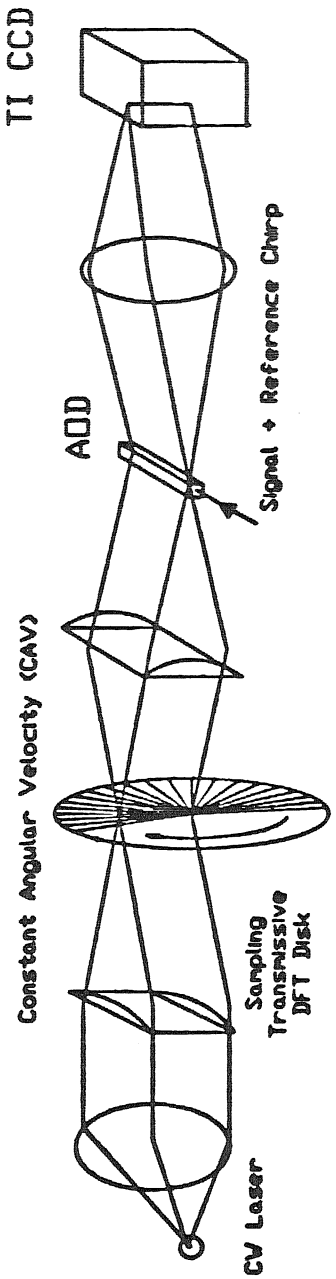

Fig. 4.4.2 A multiplicative 2-D acousto-optic folded spectrum processor that uses a transmissive DFT reference disk for fine frequency temporal processing.

that uses a transmissive DFT reference disk for fine frequency temporal processing. Depending on the disk material and surface roughness, it can be employed for incoherent (intensity) or coherent (amplitude and phase) optical processing along the 1-D slit direction. The light from a CW light source is collimated by a spherical lens, and focussed as a slit of light along the radial direction of the optical disk. The disk spins, and the slit of light samples the different DFT matrix columns positioned radially around the disk. After appropriate spatial filtering, the DFT signal modulated slit of light is incident on an AOD, that is fed by an input signal and a reference chirp. The diffracted light from the AOD is Fourier transformed by a spherical lens, and the desired folded spectrum is detected by a 2-D CCD. Note that this processor is very similar to the multiplicative TSI processor introduced in Chapter 3. The difference lies in the fact that the DFT reference AOD in the earlier processor has been replaced by the sampling optical disk spatial light modulator.

Next, we will describe how the disk can be used to generate a continuous wave distributed local oscillator that can be used for CW light time integrating spectrum analysis. An experimental system is set up in the laboratory, and results are described in the next section.

4.5 Disk based Continuous Wave Time Integrating Spectrum Analyzer

The circular nature of the disk along with its constant angular motion can be used to generate a continuous time distributed local oscillator. The fundamental relation of rotating rigid bodies,

$$v = r\omega_0,$$

is used where v is the linear velocity of a point at a radial distance r from the center of the disk, and ω_0 is the angular velocity. Note that for a constant angular velocity, the linear velocity of a point on the rotating disk increases linearly with radial distance from the center of rotation. Fig. 4.5.1 shows the format for recording

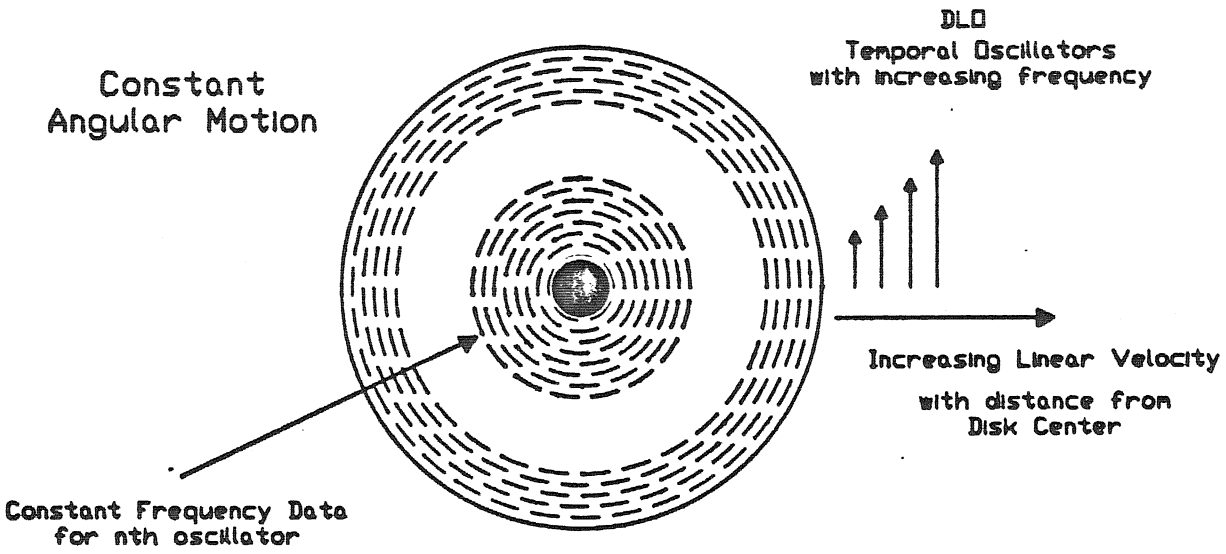

Fig. 4.5.1 Spinning disk DLO data format on optical disk.

reference data on the disk. These data points are recorded on concentric circular tracks, where the size of the data point is kept constant on each track. This implies that the outermost track will have many more data points than the inner tracks, as the outer tracks have a longer recording length. Each track records a periodic data bit stream giving a desired spatial carrier. When the disk rotates at a constant angular velocity, the temporal frequency of data variation increases linearly along any outward radial direction on the disk. In other words, along any fixed radial line, we have created a temporal linear distributed local oscillator (DLO), with the maximum temporal frequency variation corresponding to the outermost track on the disk. In the next section, we will see how this disk DLO can be implemented in the laboratory.

4.5.1 The Distributed Local Oscillator Experiment

In order to study the spectral components of a signal, it is necessary to correlate the signal with a band of reference sinusoids. If the signal bandwidth is contained within the reference signal bandwidth, we can isolate those matched frequency components. Fig. 4.5.1.1 shows the optical system architecture which generates the reference signal called the distributed local oscillator, that is used for signal spectrum analysis. As shown in Fig. 4.5.1.1, the light from an He-Ne laser is collimated by an $F_1 = 20$ cm focal length spherical lens. This collimated light is incident on a beam splitter that reflects part of the light by 90 degrees, directing it through an $F_2 = 10$ cm focal length cylindrical lens. This F_2 focal length cylindrical lens converts the collimated light into a slit along the radial direction of a reflective optical disk. The disk is mounted on a mechanical rotating stage that is driven by a DC motor. The light reflected from the disk travels up through the cylinder and beam splitter to strike a mirror that aligns the beam along its original He-Ne laser path that runs parallel to the optical table. An $F_3 = 8.5$ cm focal length cylindri-

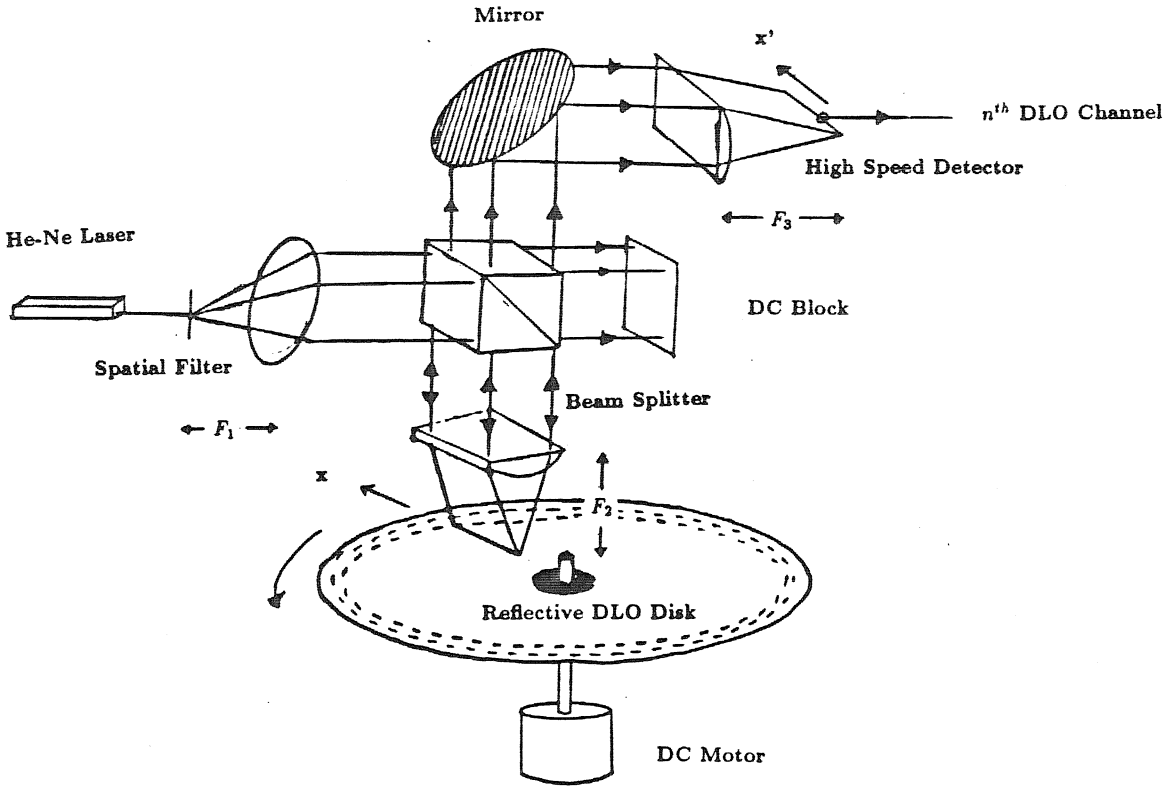

DISK DISTRIBUTED LOCAL OSCILLATOR

Fig. 4.5.1.1 Disk distributed local oscillator architecture.

cal lens in combination with the $F_2 = 10$ cm cylindrical lens is used to image this reflected slit of light on to an output 1-D light sensor. By recording the reference signal sinusoids as spatial sinusoids in concentric and spatially separated channels on an optical disk, a distributed local oscillator is generated along the radial slit of light incident on the rotating disk. As the optical disk has a very high data storage density, we can store a very large number of reference signal channels allowing a large instantaneous processing bandwidth. The disk distributed local oscillator laboratory system is shown in Fig. 4.5.1.2.

The reference signal temporal frequency in a disk channel can be controlled by different design parameters such as disk angular velocity ω_d, radial distance x_n of the n^{th} channel from the disk rotation center, and spatial period l_n of the n^{th} channel.

The temporal frequency of the n^{th} DLO channel is given by:

$$f_n = \frac{x_n \omega_d}{l_n}, \tag{4.5.1.1}$$

where

$$l_n = x_n \theta_n. \tag{4.5.1.2}$$

Here θ_n is the sector angle subtended by a spatial period of the n^{th} DLO channel at the center of the disk. The light intensity incident at the detector plane at the position of the n^{th} DLO channel is given by:

$$I(x'_n, t) = I_1[1 + m_n \cos(2\pi f_n t)], \tag{4.5.1.3}$$

where m_n is the signal modulation depth of the n^{th} DLO channel, and $x'_n = Mx_n$ is the output plane coordinate. M is the magnification of the cylindrical lens imaging system.

For the case that the spatial period l_n is chosen to be a fixed value over all channels, that is, $l_n = l$, the distributed local oscillator frequency varies linearly

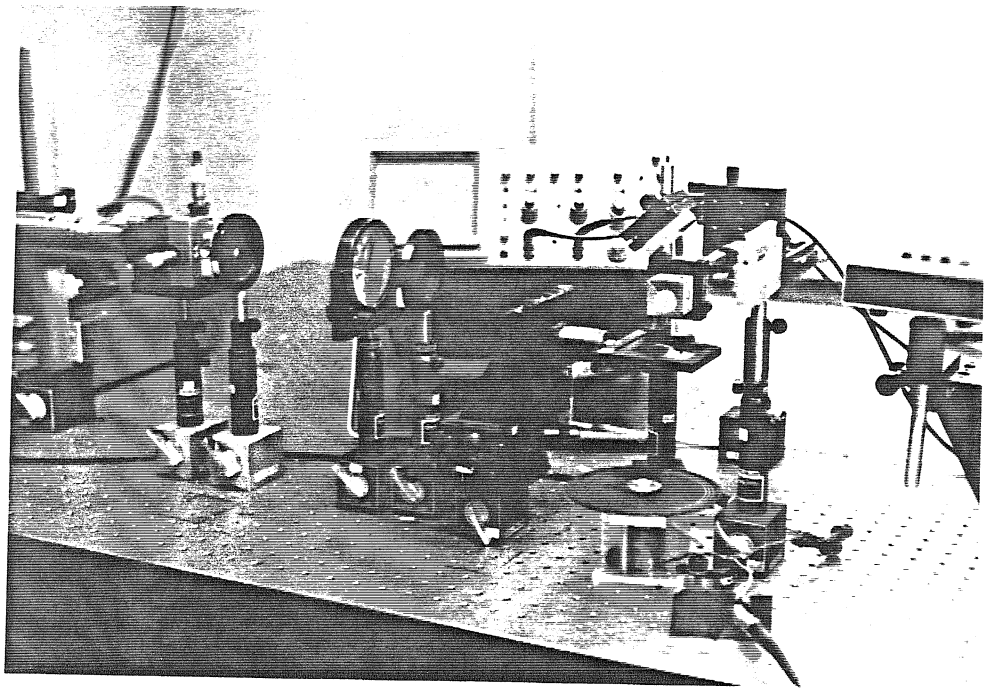

Fig. 4.5.1.2 The disk distributed local oscillator laboratory system.

with radial distance for a fixed disk rotation speed. This format is applied in the DLO experiment using 5 channels with $l = 0.52mm$, x_n ranging from 4.6 mm to 5.8 mm, with a channel spacing of 3 mm. This data format is generated by a computer as black and white on-off regions, and written by a laser printer on to a transparency that is carefully mounted on to the disk surface. The 5 channels, each 1 mm thick are shown in Fig. 4.5.1.3. These design values are chosen based on the computer printing capabilities and the degree of motor mechanical stability, in order to demonstrate the basic concepts of optical disk based spectrum analysis. Fig. 4.5.1.4 shows two of the five reference DLO channel signals detected by a high speed detector positioned along the output slit of light at the appropriate DLO channel position respectively. Fig. 4.5.1.5 shows the expected linear frequency relationship with radial channel distance for the five experimental DLO channels and compares them to their analytical values, respectively. Note that the experimental data match well with the theoretical calculations. Also, since the recorded disk data correspond to binary on-off square waves, we are using the square wave fundamental harmonic frequency in the analysis and experiments. The motor speed used in this experiment corresponded to 3061 rpm, which gives a 19.6 msec disk revolution time. The optical disk being used as a reflective surface is a SONY 12 cm diameter disk shown in Fig. 4.5.1.6, while the DC motor is an inexpensive off the shelf component.

Fig. 4.5.1.7 shows the non-linear behavior of the DLO frequency with radial distance when the spatial period is not constant over all the DLO channels. This approach can be exploited if we know a priori that the input signal spectral components show a certain non-linear distribution.

Another approach to recording the reference signals is to use the spatial period sector angle θ_n for the respective n^{th} DLO channel. In other words,

$$f_n = \frac{\omega_d}{\theta_n}. \tag{4.5.1.4}$$

Spatial Period = 0.52 mm for all 5 channels

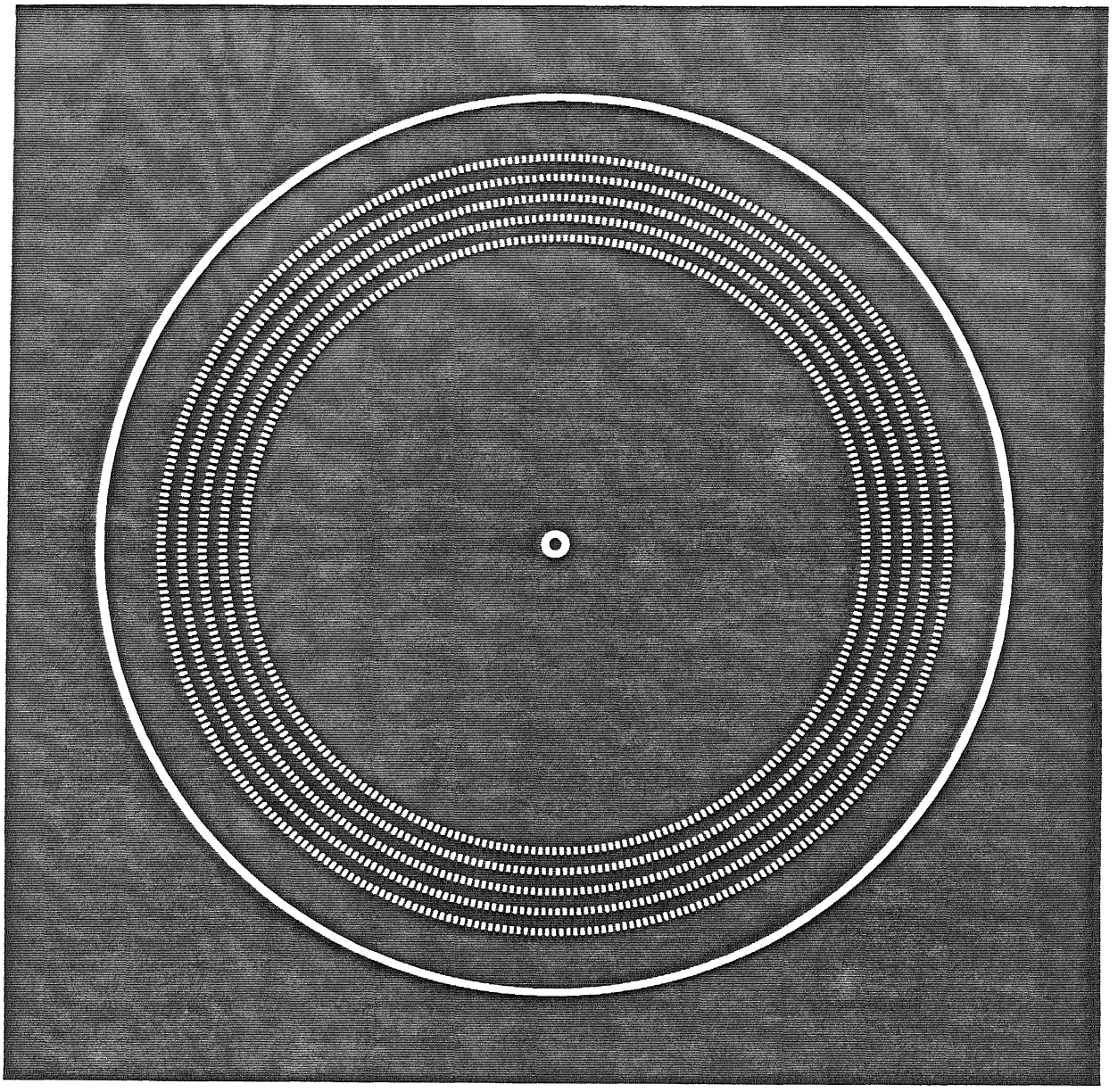

Fig. 4.5.1.3 Disk pattern for 5 DLO channels using constant spatial period format.

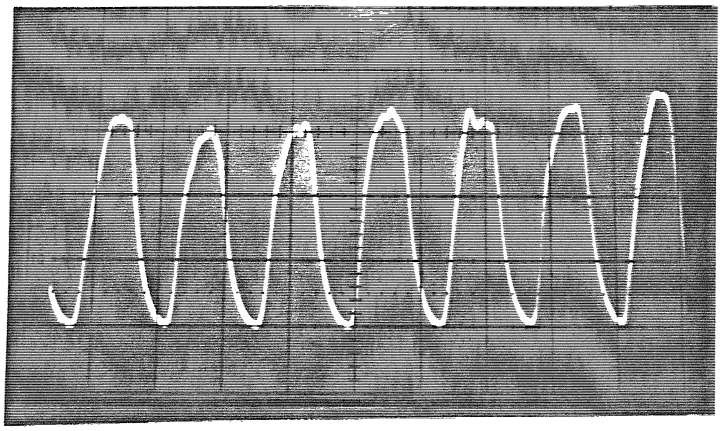

at x =4.6 cm

DLO CHANNEL 1:

DLO Frequency = 14.28 KHz

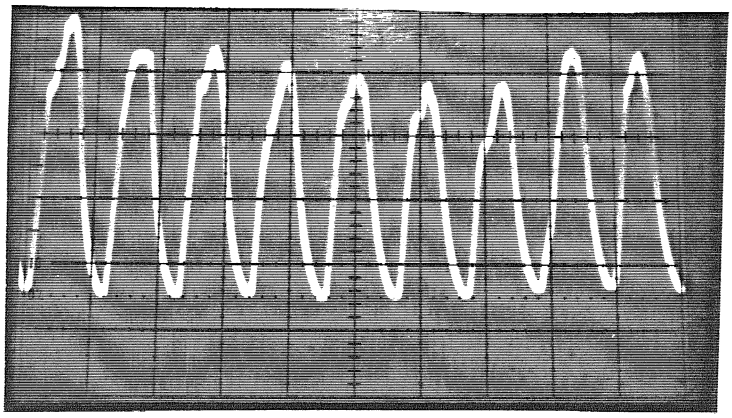

at x =5.8 cm

DLO CHANNEL 5:

DLO Frequency = 18.2 KHz

Time Scale: 50μsec/div

Fig. 4.5.1.4 Detected DLO channels from the laboratory system showing signals from channel 1 and 5 respectively.

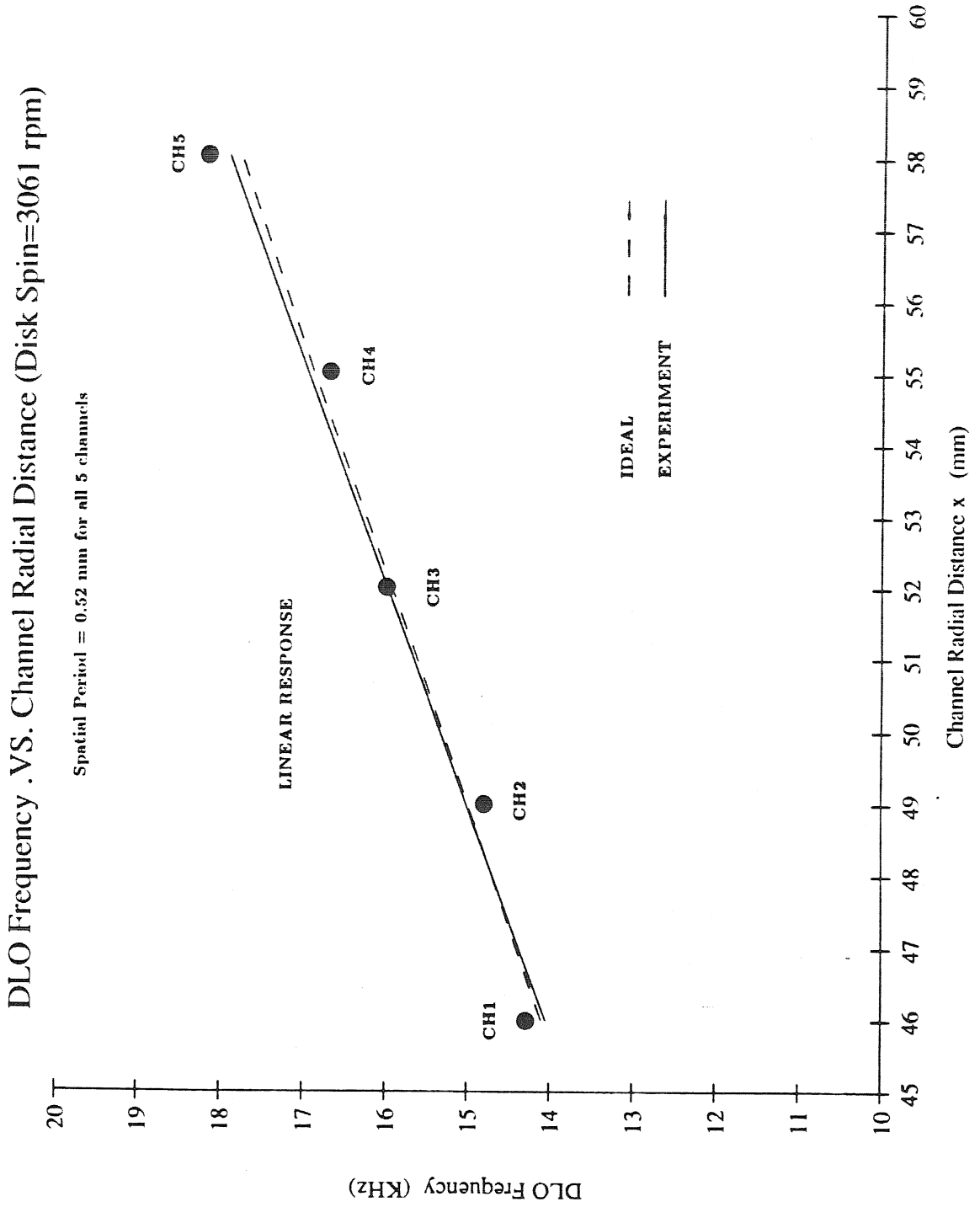

Fig. 4.5.1.5 Plot of the measured DLO frequency versus channel radial distance for the experimental system.

Fig. 4.5.1.6 12 cm diameter WORM reflective SONY disk with computer generated DLO pattern mounted on the disk surface.

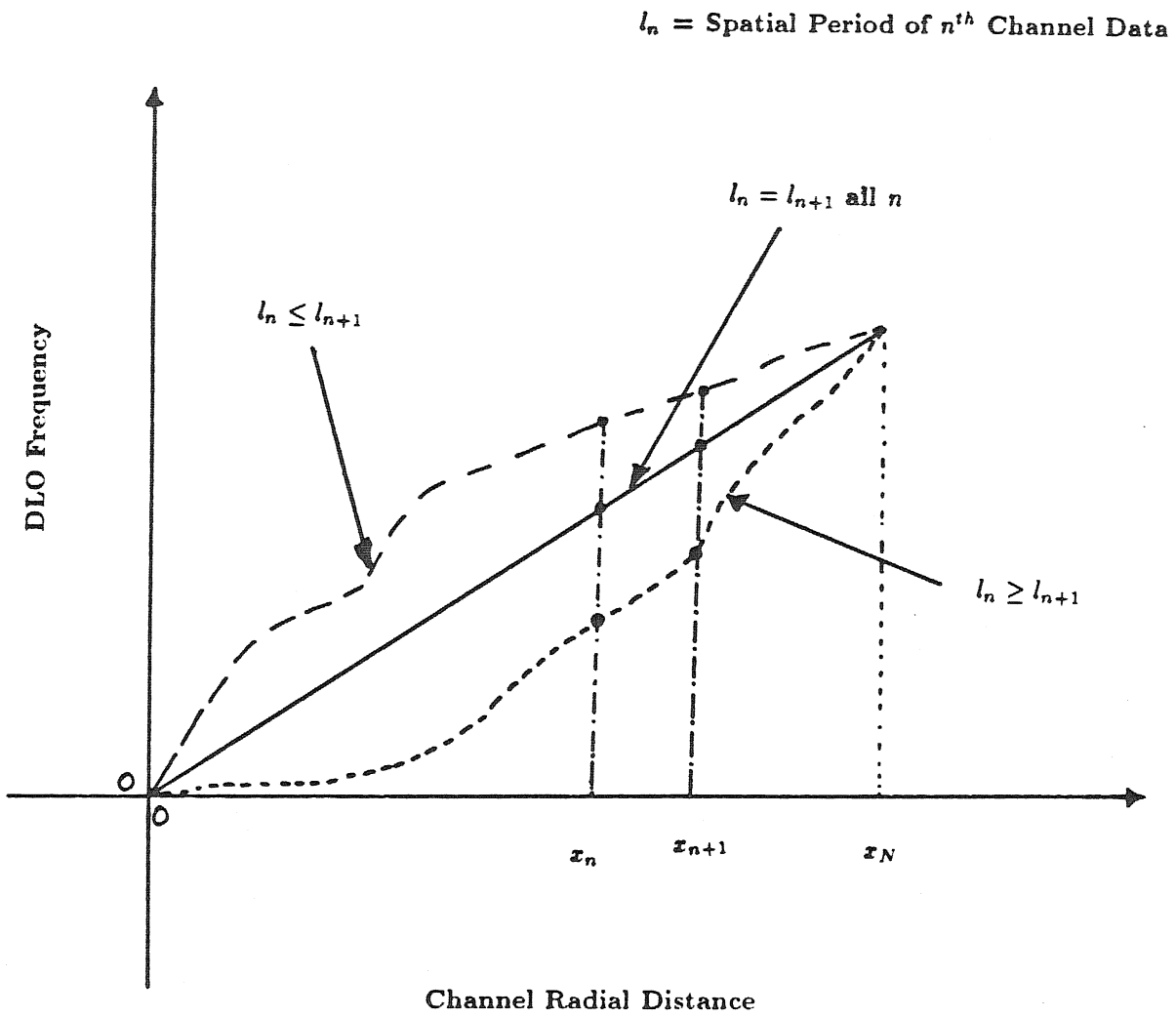

Fig. 4.5.1.7 General DLO frequency behavior with different channel spatial period formats.

Fig. 4.5.1.8 shows 3 DLO channels recorded using this technique with θ_n equal to 3, 2, and 1 degree corresponding to channels 1,2 and 3, respectively. Note that this approach does not depend on the radial distance x_n. The output reference signals from the DLO system are shown in Fig. 4.5.1.9 and agree very well with the analytical frequency values. The disk used a 20 msec revolution time, giving analytical DLO frequencies of 6, 9, and 18 KHz, respectively. The experimental system gave 6.06, 9.09, and 18.18 KHz frequencies for channels 1,2, and 3, respectively. This reference generation approach provides a larger DLO bandwidth compared to the constant spatial period DLO format.

Note that if we record an integer number of spatial cycles in each DLO channel, the DLO signal is phase coherent over disk revolutions, allowing long spectrum processing windows that provide excellent frequency resolution. For example, there are 360 complete spatial cycles in channel 3 shown in Fig. 4.5.1.8.

4.5.2 The Optical Disk Spectrum Analyzer Experiment

The DLO system described earlier can be modified to make an optical spectrum analyzer. This is accomplished by intensity modulating the light by an input test signal. For instance, a light source such as an LED or semiconductor laser diode can be directly modulated by the test signal. On the other hand, the light can be indirectly modulated by an acousto-optic point modulator as shown in the architecture in Fig. 4.5.2.1. Electro-optic intensity modulators could also be employed in such systems.

Fig. 4.5.2.2 shows the acousto-optic disk spectrum analyzer setup in the laboratory. The raw beam from the Argon ion laser is incident on a Bragg matched acousto-optic device that is driven with a carrier frequency of 60 MHz. The test signal is mixed with the carrier in an RF mixer to produce the AM signal that intensity modulates the light. Depending on the DC offset of the signal, the frequency

$\theta_1 = 3°$ **Innermost Channel**

$\theta_2 = 2°$ **Middle Channel**

$\theta_3 = 1°$ **Outermost Channel**

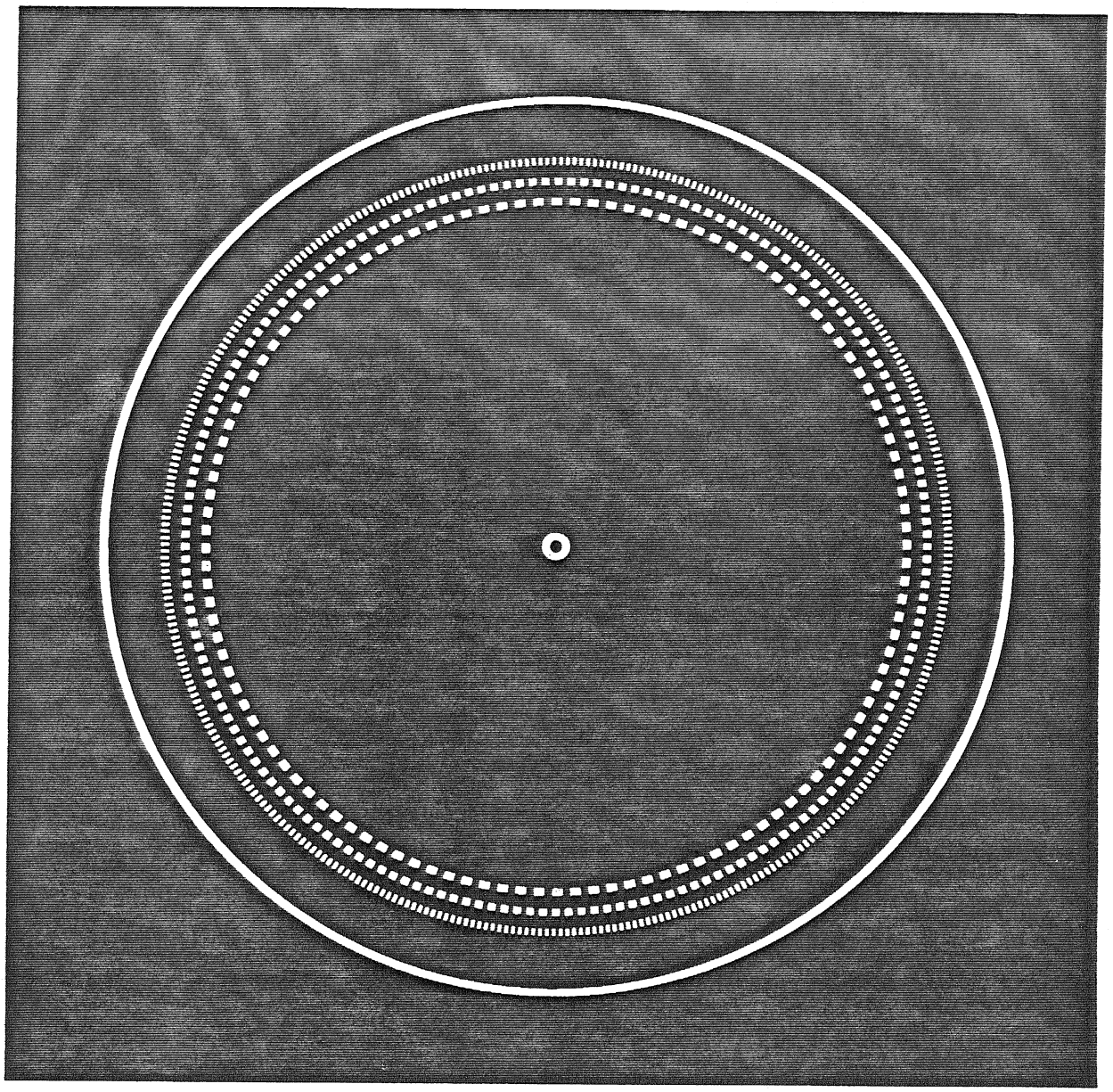

Fig. 4.5.1.8 Disk pattern for 3 DLO channels using the angular division format.

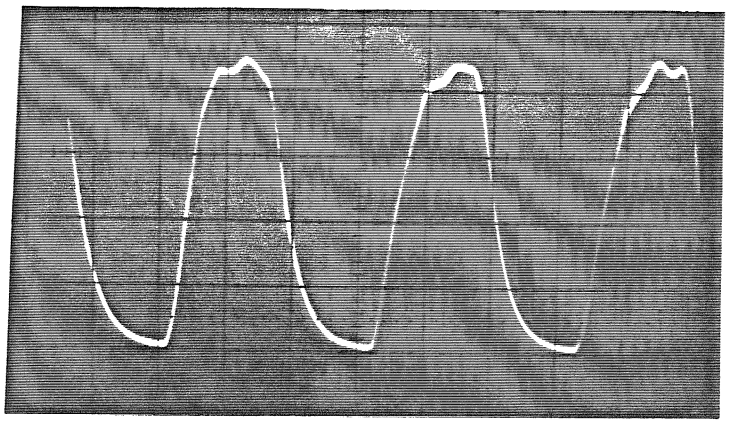

DLO CHANNEL 1:

DLO Frequency = 6.06 KHz at $\theta_1 = 3°$

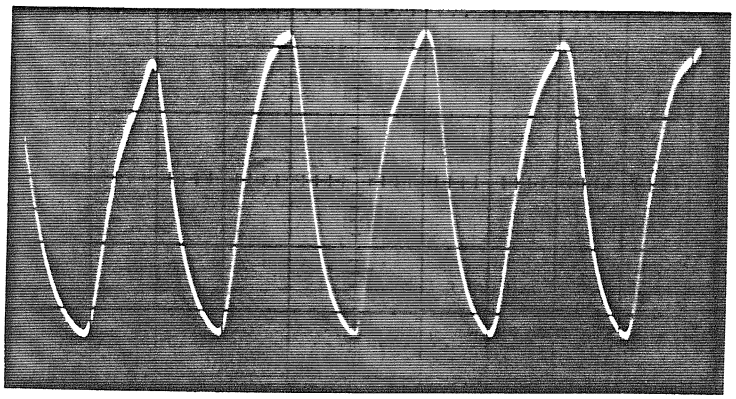

DLO CHANNEL 2:

DLO Frequency = 9.09 KHz at $\theta_2 = 2°$

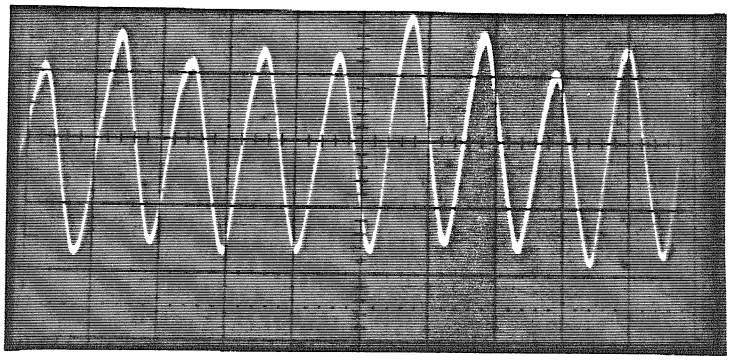

DLO CHANNEL 3:

DLO Frequency = 18.18 KHz at $\theta_3 = 1°$

Fig. 4.5.1.9 Detected DLO channels from the laboratory system showing signals from channel 1,2, and 3 respectively. The angular format in Fig. 4.5.1.8 was used for these channels. **Time Scale: 50μsecdiv**

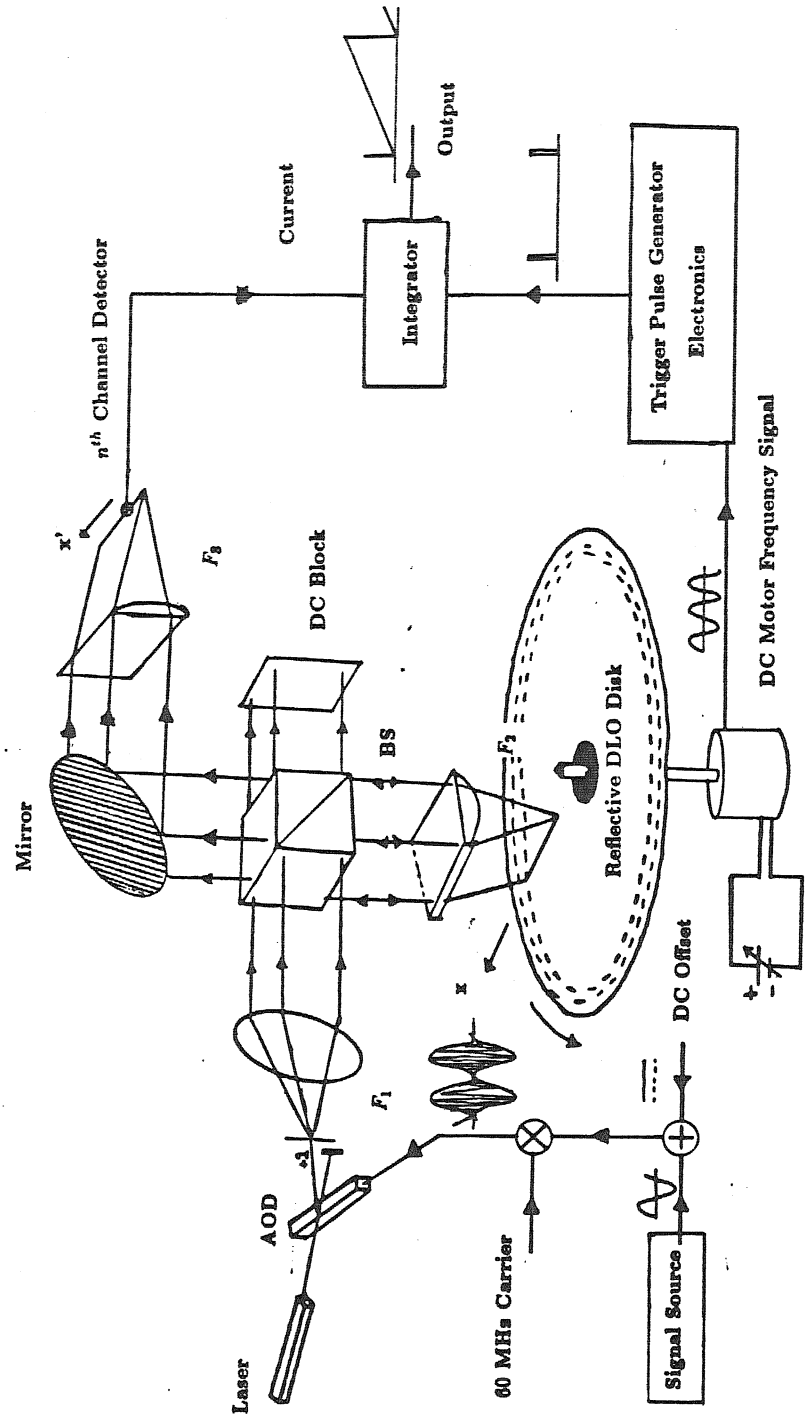

Fig. 4.5.2.1 Acousto-optic disk spectrum analyzer architecture.

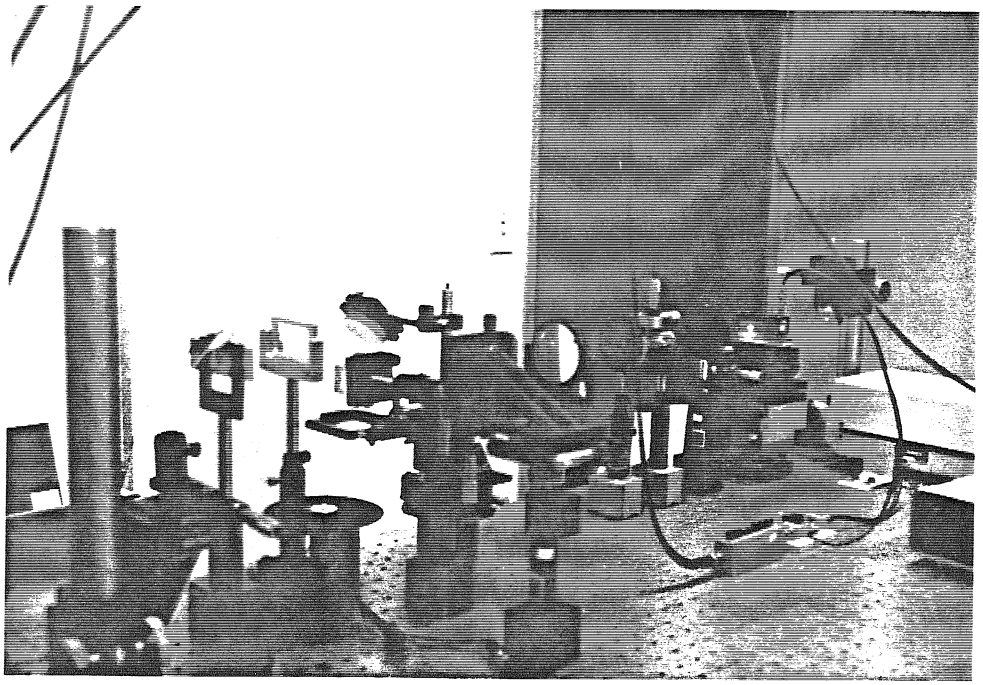

Fig. 4.5.2.2 Acousto-optic disk spectrum analyzer laboratory system.

and modulation depth of the light signal can be controlled. Fig. 4.5.2.3 shows the input AM signals in the lower trace and the detected light modulation in the upper trace. Note that when the DC offset is zero, the light modulation frequency is half the AM modulation frequency. This is because the negative variations are detected as positive variations in intensity on the detector. With a DC offset V_m of half the peak to peak voltage of the modulating signal, almost 100% modulation depth of the light signal is detected with no change in modulating frequency. The disk was stationary while performing this test, with the reflective surface of the disk exposed to the light.

Fig. 4.5.2.4 shows the output signals from two detectors positioned along two different DLO channels imaged from the disk. Note that there is an amplitude modulation associated with each DLO channel, causing the signal to diminish over a certain disk spin region. This amplitude modulation is periodic with each disk revolution; in this case one revolution time is 19.6 msec. This problem occurs because the center of motion of the rotating stage and the center point of the concentric channels on the disk are not the same. Any slight misalignment of the centers causes the channel to drift in the radial (track) direction, causing varying interactions between the channel spatial modulation and the incident light. The next section on system issues suggests various ways to reduce this problem. In our experiment, in order to reduce the effect of this modulation over successive disk spins, temporal processing is done over separate single disk revolution times. This is done by externally triggering the time integrating detectors. The detectors used in the experiment are photo-transistors. The current from the photo-transistor is fed to an integrator circuit that collects charge in a capacitor for a desired duration. The DC motor provides a sinusoidal output signal whose frequency is 8 times the rotation frequency. This signal is fed to a digital divide by 8 circuit to provide a trigger signal for the charge integrator. The output voltage of the integrator

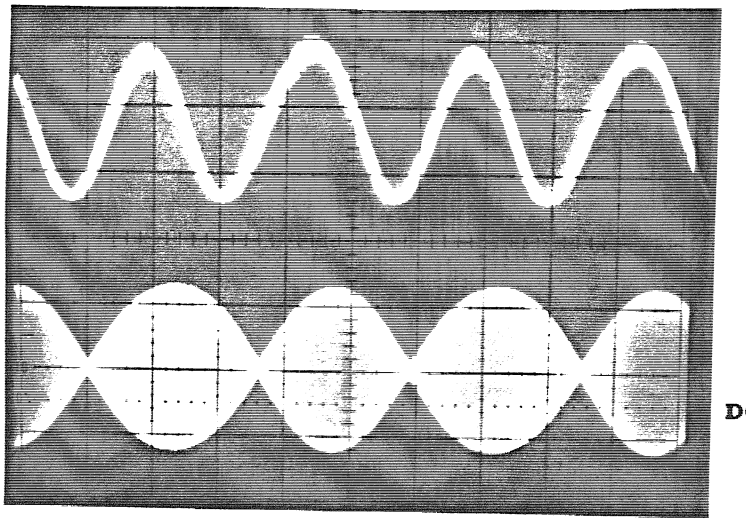

Light Output 20 KHz Signal

INPUT AM SIGNAL

DC=0 and 10 KHz Modulation

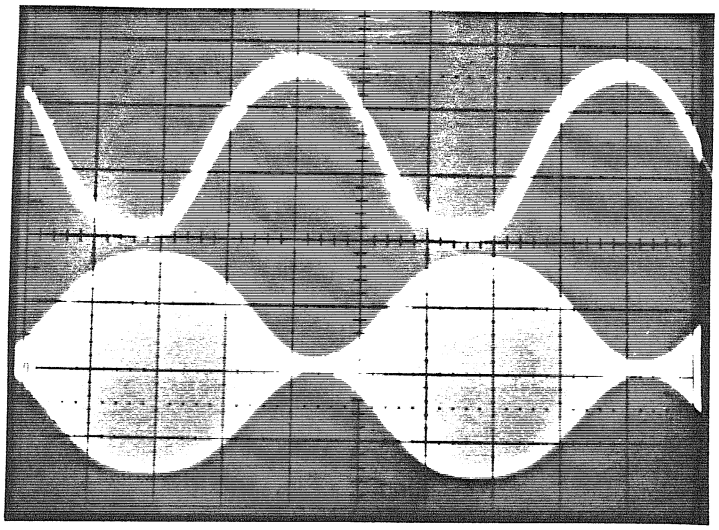

Light Output 10 KHz Signal

INPUT AM SIGNAL

DC=V_m and 10 KHz Modulation

Fig. 4.5.2.3 Each photograph shows the AOD input AM signal in the lower trace, while the upper oscilloscope trace gives the optically detected modulation signal from the experimental spectrum analyzer system.

Time Scale = 50 μsecdiv

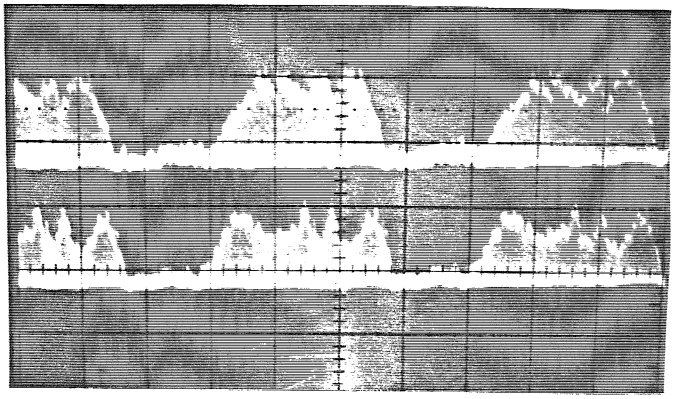

Fig. 4.5.2.4 Amplitude modulation on DLO channels 1 and 2 outputs over disk revolutions. One disk revolution is $\approx$ 4 time divisions.

DLO CHANNEL 2 OUTPUT SIGNAL

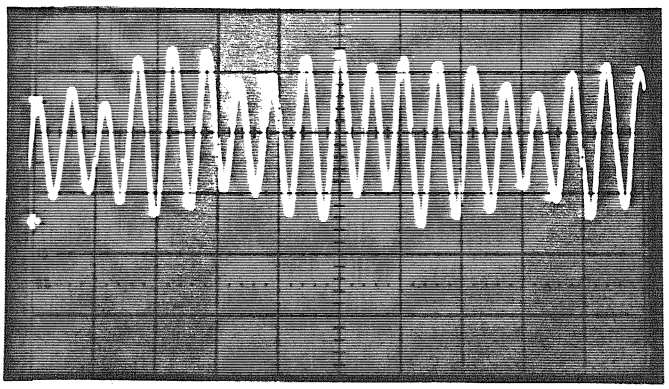

DLO Frequency = 8.93 KHz with $\theta_2 = 2°$

Time Scale = 200 μsecdiv

Fig. 4.5.2.5 Detector output of the 8.93 KHz DLO channel using a 19.6 msec disk revolution time.

is monitored on the scope. Fig. 4.5.2.5 is the detector output of a 8.93 KHz DLO channel using a 19.6 msec revolution time. Note that this DLO signal shows a slight amplitude modulation. This is caused by the slight fluctuations of the grey levels generated by the computer laser printer output that generates the transparency pattern covering the disk reflective surface.

For analysis purposes, a single DLO channel is considered with reference to the architecture in Fig. 4.5.2.1. The current generated by the phototransistor positioned at the n^{th} DLO channel image line position $x'_n = Mx_n$ is given by:

$$i(x'_n, t) = KI_s(t)I(x'_n, t), \tag{4.5.2.1}$$

where the constant K considers experimental factors such as loss of light that is due to track carrier diffraction effects, detector quantum efficiency, and amplifier gain. $I_s(t)$ is the signal intensity modulation given by:

$$I_s(t) = I_0[1 + m\, s(t)], \tag{4.5.2.2}$$

with amplitude I_0 and modulation depth m. $I(x'_n, t)$ is the n^{th} DLO channel intensity modulation given by:

$$I(x'_n, t) = I_1[1 + m_n \cos(2\pi f_n t)], \tag{4.5.2.3}$$

where I_1 is the amplitude term, and m_n is the modulation depth of the n^{th} DLO channel. The DLO frequency was defined earlier as:

$$f_n = \frac{\omega_d}{\theta_n}. \tag{4.5.2.4}$$

The voltage at the output of the integrator at time t is:

$$\begin{aligned} v(x'_n, t) &= \frac{K}{C}\int_0^t i(x'_n, t')dt' \\ &= \frac{K}{C}\int_0^t I_0[1 + m\, s(t)]I_1[1 + m_n \cos(2\pi f_n t)]dt' \\ &= K_1\int_0^t [1 + m\, s(t)][1 + m_n \cos(2\pi f_n t)]dt', \end{aligned} \tag{4.5.2.5}$$

where

$$K_1 = \frac{KI_0I_1}{C}, \tag{4.5.2.6}$$

and C is the capacitance in Farads of the capacitor used in the integrator circuit. Solving the integral and assuming the initial condition that $v(x'_n, 0) = 0$, and that the detector integration time T is much larger than the inverse of any DLO frequency, that is:

$$f_n T \gg 1, \tag{4.5.2.7}$$

we get the output voltage signal to be approximately given by:

$$v(x'_n, t) \approx K_1 t + K_1 m m_n \int_0^t s(t') \cos(2\pi f_n t') dt'. \tag{4.5.2.8}$$

The first term of this expression gives the linear charging of the capacitor with respect to time. The second term gives the temporal Fourier transform of the input signal $s(t)$ with respect to the DLO frequency f_n. For a single tone input $s(t)$ given by:

$$s(t) = \cos(2\pi f_0 t), \tag{4.5.2.9}$$

the signal output can be given by:

$$\begin{aligned} v(x'_n, t) &= K_1 t + m' K_1 \int_0^t \cos(2\pi f_0 t') \cos(2\pi f_n t') dt' \\ &= K_1 t + \frac{m' K_1}{2} \int_0^t \Big[\cos[2\pi (f_0 + f_n) t'] + \cos[2\pi (f_0 - f_n) t'] \Big] dt', \end{aligned} \tag{4.5.2.10}$$

where $m' = m m_n$. Again, because we have:

$$(f_0 + f_n) T \gg 1, \tag{4.5.2.11}$$

the first integral averages out to zero, and we get:

$$v(x'_n, t) \approx K_1 t + \frac{m' K_1}{2} \int_0^t \cos[2\pi (f_0 - f_n) t'] dt'. \tag{4.5.2.12}$$

The voltage after a time T is given by:

$$v(x'_n, T) = K_1 T[1 + \frac{m}{2}\text{sinc}(\eta)], \tag{4.5.2.13}$$

where

$$\eta = 2\pi(f_o - f_n)T. \tag{4.5.2.14}$$

When the input frequency matches the n^{th} channel frequency, that is,

$$f_0 = f_n, \tag{4.5.2.15}$$

the voltage at the output of the n^{th} channel DLO detector is maximized, and is given by:

$$v(x'_n, T) = K_1 T[1 + \frac{m'}{2}]. \tag{4.5.2.16a}$$

For $m' = 1$, that is a 100% signal and reference DLO modulation depth, we get:

$$v(x'_n, T) = \frac{3K_1 T}{2}. \tag{4.5.2.16b}$$

In effect, when the signal spectral components overlap certain DLO channel frequencies, those channels build up charge to indicate frequency match. When $f_0 \neq f_n$, and

$$\left|(f_0 - f_n)\right| \geq \frac{1}{T}, \tag{4.5.2.17}$$

the voltage at the n^{th} channel is approximately given by:

$$v(x'_n, T) \approx K_1 T. \tag{4.5.2.18}$$

This matched filtering operation is tested using the optical disk system shown in Fig. 4.5.2.2, using T = 19.6 msec, f_n = 8.93 KHz, and m' = 0.714. When the input signal frequency generator dial is brought near the DLO frequency of 8.93 KHz, the output of the time integrating detector increases greatly. This AM input signal is shown in Fig. 4.5.2.6, while Fig. 4.5.2.7 shows the voltage of the time

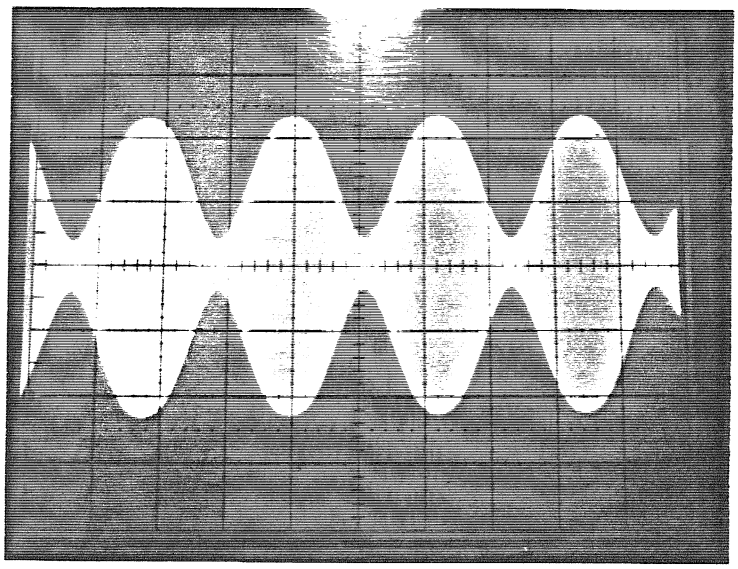

Fig. 4.5.2.6 Test signal input to AOD with frequency $f_0 = 8.88KHz$ and modulation depth $m = 0.714$.

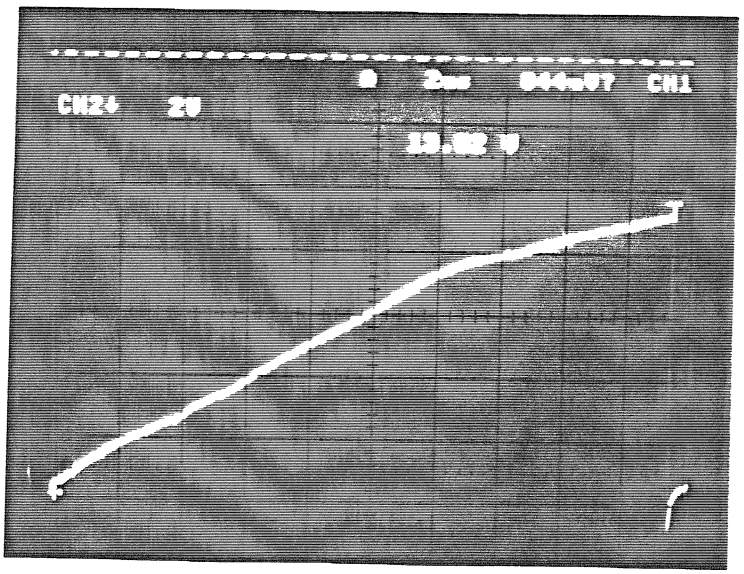

NO FREQUENCY MATCH

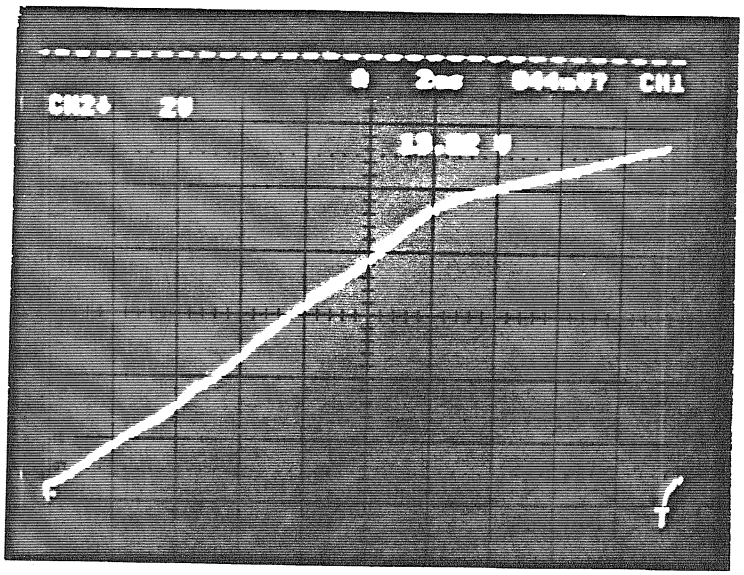

FREQUENCY MATCH

Fig. 4.5.2.7 Spectrum analyzer time integrated DLO detector output for (a) no frequency match and (b) frequency match ($f_{DLO} = f_0$).

integrator output when the input signal frequency differs from the DLO frequency, and also when it matches the reference DLO frequency, respectively. Note the linear buildup of voltage with time in both the matched and unmatched frequency cases, respectively, as was predicted by analysis. In this case with $m' = 0.714$, for the matched case, $v(x'_n, T) \approx 1.36 K_1 T$, while for the unmatched case, $v(x'_n, T) \approx K_1 T$. This analytical result agrees very well with the experimental results in Fig. 4.5.2.7. Note that for the case with the matched frequency, the slope of the voltage build up is steeper, as is expected by earlier analysis. Also, the signal level in the two time integrated outputs falls off towards the end of the time integration cycle. This corresponds to the time interval when the DLO channel center is misaligned with the disk rotation center. Also, the continued rise in voltage after the knee in the outputs is caused by the integration of background light.

4.5.3 System Issues

For N DLO channels on the disk, one would require an N detector array placed at the output plane of the system. For a typical $10\mu m$ channel track pitch on a 15 cm radius disk, $N = 15{,}000$, and the interdetector spacing has to be at least $10\mu m$ for a positive magnification imaging system. In order to compensate for a relatively large detector size, a large value of the imaging system magnification M can be used, or a single mode fiber array could be used to detect the light in parallel from the respective DLO channels. This fiber sampling architecture is shown in Fig.. 4.5.3.1. On the other hand, a more robust technique is to use a 1-D CCD solid state detector array having a large number of small ($\approx 10\mu m$) pixels to simultaneously detect charge from all the DLO channels using the serial CCD read out format (see Fig. 4.5.3.2). For such a system using a 1-D time integrating CCD,

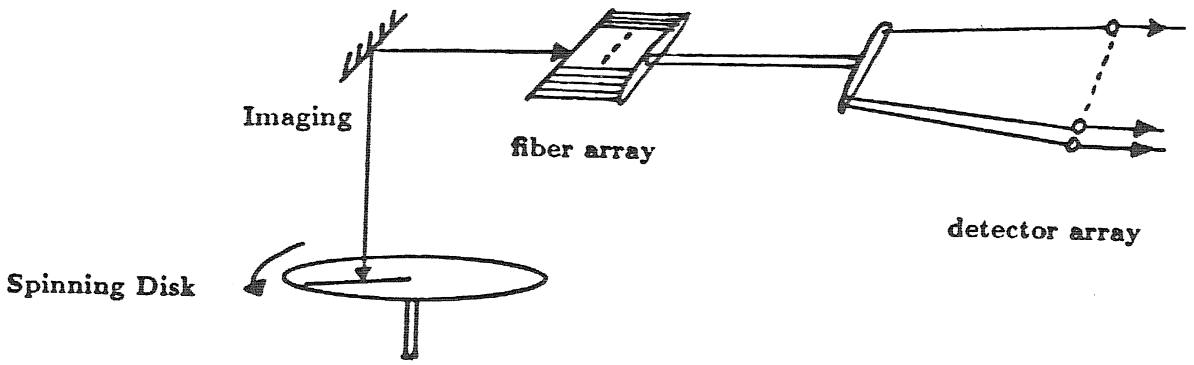

Fig.. 4.5.3.1 Fiber parallel readout system.

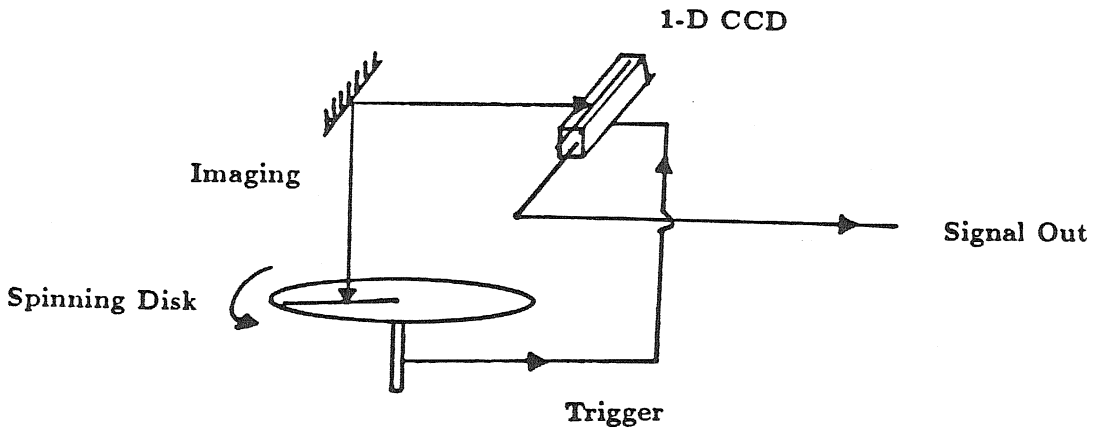

Fig. 4.5.3.2 1-D CCD serial readout system.

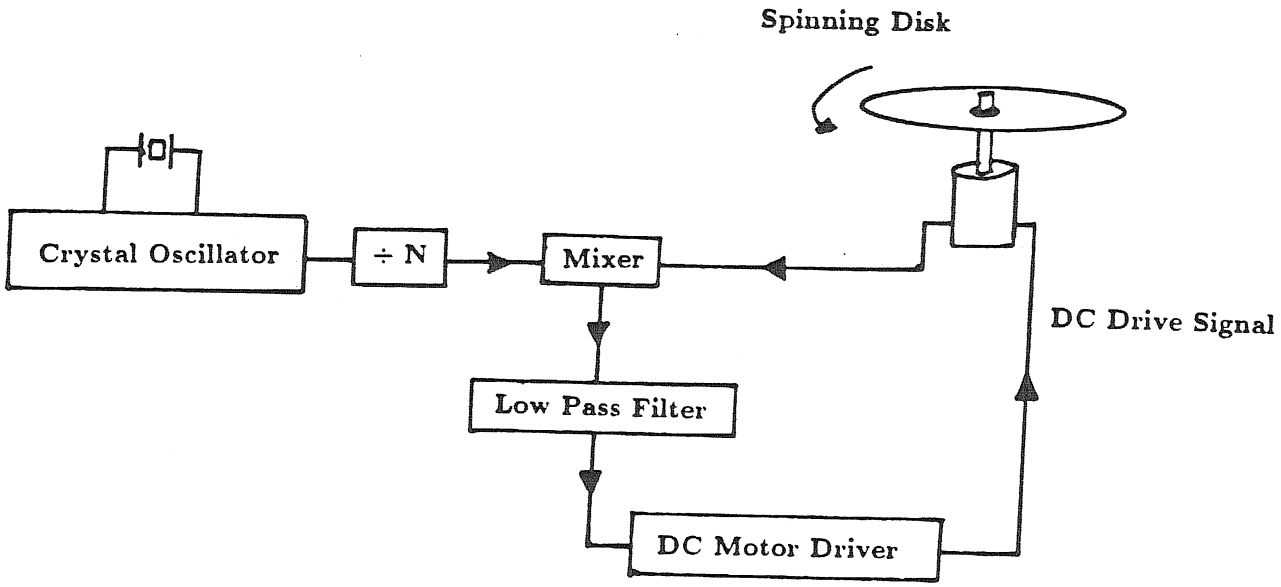

Fig. 4.5.3.3 Phase locked loop system for temporal motor stability.

the charge pattern after time T can be written approximately as:

$$Q(x',y') \approx \sum_{n=1}^{N} [\int_0^T m' K_1 s(t) \cos(2\pi f_n t) dt + K_1 T] \text{rect}[\frac{x' - x'_n}{\Delta w}] \text{rect}[\frac{y'}{\Delta y}], \tag{4.5.3.1}$$

where x', y' are the detector output plane coordinates, Δw and Δy are the width and height, respectively, of a DLO channel at the output plane, and the other terms are as defined earlier. Note that the output signal from the CCD has peaks at locations corresponding to DLO channel locations where the signal has frequency components equal to the DLO frequencies, respectively.

An important system parameter for disk based spectrum analyzers is the temporal coherence stability of the system. As the DLO frequencies are generated by a spinning system, the coherence stability of these signals depends on the spin stability of the rotating disk system. In order to maintain a steady rotation speed, it is typical to use a phase locked loop system shown in Fig. 4.5.3.3, whose stability is controlled by a stable reference crystal oscillator. Today, many such phase locked loop motor stability systems exist in the market.

Another issue that affects these disk systems is the radial or across track motion of the disk during spins. This problem is caused by the misalignment of the disk system rotation center with the center of the concentric data channels. Present state of the art optical disk rotation systems have a spin accuracy of $\approx \pm 5\mu m$ [19]. So far, the disk systems described require a one to one imaging of the disk channels on to their respective detector elements. As the disk moves slightly $\approx \pm 5\mu m$ in the radial direction, the channels get slightly displaced over their respective sensor elements. This effect can be reduced or compensated by a number of techniques shown in Fig. 4.5.3.4. The system shown in Fig. 4.5.3.4(a) generates a tracking error signal that can be used to drive sensitive servo motors that control the radial motion of a spinning disk. Also, this same tracking signal can be used to move the sensor platform if the sensor is light (e.g., array of fibers). Either way, the

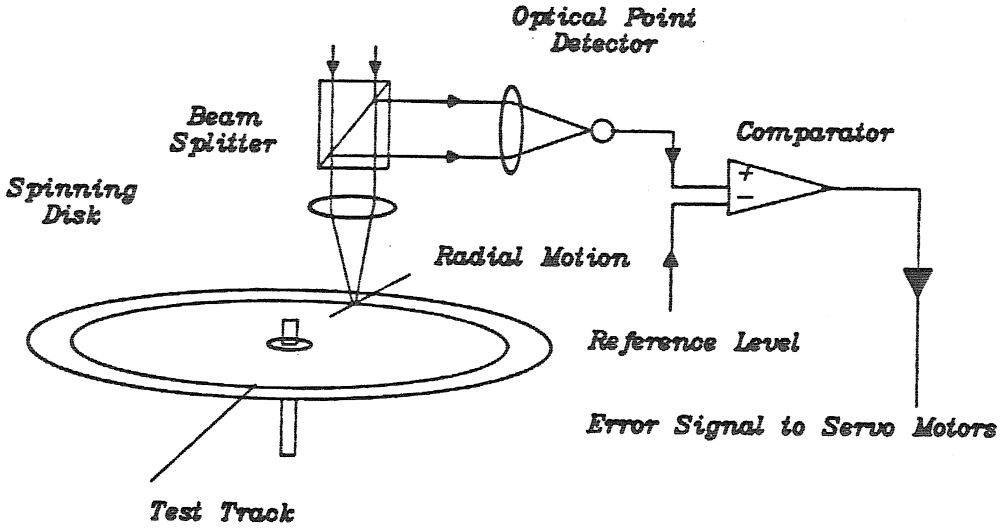

Fig. 4.5.3.4(a) This system generates a tracking error signal that can be used to drive sensitive servo motors that control the radial motion of a spinning disk.

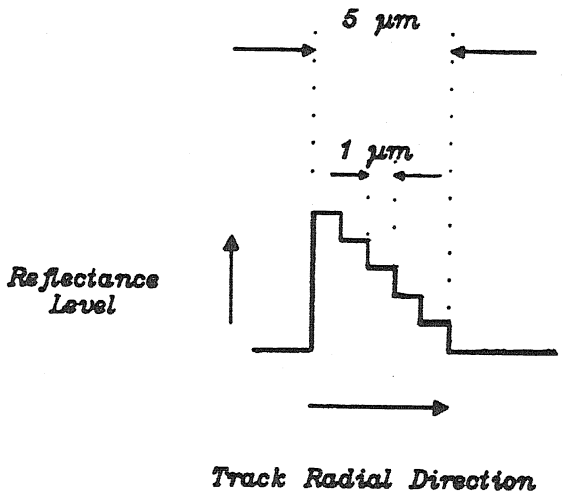

Fig. 4.5.3.4(b) A $5\mu m$ wide step type reflectance pattern that is recorded on the outermost track of the disk to generate the tracking signal.

system tracks the disk radial motion, and compensates for it. The tracking signal is generated from the following procedure. Fig. 4.5.3.4(b) shows a $5\mu m$ wide step type reflectance pattern that is recorded on the outermost track of the disk. A $1\mu m$ focussed light spot is used to illuminate the center of this $5\mu m$ track. The disk rotates and the reflected light signal from this test track is detected at a point detector. The signal level generated by this detector depends on where the focussed light strikes the 5 step shaded track. This reflected signal is compared to a reference level corresponding to the central step in the $5\mu m$ track. The output of the operational amplifier (comparator) gives the direction of the radial shift, along with the position of the disk with respect to its rest center. This tracking signal is then used to drive the servo motors that control the disk or the light sensor position. An alternate technique that does not require any tracking signal is shown in Fig. 4.5.3.4(c,d). This approach reduces the disk radial motion effects by appropriately designing the channel width, interchannel spacing, and the relative sensor size. Fig. 4.5.3.4(c) shows a design where the channel width and pitch are $10\mu m$, respectively, while the sensor elements have a size of $1\mu m$, and a separation of $10\mu m$, respectively. Appropriate sensors for this small sensor design would be single mode optical fibers. In this technique, a $\pm 5\mu m$ radial motion of the optical disk channels does not alter the one to one correspondence between the DLO channels and their respective sensors. Fig. 4.5.3.4(d) shows a similar technique to reduce this motion problem. The difference lies in the fact that in this design, the channel width is $1\mu m$ with an interchannel spacing of $10\mu m$, and the sensor size used is $10\mu m$. This approach also allows a radial motion compensation of $\pm 5\mu m$ as the large detector size compared to the channel width retains the one to one correspondence between the channels and their respective sensors.

Another approach for compensating this disk radial motion is to write motion compensated channels on the disk surface [see Fig. 4.5.3.4(e)]. These channels

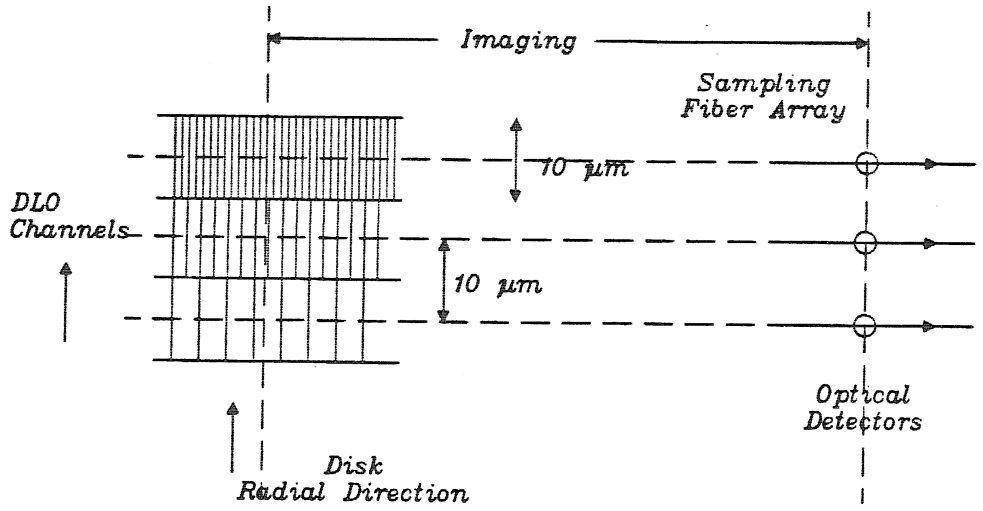

(c)

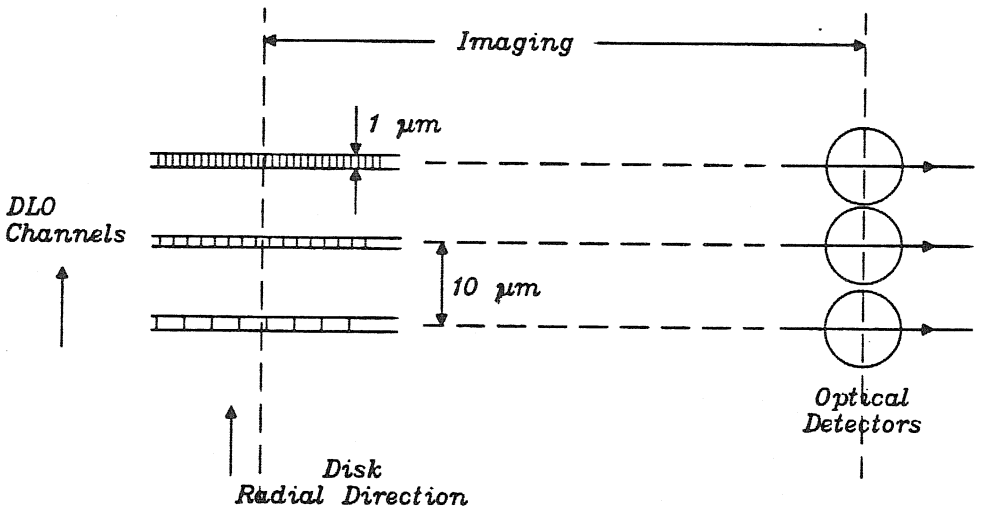

(d)

Fig. 4.5.3.4(c,d) This approach reduces the disk radial motion effects by appropriately designing the channel width, inter-channel spacing, and the relative sensor size.

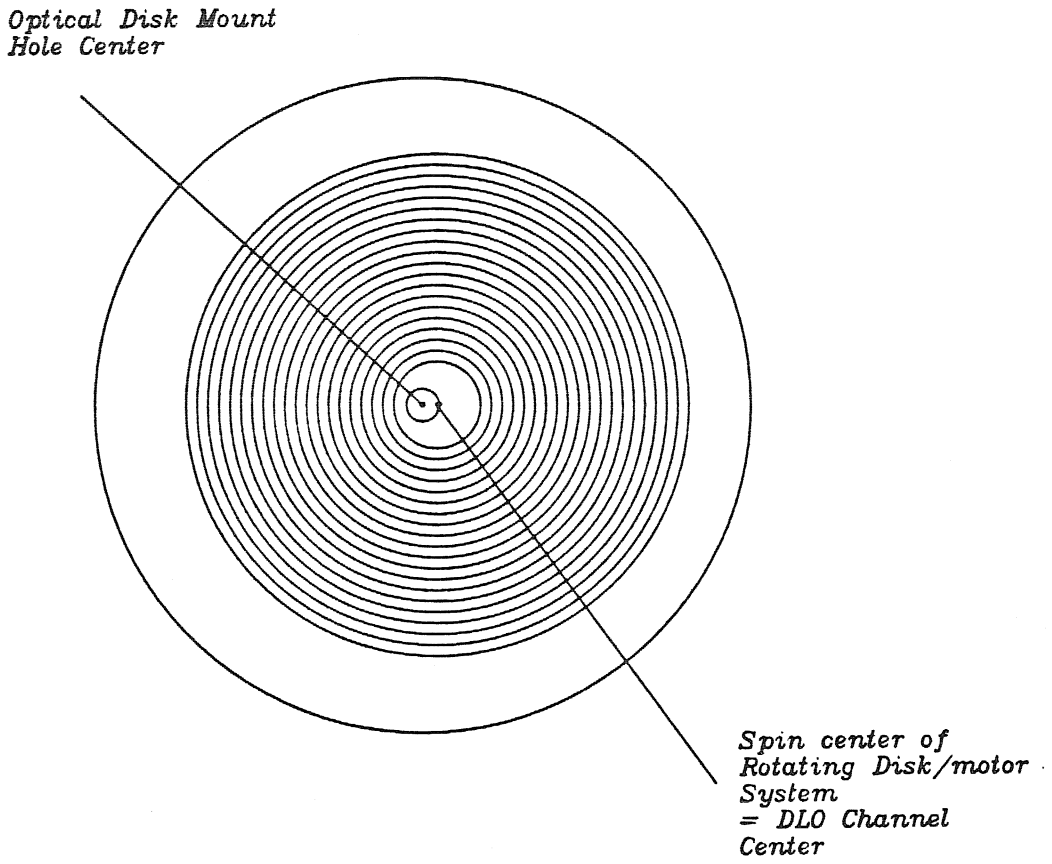

Fig. 4.5.3.4(e) Writing motion compensated channels on the disk surface.

automatically track the disk radial motion, keeping the imaged channels stationary on their respective sensors. This method is inherently stable for the particular disk system, thus keeping the rotation and data channel centers aligned. Nevertheless, it involves a careful assessment of the disk motion. A possible technique to generate these channels is by using a serial write system to write the individual DLO channels separately. A data free optical disk is tightly mounted on a rotation/motor stage. The disk is spun at some constant angular velocity, and the data for each DLO channel are written by the serial write system. This writing technique assures that the disk rotation and data channel centers are almost ($\approx 1\mu m$) aligned.

So far, the analysis conducted employed test signals $s(t)$ that were coherent with the optically generated DLO signals. In the case that the input signal has a random phase at the beginning of each CCD integration time, that is,

$$s(t) = \cos[2\pi f_0 t - \phi(t)], \tag{4.5.3.2}$$

where, for instance, at $t = 0$, the beginning of the first CCD integration, we have $\phi(0) = \phi_0$, the voltage output signal of the n^{th} DLO channel integrator when $f_0 = f_n$ is:

$$v(x'_n, T) = K_1 T[1 + \frac{m'}{2}\cos(\phi_0)]. \tag{4.5.3.3}$$

If $\phi_0 = (k + \frac{1}{2})\pi$, where $k = 0, \pm 1, \ldots$, we cannot detect the matching spectral component. One approach to avoid this effect is to use a quadrature analysis technique. This technique requires each DLO frequency to have an in-phase and quadrature phase channel. For the n^{th} DLO frequency f_n, the two channels written on the disk provide intensity modulated signals that are:

$$I(x'_n, t) = I_1[1 + m_n \cos(2\pi f_n t)] \tag{4.5.3.4}$$

$$I_Q(x'_n + \Delta x'_n, t) = I_1[1 + m_n \sin(2\pi f_n t)], \tag{4.5.3.5}$$

where the spacing between the quadrature channels is $\Delta x'_n$. The voltage output signal of the n^{th} DLO channel integrator when $f_0 = f_n$ for the in-phase channel is given in Eqn. 4.5.3.3, while for the spatially separate quadrature channel, it is given by:

$$v_Q(x'_n, T) = K_1 T[1 + \frac{m'}{2}\sin(\phi_0)]. \tag{4.5.3.6}$$

The two signals expressed in Eqns. 4.5.3.3 and 4.5.3.6, respectively, are compared with the constant signal reference value $K_1 T$ to give the difference signals:

$$v_n = K_1 T\frac{m'}{2}\cos(\phi_0) \qquad \text{and} \qquad v_{Q,n} = K_1 T\frac{m'}{2}\sin(\phi_0). \tag{4.5.3.7}$$

These difference signals are squared and added in an electronic adder to give:

$$\begin{aligned} V_n(T) &= [\frac{m'K_1T}{2}]^2 [\cos^2(\phi_0) + \sin^2(\phi_0)] \\ &= [\frac{m'K_1T}{2}]^2 [\quad 1 \quad] \\ &= [\frac{m'K_1T}{2}]^2 . \end{aligned} \tag{4.5.3.8}$$

Note that the voltage output of the n^{th} DLO channel using the quadrature technique is independent of the input signal phase ϕ_0. This was accomplished at the cost of doubling the DLO channels, and introducing additional comparator, square, and adder circuits. As shown in Fig. 4.5.3.5, the in-phase and quadrature DLO channels can be written on the disk such that one CCD picks up the intensity from the in-phase channels, while the other CCD collects light from the quadrature channels. The two CCD signals are processed by separate comparators and square operation circuits, while being added in a single adder. If the compare operation with the signal dependent reference $K_1 T$ is to be eliminated, a 4-channel quadrature technique has to be used that employs $\cos(2\pi f_n t)$, $-\cos(2\pi f_n t)$, $\sin(2\pi f_n t)$, and $-\sin(2\pi f_n t)$ DLO signals for each DLO frequency f_n as shown in Fig. 4.5.3.6.

Another issue to consider is the technique employed to generate the DLO format disk patterns. As we are using the disk surface as a reflective surface with concentric

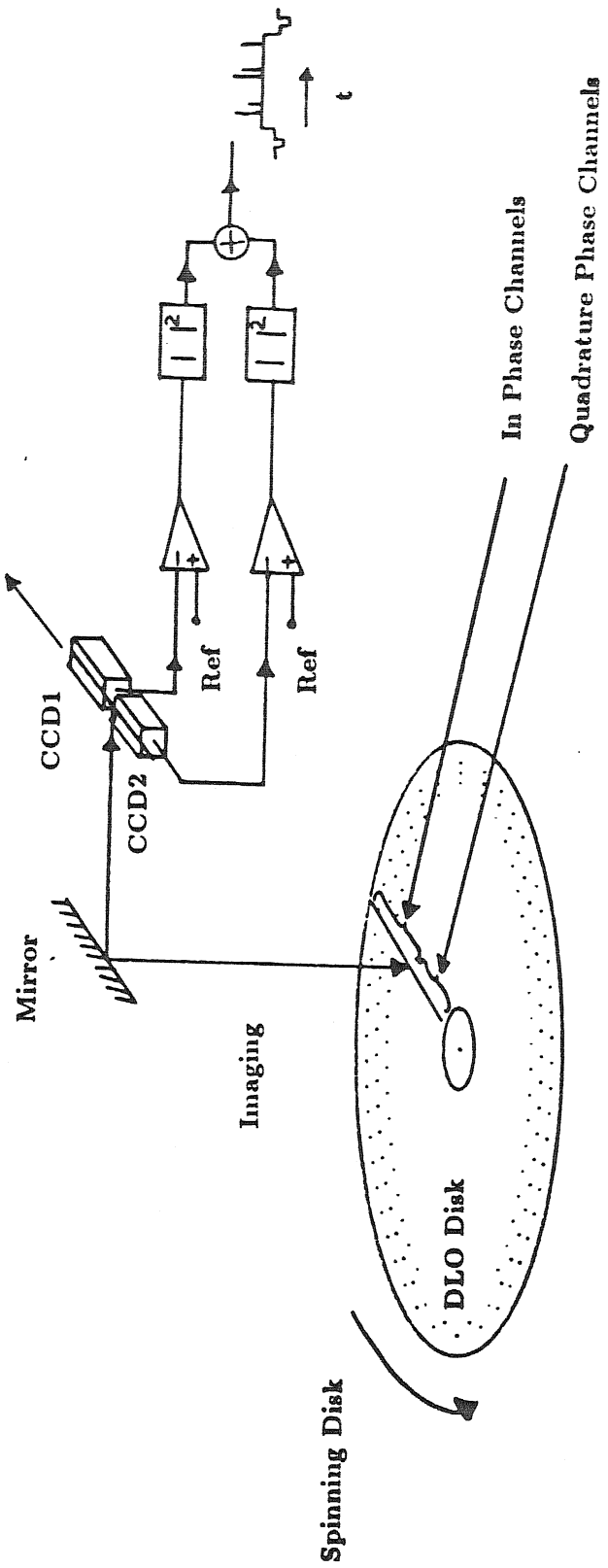

Fig. 4.5.3.5 2-CCD quadrature channel system for non-coherent spectrum analysis.

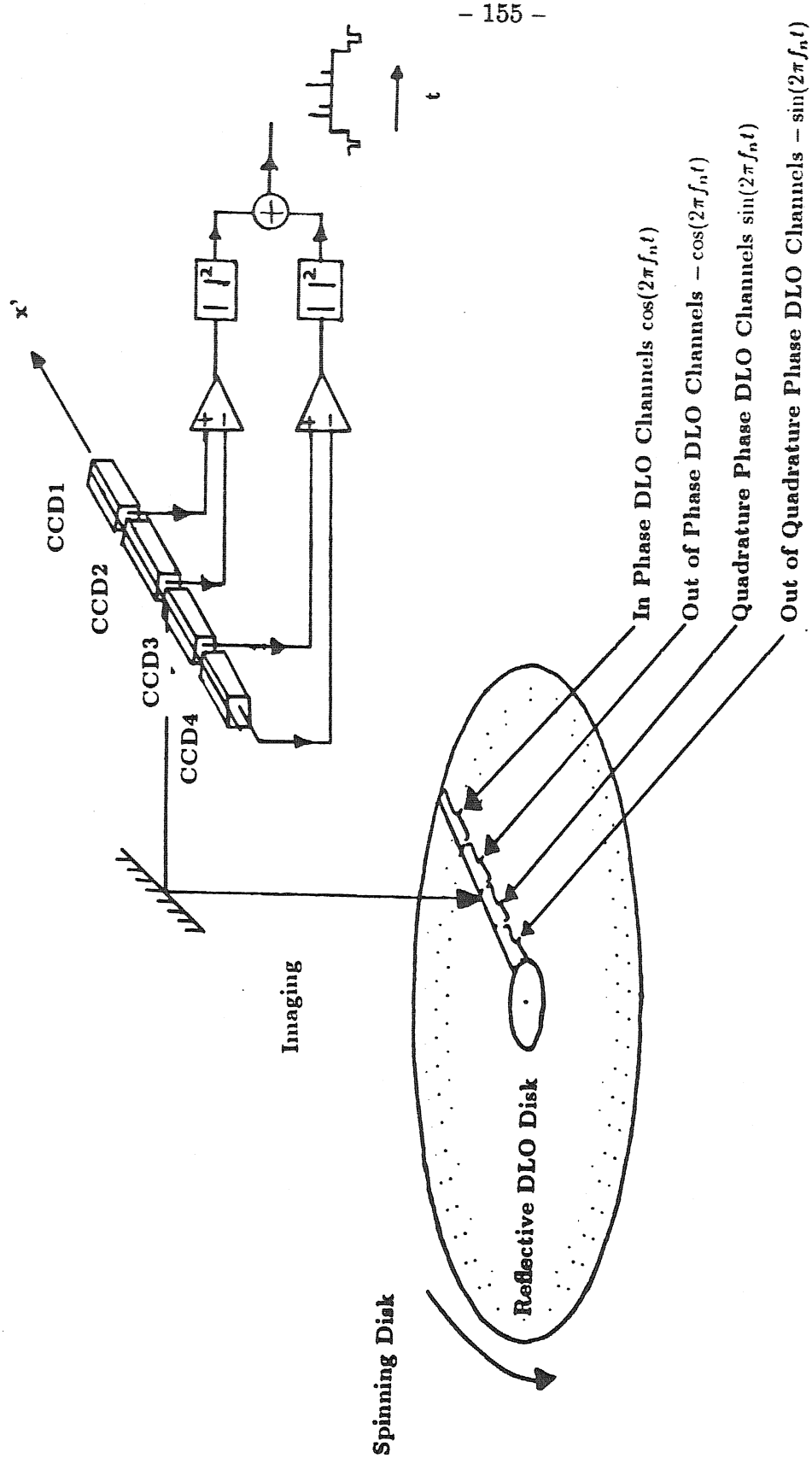

Fig. 4.5.3.6 4-CCD quadrature channel system for non-coherent spectrum analysis.

circles that have constant spatial frequency patterns per circle, we could use film based or photo-lithographic based techniques to stain the disks with these patterns. There is no need to write these data serially, bit by bit, by the hole burning process, unless we want to write the motion compensated DLO channels.

Finally, to consider the capabilities of such a disk based system, consider the following design specifications. With a 15 cm radius disk spinning at 1800 rpm (video rate), and a $1\mu m$ bit size, the maximum oscillator frequency corresponding to the outermost track is 14.2 MHz. In addition, using a track pitch of $10\mu m$, the best frequency resolution possible is 940 Hz, with a total of 15,000 frequency channels covering the 14.2 MHz bandwidth. These numbers demonstrate the processsing power that can be generated with optical disk based continuous wave spectrum analyzers using the constant spatial period DLO format. With the sector DLO format, a higher DLO bandwidth can be achieved. As mentioned earlier, we can control the processing bandwidth and frequency resolution of the processor by varying the disk rotation speed.

4.6 Conclusion

This chapter has proposed several optical disk based techniques for generating complete 2-D folded spectrum outputs from 2-D acousto-optic spectrum analyzers that are otherwise extremely hard to obtain using commercially available reference signal generation electronics. The 2-D nature of the disk storage area coupled with its angular motion are uniquely exploited to provide simultaneous temporal and spatial light modulation. This chapter has experimentally demonstrated the principle of the continuous wave distributed local oscillator based time integrating optical disk spectrum analyzer. This multichannel spinning disk architecture is applied to spectrum analysis, although the system could be used for applications such as multichannel correlation, pattern recognition, and vector matrix computations. In

particular, when combined with a 1-D space integrating high bandwidth acousto-optic spectrum analyzer, the disk spectrum analyzer can provide a very large number $(10,000)$ of high resolution spectral channels for each space integrated coarse frequency channel. Thus, the 2-D TSI acousto-optic optical disk based spectrum analyzer provides both high instantaneous bandwidth and high frequency resolution complete 2-D folded spectrum outputs, respectively, with a 20 million (2×10^7) potential channel capability.

References:

[1] Y. S. Abu-Mostafa and D. Psaltis, "Optical Neural Computers," Scientific American, March, 1987.

[2] J. H. Rilum and A. R. Tanguay, Jr., "Utilization of optical memory disks for optical information processing," 1988 Annual OSA Conference, Santa Clara, CA, Oct/Nov., 1988.

[3] D. Psaltis, A. A. Yamamura, M. A. Neifeld, and S. Kobayashi, "Parallel Read-out of Optical Disks," 1989 Topical Meeting on Optical Computing, Salt Lake City, UT, Feb./March, 1989.

[4] D. Psaltis, M. A. Neifeld, and A. A. Yamamura, "Optical Disk-Based Correlation Architectures," 1989 Topical Meeting on Optical Computing, Salt Lake City, UT, Feb./March, 1989.

[5] D. Psaltis, M. A. Neifeld, and A. A. Yamamura, "Image Correlation using Optical Memory Disks," *Optics Letters*, May, 1989.

[6] K. Wagner and D. Psaltis, "Time and Space Integrating Acousto-optic Folded Spectrum Processing for SETI,"*Proc SPIE*, Vol. 564-31, 1985.

[7] N. A. Riza and D. Psaltis,"Multiplicative Time and Space Integrating Acousto-optic Architectures for Real-Time Spectrum Processing,"*Proc. SPIE*, Vol. 827-34, 1987.

[8] T. R. Bader, "Acousto-optic Spectrum Analysis: a high performance hybrid technique," *Applied Optics*, vol.18, No.10, May, 1979.

[9] K. Wagner, "Time and Space Integrating Acousto-optic Signal Processing," Ph.D Thesis, California Institute of Technology, May, 1987.

[10] Model 4075-1A TeO_2 Bragg Cell, Crystal Technology Inc., Mini-Catalog, 1987.

[11] J. Isailović, *VideoDisk and Optical Memory Systems*, Prentice Hall, Inc, 1985.

[12] B. R. Brown, "Optical Data Storage Potential of Six Materials," *Applied Op-*

tics, Vol. 13, No. 4, April, 1974.

[13] S. Y. Suh, D. A. Snyder, and D. L. Anderson, "Writing Process in Ablative Optical Recording," *Applied Optics*, Vol. 24, No. 6, March, 1985.

[14] D. C. Kowalski, D. J. Curry, L. T. Klinger, and G. Knight, "Multichannel Digital Optical Disk Memory System," Opt. Eng. 22, 464 (1983).

[15] Y. Sasano, T. Saitou, and F. Tanaka, "Still Picture Filing/Transmitting System with Data Compression Technique," *International Symposium on Optical Memory*, Technical Digest, 26C-3, Kobe, Japan, Sept. 1989.

[16] K. Torazawa *et al.*, "Erasable Digital Audio Disk System," *Applied Optics*, Vol. 25, No. 22, November, 1986.

[17] M. Ojima *et al.*, "Compact Magneto-Optical Disk for Coded Data Storage," *Applied Optics*, Vol. 25, No. 4, February, 1986.

[18] S. Kobayashi, "Rocky: The Read-Write Magneto-optic and Write Once Optical Disk System," Sony Corporation, Japan, 1989.

[19] S. Kobayashi, Private Communication (visiting Associate Caltech) Sony Corporation, Japan, 1989.

CHAPTER 5

BIAS REMOVAL VIA PHOTOREFRACTIVE CRYSTALS

5.1 Introduction

This chapter introduces the application of photorefractive crystals as bias removers in acousto-optic signal processors. As is evident from previous chapters, many optical processing techniques utilize bias and reference signals to accomplish bipolar or complex signal processing operations. Sometimes, these signals are electrical, and are fed into the system via an electrical-to-optical transducer such as a Bragg cell [1]. Other designs use optical beams to provide the reference and bias signals [2]. Typically, the outputs of these optical signal processors consist of the desired signal terms, plus unwanted bias terms. These bias terms can be signal dependent, or can exist as constant light distributions. So far, most approaches for real-time bias removal in practical signal processing systems revolve around two techniques. The first is CCD bias subtraction, where two synchronous CCD sensors are simultaneously used to detect the processor outputs at the ports of a dielectric beam splitter, and the generated video signals are directly subtracted in an electronic circuit [3-4]. This approach is difficult in practice as the two CCDs have to be aligned on a pixel by pixel basis. The second technique for bias removal is called carrier demodulation [5]. This approach requires the desired output signal to be generated on a spatial carrier on the CCD, while all the remaining bias terms are not modulated by the carrier. When the charge pattern is electronically read out by the sensor's internal charge transfer mechanism, the spatial carrier is converted to a temporal carrier that has only the signal term riding on it, while the bias terms appear as a DC electrical level in the video signal. This CCD output signal is directly fed to an electronic band pass filter centered at the temporal car-

rier frequency. This operation removes the DC bias from the signal. Additional envelope detection and low pass filtering on the video signal results in the bias free signal output. Although this approach to bias removal is generally more robust than the CCD electronic subtraction method, this carrier demodulation technique suffers from the problem of high CCD space bandwidth product (SBWP) usage. In other words, many of the CCD pixels are used to sample the spatial carrier that the signal term rides on, thus resulting in a smaller SBWP for the optical processor output. Moreover, it is important to point out that the above mentioned real-time bias removal schemes eliminate the bias terms after the signal detection operation in an optical sensor. Thus, these schemes do not solve the bias related problems of low output signal dynamic range, and poor output signal-to-noise ratio (SNR).

As discussed earlier in Chapter 2, most acousto-optic system architectures use temporal and spatial integration of light to generate the desired output signals. In particular, long integration time is a desired feature in time integrating processors such as spectrum analyzers and correlators, as system resolution and processing gain are directly proportional to the integration time. The time integration operation is normally used to achieve long processing windows; but unfortunately, a major problem inherent to these time integrating systems is the gradual buildup of unwanted bias with time. This bias is accumulated in detectors such as CCD's, and greatly lowers the processor performance.

Previous work by Psaltis *et al.* has experimentally demonstrated the application of a photorefractive crystal for bias removal in a 1-D time integrating correlator [6]. In this chapter, we will study the feasibility of photorefractive crystals as bias removers in 1-D and 2-D optical architectures for spectrum analysis. We begin with a brief description of the photorefractive effect, and describe how a photorefractive crystal can be used as a bias remover. In order to study the bias removing property of photorefractive crystals, we choose to experimentally study continuous wave 1-D

time integrating, and 2-D time and space integrating acousto-optic architectures, that are designed for spectrum processing. First, a 1-D time integrating acousto-optic spectrum analyzer/correlator architecture is demonstrated in the laboratory, and results from this processor before bias removal are shown. This processor uses the carrier demodulation approach for bias removal. Next, a crystal based bias-free version of the 1-D architecture is built in the laboratory, and bias-free experimental results are obtained and analyzed. After studying the 1-D architecture, we extend the bias removing property of the crystal to a 2-D time and space integrating architecture. First, we describe the distributed local oscillator (DLO), and how it can be used to heterodyne high frequency signals to baseband. In particular, the DLO acts as a reference signal in continuous wave 2-D optical spectrum analysis. A DLO generation experiment is carried out in the laboratory, and experimental results are obtained. Next, a bias-free crystal based 2-D time and space integrating acousto-optic architecture is designed and constructed in the laboratory, and experimental results are highlighted. We study the performance limitations of such a processor. These experiments were conducted for continuous wave systems.

5.2 Bias Removal Using Photorefractive Crystals

We begin by briefly describing the photorefractive effect, which can be used for the holographic recording of a light interference pattern. In particular, we will exploit the dynamic holographic recording properties of a photorefractive crystal, thus allowing the processing of temporally varying intensity patterns. The photorefractive effect has been extensively modeled and studied [7–8]. Here, the effect is summarized as follows.

An intensity grating incident on a photorefractive crystal, such as bismuth silicon oxide (BSO), excites electrons from traps to the conduction band. These

charges migrate due to diffusion and drift from an external electric field, recombining in dark regions, and thus creating a space-charge field within the crystal. This field, coupled with the linear electro-optic effect, introduces refractive index perturbations, resulting in the construction of a holographic phase grating in the crystal. Given that the temporally varying intensity incident on the crystal is represented by:

$$I(x,t) = I_0 + \mathrm{Re}[I_1(x,t)e^{jkx}] \qquad t \geq 0, \tag{5.2.1}$$

where I_0 is the average light intensity incident during exposure, $I_1(x,t)$ is the temporally varying grating modulation depth, and $k/2\pi$ is the spatial carrier frequency of the grating used for holographic recording, it has been shown that the diffracted intensity can be written as [9–10]:

$$I_{out}(x,t) = \left| \frac{K_1}{\tau} e^{-\frac{t}{\tau}} \int_0^t \frac{I_1(x,t')}{I_0} e^{\frac{t'}{\tau}} dt' \right|^2 I_R, \tag{5.2.2}$$

where I_R is the intensity of the readout beam, τ is the complex time constant of the space-charge field given by $\tau = K_2/I_0$, where K_2 is a complex constant that depends on the particular material and the experimental conditions. Also, K_1 is the complex constant involving material parameters of the crystal, the grating frequency, and the applied electric field. Eqn. 5.2.2 was derived assuming that self diffraction effects are negligible, and spatial variations of $I_1(x,t)$ are much slower than k. In addition, it has been shown that for $t \gg \tau$, the response of a photorefractive crystal to a time varying intensity pattern can be approximately written as the output of a time integrator with a sliding integration window [6,10]. This expression can be written as:

$$I_{out}(x,t) \approx \left| \frac{K_1}{\tau} \int_t^{t+\tau'} \frac{I_1(x,t')}{I_0} dt' \right|^2 I_R, \tag{5.2.3}$$

where $\tau' = |\tau|^2/\mathrm{Re}\{\tau\}$ is the length of the sliding time window. Here, Eqn. 5.2.3 demonstrates that a photorefractive crystal can be used as a time integrating (TI)

detector, accumulating the bias normalized spatially modulated signal for τ' seconds. In addition, note that for a temporally stationary intensity pattern, that is, $I_1(x,t) = I_1(x)$, the diffracted output intensity depends on the ratio of the modulated light intensity I_1 to the DC light I_0.

The bias-free optical architectures introduced in this chapter use the photorefractive crystal as a time integrating detector to accomplish bias removal, where $I_1(x,t)$ is designed to be the desired output signal term, and I_0 is the constant and signal dependent bias terms that are unwelcome at the output of the processor. The desired time integrated output of the processor is diffracted from the crystal using an external read-out laser beam, thus leaving behind the undesired bias. This process forms the basis for bias removal via photorefractive crystals in time and space integrating optical processors.

5.3 Bias Removal in Continuous Wave Acousto-optic Architectures

5.3.1 1-D TI Correlator/Spectrum Analyzer without Bias Removal

(a) Architecture:

The basic 1-D time integrating Correlator/Spectrum Analyzer architecture is shown in Fig. 5.3.1.1 [11–12]. The system consists of collimating optics, two counter propagating Bragg cells, imaging optics, and a time integrating detector. The light processing chain is as follows. The light from an He-Ne laser is collimated by an $F = 20cm$ spherical lens. This collimated and expanded light is focussed by an $F = 30cm$ cylindrical lens as a Bragg matched slit of light in a glass AOD. The AOD is driven by an external electrical signal $s_1(t)$. The +1 diffracted order and DC light, respectively, from the AOD are 1:1 imaged (with inversion) on to a second glass AOD, such that the +1 order light passes essentially unaffected through this second AOD, while the DC light is Bragg matched to produce a +1 order. A pair

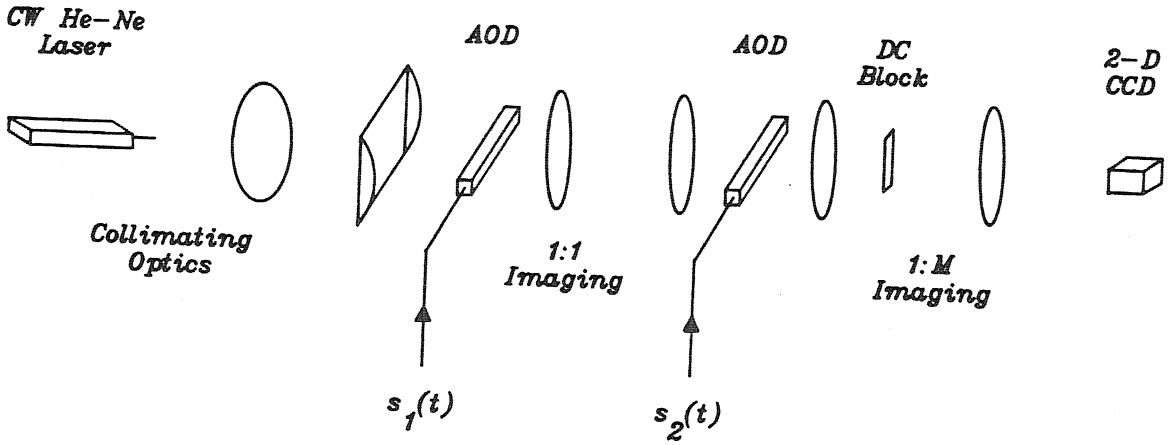

Fig.5.3.1.1 The basic 1-D time integrating correlator/spectrum analyzer architecture.

of $F = 20cm$ spherical lenses are used in the 1:1 imaging system. The +1 orders from both AOD's are imaged on to a CCD detector, after the DC light is blocked in the Fourier plane of the first imaging lens. The imaging is accomplished using $F = 20cm$ and $F = 50cm$ lenses, respectively, giving a magnification factor of 2.5. The laboratory system is shown in Fig. 5.3.1.2. The optical field incident on the CCD is proportional to:

$$E(x,t) \propto \left[\tilde{s}_1(t - \frac{x}{Mv_a}) + \tilde{s}_2(t + \frac{x}{Mv_a})\right] \text{rect}(\frac{x - MX/2}{MX}), \tag{5.3.1.1}$$

where v_a is the acoustic velocity in the Bragg cell, X is the AOD aperture, and M is the magnification of the imaging system. Here, $\tilde{s}(t)$ represents the analytic +1 order diffracted AOD drive signal. Depending on what the AOD drive signals are, this system can be used as a time integrating correlator or a 1-D spectrum analyzer, that uses carrier demodulation for bias removal. Different test experiments are carried out to demonstrate this ability.

(b) Experimental Results:

Using Eqn. 5.3.1.1, the intensity incident on the CCD can be written as:

$$\begin{aligned} I(x,t) = \Bigg[& \left|\tilde{s}_1(t - \frac{x}{Mv_a})\right|^2 + \left|\tilde{s}_2(t + \frac{x}{Mv_a})\right|^2 \\ & + 2\text{Re}\{\tilde{s}_1(t - \frac{x}{Mv_a})\tilde{s}_2^*(t + \frac{x}{Mv_a})\}\Bigg] \text{rect}(\frac{x - MX/2}{MX}), \end{aligned} \tag{5.3.1.2}$$

where the first and second terms are bias terms, while the third term gives the desired processor output. A spatial carrier modulated by the desired output can be observed across the CCD surface when the AOD's are driven by their carrier signals, that is, $\tilde{s}_1(t) = \tilde{s}_2(t) = ae^{-j\omega_0 t}$. In this case, the intensity detected on the CCD is given by:

$$I(x) = \left[2|a|^2 + 2\cos(\frac{2\omega_0}{Mv_a}x)\right] \text{rect}(\frac{x - MX/2}{MX}). \tag{5.3.1.3}$$

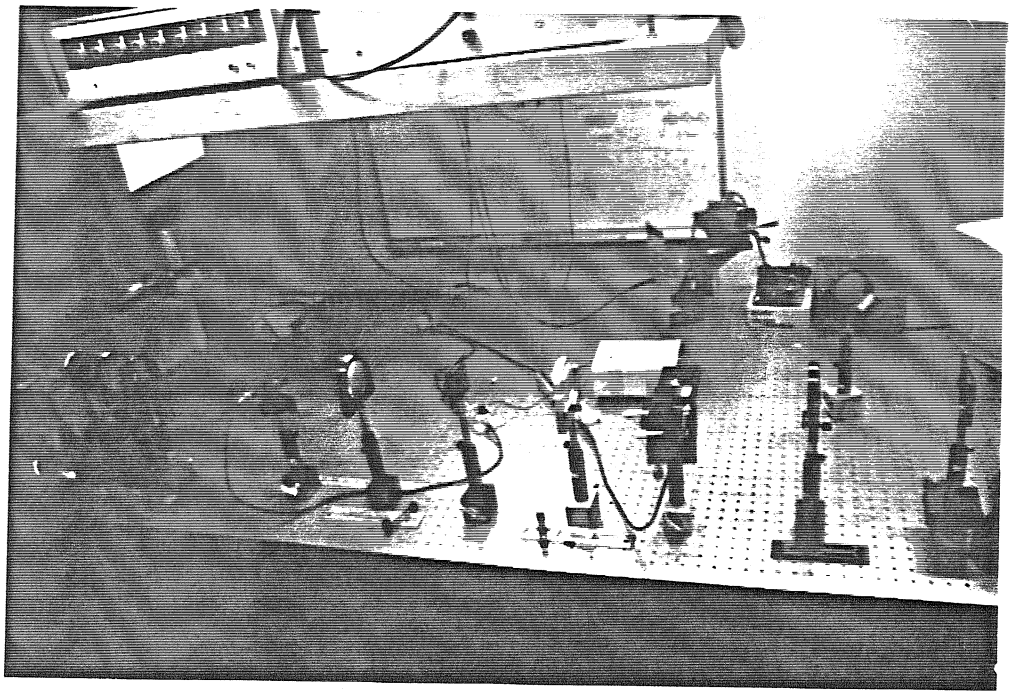

Fig.5.3.1.2 Laboratory system for the 1-D time integrating correlator/spectrum analyzer architecture.

Here a is a constant amplitude term, and $\omega_0 = 2\pi f_0$ is the AOD center frequency. Fig. 5.3.1.3 shows a 12 lines/mm spatial carrier across the CCD that was obtained using a 57 MHz carrier frequency. One spatial cycle corresponds to approximately 4 CCD pixels. It is this spatial carrier that is used to modulate the desired signal, and later is electronically demodulated to remove any bias from the signal.

The next step was to test the system to obtain autocorrelation of signals. First, the autocorrelation of linear frequency modulated (FM) signals is obtained. In this case, $\tilde{s}_1(t) = \tilde{s}_2(t) = ae^{-j2\pi(f_0 t + 0.5bt^2)}$, where b is the frequency sweep rate. The time integrated charge pattern on the CCD is given by:

$$\begin{aligned} Q(x) &= \left[K_3 + 2|a|^2 \mathrm{Re}\{e^{-j2\pi\frac{2f_0}{Mv_a}x}\int_{T_d} e^{-j2\pi\frac{2bx}{Mv_a}t}\,dt\}\right]\mathrm{rect}(\frac{x - MX/2}{MX}) \\ &= \left[K_3 + K_4\cos(\frac{2\omega_0}{Mv_a}x)\mathrm{sinc}(\frac{2T_d b}{Mv_a}x)\}\right]\mathrm{rect}(\frac{x - MX/2}{MX}), \end{aligned} \tag{5.3.1.4}$$

where K_3 and K_4 are constants, and T_d is the CCD integration time. Thus, the autocorrelation of linear FM signals consists of a uniform bias level, and a spatial carrier modulated blur spot at the $x = 0$ CCD position. The width of the blur spot is given by $\Delta x = \frac{Mv_a}{bT_d}$, and can be controlled by varying the sweep rate. Fig. 5.3.1.4 shows the time integrated, carrier modulated blur spot video signal outputs for different sweep rates. Notice that the signal rides on a large bias level that eats up much of the CCD dynamic range. As the input signal amplitudes are increased, the CCD saturates quickly due to the large bias contribution, as shown in Fig. 5.3.1.5. The plot shown in Fig. 5.3.1.6. records the behavior of the spot width as a function of FM sweep rate. This optical system using the linear FM signals can be used to perform signal spectrum analysis if one of the FM signals is frequency or amplitude modulated by the test signal. In our experiment, we introduced the test signal $s(t)$ as an amplitude modulated linear FM signal given by:

$$s_2(t) = s(t)\cos[2\pi(f_0 t + 0.5bt^2)], \tag{5.3.1.5}$$

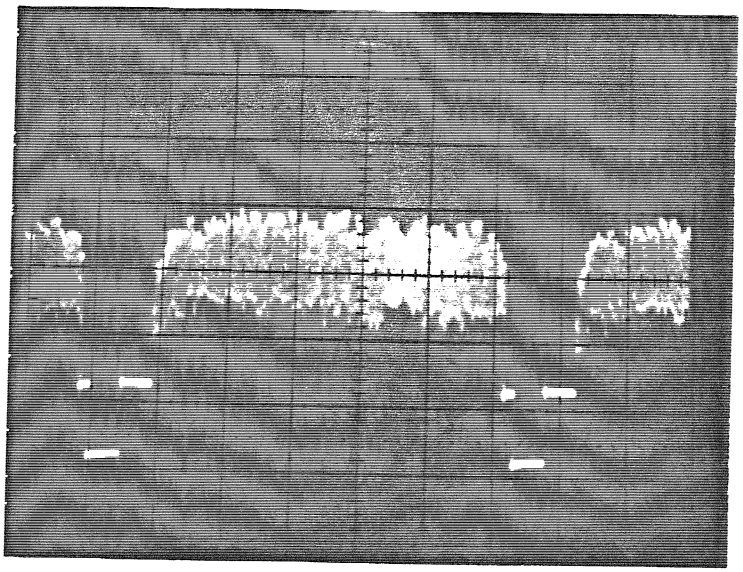

1 video line.

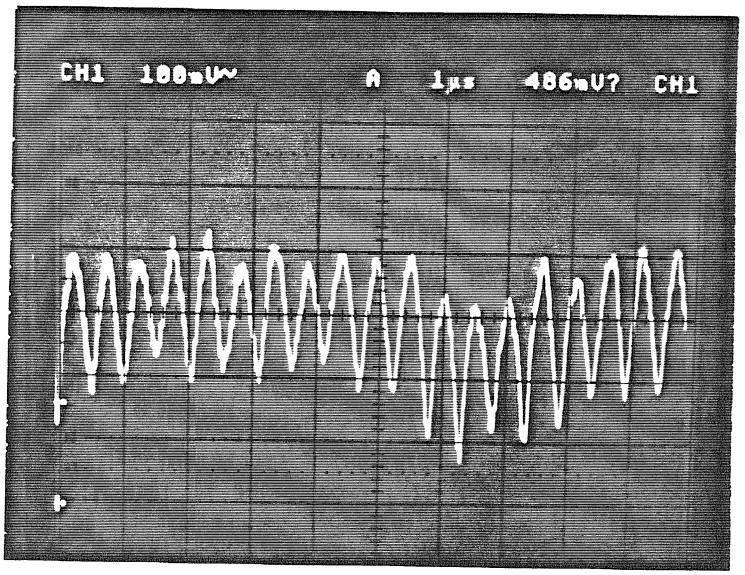

Enlarged view.

Fig.5.3.1.3 Spatial carrier of 12 lines/mm across CCD using a $57MHz$ AOD carrier signal. Here 1 cycle = 4 CCD pixels.

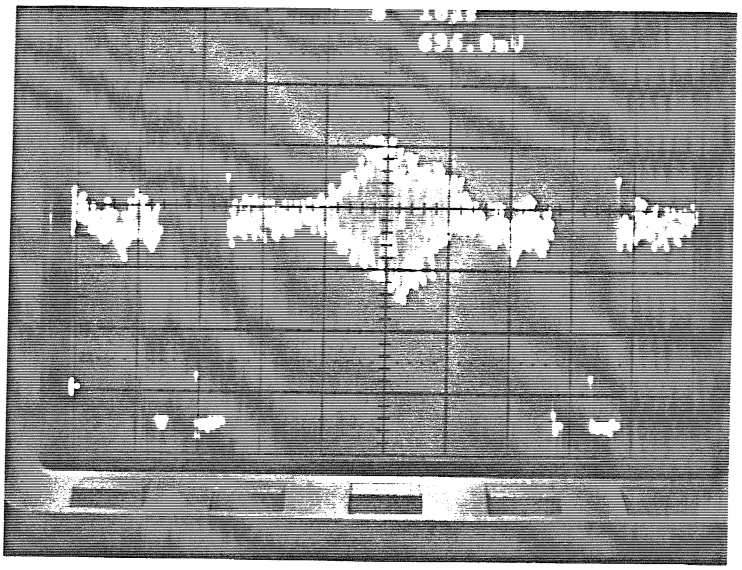

$63MHz/sec$

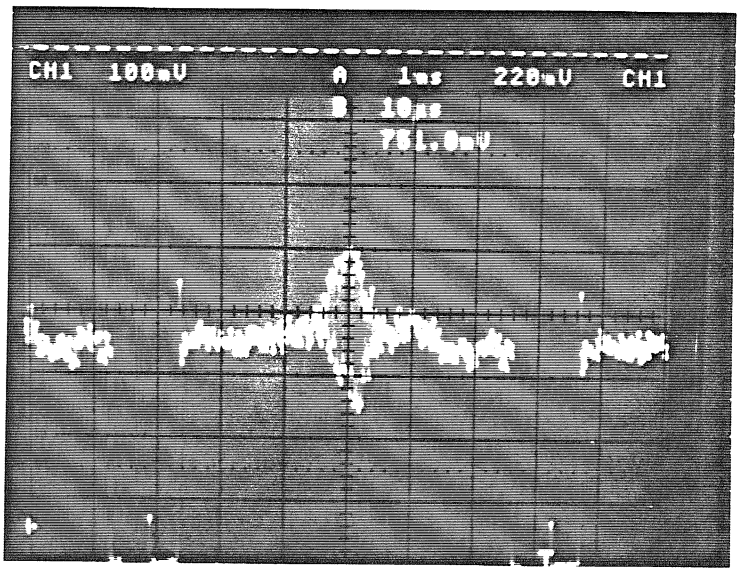

$138MHz/sec$

Fig.5.3.1.4 Time integrated carrier modulated blur spot for different sweep rates showing the autocorrelation of linear FM signals.

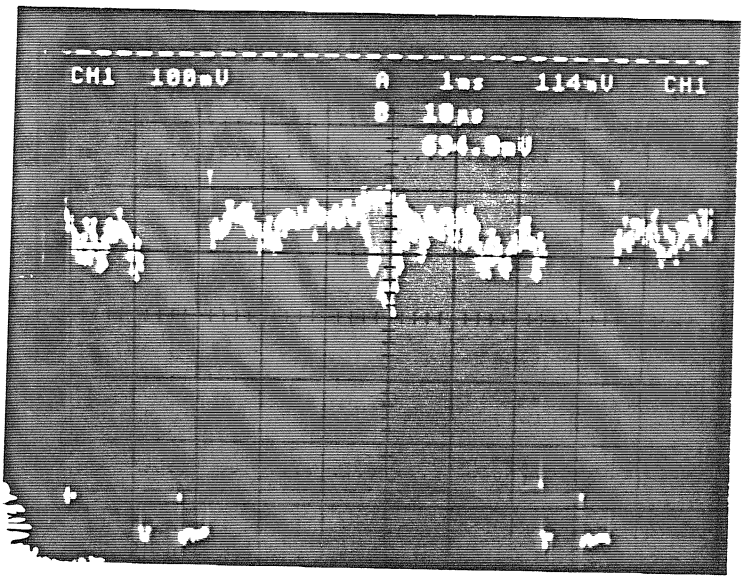

Fig.5.3.1.5 CCD saturation due to the large bias level.

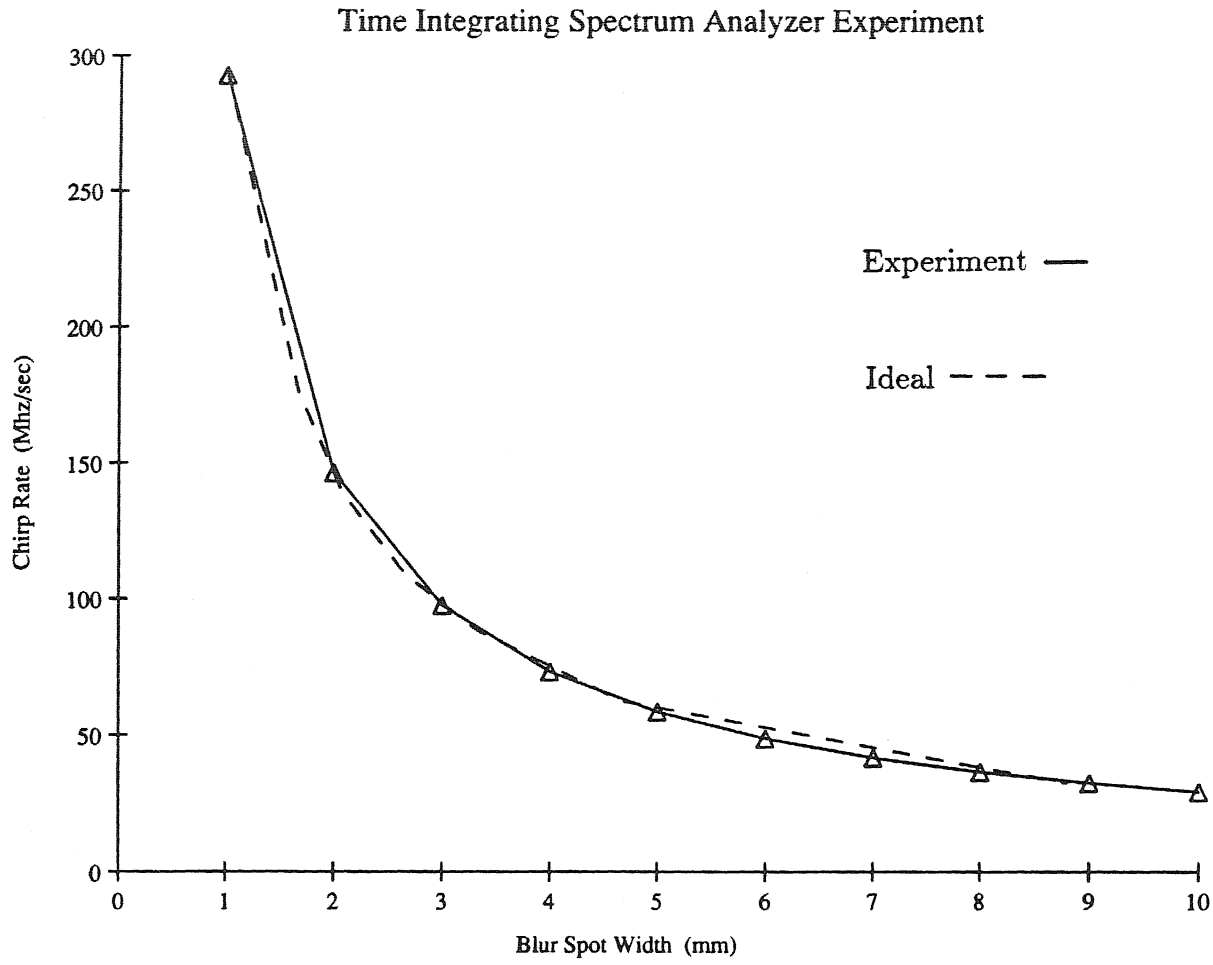

Fig.5.3.1.6 Plot of autocorrelation blur spot width versus sweep rate of linear FM signals.

where the single tone test signal of frequency f' is $s(t) = a\cos(2\pi f' t)$. The resulting time integrated charge distribution on the CCD is given by:

$$Q(x) = \left[K_3 + 2|a|^2 \mathrm{Re}\{e^{-j2\pi\frac{2f_0}{Mv_a}x}\int_{T_d}\cos(2\pi f' t)e^{-j2\pi\frac{2bx}{Mv_a}t}\,dt\}\right]\mathrm{rect}(\frac{x-MX/2}{MX})$$
$$\approx \left[K_3 + \frac{K_4}{2}\cos(\frac{2\omega_0}{Mv_a}x)\left[\mathrm{sinc}(T_d\frac{2b}{Mv_a}x + f') + \mathrm{sinc}(T_d\frac{2b}{Mv_a}x - f')\right]\}\right]$$
$$\mathrm{rect}(\frac{x-MX/2}{MX}), \tag{5.3.1.6}$$

where we have assumed that $f' \ll f_0$. This output corresponds to two carrier modulated blur spots positioned symmetrically around the $x = 0$ position, where the position offset depends on the input signal test frequency f'. Thus, the frequency of the input signal has been mapped to a spatial coordinate space on the CCD sensor. Fig. 5.3.1.7 shows the two carrier modulated spectral peaks riding on a large bias level, while Fig. 5.3.1.8 shows a frequency linearity plot of the processor. Note that the signal generators used for the FM and test signals, respectively, were free running and mutually incoherent. This resulted in a slow temporal oscillation of the time integrated spectral peaks over successive CCD integration frame times.

Next, we study the autocorrelation of AM signals, where:

$$s_1(t) = s_2(t) = a\cos(2\pi f_1 t)\cos(2\pi f_0 t). \tag{5.3.1.7}$$

Assuming that $\frac{1}{T_d} \ll f_1 \ll f_0$, the charge integrated by the CCD can be approximated as:

$$Q(x) = \left[K_5 + K_6\cos[2\pi(\frac{2f_1}{Mv_a}x)]\cos[2\pi(\frac{2f_0}{Mv_a}x)]\right]\mathrm{rect}(\frac{x-MX/2}{MX}), \tag{5.3.1.8}$$

where K_5 is the constant bias term, and K_6 is a constant factor. The expression in Eqn. 5.3.1.8 consists of an amplitude modulated spatial carrier distribution. The read-out mechanism of the CCD converts this light pattern to a amplitude modulated video signal. A typical AM signal is shown in Fig. 5.3.1.9, while the optical

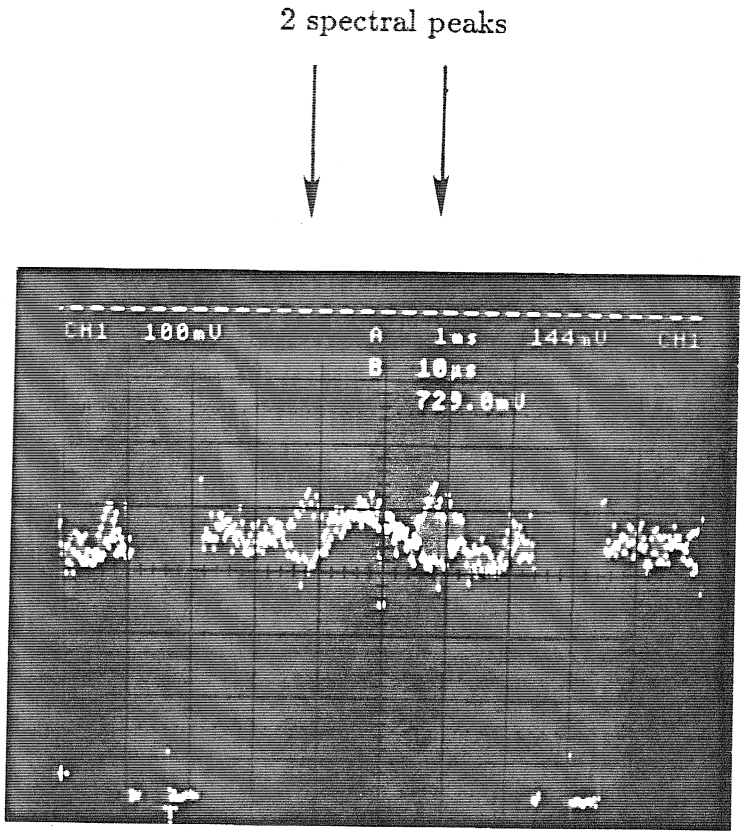

Fig.5.3.1.7 Double sided, carrier modulated spectral peaks from the time integrating spectrum analyzer for a $140Hz$ AM signal input.

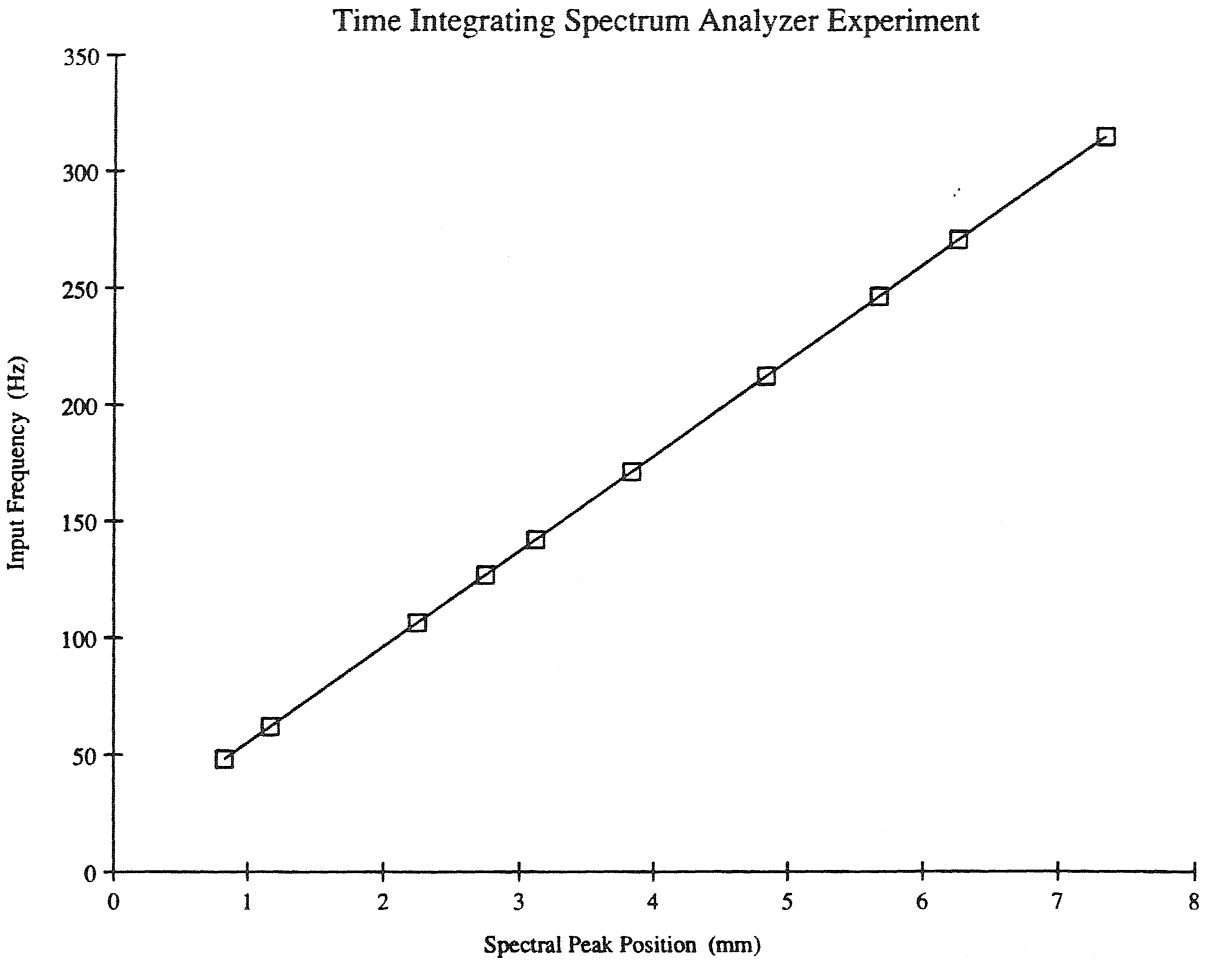

Fig.5.3.1.8 Plot of frequency linearity of the experimental spectrum analyzer.

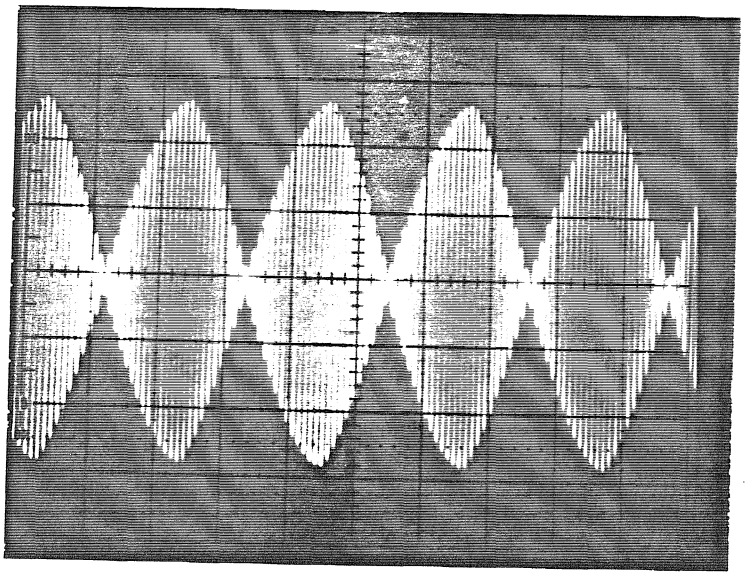

Fig.5.3.1.9 A typical AM signal input ($1.1MHz$ AM at $57MHz$ carrier) used for generating the autocorrelation from the optical processor.

processor video signal outputs are shown in Fig. 5.3.1.10. Again, notice that the desired autocorrelation envelope rides on a large bias level, thus using up much of the CCD dynamic range. The next section deals with the bias-free crystal based version of this optical processor.

5.3.2 Bias-free Crystal based 1-D TI Correlator/Spectrum Analyzer

(a) Architecture:

The basic signal processing chain in this bias-free architecture is similar to the one for the system described in Section 5.3.1. The key difference lies in the fact that the CCD sensor is replaced by a time integrating photorefractive crystal. The bias-free system architecture is shown in Fig. 5.3.2.1. The crystal chosen for this experiment is a 110 cut, $15 \times 15 \times 10$ mm bismuth silicon oxide (BSO) piece. BSO is chosen for the processor because of its relatively fast response time (10 msec to seconds, depending on the average incident light intensity I_0) compared to other available photorefractive materials.

The light from an argon ($514nm$) laser is collimated by an $F = 20cm$ spherical lens, and an $F = 30cm$ lens focusses the collimated light into a Bragg matched slit in a tellurium dioxide (TeO_2) AOD. The DC and +1 diffracted order light from the AOD are 1:1 imaged on to a second TeO_2 Bragg cell, using a pair of $F = 20cm$ spherical lenses. The DC order of the first Bragg cell is used to produce a +1 order from the second Bragg cell. The +1 orders from the two AOD's are imaged on to the crystal, with the DC light being blocked in the Fourier plane of the first imaging lens. Here, the imaging system consists of an $F = 35cm$ spherical lens, followed by an $F = 10cm$ cylindrical lens, thus providing a demagnification of $m = 3.5$ for imaging along the AOD column or x direction. The cylindrical lens is used to allow the full face (15×15mm) of the crystal to be exposed by plane waves, instead of exposing only a tiny slit region along the width (x direction) of the crystal. As

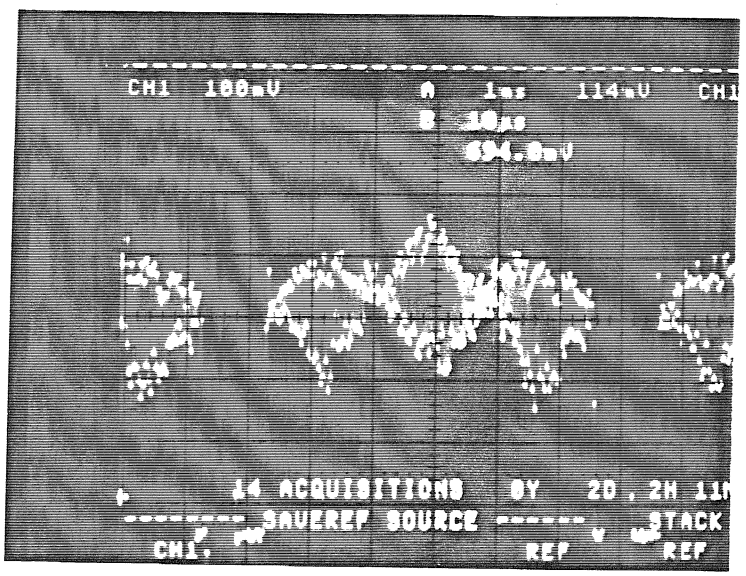

$1.0MHz$ AM

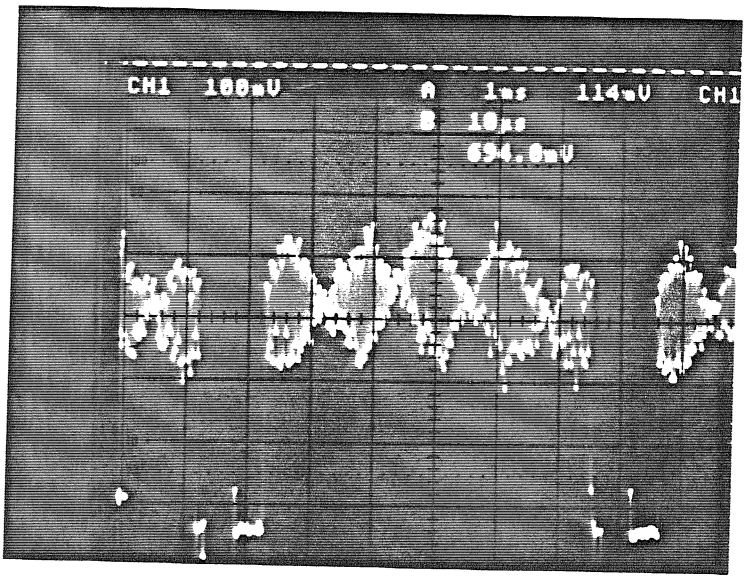

$1.35MHz$ AM

Fig.5.3.1.10 Carrier modulated AM signal autocorrelation outputs from the optical processor for different AM inputs on a $57MHz$ carrier.

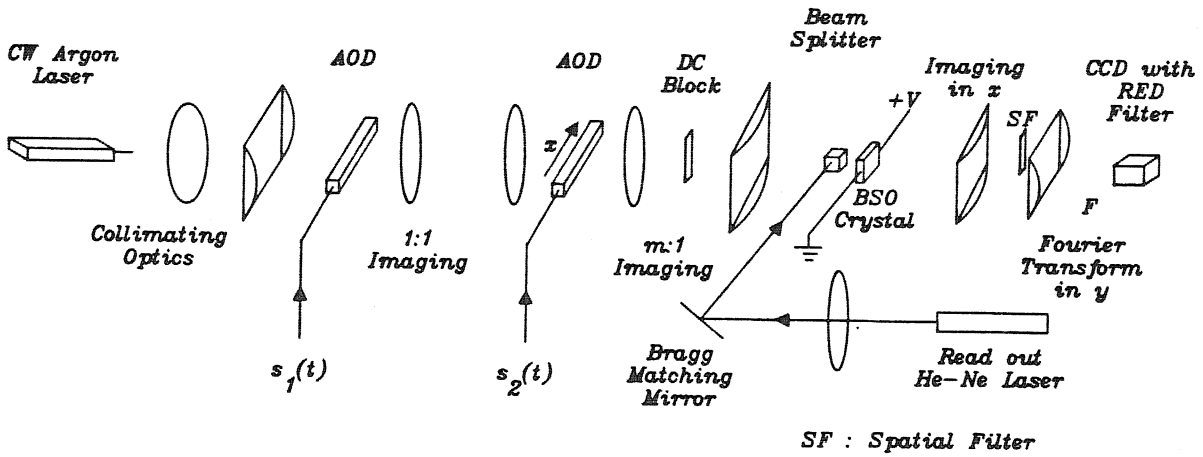

Fig.5.3.2.1 Bias free 1-D time integrating correlator/spectrum analyzer architecture using a photorefractive crystal.

BSO has a relatively low diffraction efficiency ($\leq 2\%$), it is a wise choice for the system designer to use as much of the crystal as possible, thus increasing the region over which the photorefractive effect is active, and therefore enabling a greater amount of read-out light to be diffracted from the crystal. The writing beams in this system constitute the green +1 orders from the two Bragg cells, that interfere in the crystal with an angular separation controlled by the carrier frequency f_0 of the AOD's. The spatial carrier is generated along the x direction, and the spatial carrier frequency is given by $u_0 = \frac{mf_0}{v_a}$. In our system, $f_0 = 60MHz$, giving a spatial carrier of approximately 340 lines/mm. The bias-free signal output is read out using an auxiliary He-Ne ($633nm$) beam that is carefully Bragg matched to the volume grating in the crystal. The $633nm$ light is used for the reading process, as BSO is less sensitive at this wavelength. The red light from the He-Ne laser is collimated by an $F = 20cm$ spherical lens, and reflected off a mirror on to the beam splitter face positioned along the path of the green light. The red light reflected from the cube beam splitter face is incident on the crystal front face, and the mirror is carefully rotated to provide Bragg matching for the incident red plane wave with the volume grating in the crystal. The red light that is diffracted from the crystal is imaged along the x direction on to a CCD, while focussing the light along the y direction. This is accomplished by a pair of crossed cylinders, where the first $F = 9cm$ cylinder 1:1 images along x, while the orthogonal $F = 7.5cm$ cylinder focusses in the y, thus giving a slit of light on the CCD surface. Thus, the light slit in the AOD column has been mapped to a slit on the CCD. Note that the DC red light from the crystal is blocked in the Fourier plane of the first cylinder, while the writing green beams are blocked using a red light filter. The experimental 1-D bias-free system built in the laboratory is shown in Fig. 5.3.2.2.

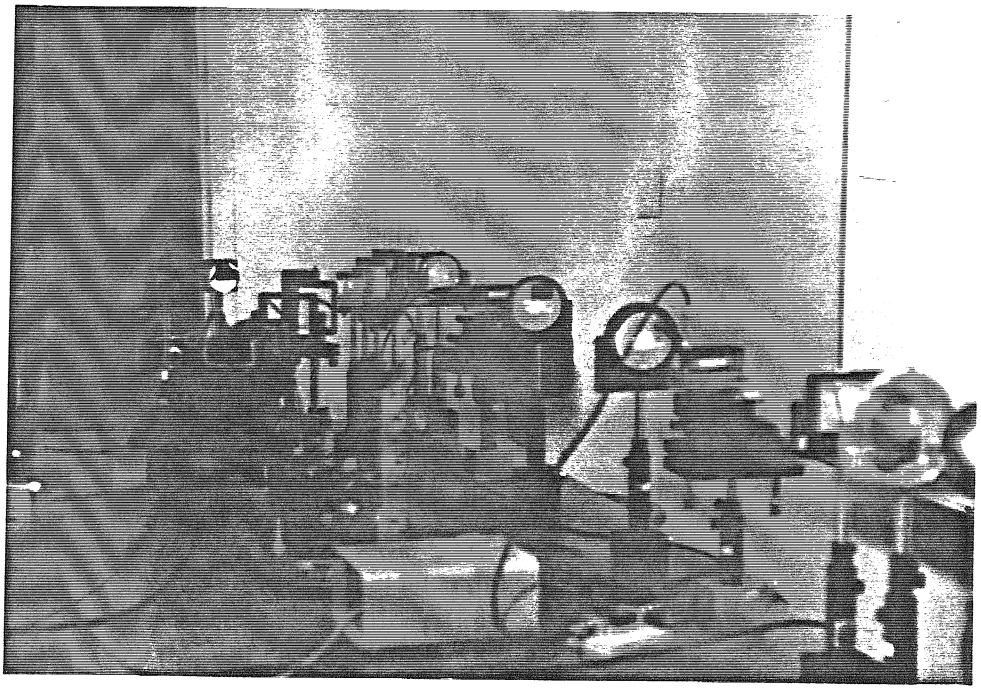

Fig.5.3.2.2 Laboratory system for the bias free 1-D correlator/spectrum analyzer architecture.

(b) Experimental Results and System Issues:

As expressed earlier in Eqn. 5.2.1, the temporally varying light intensity incident on the crystal is given by:

$$I(x,t) = I_0 + \mathrm{Re}[I_1(x,t)e^{jkx}] \qquad t \geq 0, \tag{5.3.2.1}$$

where $k = 2\pi u_0$, with the grating spatial frequency $u_0 = 2f_0 m/v_a$. For the autocorrelation of linear FM signals used in the spectrum processing, the signals driving the Bragg cells are $\tilde{s}_1(t) = \tilde{s}_2(t) = ae^{-j2\pi(f_0 t + 0.5bt^2)}$. Using the results shown earlier in Eqn. 5.3.1.4,

$$I_0 = 2|a|^2 \qquad I_1(x,t) = 2|a|^2 e^{-j2\pi\frac{2bmx}{v_a}t}, \tag{5.3.2.2}$$

giving a maximum modulation depth of 1 for the recorded grating on the crystal. Using these expressions in Eqn. 5.2.3, the intensity of the time integrated diffracted read out light from the photorefractive crystal is given by:

$$\begin{aligned} I_{out}(x,t) &\approx \left| \frac{K_1}{\tau} \int_t^{t+\tau'} \frac{2|a|^2 e^{-j2\pi\frac{2bmx}{v_a}t}}{I_0} dt' \right|^2 I_R \\ &= K\,\mathrm{sinc}^2\left(\frac{2\tau' mb}{v_a}x\right), \end{aligned} \tag{5.3.2.3}$$

where K is a constant that depends on the crystal material parameters, the crystal integration time, and experimental conditions. The expression in Eqn. 5.3.2.3 is a sinc squared function positioned at the central $x = 0$ position of the CCD. This is the expected result for the autocorrelation of linear FM signals. Note that the detected signal output is bias-free.

Fig. 5.3.2.3 shows the zero light output signal level from the processor, while Fig. 5.3.2.4 gives the bias-free signal output for the linear FM AOD drive signals. Comparing this bias-free processor output to the spatial carrier encoded output signal in Fig. 5.3.1.4, it is clear that the crystal based bias removal method provides a much larger use of the CCD dynamic range for the desired output signal. Note

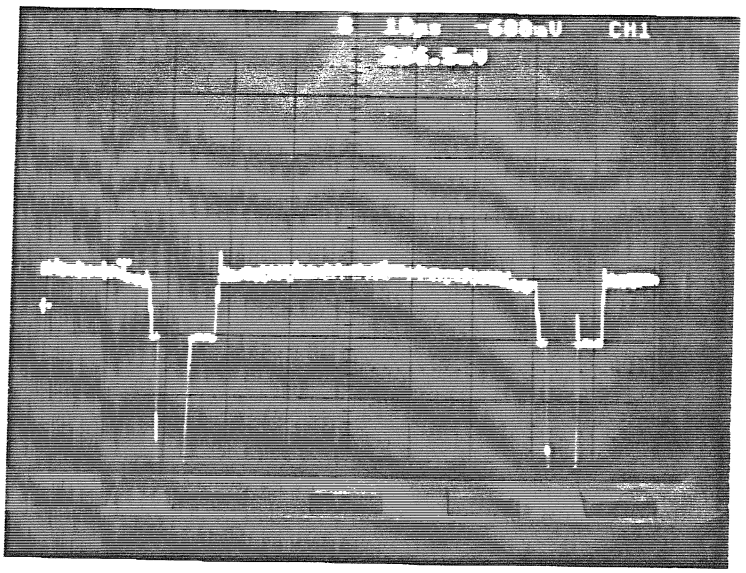

Fig.5.3.2.3 Zero light level CCD output from the optical processor.

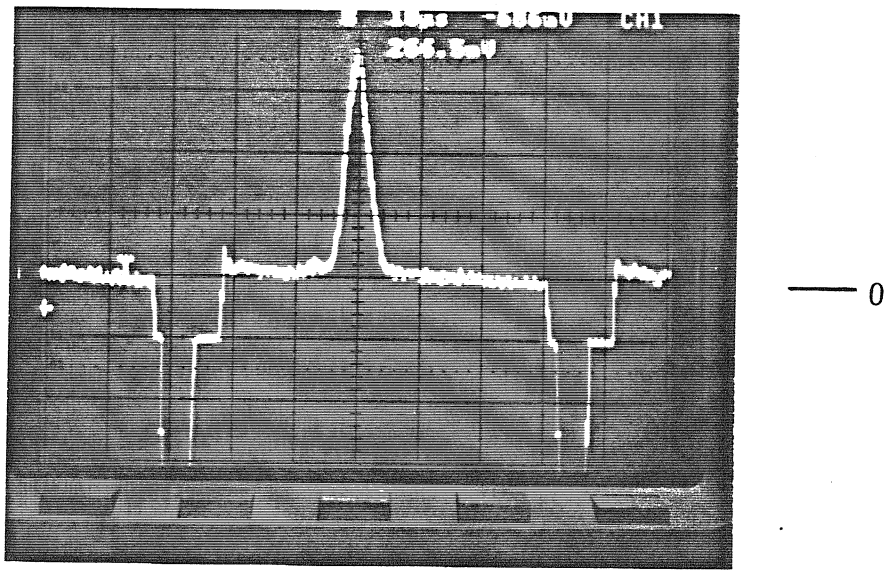

Fig.5.3.2.4 Bias free linear FM autocorrelation output from the optical processor using a $150KHz$ bandwidth, $60MHz$ center frequency, $12.8msec$ duration FM signal.

that in order to operate this bias-free processor as a spectrum analyzer, the test signal will have to be phase locked (coherent) with the linear FM signals to prevent erasure of the integrated charge on the crystal over successive processing frames.

Next, we look at the bias-free processor operating as a correlator of AM signals where $s_1(t) = s_2(t) = a\cos(2\pi f_1 t)\cos(2\pi f_0 t)$. In this case, we have:

$$I_0 = |a\cos[2\pi f_1(t - x/v_a)]|^2 + |a\cos[2\pi f_1(t + x/v_a)]|^2 \qquad (5.3.2.4a)$$

$$I_1(x,t) = 2|a|^2\cos[2\pi f_1(t - x/v_a)]\cos[2\pi f_1(t + x/v_a)]. \qquad (5.3.2.4b)$$

For the condition that $\frac{1}{\tau'} \ll f_1 \ll f_0$, the intensity of the diffracted read-out light from the crystal can be written as:

$$\begin{aligned} I_{out}(x,t) &\approx \left| \frac{K_1}{\tau}\int_t^{t+\tau'} \frac{2|a|^2\cos[2\pi f_1(t - x/v_a)]\cos[2\pi f_1(t + x/v_a)]}{I_0}dt' \right|^2 I_R \\ &\approx K'\,|\cos[2\pi(\frac{2f_1}{v_a})x]|^2, \end{aligned} \qquad (5.3.2.5)$$

where K' is a constant that depends on the crystal material parameters, the crystal integration time, and experimental conditions. The processor output signal in Eqn. 5.3.2.5 corresponds to a sinusoidal spatial variation on the CCD with a spatial period equal to $v_a/4f_1$.

Fig. 5.3.2.5 shows the bias-free AM signal correlation outputs for different values of the AM signal frequency f_1. As is expected, the number of spatial cycles detected by the CCD goes up for increasing values of f_1. Again, comparing these results to the carrier encoded output signals on a large bias level (see Fig. 5.3.1.10), one sees that the crystal based processor allows a greater utilization of the CCD dynamic range for the desired bias-free output signals. The bell shaped apodization across the bias-free signal outputs is mainly due to the non-uniform profile of the red read-out beam. In these experiments, the light intensity diffracted from the two Bragg cells was equalized to ensure a high modulation depth grating in the crystal.

AM inputs

Bias free outputs

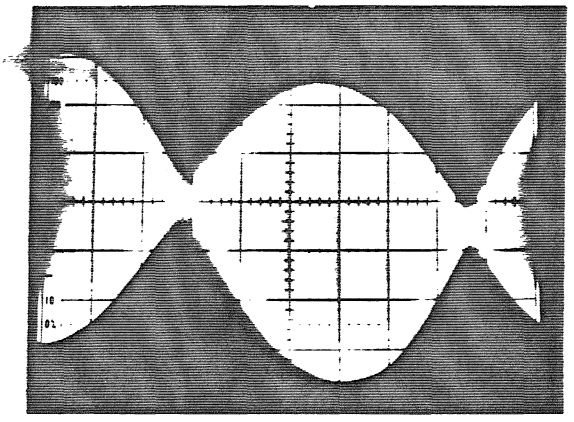

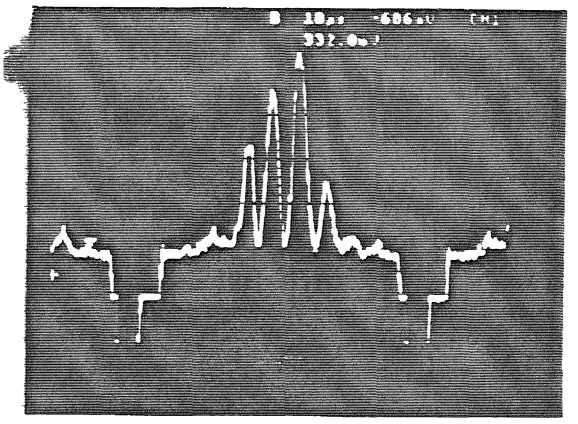

$44KHz$ AM

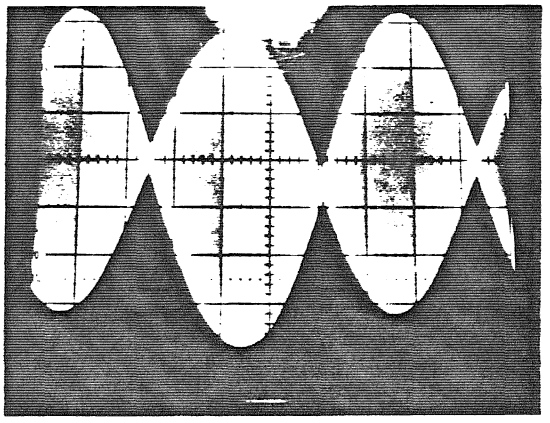

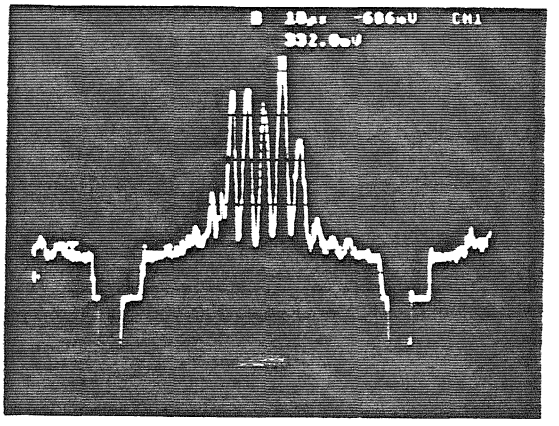

$73.5KHz$ AM

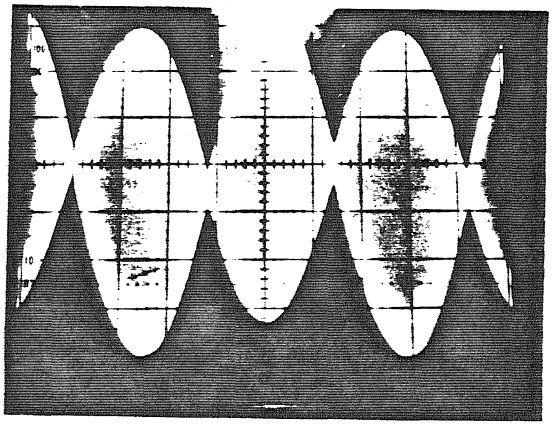

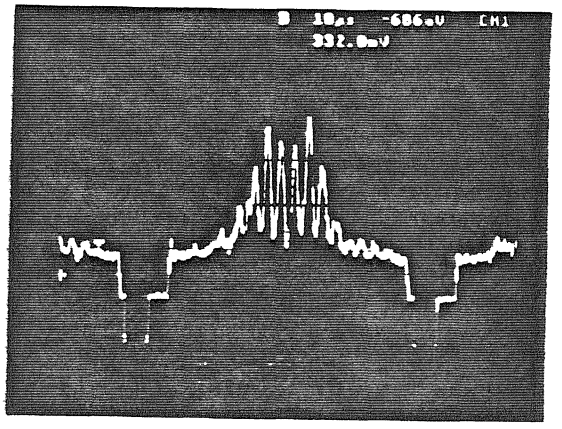

$100KHz$ AM

Fig.5.3.2.5 Bias free AM signal autocorrelation outputs from the optical processor using different AM signals on a $60MHz$ carrier.

This provides a higher recording signal dynamic range for the crystal, in addition to a higher overall diffraction efficiency [10]. Typical average light level used for the writing beams corresponded to around $19mW/cm^2$ from a $250mW$ Ar^+ laser beam. The typical crystal integration time was estimated to be around $10msec$, with a 6 kV DC applied electric field. A $10mW$ He-Ne provided a $500\mu W/cm^2$ read out beam.

Next, we describe how we can extend this 1-D bias removal technique to a 2-D bias-free time and space integrating architecture.

5.3.3 The 1-D Interferometric Space Integrating Spectrum Analyzer

(a) The Distributed Local Oscillator:

As explained earlier in Chapter 3, Section 3.3, the distributed local oscillator is a broadband reference signal that is used for heterodyning high frequency signals to baseband for fine frequency processing in 2-D folded spectrum systems. The DLO can be generated by applying a periodic high bandwidth chirp signal to the reference AOD in an interferometric space integrating spectrum analyzer, such as the architecture shown in Fig. 5.3.3.1. This system was built in the laboratory, and the signal chain is described as follows. The light from an He-Ne laser is collimated by an $F = 20cm$ spherical lens, and then focussed along the y direction by an $F = 15cm$ cylindrical lens. The Bragg matched slit of light in the TeO_2 AOD produces the DC and +1 order diffracted light signals that are spatially Fourier transformed by the $F = 30cm$ spherical lens. The DC light is blocked by a spatial filter, allowing only the +1 order light to be detected by the 2-D CCD sensor. The electronic AOD drive signals for this processor are generated by two separate signal generators that are phased locked to a stable $10MHz$ oscillator. The input test signal for the spectrum analyzer is generated from a frequency synthesizer, whose frequency is varied around $60MHz$, the chosen AOD carrier frequency. The repet-

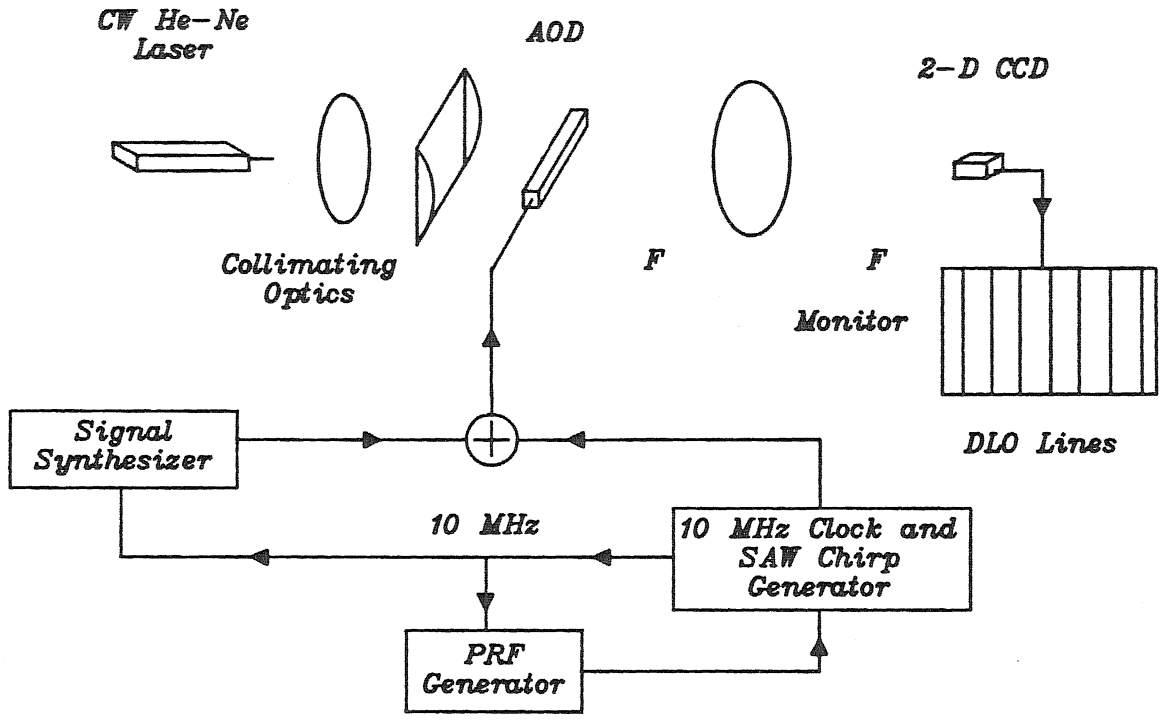

Fig.5.3.3.1 Interferometric 1-D space integrating spectrum analyzer.

itive broadband chirp signal is generated by applying a periodic impulse train to a surface acoustic wave (SAW) device. This periodic impulse train (comb function) is generated from the system $10MHz$ oscillator. The output of the SAW device is a $50-70MHz$, $60MHz$ centered, $6\mu sec$ duration, linear FM signal, that has a period equal to the impulse train period. The test and reference chirp signals are electronically added in a microwave adder circuit, and the output signal is used to drive the AOD. The repetitive chirp signal can be expressed as:

$$\begin{aligned} r(t) &= \text{rect}(\frac{t}{T_1})\cos[2\pi(f_0 t + 0.5bt^2)] * \sum_{n=0}^{N-1}\delta(t-nT) \\ &= \text{rect}(\frac{t}{T_1})\cos[2\pi(f_0 t + 0.5bt^2)] * \left[\text{comb}(t/T)\text{rect}(\frac{t}{NT}-\frac{1}{2})\right], \end{aligned} \tag{5.3.3.1}$$

where $*$ is the convolution symbol. Using the chirp analysis in Chapter 3, Section 3.4, we can approximately express the field distribution in the Fourier plane of the chirp signal driven AOD to be:

$$\begin{aligned} E_r(u,y,t) \approx A\,\text{rect}(y/Y)\Big[&\text{rect}(\frac{uv_a - f_0}{B})e^{-j\pi(uv_a-f_0)^2/b} \\ &[T\text{comb}(uv_aT) * NT\text{sinc}(NTuv_a)e^{-j\pi NTuv_a}]e^{-j2\pi uv_a t}\Big] * B(uv_a). \end{aligned} \tag{5.3.3.2}$$

The expression in Eqn. 5.3.3.2 is a spatially sampled DLO with a quadratic phase curvature that is due to the focussing of the diffracted wave front. Each impulse of the comb function spatially selects a spatial position $u = n/v_aT$, along with its linearly proportional temporal oscillator term $e^{-j2\pi\frac{n}{T}t}$. These discrete spatial positions of length Y are further blurred by the convolution with $B(uv_a)$, the term that accounts for the finite aperture of the AOD. In essence, the CCD shows an array of equally spaced lines, each line oscillating with its discrete temporal frequency. The separation between the lines is $\lambda F/v_aT$, while the lines spread over the chirp bandwidth B, centered at the AOD center frequency f_0.

(b) The Heterodyning Experiment:

The DLO was generated using different values of the repetition period T. Fig. 5.3.3.2 shows the CCD output with the DLO lines for a chirp repetition rate of 500 KHz. The DLO lines range from $71 - 55MHz$, with a 500 KHz separation. The apodization over the chirp spectrum is mainly due to the non-uniform frequency response of the AOD amplifier used in the system.

Note that the discrete temporal oscillation of each DLO line becomes the reference for heterodyning the high frequency test signals to baseband. The optical interference between the +1 diffracted order test signal and its temporally matching +1 diffracted order DLO line results in the baseband conversion. For a test signal $s(t) = 2a\cos(2\pi f't)$, the intensity detected at the CCD in Fig. 5.3.3.1 is approximated as:

$$\begin{aligned} I(u,y,t) &= \left|a\,e^{-j\phi}e^{-j2\pi f't}B(uv_a - f')\mathrm{rect}(y/Y) + E_r(u,y,t)\right|^2 \\ &= |a\,B(uv_a - f')|^2\mathrm{rect}(y/Y) + |E_r(u,y,t)|^2 \\ &+ 2B(uv_a - f')\,B(uv_a - \frac{n}{T})\cos[2\pi(f' - \frac{n}{T})t + \phi']\mathrm{rect}(y/Y), \end{aligned} \tag{5.3.3.3}$$

where $|f' - \frac{n}{T}| \leq 1/2T$, implying that the signal frequency blur spot lies within the temporally nearest DLO line. Here ϕ and ϕ' are phase terms. Note that the last term contains a temporal term that oscillates at the difference frequency $f' - \frac{n}{T}$, which is a baseband frequency term suitable for further spectrum processing with a 1- D time integrating processor implemented on this DLO line. Fig. 5.3.3.3 shows the baseband $1Hz$ temporal oscillation when $f' = 64MHz + 1Hz$ and $\frac{n}{T} = 64MHz$. Here, the $64MHz + 1Hz$ signal frequency interferes with the $64MHz$ DLO line, producing a temporally blinking line positioned at the $u = f'/v_a$ signal coarse frequency position.

In the next section, we will investigate how the DLO heterodyning principle can be combined with a 1- D time integrating spectrum processor and photorefractive

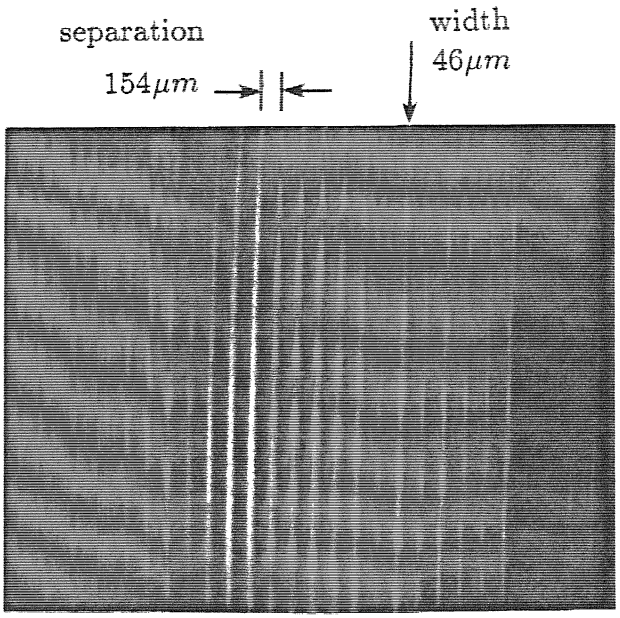

TV Monitor output

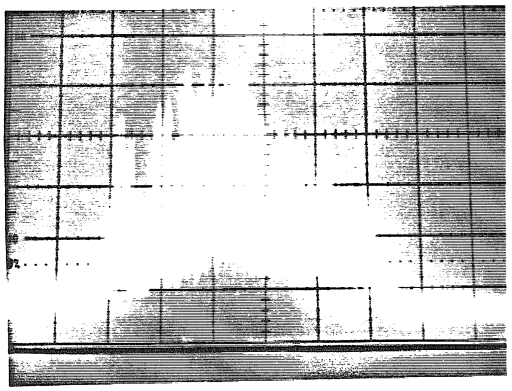

Video signal output

Fig.5.3.3.2 CCD outputs showing the different DLO lines for a $500KHz$ repetition rate reference chirp signal.

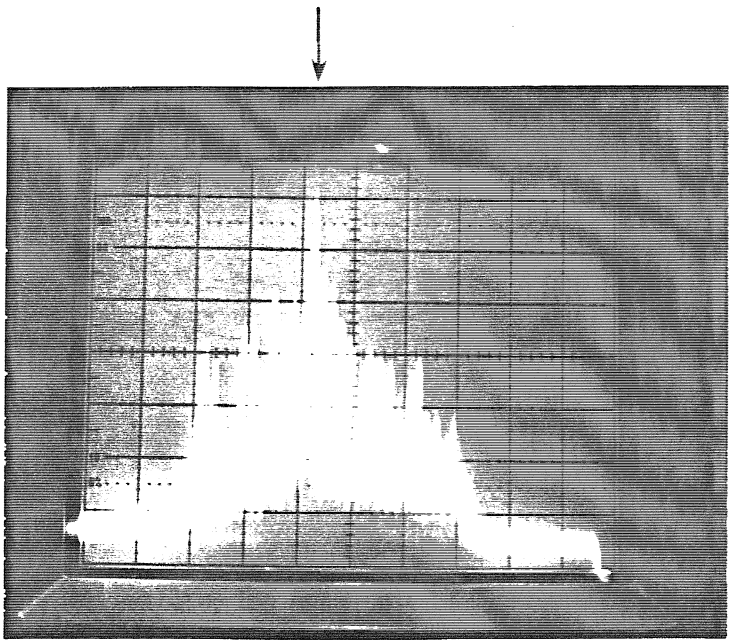

Positive interference

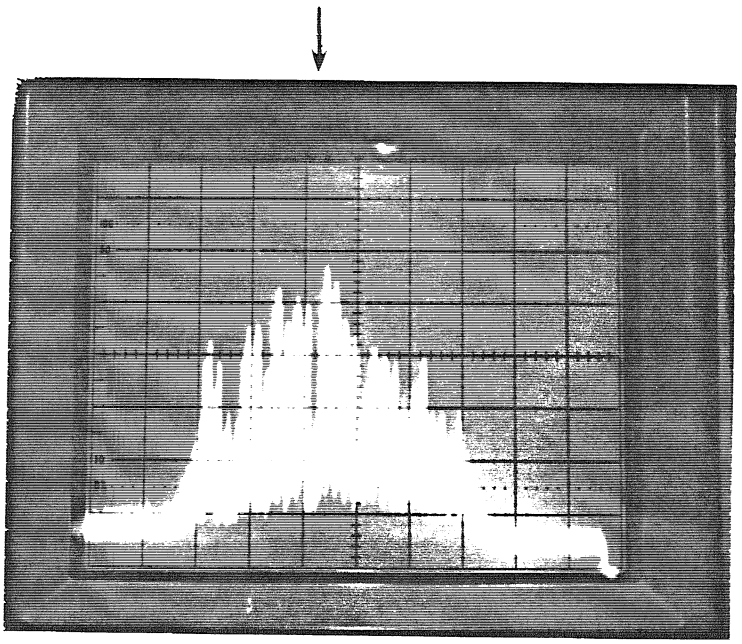

Negative interference

Fig.5.3.3.3 Baseband $1Hz$ temporal oscillation from optical interference between a $64MHz + 1Hz$ input signal and a $64MHz$ reference DLO line.

crystal to provide a 2-D bias-free signal output format.

5.3.4 Bias-free Crystal based 2-D Time and Space Integrating Architecture

(a) Architecture:

The bias-free continuous wave time and space integrating (TSI) architecture investigated in this section is based on Bader's TSI 2-D spectrum analyzer [13]. This processor uses the DLO for heterodyning coarse frequency signals to baseband, instead of the pulsed source used in the 2-D architectures discussed in Chapter 3 in this thesis. The 2-D bias-free architecture shown in Fig. 5.3.4.1 is based on the Mach-Zehnder interferometer, and contains a pair of orthogonally oriented Bragg cells in its two independent arms. The optical design for the two arms is similar in order to minimize optical path differences in the interferometer. Each arm is multiplicative, as the +1 order light from the first Bragg cell is used to produce a +1 diffracted order from the second Bragg cell, while the DC light from both cells is blocked. AOD's 1 and 2 are driven by slow chirp rate linear FM signals $c(t)$ that are imaged on to the CCD2 (I_1') and spatial filter $SF1$ (I_1) planes. AOD's 3 and 5 are fed by the input test signal $s(t)$, while AOD4 is driven by the high bandwidth repetitive chirp reference signal $r(t)$. The spherical lens S_3 in the two respective arms of the interferometer produces the signal (AOD3) and reference (AOD4) waveform spatial Fourier transforms at planes I_1 and I_1' respectively.

The optical field incident at the CCD2 plane I_1' (or the spatial filter $SF1$ plane I_1) is given by:

$$E(x,y,t) = \tilde{c}(t - \frac{x - X/2}{m_x v_a})\text{rect}(x/m_x X) FT_y[\tilde{s}(t - \frac{y - Y/2}{v_a})\text{rect}(y/Y)] + \tilde{c}(t + \frac{x - X/2}{m_x v_a})\text{rect}(x/m_x X) FT_y[\tilde{r}(t - \frac{y - Y/2}{v_a})\text{rect}(y/Y)], \quad (5.3.4.1)$$

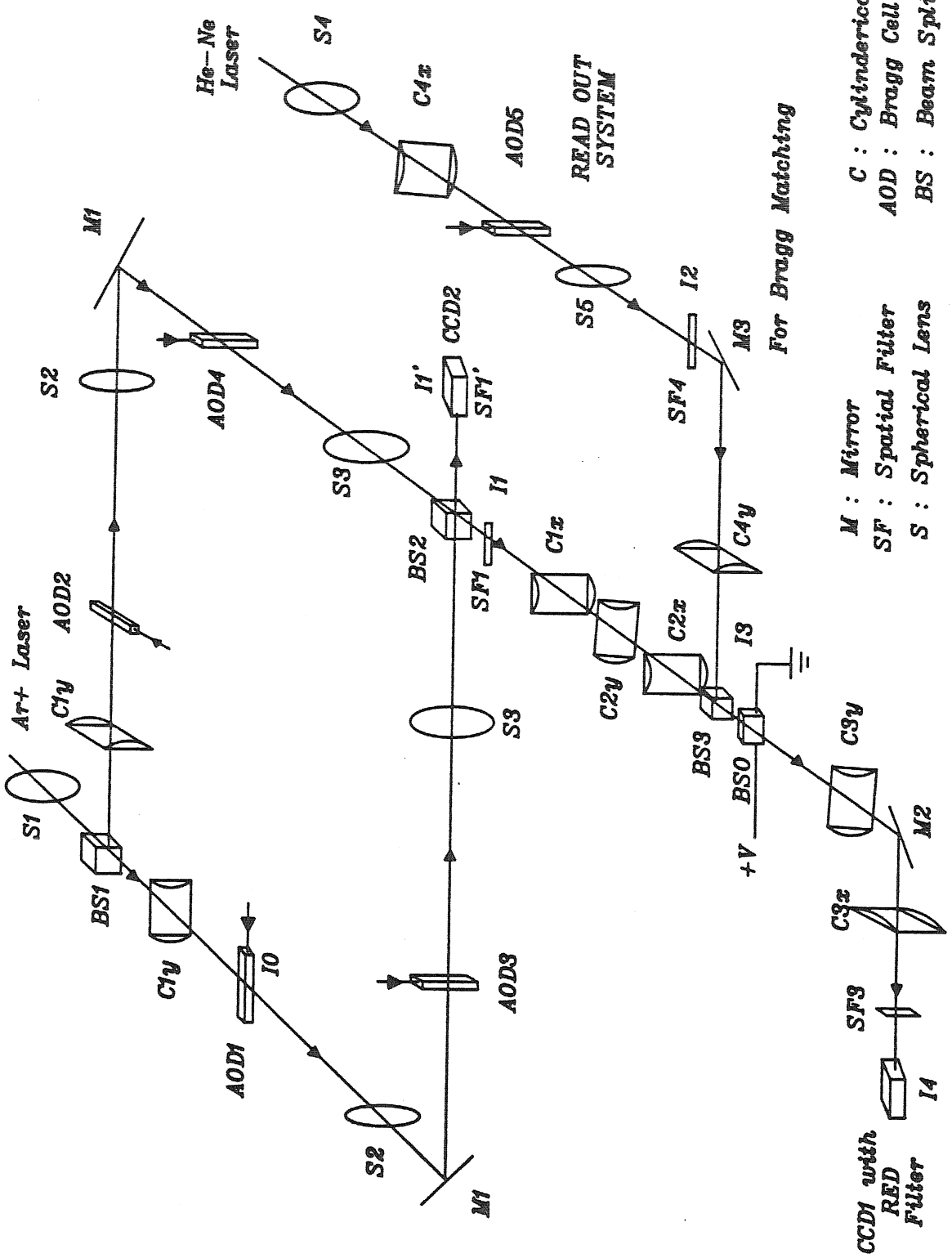

Fig.5.3.4.1 Bias free 2-D time and space integrating acousto-optic architecture for folded spectrum analysis.

where FT_y stands for the lens S_3 spatial Fourier transform along the y direction, and m_x is the imaging system magnification along x direction. The light intensity at I_1 or (I_1') plane can be expressed as:

$$I(x,y,t) \approx \Bigg\{ \Big| FT_y[\tilde{s}(t - \frac{y - Y/2}{v_a})\mathrm{rect}(y/Y)] \Big|^2 + \Big| FT_y[\tilde{r}(t - \frac{y - Y/2}{v_a})\mathrm{rect}(y/Y)] \Big|^2 \Bigg\} \mathrm{rect}(x/m_x X) + 2\mathrm{Re}\Bigg\{ \tilde{c}(t + \frac{x - X/2}{m_x v_a}) \tilde{c}^*(t - \frac{x - X/2}{m_x v_a}) \mathrm{rect}(x/m_x X) \cdot FT_y^*[\tilde{s}(t - \frac{y - Y/2}{v_a})\mathrm{rect}(y/Y)] FT_y[\tilde{r}(t - \frac{y - Y/2}{v_a})\mathrm{rect}(y/Y)] \Bigg\}. \tag{5.3.4.2}$$

The first two terms in Eqn. 5.3.4.2 are constant bias terms that are due to the signal and reference chirp spectra, respectively. For a single tone signal $s(t) = 2a\cos(2\pi f' t)$, and $r(t)$ as defined in Eqn. 5.3.3.1, we can write the expression for the bias terms as:

$$\text{Bias} \approx \Bigg\{ \Big| aB(vv_a - f') \Big|^2 + \sum_{n=n_0}^{n_0+N} \Big| a_n B(vv_a - \frac{n}{T}) \Big|^2 \Bigg\} \mathrm{rect}(x/m_x X), \tag{5.3.4.3}$$

where N/T is equal to the bandwidth of the reference chirp. This expression for the bias consists of the signal coarse frequency line, plus the reference DLO lines positioned at the output coordinate $v = n/v_a T$, where $v = y'/\lambda F_3$. The third term in Eqn. 5.3.4.2 gives the desired interferometric 2-D folded spectrum term. Substituting the value for the slow FM signal $c(t)$, the CCD2 time integrated charge pattern for this folded spectrum term can be written as:

$$Q(x,v) \approx 2aa_M B(vv_a - f') B(vv_a - \frac{n}{T}) \mathrm{Re}\Bigg\{ \int_{T_d} e^{j2\pi(f' - \frac{M}{T})t} e^{-j2\pi \frac{2bx}{m_x v_a} t} \, dt \Bigg\} \mathrm{rect}(x/m_x X), \tag{5.3.4.4}$$

where the spatial carrier along the x direction generated by the slow scanning chirps has been removed by rotation of the beam splitter $BS2$. The input signal frequency

f' can be broken up into its coarse f_c and fine δ_f frequency components, that is,

$$f' = f_c + \delta_f = \frac{M}{T} + \delta_f, \tag{5.3.4.5}$$

where M is a constant corresponding to the DLO line that overlaps the signal line. The folded spectrum can be further written as:

$$\begin{aligned} Q(x,v) \approx & 2aa_M B^2(vv_a - f_c)\mathrm{Re}\left\{\int_{T_d} e^{j2\pi\delta_f t} e^{-j2\pi\frac{2bx}{m_x v_a}t}\, dt\right\}\mathrm{rect}(x/m_x X) \\ & = A_1 B^2(vv_a - f_c)\mathrm{sinc}[T_d(\delta_f - \frac{2b}{m_x v_a}x)], \end{aligned} \tag{5.3.4.6}$$

where A_1 is a constant. The expression in Eqn. 5.3.4.6 represents a spectral peak located at the coordinates $x = \frac{m_x v_a}{2b}\delta_f$, $v = \frac{f_c}{v_a}$, that are proportional to the signal coarse and fine frequency components, respectively. Thus, the Mach-Zehnder processor output is given by:

$$Q'(x,v) = \text{Bias} \quad + \quad A_1 B^2(vv_a - f_c)\mathrm{sinc}[T_d(\delta_f - \frac{2b}{m_x v_a}x)]. \tag{5.3.4.7}$$

One approach to obtaining a bias-free 2-D folded spectrum output is to generate a spatial carrier along the fine frequency processing x direction by combining the two beams from the interferometer at an appropriate angle. The spatial carrier on this signal plus reference ridge can be controlled by rotating the beam splitter $BS2$. In principle, a photorefractive crystal can be placed at the Fourier plane (I_1) of lens S_3, where the signal spectral lines would interfere with one or more of the spatially separate DLO lines, generating a light pattern on a spatial carrier along the x (line) direction. The crystal would time integrate the charge pattern to accomplish the fine frequency processing, generating a carrier modulated blur spot along the coarse frequency line, whose position is proportional to the signal fine frequency. This blur spot can then be read out by an external cylindrical wave that focusses on the appropriate signal line.

The main problem with this approach is that the interference pattern recorded on the crystal consists of a very thin ($\leq 200\mu m$) slit of light, resulting in a very

small region where the photorefractive effect is active, and therefore where a hologram is recorded. In particular, from a practical point of view, when using a low diffraction efficiency crystal like BSO, this approach of placing the crystal in the Fourier plane of lens S_3 will result in a negligible amount of diffracted read out light from the crystal, thus making it almost impossible to detect any light. Therefore, because of the current material limits of fast response photorefractive materials, an alternate quasi-real time approach for recording the signal plus reference hologram is considered.

In this approach, the DLO lines in the Fourier plane I_1 are expanded along the y direction by a cylindrical lens C_{2y}, thus producing plane waves of different angular displacement illuminating the full face of the crystal. The DLO lines preserve imaging along the x direction from plane I_1 to the crystal plane using two cylindrical lenses C_{1x} and C_{2x}. The electric field on the crystal for a single tone signal can be approximately expressed as:

$$E(x,y,t) \approx \Big\{ \tilde{c}(t - \frac{x - X/2}{m_x v_a})\Big[\sum_{n=n_0}^{n_0+N} a_n e^{-j2\pi v_n y} e^{-j2\pi \frac{n}{T} t}\Big] + \tilde{c}(t + \frac{x - X/2}{m_x v_a}) e^{-j2\pi \frac{\sin\theta}{\lambda} x} \Big[a e^{-j2\pi v_{f'} y} e^{-j2\pi f' t}\Big] \Big\} \mathrm{rect}(x/X_c)\mathrm{rect}(y/Y_c), \tag{5.3.4.8}$$

where $\frac{\sin\theta}{\lambda}$ is a spatial frequency introduced by the rotation of the beam splitter $BS2$. The summation term in Eqn. 5.3.4.8 represents the reference DLO plane waves on their respective spatial and temporal carriers, while the second term in the equation contains the signal plane wave on its spatial and temporal carriers, respectively. Here, X_c and Y_c are the respective width and height of the illuminated

crystal face. The intensity on the crystal is proportional to:

$$I(x,y,t) \propto \Bigg[\Big| \sum_{n=n_0}^{n_0+N} a_n e^{-j2\pi v_n y} e^{-j2\pi \frac{n}{T} t} \Big|^2 \quad + \quad |a|^2 + 2\mathrm{Re}\Bigg\{ \tilde{c}(t - \frac{x - X/2}{m_x v_a}) \tilde{c}^*(t + \frac{x - X/2}{m_x v_a}) e^{j2\pi \frac{\sin\theta}{\lambda} x} [a e^{-j2\pi v_{f'} y} e^{-j2\pi f' t}][\sum_{n=n_0}^{n_0+N} a_n e^{-j2\pi v_n y} e^{-j2\pi \frac{n}{T} t}] \Bigg\} \Bigg] \mathrm{rect}(x/X_c)\mathrm{rect}(y/Y_c). \tag{5.3.4.9}$$

If the reference chirp repetitive period T is much less than the crystal integration time τ', that is, $T \ll \tau'$, we can approximate the first term in Eqn. 5.3.4.9 to be a constant bias contribution. The second term $|a|^2$ is the signal constant bias term. Hence, we can write the bias term I_0 in Eqn. 5.2.1, Section 5.2, as:

$$I_0 \approx \sum_{n=n_0}^{n_0+N} |a_n|^2 \quad + \quad |a|^2. \tag{5.3.4.10}$$

Furthermore, for $T \ll \tau'$, we can approximate the third term in Eqn. 5.3.4.9 such that over the integration time of the crystal, the cross terms between the signal and reference waves average out to zero, leaving only an interference pattern for the temporally and spatially matching signal and DLO waves corresponding to $n = M$. Therefore, the intensity is proportional to:

$$I(x,y,t) \propto \Bigg[I_0 \quad + \quad 2\mathrm{Re}\Bigg\{ \tilde{c}(t - \frac{x - X/2}{m_x v_a}) \tilde{c}^*(t + \frac{x - X/2}{m_x v_a}) e^{j2\pi \frac{\sin\theta}{\lambda} x} a a_M e^{j2\pi(v_{f'} - v_M) y} e^{-j2\pi(f' - \frac{M}{T}) t} \Bigg\} \Bigg] \mathrm{rect}(x/X_c)\mathrm{rect}(y/Y_c). \tag{5.3.4.11}$$

Here, $|v_{f'} - v_M|$ is a very slow spatial variation across the crystal y direction causing negligible diffraction, allowing us to write the intensity on the crystal as:

$$I(x,y,t) \propto \Bigg[I_0 \quad + \quad 2\mathrm{Re}\Bigg\{ \tilde{c}(t - \frac{x - X/2}{m_x v_a}) \tilde{c}^*(t + \frac{x - X/2}{m_x v_a}) e^{j2\pi \frac{\sin\theta}{\lambda} x} a a_M e^{-j2\pi \delta_f t} \Bigg\} \Bigg] \mathrm{rect}(x/X_c)\mathrm{rect}(y/Y_c). \tag{5.3.4.12}$$

Substituting the expression of the slow scanning chirp signal $\tilde{c}$, we can write:

$$I(x,y,t) \propto \left[I_0 + 2\mathrm{Re}\left\{ a a_M e^{-j2\pi\delta_f t} e^{-j2\pi\frac{2bx}{m_x v_a}t} e^{j2\pi u_0 x} \right\} \right] \mathrm{rect}(x/X_c)\mathrm{rect}(y/Y_c), \tag{5.3.4.13}$$

where u_0 is the spatial carrier generated along the x direction of the crystal by the rotation of the beam splitter $BS2$, and the AOD center frequency f_0 relative Bragg deflection of the two independent interferometer beams. Looking at Eqn. 5.2.1 that represents the desired intensity pattern on a photorefractive crystal for bias removal, we have:

$$I_1(x,t) = 2a a_M e^{-j2\pi\delta_f t} e^{-j2\pi\frac{2bx}{m_x v_a}t}, \tag{5.3.4.14}$$

and the diffracted read-out light intensity from the crystal can be written as:

$$I_{out}(x,t) \approx \left| \frac{K_1}{\tau} \int_t^{t+\tau'} \frac{2a a_M e^{-j2\pi\delta_f t} e^{-j2\pi\frac{2bx}{m_x v_a}t}}{I_0} dt' \right|^2 I_R. \tag{5.3.4.15}$$

Note that this expression will give us only the fine frequency component of the input signal. In order to retain the coarse frequency information in the processor output signal, we need to introduce a special read-out procedure using the input signal. This read-out architecture is shown in Fig. 5.3.4.1, where a fifth AOD5 oriented along the y direction is introduced in the He-Ne read out optical system. This AOD5 generates a signal dependent plane wave whose spatial frequency along the y direction is proportional to the signal coarse frequency, and is equal to f'/v_a. This tilted (in y) plane wave illuminates the full face of the crystal, with Bragg matching along the x direction due to the carrier u_0. Note that as the signal frequency is changed, the read out beam stays Bragg matched as the wave tilts only in the y direction, and not along the x direction that is required for Bragg angle matching (See Fig. 5.3.4.2). As such, AOD5 is used to track the correct coarse frequency ridge due to the input test signal $s(t)$. The light diffracted from the crystal is imaged along the x direction on to the 2-D CCD1, while being Fourier

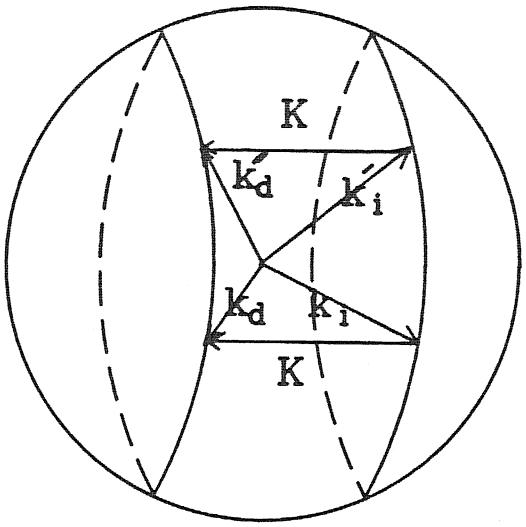

K : Grating Vector

k_i : Incident Vector

k_d : Diffracted Vector

$$k_d - k_i = K$$
$$\parallel$$
$$k'_d - k'_i = K$$

Fig.5.3.4.2 Crystal grating degeneracy behavior shown using the momentum space diagram. Here, the vector pairs k_i, k_d and k'_i, k'_d are both Bragg matched to the same grating vector K.

transformed along the y direction. The resulting diffracted light intensity on the crystal can be written as:

$$I_{out}(x,t) \approx \left| \frac{K_1}{\tau} \int_t^{t+\tau'} \frac{2aa_M e^{-j2\pi\delta_f t} e^{-j2\pi \frac{2bx}{m_x v_a} t}}{I_0} dt' \right|^2 \left| FT_y[\tilde{s}(t - \frac{y - Y/2}{m_y v_a}) \mathrm{rect}(y/Y_c)] \right|^2. \quad (5.3.4.16)$$

For the single tone input $s(t)$ used in the analysis, the expression for the intensity is approximated as:

$$I_{out}(x,t) \approx A_1' B^2(v - \frac{f_c}{m_y v_a}) \mathrm{sinc}^2[\tau'(\delta_f - \frac{2b}{m_x v_a} x)], \quad (5.3.4.17)$$

where this expression represents the single tone 2-D bias free folded spectrum output. Here, A_1' is a constant that is proportional to the modulation depth of the recorded signal plus reference grating, along with other factors such as crystal integration time and experimental conditions. Note the similarity between the bias free intensity output in Eqn. 5.3.4.17, and the expression in Eqn. 5.3.4.7 from the basic Mach-Zehnder processor without bias removal. Thus, this crystal based 2-D bias free processor design provides a single tone folded spectrum output.

(b) Experimental Results and System Limitations:

The basic bias-free system architecture shown in Fig. 5.3.4.1 was setup in the laboratory. Fig. 5.3.4.3 shows the optical system. The light from an argon ion laser is collimated by a $F = 20cm$ spherical lens S_1. This collimated light is split 50:50 by a cube beam splitter $BS1$. As the light progresses through similar paths in the two arms of the interferometer, we shall describe propagation through one arm. The collimated light from the beam splitter is focussed along the y direction by a $F = 15cm$ cylindrical lens C_{1y}. This focussed slit of light lies in the acoustic column of AOD1, generating the DC and +1 order diffracted beams. The $F = 20cm$ spherical lens S_2 acts as a Fourier transforming lens, focussing the DC and +1

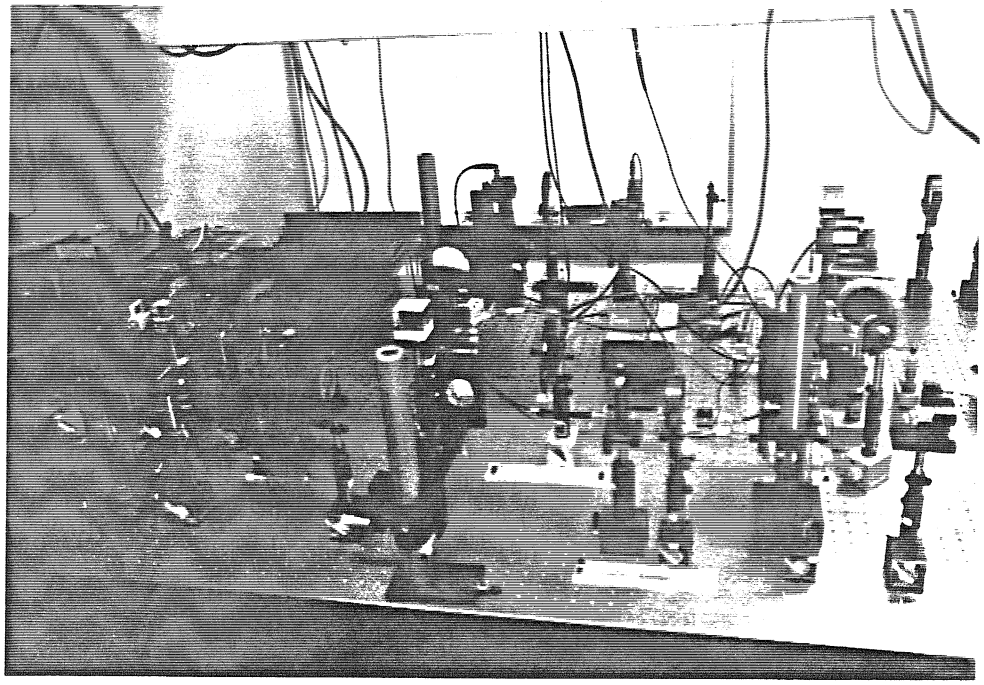

Fig.5.3.4.3 Laboratory system of the 2-D bias free crystal based architecture.

order beams as slits of light, with the DC slit being blocked by the casing of AOD3. This AOD3 also generates a DC and +1 order beam, where this +1 order is a doubly diffracted beam from the two AOD's. The $F = 38cm$ spherical lens S_3 acts as a Fourier transforming lens for the signal in AOD3, producing the signal spatial Fourier transform along the y direction in the back Fourier plane I_1. The combination of spheres S_2 and S_3 forms an imaging system from the AOD1 plane to I_1, thus imaging the acoustic signal along the x direction in AOD1 on to the I_1 plane. The light from the other (reference) arm of the interferometer follows a similar path. The cube beam combiner/splitter $BS2$ causes the two beams to interfere at planes I_1 and I_1'. A 2-D CCD2 is placed at the plane I_1' to pick up the 2-D folded spectrum output that includes a bias level. Spatial filter $SF1'$ blocks the DC light from AOD3 and AOD4 respectively. Fig. 5.3.4.4 shows the time integrated interference pattern between a $60MHz$ signal fed to AOD3, and the reference DLO lines generated using a chirp repetition rate $1/T = 1MHz$, and chirp bandwidth $B = 50 - 70MHz$, where the chirp signal is fed to AOD4. Here, AOD1 and AOD2 are fed by $60MHz$ carrier signals. The rotation of the beam splitter $BS2$ controls the angle between the two interfering beams, and thus controls the spatial carrier frequency along the x direction of the signal plus reference interference pattern. Fig. 5.3.4.5 shows different spatial carriers along the x direction for $60MHz$ signal and reference DLO inputs, respectively. These light patterns were detected at plane I_1' by CCD2. Plane I_1 is mapped on to the BSO photorefractive plane I_3. The $F = 15cm$ cylindrical lens C_{2y} acts as an inverse Fourier transforming lens along the y direction, converting the DLO lines in plane I_1 to plane waves of different angular frequency incident at the crystal. The pair of $F = 7.5cm$ cylinders C_{1x} and C_{2x} acts as an imaging system along the x direction from plane I_1 to I_3. Note that for a small angular separation between the two beams from the interferometer, the cylinders are no longer required for imaging in this scanning beams based system.

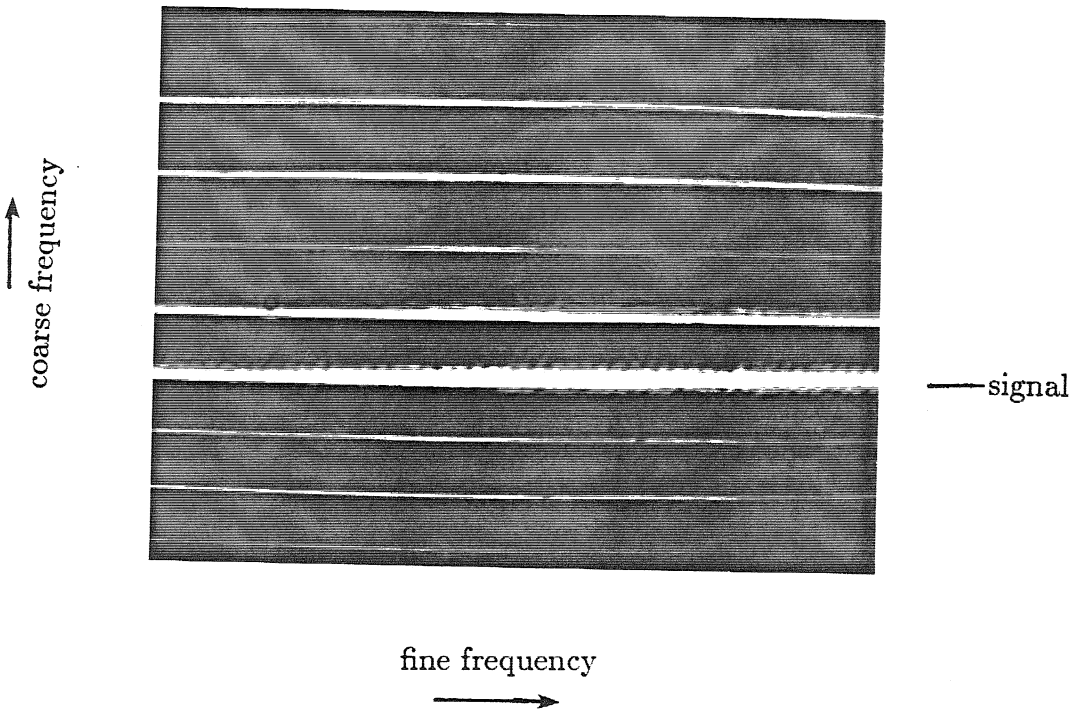

Fig.5.3.4.4 2-D CCD2 output on TV monitor showing the time integrated interference pattern between a $60MHz$ signal fed to AOD3, and the DLO lines generated for a chirp repetition rate of $1MHz$.

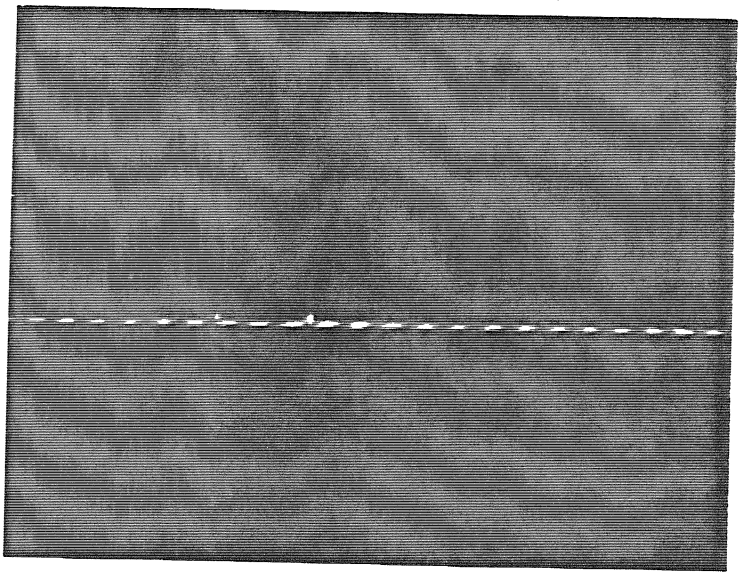

x direction

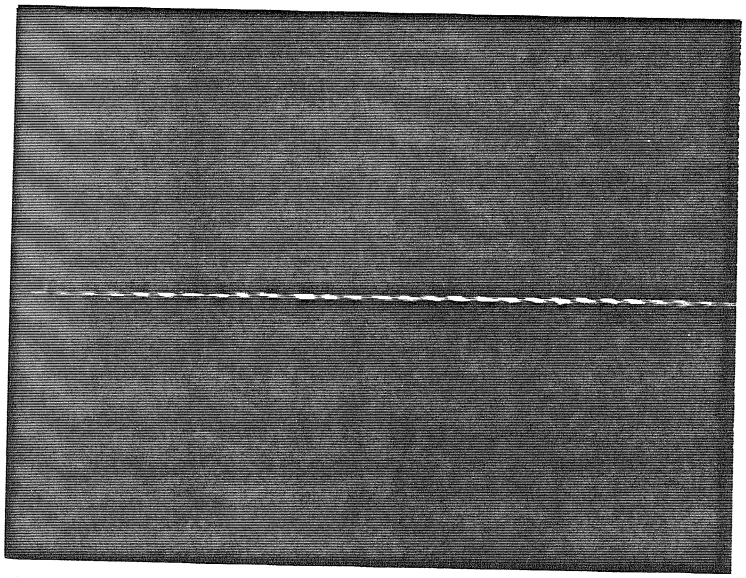

Fig.5.3.4.5 Different spatial carriers along the x direction on CCD2 for a $60MHz$ signal and $60MHz$ reference DLO line.

The read-out mechanism for the crystal is as follows. A $10mW$ He-Ne laser light is collimated by an $F = 35cm$ spherical lens S_4, and then focussed into a slit of light along the y direction by an $F = 20cm$ cylindrical lens C_{4x}. The acoustic column of a glass AOD5 is positioned along this slit of light. This AOD5, along with AOD3 in the interferometer are driven by the same input test signal $s(t)$. Note that the four AOD's used in the interferometer are TeO_2 cells, while the read-out AOD5 is a glass cell. Ideally, one would like to use the same kind of AOD's for the signal inputs at the two different ports of entry, in order to give a similar spatial Fourier transform response. The DC and +1 order diffracted light from the glass AOD5 are Fourier transformed by an $F = 24cm$ spherical lens S_5, and the spatial filter $SF4$ removes the DC light. The +1 order filtered red light strikes a mirror $M3$, and is directed towards a beam splitter $BS3$ positioned along the path of the green write beams from the interferometer. The $F = 20cm$ cylindrical lens C_{4y} inverse Fourier transforms the +1 order slit of light at $SF4$ into a plane wave at a proper angular frequency along the y direction, that after reflection from beam splitter $BS3$ illuminates the full face of the crystal. The Bragg matching of this plane wave with the grating carrier along the x direction on the crystal is achieved by careful rotation of the mirror $M3$. The crystal plane I_3 is imaged along the x direction by the $F = 10cm$ cylindrical lens C_{3x} on to the plane I_4 corresponding to the CCD1 plane. Along the y direction of the crystal, $F = 30cm$ cylinder C_{3y} takes the Fourier transform of the emerging plane wave, converting it into a slit of light detected by CCD1. The position of this diffracted slit of light from the crystal depends on the angular tilt of the red plane wave illuminating the crystal, which in turn is proportional to the signal frequency driving AOD5. In this way, the input signal coarse frequency is mapped into a slit of light positioned along the y direction on CCD1. The green light is not detected by the CCD1 as we place a red filter to block this light. The DC red light from the crystal is blocked by the spatial filter

$SF3$ placed a focal length from cylinder C_{3x}.

The argon ion laser is operated at $1.5W$, $514nm$ line, continuous light power, with the AOD's providing diffraction efficiencies of less than 10% at $60MHz$ carrier frequency AOD drive signals. The average intensity of the write beams incident on the photorefractive crystal is approximately $84\mu W/cm^2$, giving a typical response time of 10 seconds for the bias-free output. The $633nm$ helium-neon laser read beam incident on the crystal has an average intensity of $0.5mW/cm^2$. The processor is operated with $60MHz$ drive signals for AOD1 and AOD2, while AOD3 and AOD5 are fed by a single tone signal whose frequency is varied around $60MHz$. AOD4 is fed by a $20MHz$ bandwidth, $1/T = 5MHz$ repetition rate reference chirp signal that generates DLO lines in plane I_1 for 50, 55, 60, 65, and $70MHz$ signal frequencies. The plane waves from all these DLO lines, along with the signal plane wave corresponding to a specific DLO line are incident on the crystal. This results in a low modulation depth signal plus reference interference pattern recording on the crystal, as the bias contribution from all the DLO components is much larger than the interferometric term (see Eqn. 5.3.4.10-15). The low modulation depth results in a lower diffraction efficiency for the crystal, and very little diffracted light is detected by CCD1. One approach to improving the diffraction efficiency greatly is to spatially filter out the DLO components that do not match the input signal. This spatial filtering is accomplished in the Fourier plane I_1 using a mechanically positioned slit that tracks the signal spectral line, and thus allows this signal plus matching DLO line only to go through and illuminate the crystal. In this case, we have the bias term written as:

$$I_0 \approx |a_M|^2 \quad + \quad |a|^2, \tag{5.3.4.18}$$

where a and a_M are the signal and matching DLO amplitudes, respectively. Furthermore, the modulation depth of the recorded interference pattern is maximized

by equalizing the amplitudes of the signal and DLO terms, respectively. The spatial filtering was not very critical as the Fourier plane separation between the DLO lines was large ($\approx 1.6mm$). By using this approach, we observe a substantial amount of diffracted light at CCD1. In fact, the maximum light level detected corresponded to 80% of the CCD1 dynamic range (see Fig. 5.3.4.6). Fig. 5.3.4.7 shows the bias-free coarse frequency line outputs for signal frequencies of 55, 60, $65MHz$, where these frequencies match their respective DLO references. The position of the line along the y direction of the CCD corresponds to the coarse frequency axis. Recall that a glass AOD5 is being used for the read-out process, which has a 6 times smaller deflection than the TeO_2 cell used to form the signal spatial Fourier transform in the interferometer. A quasi-periodic temporal oscillation of the diffracted light was observed by the CCD1 over a 10 second period. Recall from the DLO experiment in Section 5.3.3 that the input signal and reference chirp waveforms have to be phase locked for coherent processing. The phase locking in this system is achieved by a $10MHz$ master clock. A possible reason for the fluctuation of the diffracted light is a $\geq 0.1Hz$ phase jitter of the coherent signal and reference waveforms over successive integration times of the crystal. Next, AOD1 and AOD2 are driven by slow linear FM signals to accomplish the fine processing over the integration time of the crystal. In principle, we should observe the bias-free coarse frequency line shrinking down to a point, as was observed in the earlier 1-D bias-free crystal based experiment. In this 2-D experiment, we do not observe the integrated blur spot for a number of reasons. For instance, the slow temporal oscillation of the diffracted light might average out the integrated blur spot to zero over successive processing frames. These experiments used a crystal spatial carrier of around 100 lines/mm along the x direction, with a DC electric field of $13kV/cm$ across the crystal.

A limitation of this architecture is its high optical power consumption due to its inherently low light efficiency design. The five Bragg cells used in the system

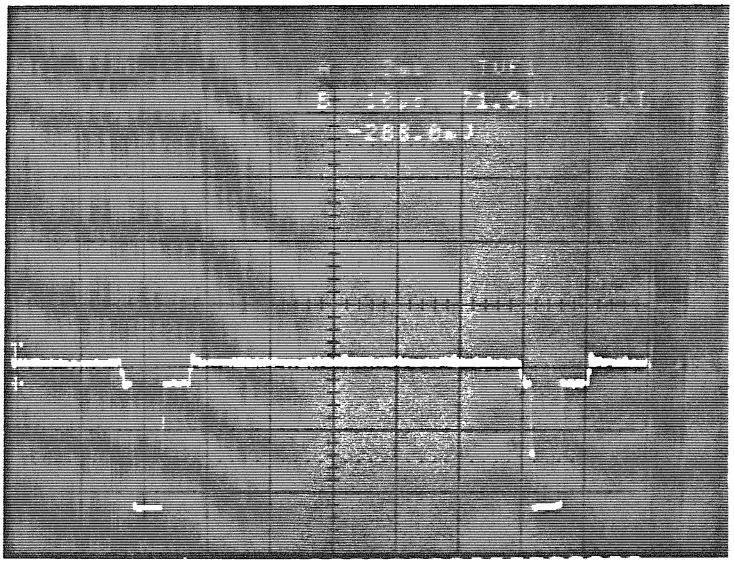

0

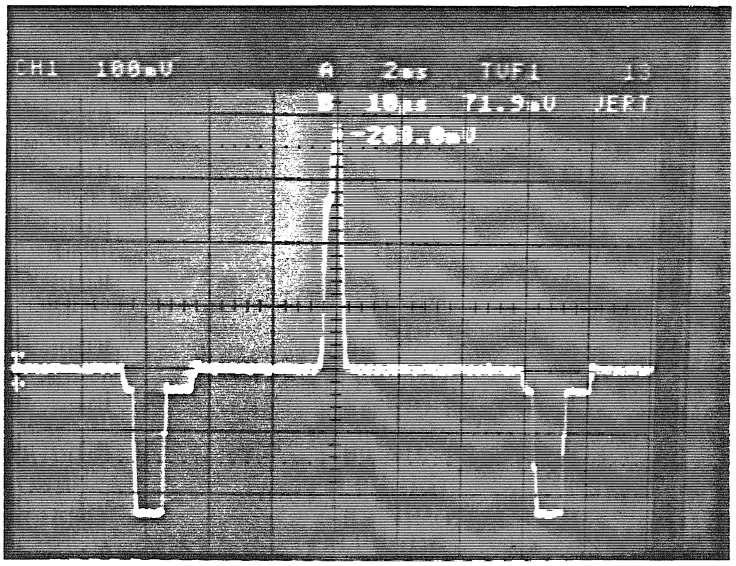

0

Fig.5.3.4.6 Processor CCD1 outputs for a zero light level, and the maximum diffracted light level from the BSO crystal. 80% of the CCD dynamic range is used by the bias free output.

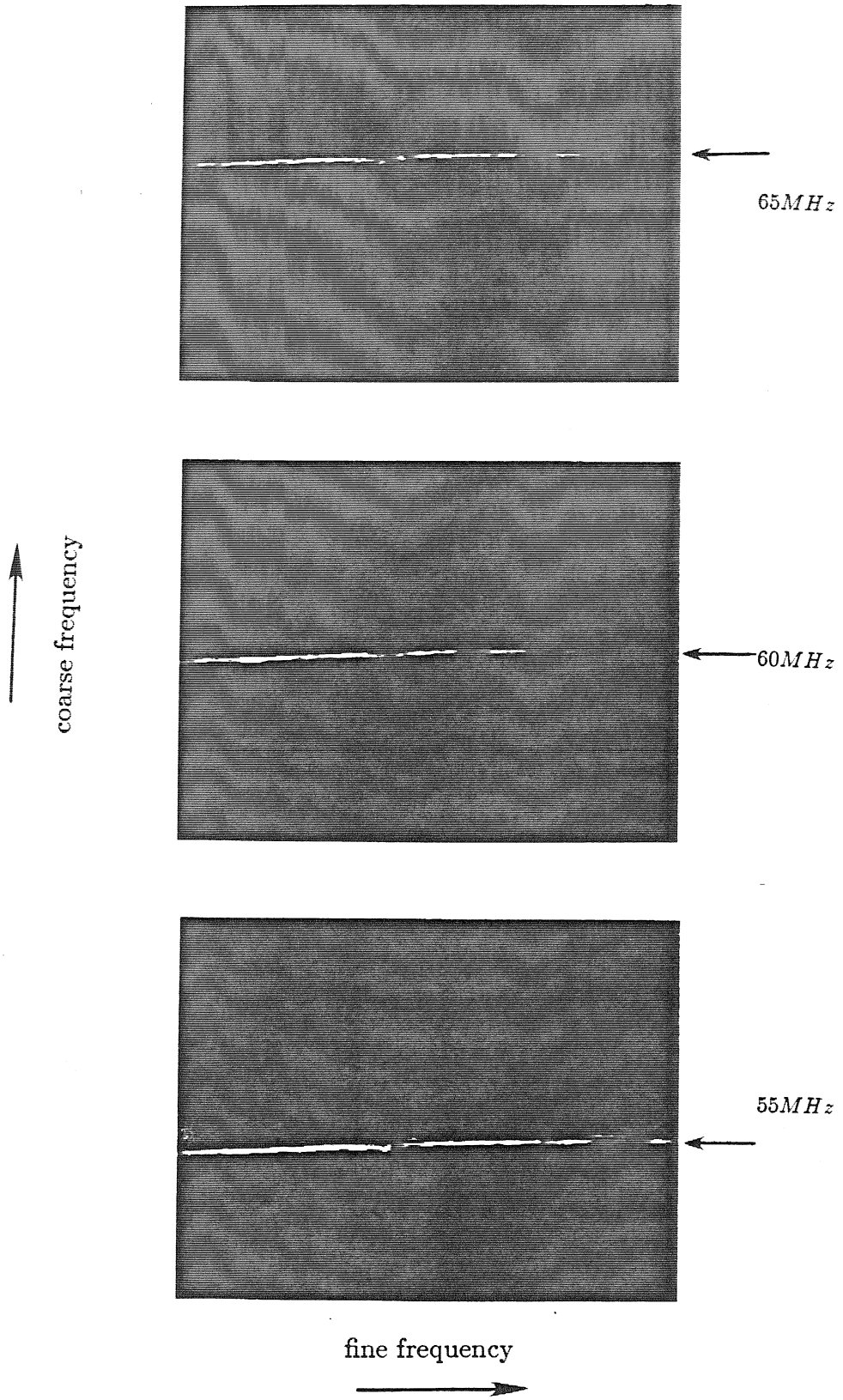

Fig.5.3.4.7 Bias free 2-D processor outputs showing coarse frequency lines for input signal coarse frequencies of 55, 60, and 65 MHz respectively.

lose some of the light, and light is also lost at the beam splitter ports $BS2$ and $BS3$. Moreover, the Bragg diffraction in each arm of the interferometer is multiplicative. In addition, the system requires many optical components that introduce further light losses. For the Caltech processor, the optical design was based on available components, resulting in a larger, less efficient optical system. Moreover, this system requires a high degree of optical and electronic coherence for the light carrier and AOD drive signals respectively.

In essence, we have investigated a 2-D bias-free optical processing system that is capable of providing bias-free outputs. The processor performance is limited by its high optical power consumption imposed by the slow response time, and poor diffraction efficiency of currently available photorefractive materials.

5.4 Conclusion

Today, a combination of different photorefractive materials (e.g., $GaAs$, BSO, SBN, $BaTiO_3$, and $LiNbO_3$) exhibit properties such as high speed, large gain, high diffraction efficiency, and low write energy/high sensitivity. These properties are desired for application in practical, real-time acousto-optic processors. Acousto-optic system architectures tend to be somewhat light starved, especially in the case of pulsed light and cascaded designs. Therefore, it is important for photorefractive crystals to have very low write energy/high sensitivity requirements, allowing fast response times for the processor. At present, there is no single material that exhibits all the desired properties. Nevertheless, the future of photorefractive materials offers certain distinct practical system applications such as direct optical cascadability of systems, adaptive computing such as adaptive beam combining, and temporary signal storage for learning based processing.

References:

[1] N. Riza and D. Psaltis, "Multiplicative time and space integrating acousto-optic architectures for real time spectrum processing," *Proc SPIE*, Vol 827-34, 1987.

[2] K. Wagner and D. Psaltis, "Time and space integrating acousto-optic folded spectrum processing for SETI," *Proc SPIE*, Vol 564-31, 1985.

[3] K. Wagner, "Time and space integrating acousto-optic signal processing," Ph.D Thesis, Caltech, May, 1987.

[4] M. W. Haney, "Acousto-optical time and space integrating processors for real-time synthetic aperture radar imaging," Ph.D. Thesis, Caltech, 1986.

[5] T. M. Turpin, "Spectrum analysis using optical processing," *Proc IEEE*, Vol. 69, No.1, 79, 1982.

[6] D. Psaltis, J. Yu and J. Hong, "Bias-free time integrating optical correlator using a photorefractive crystal," *Applied Optics*, Vol. 24, No.22, Nov., 1985.

[7] N. V. Kukhtarev, V. B. Markov, S. G. Odulov, and M. S. Soskin, "Holographic storage in crystals. I: Steady State," *Ferroelectrics*, No.22, 949, 1979.

[8] J. Feinberg, D. Heiman, A. R. Tanguay, and R. W. Hellwarth, "Photorefractive effects and light induced charge migration in barium titanate," *J. Applied Physics*, Vol. 51, 1297, 1980.

[9] M. Cronin-Golomb, "Large nonlinearities in four-wave mixing in photorefractive crystals and applications in passive optical phase conjugation," Ph.D. Thesis, Caltech, March, 1983.

[10] Jeffrey W. Yu, "Optical processing using photorefractive crystals," Ph.D Thesis, Caltech, March 1988.

[11] R. A. Sprague and C. L. Koliopoulos, "Time integrating acousto-optic correlator," *Applied Optics*, Vol. 15(1), 89, 1976.

[12] W. T. Rhodes, "Acousto-optic signal processing: convolution and correlation," *Proc IEEE*, Vol. 69-1, 65, 1981.

[13] T. R. Bader, "Acoustooptic spectrum analysis: a high performance hybrid technique,"*Applied Optics*, Vol. 18, No.10, May, 1979.

CHAPTER 6

ACOUSTO-OPTIC SYSTEMS FOR PHASED ARRAY RADAR SIGNAL PROCESSING

6.1 Introduction

In general, past and present techniques used in phased array radars utilize electronic signal processing for transmission and reception of radar signals [1,2]. Today, depending on the operating frequency of the radar, different electronic radar technologies are considered optimum in terms of cost, practicality and performance. In the lower half of the radar frequency spectrum, 10 GHz and below, hybrid microwave integrated circuit technology (HMIC) is being employed to build current phased array radars. This hybrid technology consists of a combination of discrete electronic components coupled with microstrip transmission lines. In the 10 GHz and higher frequency range, a new technology called the monolithic microwave integrated circuits (MMIC) technology is being developed by the radar community. This MMIC technology promises to be the ideal technology for the high end of the microwave spectrum phased array radars [3,4].

The application of optical processing for phased array radars was formally introduced by Lambert et al. at Columbia University in the 1960's [5]. The Columbia group proposed a signal processing technique for extracting angle/doppler target information from the many target return signals provided by the phased array antennas [6]. This approach was limited to processing of received antenna signals, thus making the optical processor irreversible. In other words, this processor could not be used for generation of phased array antenna drive signals to provide desired antenna beam shape and direction. Later research in optical phased array radar processing revolved around the Lambert processor, and most efforts used more ad-

vanced hardware to get improved experimental results [7,8]. Only recently, there has been some interest in using optical techniques for signal generation and control of phased array radars [9–15]. It is with the intent of achieving a reversible optical phased array radar processor providing transmission as well as reception capabilities that we pursue the research efforts in this chapter.

In particular, this chapter introduces optical techniques for signal generation and analysis in phased array radars operating in the lower half of the radar frequency spectrum (10 GHz and below) that are competitive with the larger electronic hybrid technology employed for building present radar arrays. The optical systems are designed with currently existing highly mature optical component technology. These components include continuous wave semiconductor lasers, acousto-optic devices, high speed detectors, lenses, and optical fibers. In particular, we introduce an optical technique for generation of phased array antenna drive signals for single and continuous mode beam scanning and beam formation in linear phased array radars. This processor can be adapted to operate in both the radar transmission and reception modes, thus making it reversible. The optical system uses two acousto-optic devices, imaging optics, and an array of high speed detectors to generate the correctly phased signals. The required phase change on each detector is brought about by a frequency change in the acousto-optic device drive signal which in turn maps frequency changes to changes in angular deflections. This results in a spatial frequency change on the detector plane. The detector array samples the generated phase distribution to produce the driving currents for the antenna elements. The doppler shift in the acousto-optic interaction in the Bragg cells is used to produce the high frequency carrier signal for the RF antennas. The use of the doppler effect eliminates the expensive, lossy, and bulky microwave frequency mixers used in the transmission mode of typical phased array radars. Moreover, a key feature of this radar processor is that it requires no phase shifting devices to accomplish antenna

beam scanning and beam formation, thus making the overall radar system much smaller and less hardware intensive.

We begin with an introduction to phased array radar theory and the principles of antenna beam steering and beam formation. We look at the existing phased array radar systems and the technology employed in building them. The acousto-optic phased array radar signal processors are introduced along with a complete analytical description of processor operation. Two processors are built in the laboratory using glass and tellurium dioxide acousto-optic devices, and an explanation of design rules and options is given. The test processors are built for a radar carrier frequency of 120 MHz. A number of test experiments are performed on the processor such as frequency scan linearity, zero to 2π phase shift of carrier with control frequency change, and antenna beam scan angle vs. frequency change. Data from the processors are compared to the ideal performance predicted by the system analysis, and good results have been achieved. A section is dedicated to experimental results from the processors along with their performance analysis. Next we describe the future prospects of such processors in various applications such as target tracking and detection, and explain the features that these optical techniques have to offer, compared to electronic approaches. An all optical transceiver system is proposed that uses the Lambert processor for post processing. The proposed optical technique for linear arrays is extended to planar and conformal arrays, and corresponding optical systems are described. In conclusion, we describe why this optical approach to phased array radar signal processing can provide a great reduction in system complexity, ease of assembly, operation and control, and better system performance, compared to electronic phased array radars in the 10 GHz and below frequency range.

6.2 Phased Array Radar Theory

Phased array radar theory has been extensively worked out by the radar community over the past 40 years. Here we will describe the basic concepts underlying phased array antenna operation. An array antenna consists of a number of individual radiating elements placed at a suitable distance with respect to each other. The relative amplitude and phase of the currents driving the individual antenna elements are externally controlled to generate a particular antenna beam pattern resulting from a sum of all the array radiating elements. There are three main array configurations used in phased array antennas. A linear array consists of antenna elements arranged along a straight line. This type of array can be used to provide broad coverage in one direction and narrow beamwidth in the orthogonal direction. The planar array consists of elements arranged in a two dimensional format in a plane. It can be considered as a linear array of linear arrays. A planar array with a rectangular aperture gives a narrow beamwidth fan shaped beam, while a circular aperture produces a pencil beam. The conformal array consists of radiating elements placed on a non-planar surface. For example, a cylindrical surface could be used to provide a 360 degree coverage. This type of array has been used in airborne radars on fighter aircrafts [16].

For analysis purposes, we shall consider a linear array of N elements equally spaced a distance **a** apart, with each element equivalent to an isotropic point source(sink) radiating (receiving) uniformly in all directions. The array antenna shown in Fig.6.2.1 is a transmitting antenna, although via the reciprocity principle of electromagnetics, the same array can be considered as a receiving antenna. In order to transmit energy at an angle θ with respect to the array normal direction, the plane wave interference condition requires that the phase difference of signals

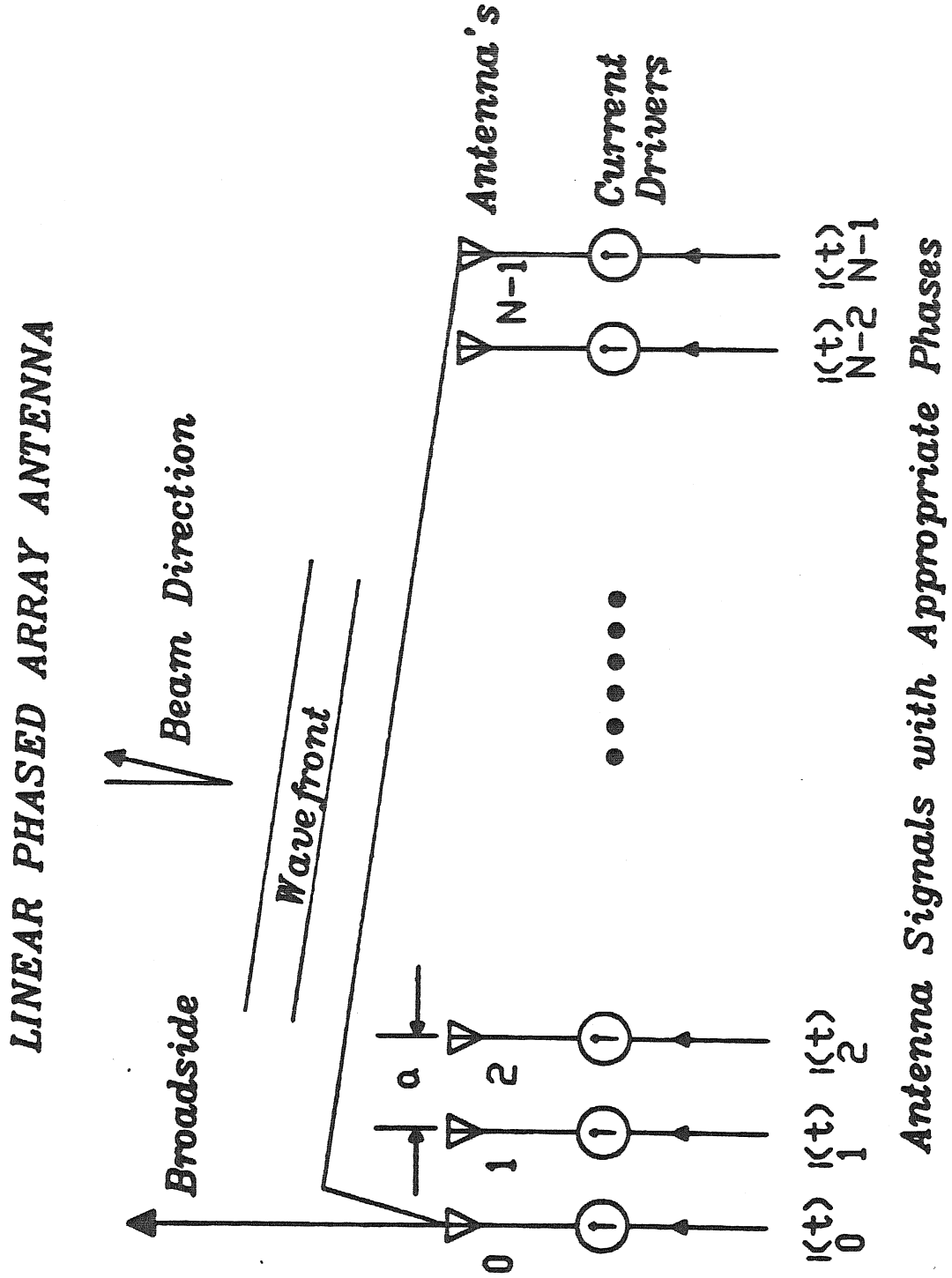

Fig.6.2.1 Linear phased array antenna configuration.

driving adjacent elements be [17]:

$$\alpha = 2\pi(a/\lambda)\sin\theta, \tag{6.2.1}$$

where λ is the radiated wavelength. Thus, the adjacent antenna elements in the array are driven by currents satisfying the phase condition in Eqn.6.2.1. The amplitudes of these currents can be suitably selected to yield desired beam shapes. For simplicity of analysis, we will consider the amplitudes to be constant and equal to unity. Element 0 in Fig.6.2.1 is taken as the reference antenna with zero phase. Each individual antenna radiates its own pattern, and the combined far field radiation observed at an angle θ due to all the elements in the array is approximated as the sum:

$$\begin{aligned} E &\approx \sum_{n=0}^{N-1} \sin(\omega t + n\alpha) \\ &= \sin\omega t + \sin(\omega t + \alpha) + \sin(\omega t + 2\alpha) + \cdots + \sin[\omega t + (N-1)\alpha], \end{aligned} \tag{6.2.2}$$

where ω is the angular carrier frequency of the radar. The sum in Eqn.6.2.2 can be written as:

$$E = \sin\Big[\omega t + (N-1)\alpha/2\Big]\frac{\sin(N\alpha/2)}{\sin(\alpha/2)}, \tag{6.2.3}$$

where the first term is the radar carrier signal with angular frequency ω and a phase $(N-1)\alpha/2$. This phase can be set to zero if the phase reference is taken at the center of the array. The second term gives the amplitude of the radiation pattern, and its magnitude is given by:

$$|E(\theta)| = \Big|\frac{\sin[N\pi(a/\lambda)\sin\theta]}{\sin[\pi(a/\lambda)\sin\theta]}\Big|. \tag{6.2.4}$$

Note the Fourier transform pair relationship between the excitation of the elements of the phased array and the resulting far field radiation pattern of the antenna. This result is expected from the Fraunhofer diffraction wave theory where the object and far fields are Fourier transform pairs [18]. The expression

in Eqn.6.2.4 behaves like a sinc function in space. The pattern nulls occur when $N\pi(a/\lambda)\sin\theta = 0, \pm\pi, \ldots, \pm n\pi$, while pattern maxima occur when $\sin\theta = \pm na/\lambda$, where n is an integer. The maximum at $\sin\theta = 0$ defines the main beam, while the other maxima are called grating lobes. All maxima have an amplitude of N. $E(\theta) = E(\pi - \theta)$ implies that the radiation pattern in front and at the rear of the antenna are the same. In general, a reflecting screen is placed behind the array to minimize the backward radiation. Thus, only radiation in front of the array ($-90° \leq \theta \leq 90°$) is considered. The normalized radiation intensity pattern is given by:

$$G(\theta) = \frac{|E(\theta)|^2}{N^2} = \frac{\sin^2[N\pi(a/\lambda)\sin\theta]}{N^2\sin^2[\pi(a/\lambda)\sin\theta]}. \tag{6.2.5}$$

When the main beam is pointing in the direction $\theta = \theta_0$, the normalized radiation intensity pattern can be expressed as:

$$G(\theta) = \frac{\sin^2[N\pi(a/\lambda)(\sin\theta - \sin\theta_0)]}{N^2\sin^2[\pi(a/\lambda)(\sin\theta - \sin\theta_0)]}, \tag{6.2.6}$$

which is maximum when $\sin\theta = \sin\theta_0$. The main beam can be rotated by varying the phase difference $\alpha = 2\pi(a/\lambda)\sin\theta_0$ of the signals driving the array antennas. In order to prevent grating lobes from appearing over the antenna beam scan width, the element spacing has to be of the order of half the carrier wavelength. This can be seen by setting the denominator in Eqn.6.2.6 equal to zero giving:

$$\begin{aligned} \pi(a/\lambda)(\sin\theta_g - \sin\theta_0) &= \pm n\pi \\ |\sin\theta_g - \sin\theta_0| &= \pm n\lambda/a, \end{aligned} \tag{6.2.7}$$

where the grating lobe appears at angle θ_g. If a grating lobe is allowed at $-90°$ when the main beam is steered to $+90°$, Eqn.6.2.7 gives $a = .5\lambda$. In practical systems where the maximum desired scan angle is $\pm 60°$, the element spacing has to be less than $.54\lambda$. The above analysis applies to a linear array, although a similar analysis can be applied for a planar array giving an approximate expression for the

normalized radiation intensity pattern for a rectangular array as:

$$G(\theta_a, \theta_e) = \frac{\sin^2[N\pi(a/\lambda)\sin\theta_a]\ \sin^2[M\pi(a/\lambda)\sin\theta_e]}{N^2\sin^2[\pi(a/\lambda)\sin\theta_a]\ M^2\sin^2[\pi(a/\lambda)\sin\theta_e]}, \qquad (6.2.8)$$

where N is the number of radiating elements in the θ_a direction and M is the number of radiating elements in the θ_e direction.

Now that we are familiar with the basic operation of phased array radars, let's look at the current technology for such systems.

6.3 A Look at Current Phased Array Radar Systems

The type of technology that is used in assembling the phased array radar is dependent on the radar carrier frequency . For arrays in the lower half of the radar spectrum, 30MHz (HF) to near 10GHz, the hybrid technology is being introduced for building active elements. For example, a combination of discrete PIN diodes connected to microstrip transmission lines etched on a substrate are used to form the N-bit digital phase shifter modules where N varies from 3 to 7. This type of device is called a switched line phase shifter where discrete diodes are used as switches and microstrip transmission lines are used to introduce the phase shift. For a typical 5-bit device, the phase resolution is $11.25°/bit$ [19]. The Jet Propulsion Laboratory in Pasadena, California, is currently building the shuttle SIR-C phased array radar at L Band (1.25GHz) using a hybrid technology 4-bit digital phase shifters with phase resolution of $22.5°/bit$ [20]. Each phase shifter has external driver electronics to set the 4 control bits that change the phase of the transmit/receive signal. Also, each module is around 4 by 12 inches in size, and is externally connected to patch antennas on a planar array with 972 elements. Fig.6.3.1 shows the JPL radar corporate feed network for a 9 element section of the planar array. Note that each radiating element has its own phase shifting module, thus making a hardware intensive radar system. Fig. 6.3.2(a,b) shows the JPL 4 bit phase shifter and a

Hughes aircraft transmit/receive phase shifter module [20,16]. In addition, similar phased array radars using the hybrid technology are being developed [21,22].

In the upper half of the radar spectrum, i.e. above 10GHz, monolithic microwave integrated circuits (MMIC) are being developed for application in phased array radars. At these extremely high frequencies, the active and passive devices used for signal processing become an integral part of the antenna. Therefore, it becomes necessary to build the antennas, feed networks, phase shifters, amplifiers, and control circuits on a single substrate. Gallium arsenide (GaAs) technology has provided the base for MMIC's, and currently, active GaAs devices are being custom built at a very high cost for the 10GHz and higher frequency range [23,24]. For instance, 3-bit and 5-bit digital MMIC phase shifters at 44 and 10GHz frequencies, respectively, are being built using FET's as switches and etched transmission lines [21]. Similarly, a Ku-Band (16-18GHz) MMIC analog phase shifter has been demonstrated [25]. The performance and advantages provided by MMIC's at these high frequencies have somewhat compensated for the high production cost. Below 10GHz, GaAs device production costs are not as yet practical to replace the hybrid technology using PIN diodes,etc. In addition, the power handling capability of MMIC's is relatively poor compared to the hybrid technology.

The proposed optical phased array radar signal processors to be described later in the chapter will be competitive over the lower half of the radar frequency spectrum, i.e., below 10GHz, where they have to compete with the hybrid technology. This frequency limit on the optical processors is imposed by the maximum available bandwidth and center frequency of the currently available acousto-optic devices.

JPL SIR-C RADAR CORPORATE FEED

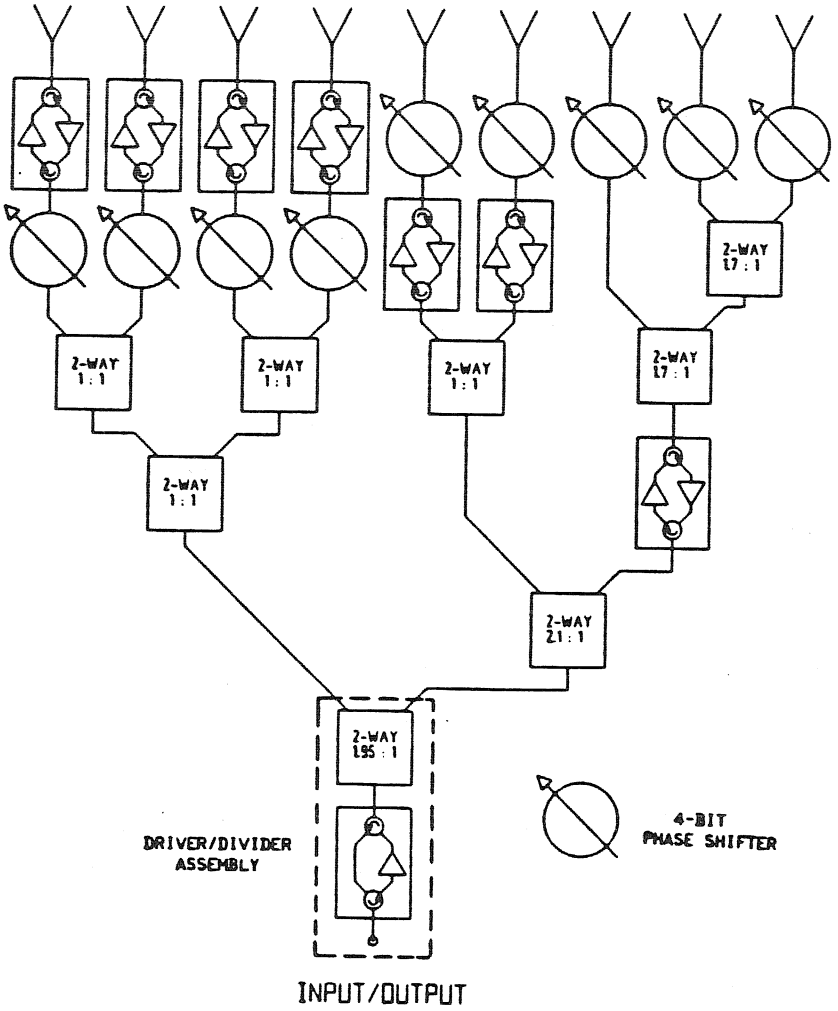

Fig.6.3.1 JPL SIR-C phased array radar corporate feed network.

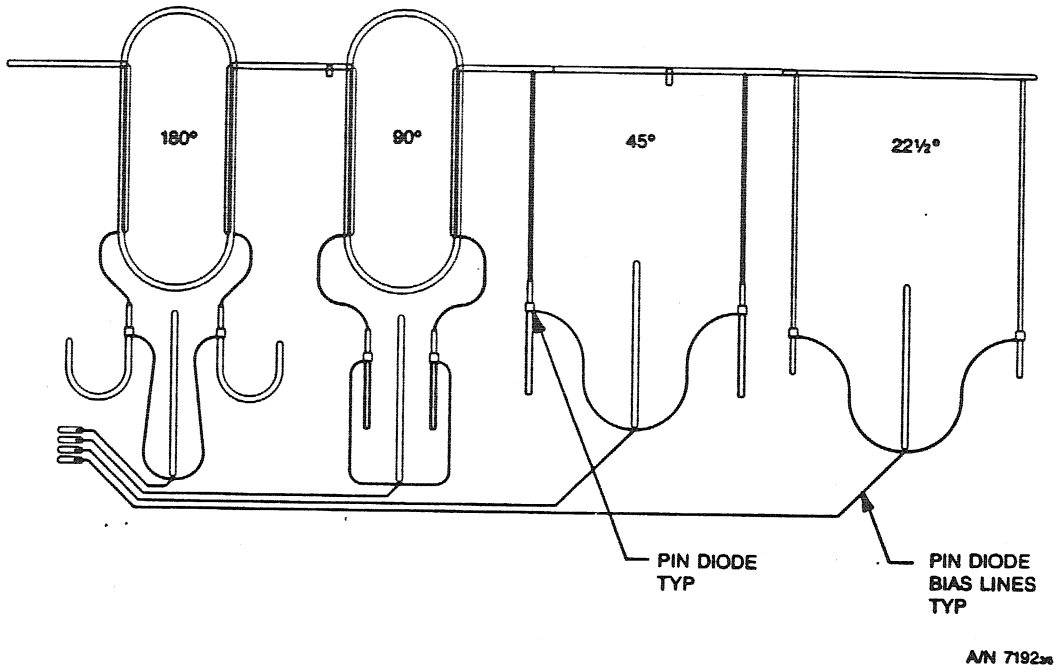

Fig.6.3.2(a) JPL 4-bit digital phase shifter.

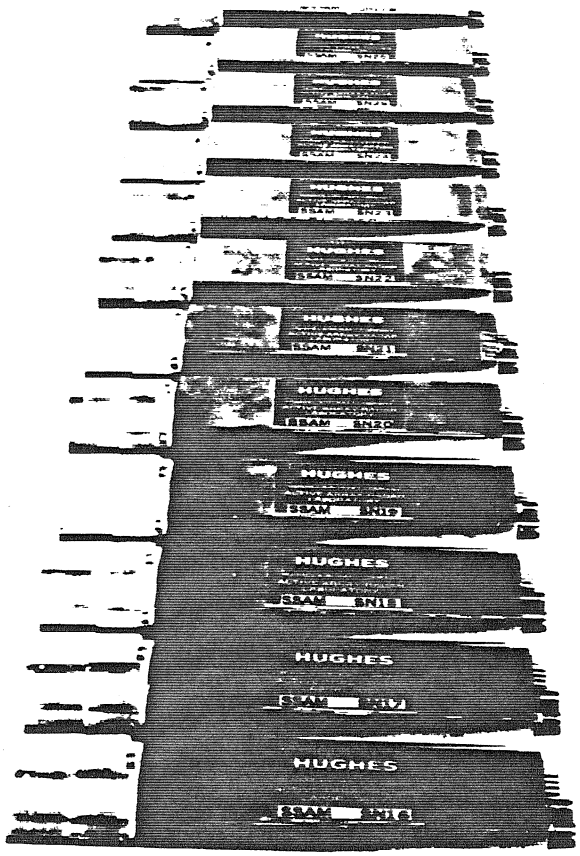

Fig.6.3.2(b) Hughes Aircraft transmit/receive phase shifter modules.

6.4 The Acousto-optic Phased Array Radar Signal Processors

The Frequency Controlled Beam Steerer 1 shown in Fig.6.4.1 is an optical phased array radar signal generator applicable for generating the signals necessary for beam formation and beam scanning in linear radar arrays. The processor consists of two AOD's, a high speed detector array, a coherent light source, imaging and Fourier transforming optics, and two signal generators to provide the radar carrier and control frequency signals, respectively. The signals $s_1(t)$ and $s_2(t)$ are fed into AOD1 and AOD2, respectively, where

$$s_1(t) = a\ \cos\omega_c t \tag{6.4.1}$$

$$s_2(t) = a\ \cos[(\omega_c + \omega_0)t], \tag{6.4.2}$$

where ω_c is the center angular frequency of the AOD's and ω_0 is the control angular frequency for steering the array antenna beam. Light from the laser after being collimated along the x direction and focussed along the y direction, is made incident at the Bragg angle in AOD1. The DC and +1 order diffracted light from AOD1 is 1:1 imaged on to the acoustic column in AOD2 such that the DC light from AOD1 is Bragg matched to AOD2. This results in a -1 order diffracted light from AOD2, while the +1 order from AOD1 passes through AOD2 essentially unaffected. These almost collinear +1 and -1 order diffracted beams from AOD1 and AOD2, respectively, are imaged on to a detector array after an M times magnification. The DC light is blocked in the Fourier plane of AOD2, and the resulting electric field incident on the detector plane is given by:

$$E(x,t) = \left[e^{-j2\pi\frac{\sin\theta_B}{\lambda}x}\tilde{s}_1(t - x/Mv_a) + e^{j2\pi\frac{\sin\theta_B}{\lambda}x}\tilde{s}_2^*(t + x/Mv_a)\right]\ \mathrm{rect}[\frac{x - .5MX}{MX}], \tag{6.4.3}$$

where $\frac{\sin\theta_B}{\lambda} = \frac{f_c}{2v_a}$, v_a is the acoustic signal velocity in the AOD's, and $\tilde{s}_1$, $\tilde{s}_2^*$ are the analytic +1 and -1 diffracted signal representations, respectively, given by:

$$\tilde{s}_1 = \frac{1}{2}ae^{-j\omega_c t} \qquad \tilde{s}_2^* = \frac{1}{2}ae^{j(\omega_c+\omega_0)t}. \tag{6.4.4}$$

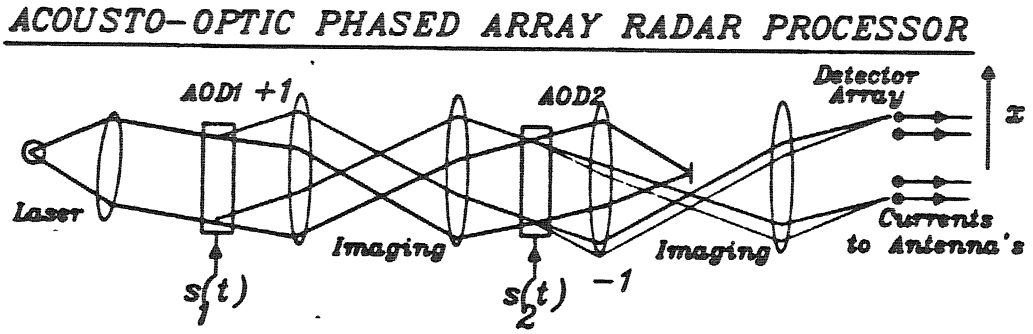

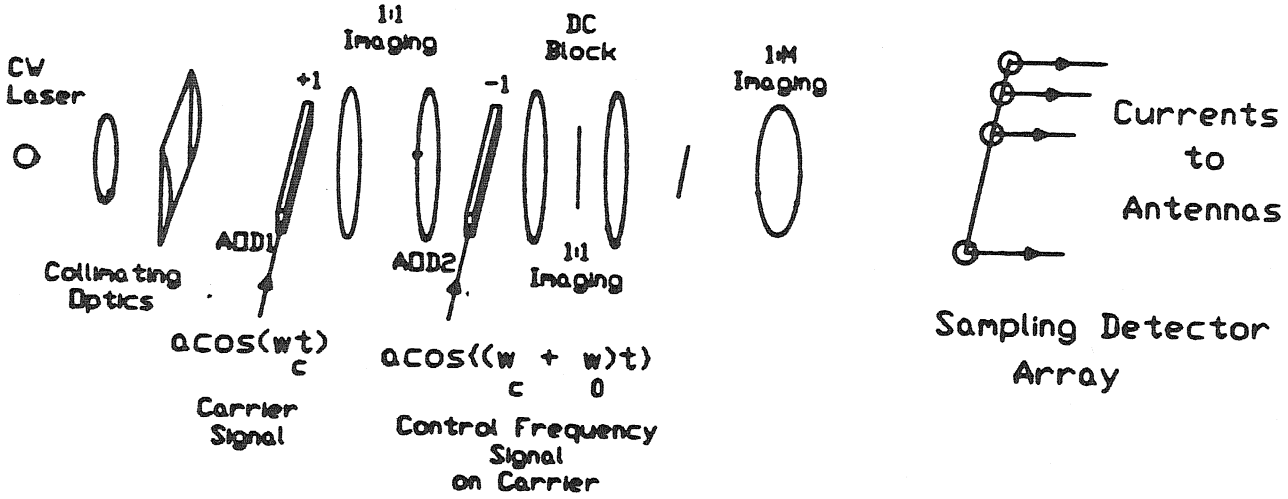

Fig.6.4.1 Frequency controlled beam steerer 1.

The intensity at the detector plane is:

$$I(x,t) = \left| \left[e^{-j2\pi \frac{\sin\theta_B}{\lambda} x} e^{-j\omega_c(t-x/Mv_a)} + e^{j2\pi \frac{\sin\theta_B}{\lambda} x} e^{j(\omega_c+\omega_0)(t+x/Mv_a)} \right] \right|^2 \text{rect}[\frac{x-.5MX}{MX}]. \tag{6.4.5}$$

On expanding Eqn.6.4.5 we get:

$$I(x,t) = Constant\ Bias + G_0 \cos[(2\omega_c+\omega_0)t - \frac{\omega_0}{Mv_a}x]\,\text{rect}[\frac{x-.5MX}{MX}], \tag{6.4.6}$$

where $Constant\ Bias = a/\sqrt{2}$ and $G_0 = a^2/4$. The expression in Eqn.6.4.6 consists of a uniform bias term, and a signal term with both temporal and spatial modulation. Recall from our discussion on phased array beam steering in Section 6.2 that phase based beam steering requires a set of antenna drive signals on the radar temporal carrier with appropriate phase values. The expression in Eqn.6.4.6 shows that we can obtain this set of antenna drive signals by simply using a detector array to sample the phase distribution of the temporally varying intensity pattern appropriately. In the case of uniform linear phase sampling, the detectors are placed at an equal distance d from each other. The current generated at the n^{th} detector after spatial integration over the detector photo-sensitive area, $d_x \times d_y$ is amplified by a high frequency amplifier. If the spatial period of the intensity pattern is much greater than the sampling direction detector size, that is,

$$u_x d_x \ll 1, \tag{6.4.7}$$

where $u_x = f_0/Mv_a$ is the spatial frequency generated along the detector array, d_x is the width of the detector along the sampling x direction, then the current produced by the n^{th} detector can be approximated as:

$$i_n(t) \approx G\cos[(2\omega_c+\omega_0)t - n\frac{\omega_0 d}{Mv_a}], \tag{6.4.8}$$

where $G = .5G_0 d_x d_y$, $n = 0, 1, 2, \ldots, N-1$, and N is the total number of detectors used in the linear sampling array. This expression (i.e. Eqn. 6.4.8) is justified later in the section on detector phase sampling. Note that Eqn.6.4.8 gives the drive current that is fed to the n^{th} antenna in a uniform linear phased array radar for achieving beam steering. This current can be expressed as:

$$i_n(t) = G\cos(\omega t - n\psi), \tag{6.4.9}$$

where the radar carrier angular frequency is:

$$\omega = 2\omega_c + \omega_0, \tag{6.4.10}$$

and the phase difference between signals in adjacent antennas in the array is:

$$\psi = \frac{\omega_0 d}{M v_a}. \tag{6.4.11}$$

From phased array radar theory, recall that to position the antenna beam at an angle $\theta = \theta_0$, we would require:

$$\psi = \alpha + 2m\pi, \tag{6.4.12}$$

where $m = 0, \pm 1, \pm 2, \ldots$. Substituting the values of α and ψ in Eqn.6.4.12, we get:

$$\begin{aligned} 2\pi(a/\lambda)\sin\theta_0 &= \frac{\omega_0 d}{M v_a} - m2\pi \\ \sin\theta_0 &= (\lambda/a)[\frac{f_0 d}{M v_a} - m]. \end{aligned} \tag{6.4.13}$$

Using Eqn.6.4.13, the design equations for the optical processor to achieve a beam position θ_0 for a control frequency f_0 is:

$$\begin{aligned} \theta_0 &= \sin^{-1}\left[(\lambda/a)[\frac{f_0 d}{M v_a} + m]\right] \\ \text{OR} \qquad f_0 &= [(a/\lambda)\sin\theta_0 + m](\frac{M v_a}{d}). \end{aligned} \tag{6.4.14}$$

Fig.6.4.2 shows the graphical relationship between the antenna beam scan angle and the processor control frequency. Note that the same angle θ_0 can be obtained for multiple values of the frequency f_0 corresponding to different values of m. This allows the generation of multiple, simultaneous beams creating many applications such as multitarget tracking and secured transmission. Later in the chapter, an optical receiver system based on frequency discrimination techniques is described for this type of multiple beam steerer.

There are two main approaches to beam steering in phased array antennas. First, there is the time delay beam steering approach that provides a very high instantaneous microwave bandwidth for the antenna. On the other hand, there is the phase shift beam steering technique that provides accurate beam pointing if the antenna instantaneous microwave bandwidth is less than 2% of the antenna carrier frequency [2]. The proposed acousto-optic radar signal processor is based on the phase shift beam steering approach, and requires a relatively small instantaneous antenna bandwidth for accurate beam scanning. Specifically,

$$\frac{\Delta f_0}{f'} \ll 1, \tag{6.4.15}$$

where Δf_0 is the maximum control frequency change required for the maximum beam scan angle and f' is the radar carrier center frequency, where

$$f' = 2f_c + \frac{\Delta f_0}{2}. \tag{6.4.16}$$

An alternate **Frequency Controlled Beam Steerer 2** design is shown in Fig.6.4.3, where the transmitted radar carrier frequency f' is independent of the control frequency f_0. The optical apparatus of this signal processor is similar to the signal processor in Fig. 6.4.1, except that different electronic signals are used. Two kinds of oscillators are required for this system. One oscillator is a low frequency signal generator providing the scan control frequency f_0, while the other is a very

COEXISTENT MUTI-FREQUENCY BEAMS

Design:

$$f_0 = [(a/\lambda)\sin\theta_0 + m](Mv/d)$$

$m=0,\ 1,\ 2,\ \ldots\ldots$ for $\theta = \theta_0$ beam

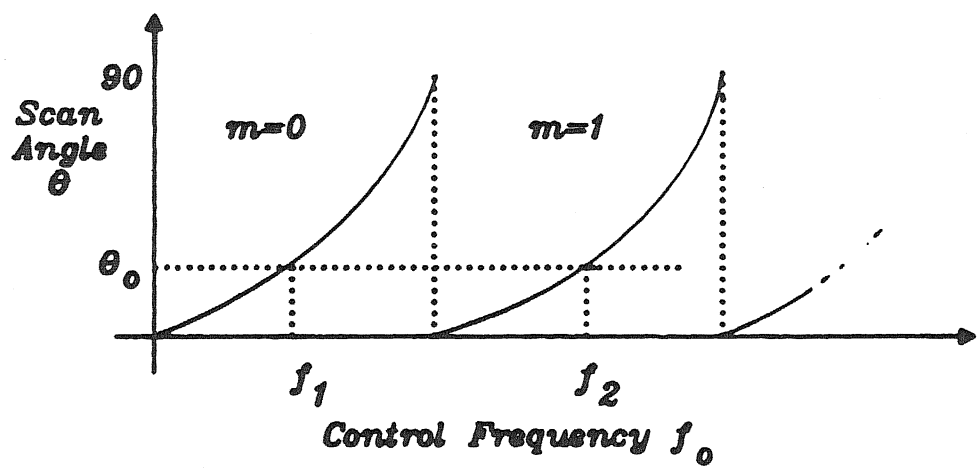

Fig.6.4.2 Antenna beam scan angle .vs. Processor control frequency behavior.

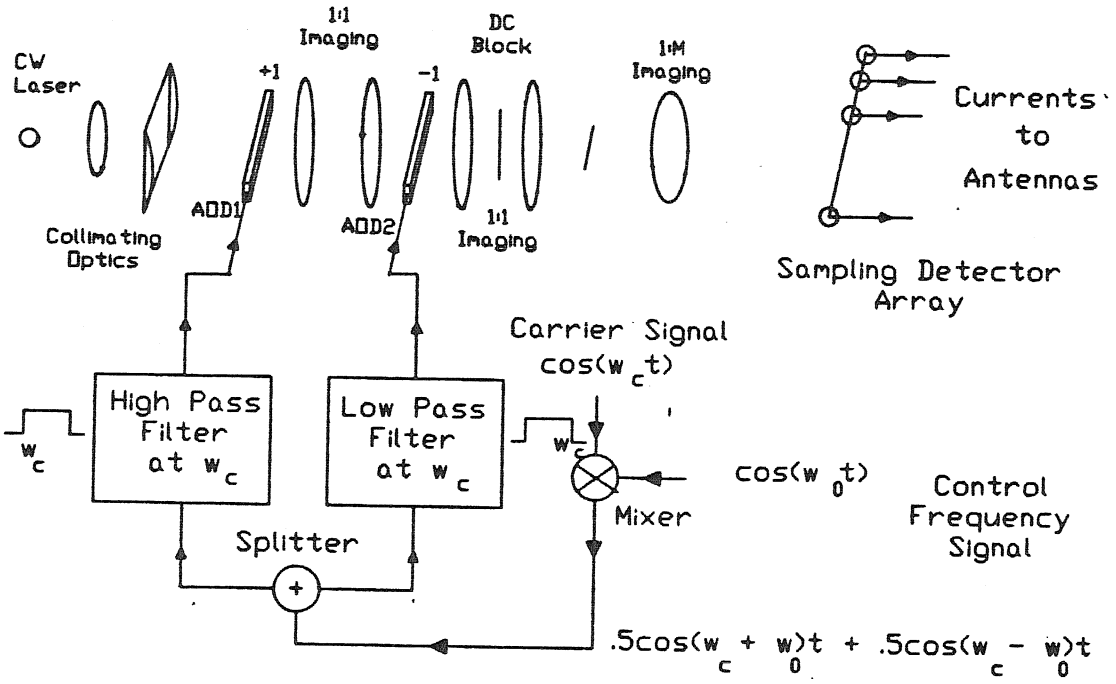

Fig.6.4.3 Frequency controlled beam steerer 2.

high frequency oscillator operating at half the desired radar carrier frequency (also equal to the AOD center frequency). The two signals are mixed together in a standard microwave mixer giving:

$$\begin{aligned} s(t) &= 2a\cos\omega_0 t\ \cos\omega_c t \\ &= a\cos(\omega_c+\omega_0)t + a\cos(\omega_c-\omega_0)t. \end{aligned} \tag{6.4.17}$$

This signal is split by a microwave power divider into two paths. One path goes through an upper sideband filter at frequency ω_c, giving the signal:

$$s_1(t) = a\cos(\omega_c+\omega_0)t, \tag{6.4.18}$$

that is fed to AOD1. The other path goes to a lower sideband filter at frequency ω_c, giving the signal:

$$s_2(t) = a\cos(\omega_c-\omega_0)t, \tag{6.4.19}$$

that is used to drive AOD2. The electronic single sideband filtering can also be done optically by using spatial filtering in the Fourier planes of AOD1 and AOD2, respectively. By evaluating Eqn.6.4.3 with the new signal values inserted, the intensity on the detector plane is given by:

$$I(x,t) = Constant\ Bias + G_0\cos[2\omega_c t - \frac{\omega_0}{Mv_a}x]\,\mathrm{rect}[\frac{x-.5MX}{MX}]. \tag{6.4.20}$$

In this case, the current generated by the n^{th} detector/amplifier combination is approximated as:

$$i_n(t) \approx G\cos[2\omega_c t - n\frac{\omega_0 d}{Mv_a}]. \tag{6.4.21}$$

Note that in this case, the radar carrier frequency stays fixed at $2\omega_c$ and is independent of the scan control frequency ω_0. In other words, when the antenna beam is scanned by changing the control frequency ω_0, the radar carrier remains unchanged. This type of radar has particular applications when the available radar bandwidth is limited and should be used only for transmitting information signals.

In the next section, we describe the design process of the first acousto-optic beam steerer 1, along with the experimental results from the Caltech laboratory system.

6.5 Optical Design for the Radar Processors: Experimental Results

Two designs of the acousto-optic beam steerer 1 were demonstrated in the laboratory. The first processor uses a pair of glass AOD's, while the second one employs Tellurium dioxide Bragg cells. The optics used in both processors consists of:

1. 20cm collimating spherical lens
2. 30cm focussing cylindrical lens for AOD1
3. 20cm spheres for 1:1 imaging
4. 25cm and 30cm spheres for imaging and Fourier plane filtering
5. 7.5cm spherical lens for magnification

The specifications of the Bragg cells used that are critical to the optical processors are:

1. Glass Cells: 10μsec aperture,70 MHz center frequency, Bandwidth =40 MHz giving 400 resolvable deflection spots.
2. Tellurium Dioxide Cells: 70μsec aperture,60 MHz center frequency, Bandwidth= 30 MHz, giving 2100 resolvable deflection spots.

The N element high speed detector array is simulated by using 2 detectors mounted on x-y micrometer translation stages, allowing for the detector spacing d to be adjusted according to design specifications, while placing the detectors at any position along the focussed slit of light.

The specifications for the detector/amplifier set up are:

1. High Speed Detector: UDT PIN-HR008 photo diode, 3nsec max rise time, $200\mu m$ diameter, responsivity .33 A/W at $514nm$.
2. High Speed Amplifier: UDT 700 amplifier, 3 dB bandwidth of $500KHz$ to $400MHz$, Transimpedance Gain 3.5×10^3 $Volts/Amp$.

Recall that the design equations for the optical processor to achieve a beam position θ_0 for a certain control frequency f_0 are:

$$\begin{aligned} \theta_0 &= \sin^{-1}\left[(\lambda/a)[\frac{f_0 d}{M v_a} - m]\right] \\ \text{OR} \qquad f_0 &= [(a/\lambda)\sin\theta_0 + m](\frac{M v_a}{d}). \end{aligned} \tag{6.5.1}$$

As the Bragg cell acts as a beam deflector with a finite number of deflected spots, 400 for glass, the control frequency is discretized and written as:

$$f_0 = p\,\delta f_0 \tag{6.5.2}$$

$p = 0, 1, 2, \ldots$ and $\delta f_0 = \frac{1}{T_a}$, where T_a is the illuminated Bragg cell aperture. The processor design equation can be rewritten as:

$$\theta_0 = \sin^{-1}\left[(\lambda/a)[\frac{p\delta f_0 d}{M v_a} - m]\right]. \tag{6.5.3}$$

The Design procedure for the processor is as follows:

1. Choose a value for a/λ according to how far you want the grating lobes to be placed in the array beam pattern. The analysis to follow uses $a/\lambda = .5$, giving no grating lobes over a $\pm 90°$ scan angle.
2. Choose the type of AOD to be used in the processor. This will determine the minimum value of control frequency resolution δf_0, the acoustic velocity v_a, and the maximum radar carrier frequency possible.
3. Choose θ_{0min}, the minimum scan angle required for the antenna, where

$$\theta_{0min} = \sin^{-1}\left[(\lambda/a)[\frac{\delta f_0 d}{M v_a} - m]\right]. \tag{6.5.4}$$

4. Now solve Eqn.6.5.4 with $m = 0$ to get a value for M/d necessary to give the desired minimum scan angle for the smallest value of f_0.
5. Choose a tolerable phase sampling error η that is due to the finite size of the detector. This is given by:

$$\eta = \frac{d_x}{d} \times 100, \tag{6.5.5}$$

where d_x is the width of the detector light sensitive area along the phase sampling direction. This gives the value for d, the detector spacing.

6. Calculate the required optical magnification M, given the value of d. The processor design is complete.

The design for the Caltech processors was chosen as:

1. $a/\lambda = .5$
2. $\delta f_0 = 100KHz$ and $v_a = 3.9mm/\mu sec$ for glass cells in System A.
3. $\delta f_0 = 14.29KHz$ and $v_a = .617mm/\mu sec$ for TeO_2 cells in System B.
4. $M = 4.17$ in both systems.
5. Center Frequency for both Bragg cells used is $f_c = 60MHz$.
6. Argon Ion laser ($514nm$) light source used.

For System A:

7. $d = 5.5mm$ or $d = 10.16mm$.
8. $\eta = 3.6\%$ at $d = 5.5mm$ and $\eta = 1.9\%$ at $d = 10.16mm$.
9. $\theta_{0min} = 3.9°$ at $d = 5.5mm$ and $\theta_{0min} = 7.2°$ at $d = 10.16mm$.
10. For $d = 5.5mm$ total number of detectors $N = 30$.
11. For $d = 10.16mm$ total number of detectors $N = 17$.

For System B:

12. $d = 5.9mm$ or $d = 10.7mm$.
13. $\eta = 3.4\%$ at $d = 5.9mm$ and $\eta = 1.9\%$ at $d = 10.7mm$.
14. $\theta_{0min} = 3.8°$ at $d = 5.9mm$ and $\theta_{0min} = 6.8°$ at $d = 10.7mm$.

15. For $d = 5.9mm$ total number of detectors $N = 31$.
16. For $d = 10.7mm$ total number of detectors $N = 17$.

Both the glass and TeO_2 Bragg cell systems were built in the laboratory and are shown in Fig.6.5.1 and Fig.6.5.2, respectively. Fig.6.5.3 shows the x-y translational stage mounted detector pair used to simulate the complete detector array.

Experimental Results are shown in Figures 6.5.4-7 for the TeO_2 processor. Similar results are obtained for the glass cell beam steerer. In order to look at the spatial phase pattern that the detectors sample, the optical system is changed such that we use the +1 orders from both the Bragg cells, thus detecting a fringe pattern that is not on a temporal carrier. This allows the CCD to pick up the spatial phase pattern. Fig.6.5.4 shows this pattern for an increasing scan control frequency signal that is fed to both the Bragg cells. Notice the increase in spatial variation with increasing control frequency. This behavior becomes the basis for generating appropriately phased radar signals for the array antenna. Fig.6.5.5 shows the frequency doubling effect that is due to the doppler phenomenon in the two Bragg cells. Here, a 60 MHz AOD input signal has been doubled to a 120 MHz carrier signal that is generated at the detector array. Fig.6.5.6(a,b) shows the varying phase difference between the two signals generated from the detector pair positioned with a certain interdetector distance d. Here, the control frequency is varied for a zero to 2π phase shift for the generated carrier signals. Fig.6.5.7 shows the phase change for a fixed control frequency when the distance between the detectors is changed. The next section deals with important processor performance issues relating to the experimental system.

6.6 Processor Performance Analysis

Data from the processors agree very well with the analytical results. In

Fig.6.5.1 Glass cell (system A) optical radar processor laboratory system.

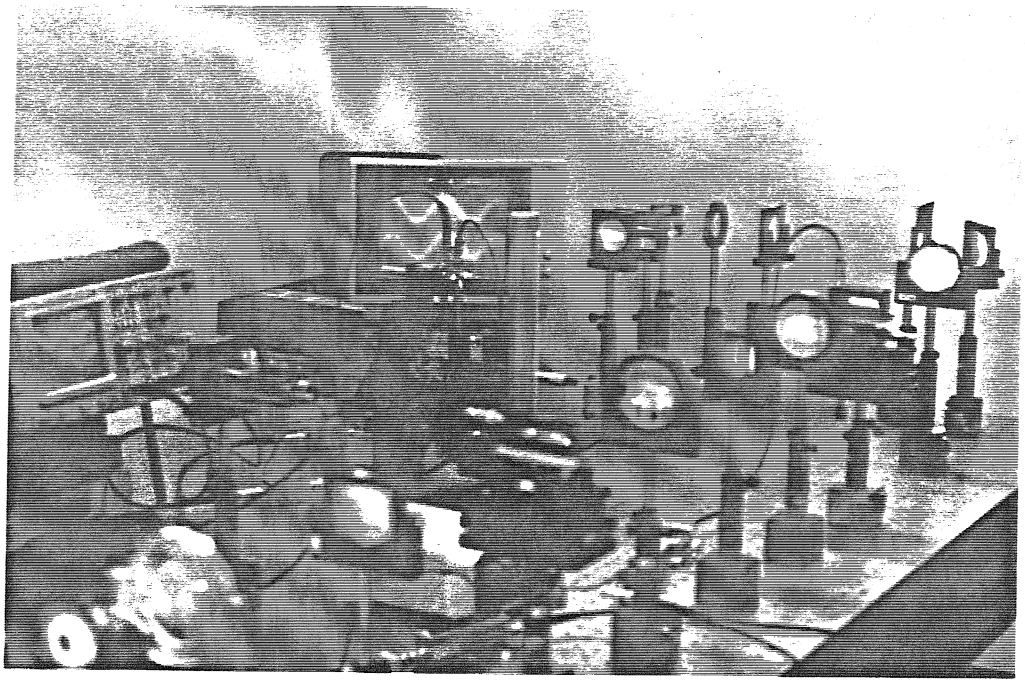

Fig.6.5.2 Tellurium dioxide cell (system B) optical radar processor laboratory system.

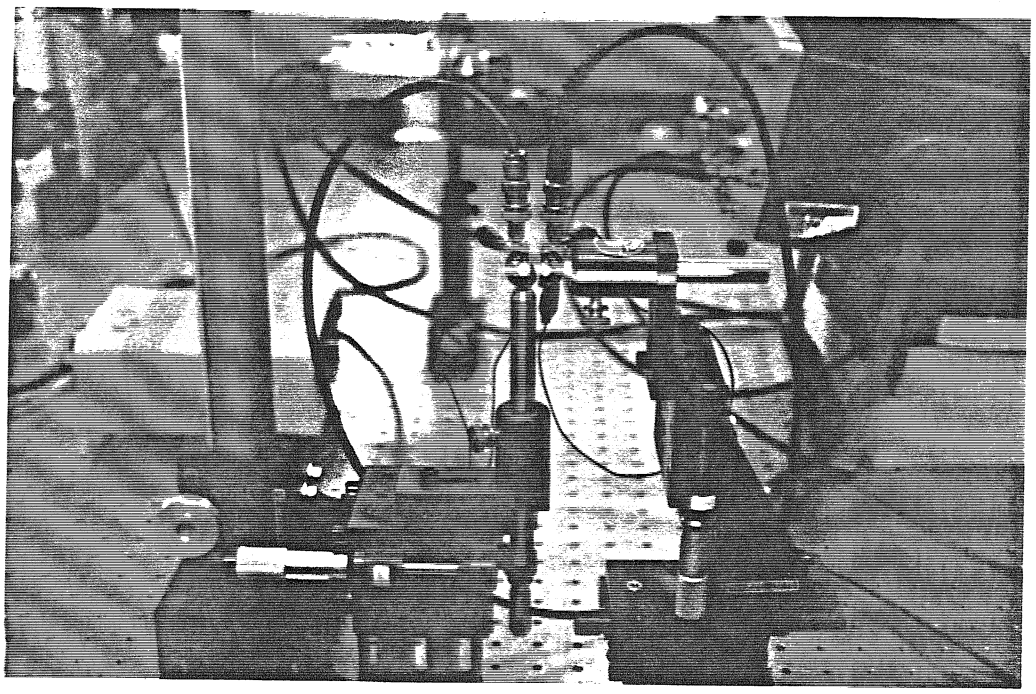

Fig.6.5.3 X-Y translational stage mounted high speed detector pair.

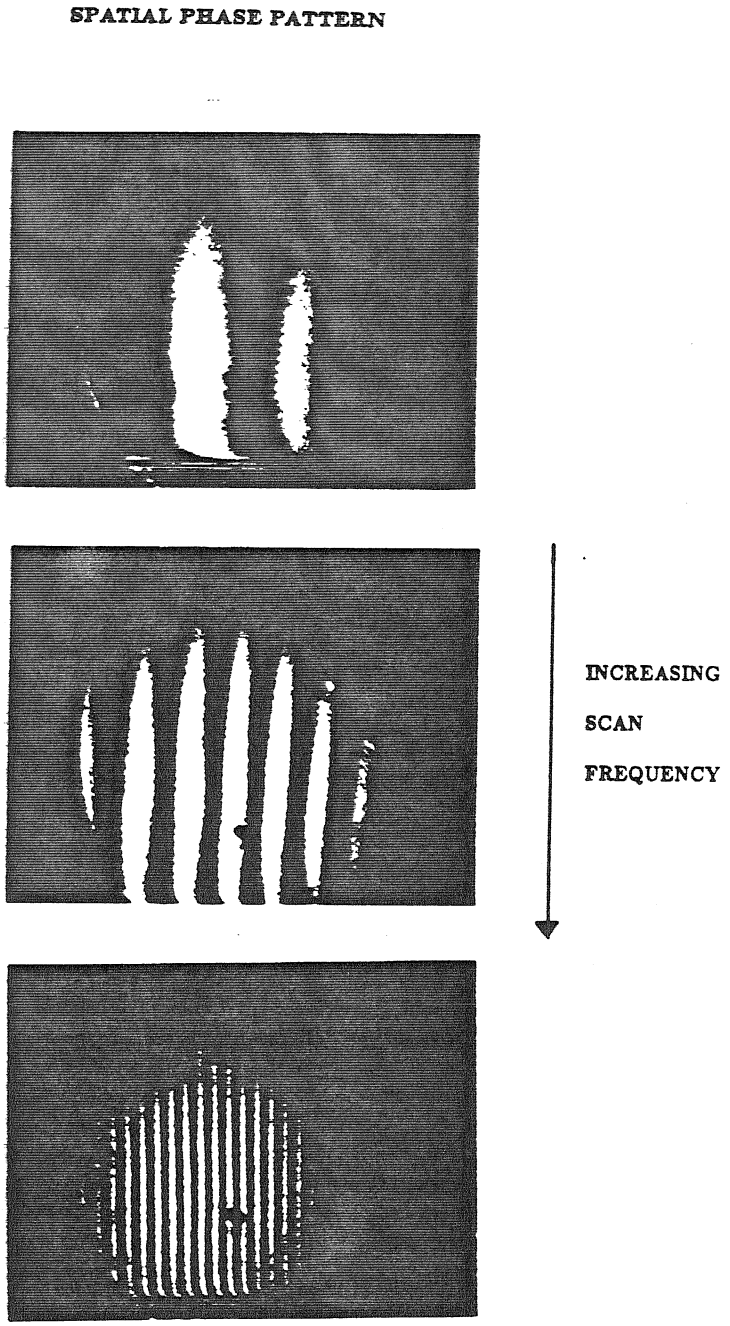

Fig.6.5.4 Spatial phase pattern that detectors sample shown with increasing control frequency.

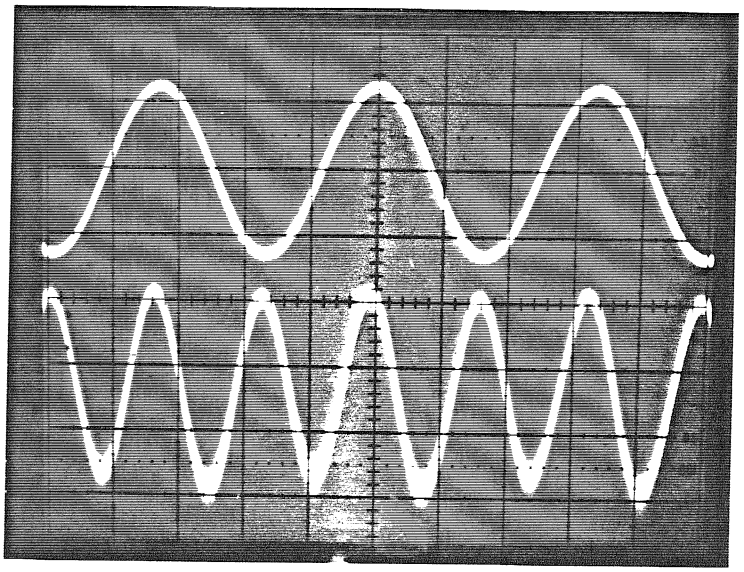

$1 \quad div = 5 \quad nsec$

Fig.6.5.5 Frequency doubling effect via the doppler phenomenon in the AOD's.

PHASE CHANGE WITH CONTROL FREQUENCY CHANGE

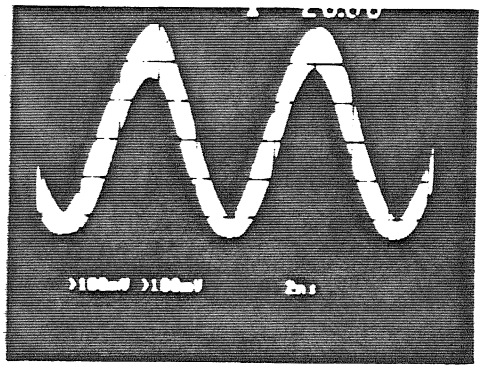

$\Delta\psi = 0$

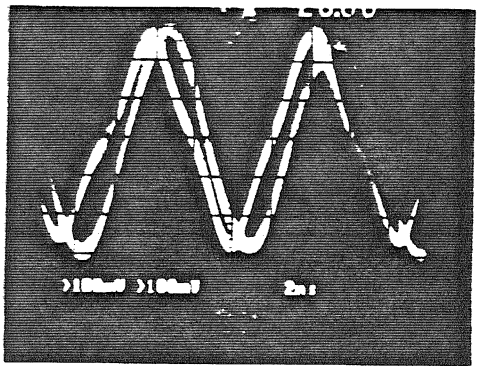

$\Delta\psi = \frac{\pi}{4}$

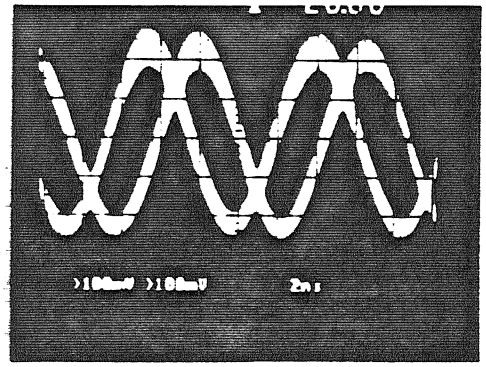

$\Delta\psi = \frac{\pi}{2}$

Fig.6.5.6(a) Varying phase difference $(0 - \frac{\pi}{2})$ between the two signals generated from the detector pair positioned with a fixed inter-detector spacing d.

PHASE CHANGE WITH CONTROL FREQUENCY CHANGE

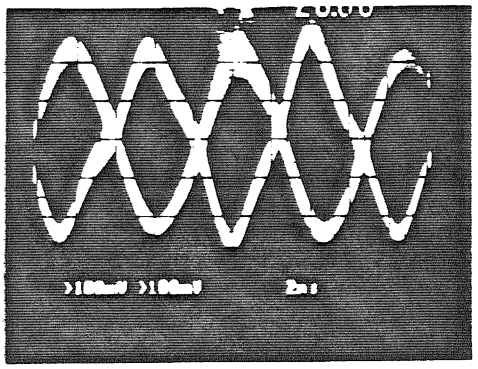

$\Delta\psi = \pi$

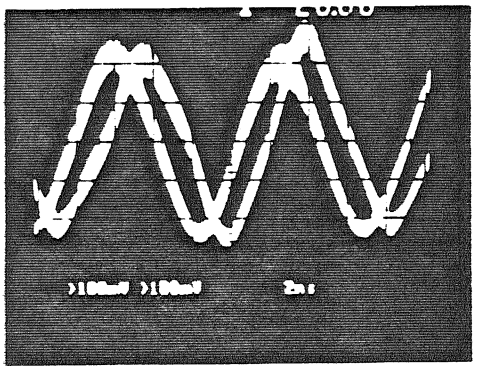

$\Delta\psi = \frac{3\pi}{2}$

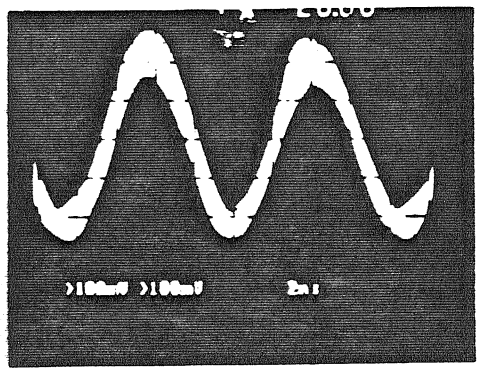

$\Delta\psi = 2\pi$

Fig.6.5.6(b) Varying phase difference $(\pi - 2\pi)$ between the two signals generated from the detector pair positioned with a fixed inter-detector spacing d.

PHASE CHANGE WITH INCREASING DETECTOR SPACING AT A FIXED CONTROL FREQUENCY

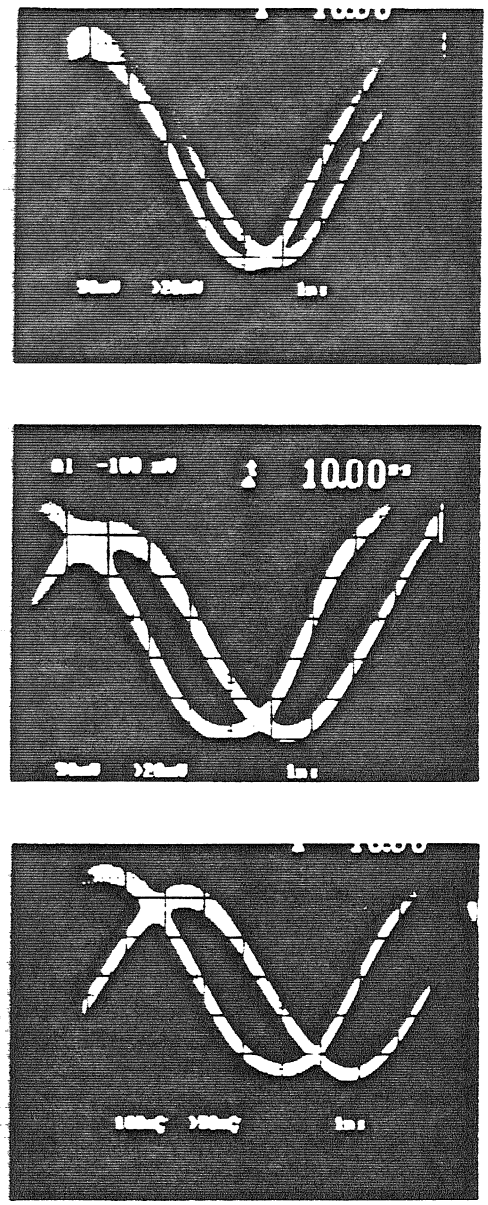

Fig.6.5.7 Phase change for a fixed control frequency when the distance between the detectors is changed.

particular, we will address the following processor issues:

6.6.1 Phase Linearity

The relationship between the detected signal phase change and the control frequency is a linear one. This rate of phase change with frequency is expressed as:

$$s_a = \frac{\psi}{f_0} = .36\frac{d}{Mv_a} \qquad deg/KHz. \tag{6.6.1.1}$$

The slope error is defined as:

$$E_s = \frac{|s_a - s_e|}{s_a} \times 100\%, \tag{6.6.1.2}$$

where s_e is the slope measured from the experimental data. The rate of phase change with frequency in the experimental processors is as follows:

System A (Glass Cells):

1. At $d = 5.5mm$, $s_a = .1218°/KHz$, $s_e = .1224°/KHz$, and $E_s = .49\%$
2. At $d = 10.16mm$, $s_a = .2251°/KHz$, $s_e = .21°/KHz$, and $E_s = 6.7\%$

System B (Tellurium Dioxide Cells):

1. At $d = 5.9mm$, $s_a = .826°/KHz$, $s_e = .83°/KHz$, and $E_s = .48\%$
2. At $d = 10.7mm$, $s_a = 1.5°/KHz$, $s_e = 1.512°/KHz$, and $E_s = .8\%$

The experimental plots for phase change with change in control frequency show a linear relationship (See Fig. 6.6.1.1(a,b):plots 1-2). In addition, the plots demonstrate that if the detector spacing d is doubled, the slope s_e is also doubled. The slope error E_s is calculated and is very small for the different experimental setups. This slope error is useful when calibrating the processor for applications such as frequency controlled beam scanning. The error will tell how far the processor is from

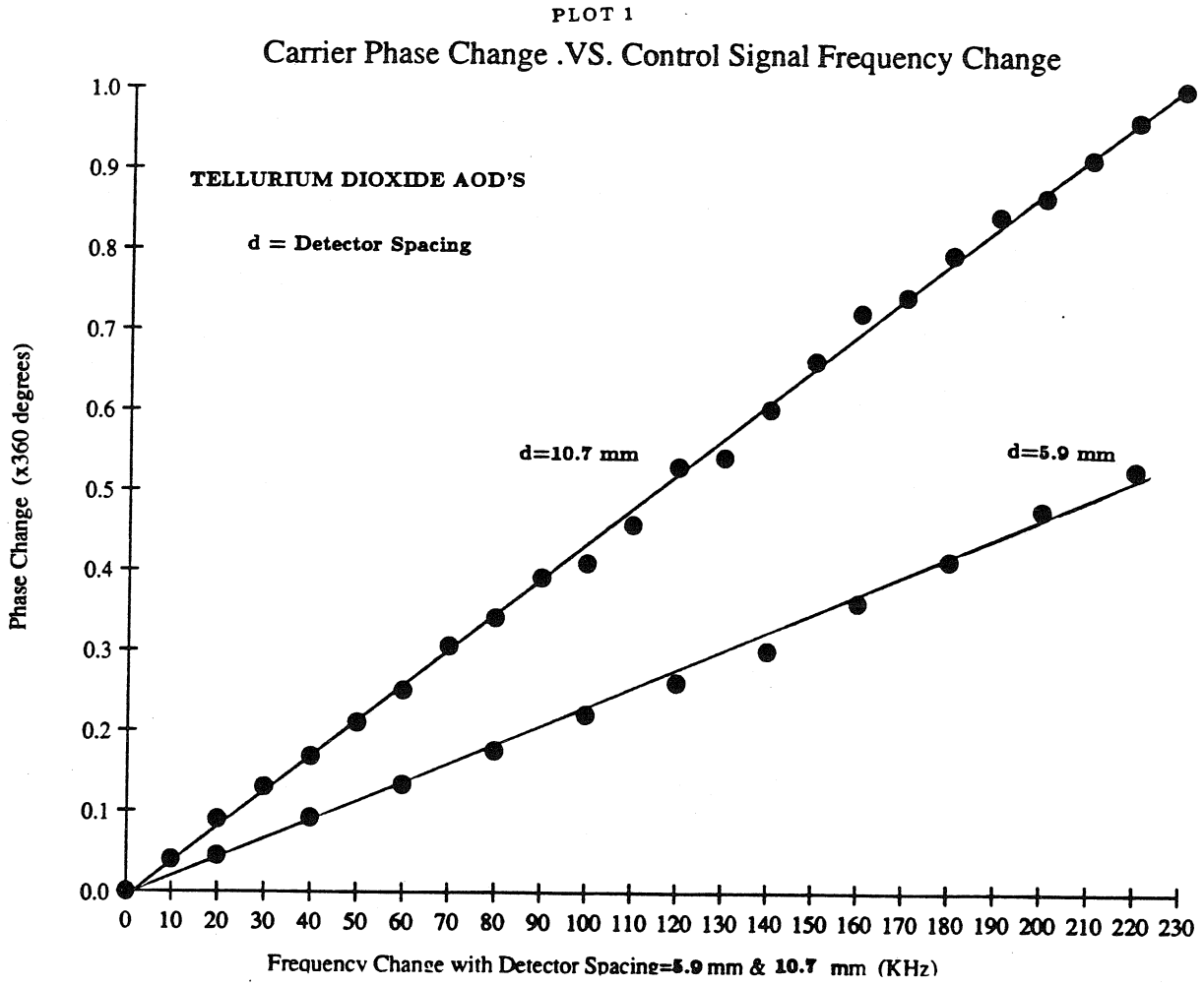

Fig.6.6.1.1(a) Plot 1.

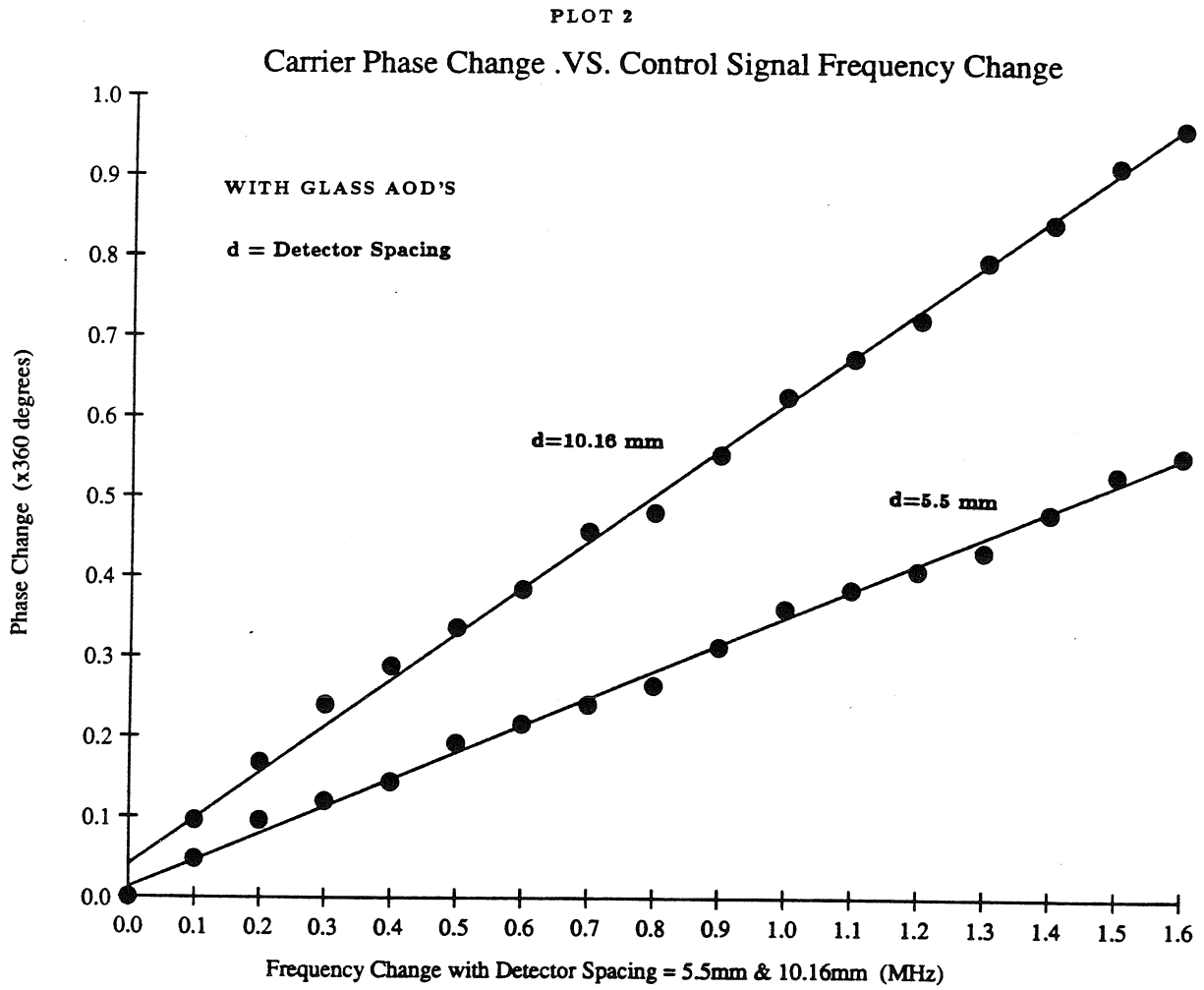

Fig.6.6.1.1(b) Plot 2.

its analytically designed performance. Note that the signal phase change data are measured by recording the signal time delay on the oscilloscope. Improved phase measurements could be achieved if phase detector circuits and phase locked loop electronics are employed.

6.6.2 Beam Scan Angle

The phased array antenna beam position is given by $\theta = \theta_0$, where

$$\theta_0 = \sin^{-1}\left[(\lambda/a)[\frac{p\delta f_0 d}{M v_a} - m]\right], \qquad (6.6.2.1)$$

where $\theta = 0°$ corresponds to the beam at broadside position and p and m are the control frequency and 2π phase multiple indices, respectively. Using the processor design values, the analytical expressions for the different experimental conditions are as follows:

System A (Glass Cells):

$$\theta_0 = \sin^{-1}\left[2(p \times .033845 - m)\right] \qquad d = 5.5mm$$

$$\theta_0 = \sin^{-1}\left[2(p \times .0625 - m)\right] \qquad d = 10.16mm$$

System B (Tellurium Dioxide Cells):

$$\theta_0 = \sin^{-1}\left[2(p \times .03278 - m)\right] \qquad d = 5.9mm$$

$$\theta_0 = \sin^{-1}\left[2(p \times .05945 - m)\right] \qquad d = 10.7mm.$$

These expressions for beam scan angle (degrees) versus control frequency are plotted to compute the expected beam scan behavior (See Fig. 6.6.2.1(a,b):plots 3-4). The experimental beam scan performance for the different designs is calculated from the expression:

$$\theta_{0Expt} = \sin^{-1}\left[(\lambda/a)[\frac{ps_e\delta f_0}{360} - m]\right], \qquad (6.6.2.2)$$

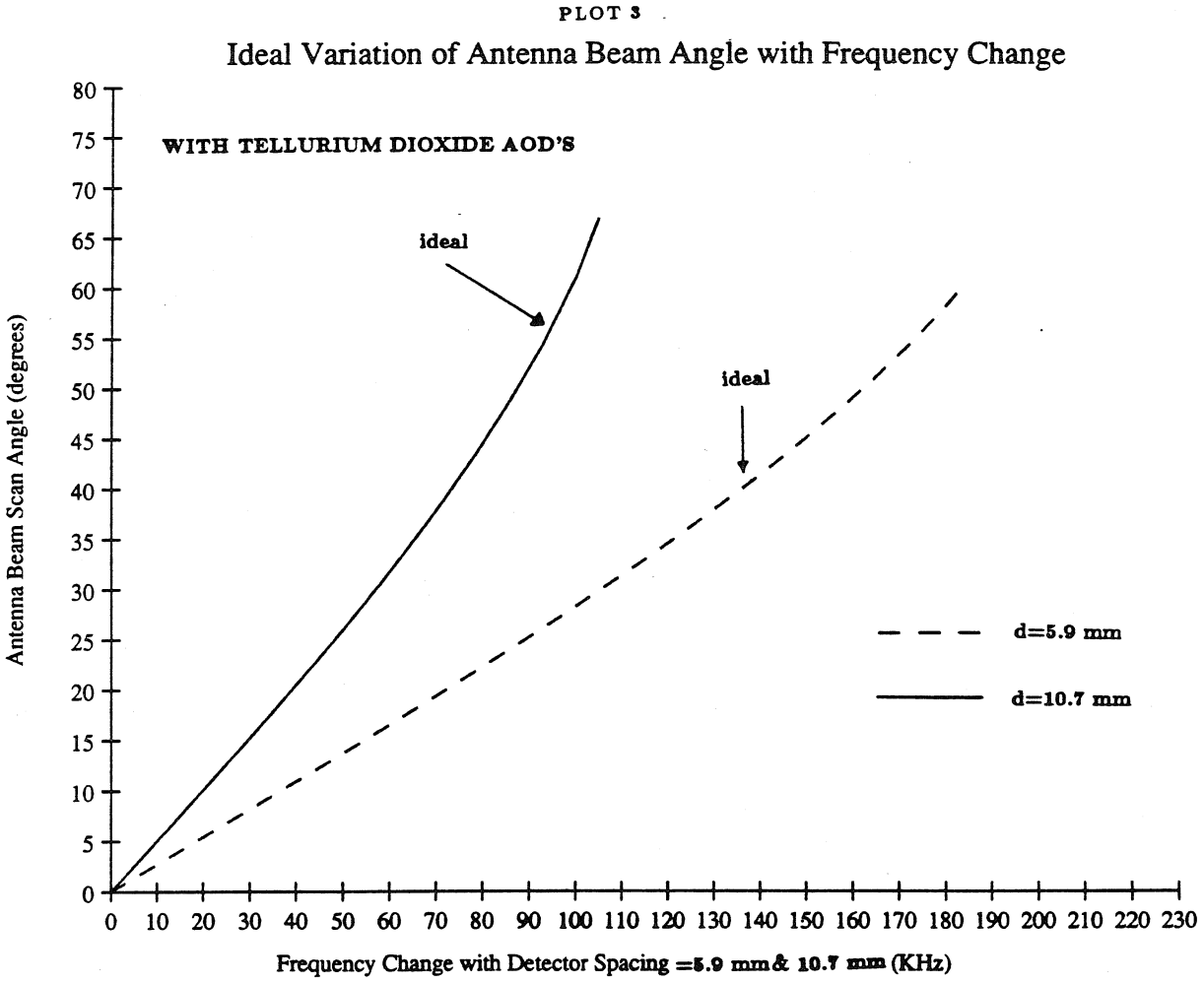

Fig.6.6.2.1(a) Plot 3.

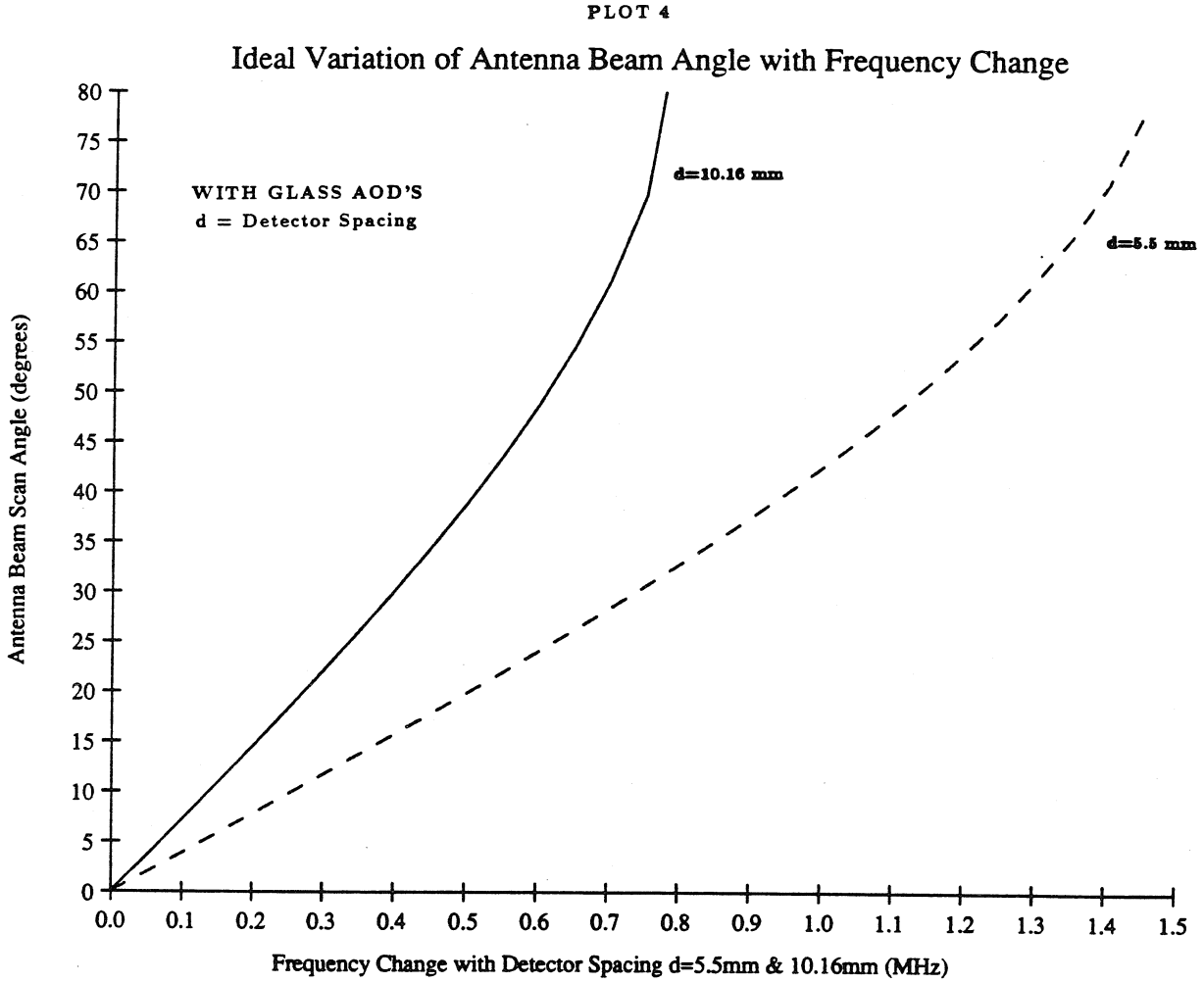

Fig.6.6.2.1(b) Plot 4.

where s_e is the rate of signal phase change with frequency calculated from the experimental phase measurements. The scan angle expressions for the experimental processors are:

System A (Glass Cells):

$$\theta_{0Expt} = \sin^{-1}\Big[2(p \times .034 - m)\Big] \qquad d = 5.5mm$$

$$\theta_{0Expt} = \sin^{-1}\Big[2(p \times .0583 - m)\Big] \qquad d = 10.16mm$$

System B (Tellurium Dioxide Cells):

$$\theta_{0Expt} = \sin^{-1}\Big[2(p \times .0329 - m)\Big] \qquad d = 5.9mm$$

$$\theta_{0Expt} = \sin^{-1}\Big[2(p \times .06 - m)\Big] \qquad d = 10.7mm.$$

Measured data values are used to plot the scan angle vs. control frequency graphs, and curve fitting shows the expected arc sine behavior (see Fig. 6.6.2.2(a,b): plots 5-6). The experimental scan angle variation matches closely with the analytically designed behavior, as can also be seen by comparing the scan angle expressions for the two cases.

The minimum scan angle occurs when $p = 1$, while the maximum scan angle is obtained from the condition:

$$\sin\theta_0 \leq 1, \tag{6.6.2.3}$$

for $p = 0, 1, 2, \ldots$. These minimum and maximum scan angles are calculated for the processors with $m = 0$. The results are:

System A (Glass Cells):

1 . $d = 5.5mm$, $\theta_{0min} = 3.9°$, and $\theta_{0max} = 72.2°$ at $p = 14$

2 . $d = 10.16mm$, $\theta_{0min} = 6.7°$, and $\theta_{0max} = 68.9°$ at $p = 8$

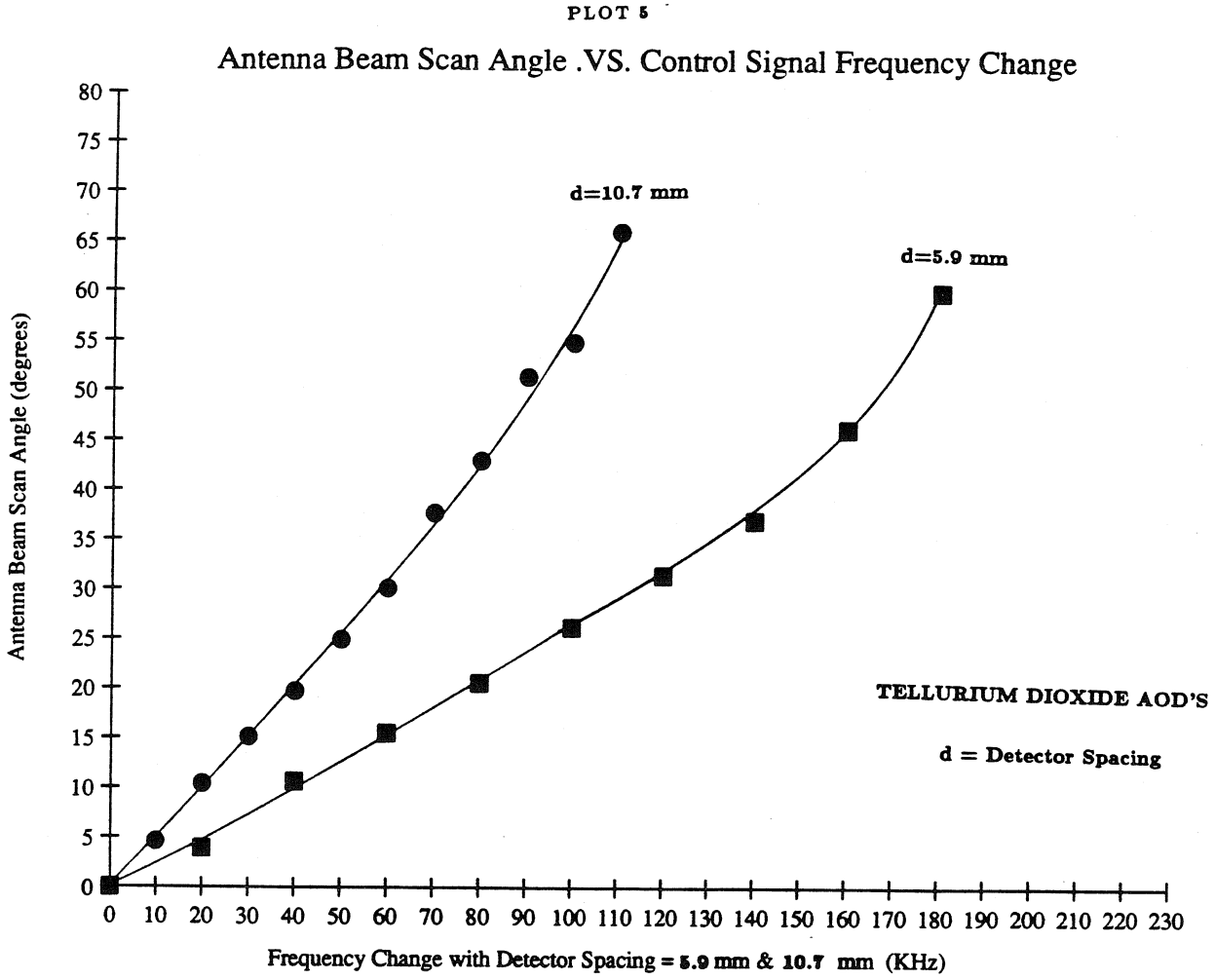

Fig.6.6.2.2(a) Plot 5.

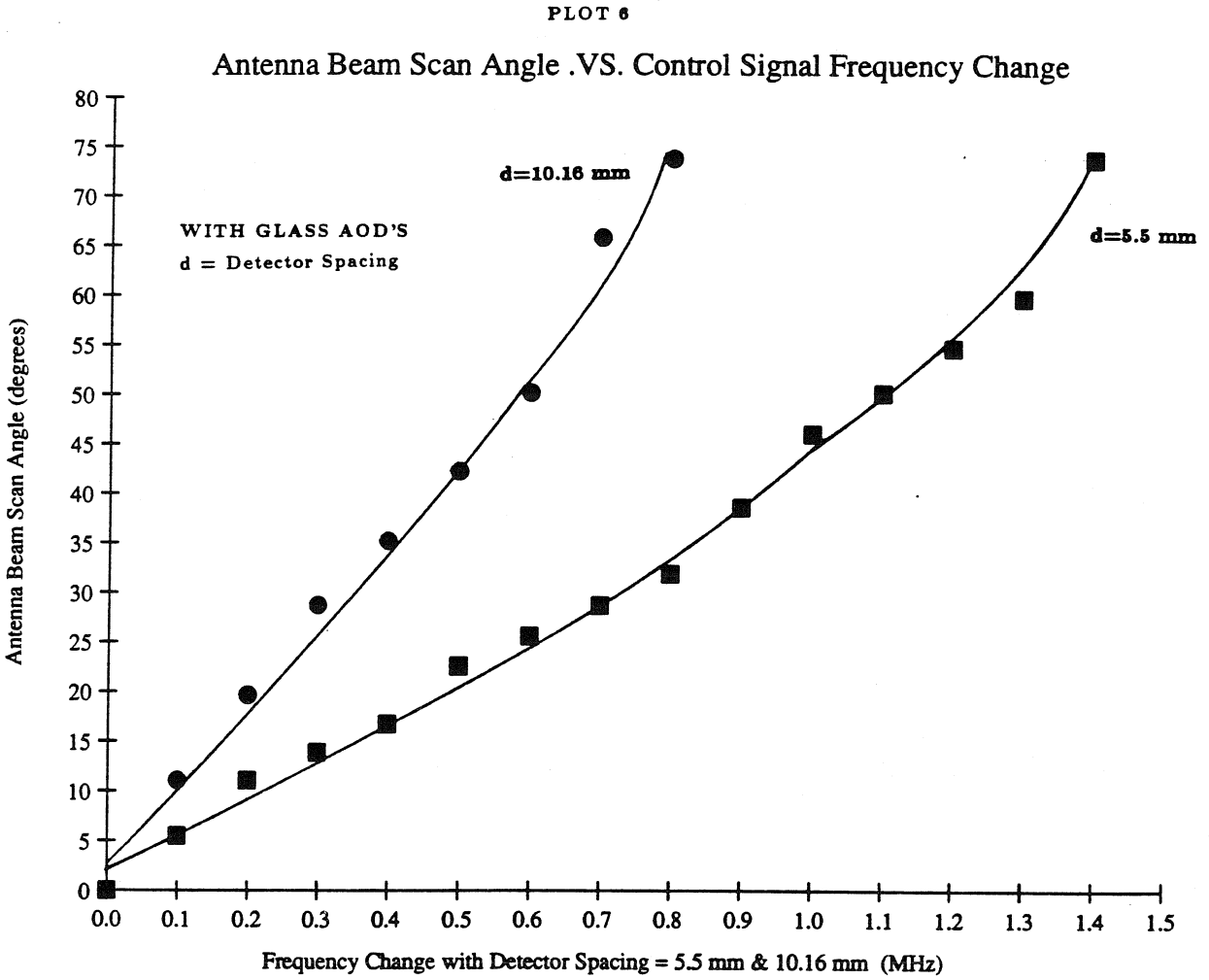

Fig.6.6.2.2(b) Plot 6.

System B (Tellurium Dioxide Cells):

1 . $d = 5.9mm$, $\theta_{0min} = 3.8°$, and $\theta_{0max} = 80.75°$ at $p = 15$

2 . $d = 10.7mm$, $\theta_{0min} = 6.9°$, and $\theta_{0max} = 73.7°$ at $p = 8$

6.6.3 Number of Beam Positions

The maximum number of beam positions for the phased array antenna is given by:

$$N_{beam} = p_{max} + 1, \tag{6.6.3.1}$$

where p_{max} corresponds to the frequency index for the maximum scan angle. The $+1$ is added to include the broadside beam position. Notice from the previous discussion that there exists an inverse relationship between the processor detector spacing and the number of independent beam positions for the phased array antenna. For instance, in system B with $d = 5.9mm$, there are 16 beam positions. When d is almost doubled to $10.7mm$, the number of beam positions drops to 9. Also note that the increase in beam positions is at the cost of increased control frequency bandwidth and higher detector phase sampling error. The increased bandwidth of the radar carrier can be eliminated if we use the beam steerer 2 optical architecture earlier introduced in Section 6.4.

6.6.4 Control Frequency Bandwidth

The control frequency bandwidth is determined by the frequency required for the maximum scan angle θ_{0max} and is given by:

$$BW = \Delta f_0 = p_{max} \delta f_0. \tag{6.6.4.1}$$

The bandwidth values for the experimental processors are:

System A (Glass Cells):

1 . $BW = 1.4MHz$ at $d = 5.5mm$

2 . $BW = 0.8MHz$ at $d = 10.16mm$

System B (Tellurium Dioxide Cells):

1 . $BW = .214MHz$ at $d = 5.9mm$

2 . $BW = .114MHz$ at $d = 10.7mm.$

The narrowband nature of the processors can be calculated from :

$$\eta = \frac{BW}{f'} \times 100\%, \tag{6.6.4.2}$$

where the radar carrier $f' = 2f_c + BW/2$. The AOD center frequency used is $f_c = 60MHz$, giving a carrier around $120MHz$. For the experimental processors, η is:

System A (Glass Cells):

1 . $\eta = 1.16\%$ at $d = 5.5mm$

2 . $\eta = 0.66\%$ at $d = 10.16mm$

System B (Tellurium Dioxide Cells):

1 . $\eta = 0.18\%$ at $d = 5.9mm$

2 . $\eta = 0.09\%$ at $d = 10.7mm.$

The small values of η ($\leq 2\%$) for the experimental processors show that indeed the design is narrowband in nature, insuring accurate beam pointing for the phased array antenna. Note that for the alternate beam steerer 2 shown earlier in Fig. 6.4.3, the radar carrier is unaffected by changes in the processor phase control frequency, giving a single tone carrier signal ($BW \approx 0$).

6.6.5 Detector Phase Sampling

Ideally, the detector array is supposed to act as a spatial impulse train that samples phase values along the optically generated spatial carrier in the x direction. In this section, we analyze the effects of the finite size of the detector elements. The intensity incident on the n^{th} detector is given by:

$$I_n(x,t) = Bias + G_0 \cos[\omega t - \frac{\omega_0}{Mv_a}x] \,\mathrm{rect}[\frac{x-nd}{d_x}] \,\mathrm{rect}[\frac{y-.5d_y}{d_y}], \qquad (6.6.5.1)$$

where d_x and d_y are the width and height of the detector respectively. The current generated after spatial integration of the incident light on the detector's photo-sensitive area is:

$$i_n(t) = \int_0^{d_y} \int_{-.5d_x+nd}^{.5d_x+nd} G_0 \cos[\omega t - \frac{\omega_0}{Mv_a}x]\, dx\, dy \quad + Bias. \qquad (6.6.5.2)$$

Solving the integral by substituting $x' = \omega t - \frac{\omega_0}{Mv_a}x$, we get :

$$\begin{aligned} i_n(t) &= -\frac{G_0 d_y M v_a}{\omega_0} \sin(x') \Big|_{\omega t - \frac{\omega_0}{Mv_a}(-.5d_x+nd)}^{\omega t - \frac{\omega_0}{Mv_a}(.5d_x+nd)} \\ &= \frac{G_0 d_y M v_a}{\omega_0} \sin(\frac{\omega_0 d_x}{2Mv_a}) \cos[\omega t - n\frac{\omega_0 d_x}{Mv_a}] \quad + Bias. \end{aligned} \qquad (6.6.5.3)$$

Substituting $u_x = \frac{f_0}{Mv_a}$ in the expression for the current, it can be expressed as:

$$i_n(t) = \frac{G_0 d_y}{2\pi u_x} \sin(\pi u_x d_x) \cos[\omega t - n2\pi u_x d] \quad + Bias. \qquad (6.6.5.4)$$

It is interesting to note that the phase of the signal $i_n(t)$ is unaffected by the detector size. Let us look at two cases.

1 . If $u_x = 0$, the current is $i_n(t) = \frac{G_0 d_x d_y}{2} \cos[\omega t] \quad + Bias.$ As expected, when there is no spatial carrier on the detector plane, only a temporal signal is generated without a phase term.

2 . If the condition $u_x d_x \ll 1$ holds, we can use the approximation $sin\alpha \approx \alpha$ for small α, giving the current:

$$i_n(t) \approx \frac{G_0 d_y}{2\pi u_x} \pi u_x d_x \cos[\omega t - n2\pi u_x d] \quad + Bias \tag{6.6.5.5}$$

$$i_n(t) = \frac{G_0 d_x d_y}{2} \cos[\omega t - n2\pi u_x d] \quad + Bias. \tag{6.6.5.6}$$

In other words, if the detector width is much smaller than the spatial carrier period, we can approximate the finite size detector phase sampling as an impulse function sampling train. Of course, this result is also physically obvious. The current from the high speed amplifier connected to the detector output can be expressed as:

$$i_n(t) \approx G \cos[\omega t - n2\pi u_x d], \tag{6.6.5.7}$$

where the signal gain is $G = \frac{G_1 G_0 d_x d_y}{2}$ and G_1 is the amplifier gain.

The values of $u_x d_x$ for the experimental processors are calculated with the detector width $d_x = 200\mu m$, and are listed as:

System A (Glass Cells):

1 . $u_x d_x = 0.017$ at $d = 5.5mm$

2 . $u_x d_x = 0.0098$at $d = 10.16mm$

System B (Tellurium Dioxide Cells):

1 . $u_x d_x = 0.0167$ at $d = 5.9mm$

2 . $u_x d_x = 0.0089$ at $d = 10.7mm$.

These data show that indeed the experimental designs satisfy the detector phase sampling condition:

$$u_x d_x \ll 1. \tag{6.6.5.8}$$

Looking at Eqn.6.6.5.4, the current signal amplitude term consists of the gain term:

$$\frac{G_0 d_y}{2\pi u_x} \sin(\pi u_x d_x).$$

If the condition in Eqn.6.6.5.8 is not satisfied, the signal gain varies inversely with the spatial frequency u_x. As the spatial frequency is increased, the finite detector samples a greater phase variation, eventually averaging over more than a single spatial fringe cycle, leading to an averaging to zero effect. This leads to the diminishing of the output signal.

Note that the signal gain is proportional to the detector area. In order to get a larger signal, the height of the detector d_y can be increased, keeping d_x such that it satisfies the condition in Eqn.6.6.5.8.

6.6.6 Number of Antenna Current Drivers

The maximum number of individual phase controlled currents that can be generated by the linear phased array processors is:

$$N = int[\frac{MX}{d}] + 1, \tag{6.6.6.1}$$

where M is the optical system magnification, d the detector spacing, and X the length of the AOD used in the optical processor. N also gives the maximum number of individual phased array antenna elements that the processor is capable of driving. For the experimental processors, we have:

System A (Glass Cells):

1 . $N = 30$ at $d = 5.5mm$

2 . $N = 17$at $d = 10.16mm$

System B (Tellurium Dioxide Cells):

1 . $N = 31$ at $d = 5.9mm$

2 . $N = 17$ at $d = 10.7mm$.

It is important to point out that in the processors described so far, the space between any pair of adjacent detectors on the slit of light was not utilized. In effect,

if we place additional arrays of detectors in these empty positions, the effective number of detectors (corresponding to antennas) that can be employed approaches

$$N \rightarrow \frac{MX}{d_x},$$

where this number is limited by the AOD space bandwidth product (SBWP) and the diffraction limited resolution of the optical imaging system. Section 6.10 describes some alternate techniques for detector phase sampling.

6.6.7 Processor Bandwidth/Beam Switching Speed

How fast we can switch a beam from one angular position to another depends on how quickly all the detectors provide steady state correctly phased antenna drive signals. The processor frequency response depends on the Bragg cell fill time given by $T_a = X/v_a$, where X is the AOD aperture utilized. T_a is also called the array fill time and affects the transient response of the antenna when the transmitted pulse width T_p is of the order of the array fill time. A more formal analysis of the **antenna impulse response** is as follows.

In the analysis to follow, we assume that the bandwidth of the optical processor elements and the antenna radiating elements is much greater than the radiated signal bandwidth. Also, the complete radar system is assumed to have a linear input-output relationship. The impulse response $h(t)$ of the radar system is useful as the response at a target which is due to a signal $s(t)$ is the convolution of $h(t)$ with $s(t)$.

Although the proposed phased array radar has a parallel current feed format, the individual signal generation is based on a series fed structure, similar to a $1-D$ end fed array of total length X. The array signal generation is based on the interaction between the two counter propagating acoustic signals in the two AOD's

and the light carrier. Assuming that a length X of the two respective AOD's is illuminated with Bragg matched light beams, it takes $X/2v_a$ seconds for the two acoustic signals to cross, and X/v_a seconds for complete interaction between the two signals to occur. At this stage, all the detectors are illuminated by the acoustically modulated light signals, and phased currents are being generated for the radiating antennas.

The array antenna aperture illumination function can be written as [26]:

$$A(x,\omega) = B(x) \quad e^{-j\frac{(\omega-\omega_{RF})}{MM_1 v_a}x} \quad \text{rect}(\frac{x}{MM_1X}) \tag{6.6.7.1}$$

where $T_a = X/v_a$: total delay time through the AOD

M : Magnification of the illuminated AOD to detector plane

M_1 : Magnification of the detector plane to the antenna plane

ω_{RF} : Radar carrier frequency with beam at broadside

ω : Transmit radian frequency equal to $\omega_{RF} + p\delta\omega$

$B(x)$: Normalized illumination across the AOD aperture

$(\omega - \omega_{RF})T_a$: Total phase variation across the array aperture,

and the 1-D detector array corresponds to the antenna array aperture. The steady state (CW) amplitude pattern for a beam directed at an angle θ with respect to broadside is given by:

$$F(\omega,\theta) = \int_{-\infty}^{+\infty} A(x,\omega)e^{j\frac{2\pi x}{\lambda}\sin\theta} \quad dx. \tag{6.6.7.2}$$

$F(\omega,\theta)$ can be considered as the transfer function of the linear system. For a uniformly illuminated aperture with $B(x) = 1$, $\frac{2\pi}{\lambda} = \omega/c$, and using Eqn.6.6.7.1,

we get:

$$
\begin{aligned}
F(\omega,\theta) &= \int_{-\infty}^{+\infty} e^{-j\frac{(\omega-\omega_{RF})}{MM_1v_a}x} \quad e^{j\frac{\omega x}{c}\sin\theta}\mathrm{rect}(\frac{x}{MM_1X})dx \\
&= \int_{-\infty}^{+\infty} e^{-j[\frac{(\omega-\omega_{RF})}{MM_1v_a}-\frac{\omega}{c}\sin\theta]x}\mathrm{rect}(\frac{x}{MM_1X})dx \\
&= MM_1\frac{\sin[\beta T_a/2(\omega-\omega_{RF}/a)]}{\beta T_a/2(\omega-\omega_{RF}/a)},
\end{aligned}
\tag{6.6.7.3}
$$

where $\beta = 1 - \frac{T_f}{T_a}\sin\theta$, and the free space time delay $T_f = MM_1X/c$. The impulse response $h(t,\theta)$ of the system is the inverse Fourier transform of the processor transfer function $F(\omega,\theta)$.

$$
\begin{aligned}
h(t,\theta) &= \frac{1}{2\pi}\int_{-\infty}^{+\infty} F(\omega,\theta)e^{j\omega t} \quad d\omega \\
&= \frac{MM_1X}{2\pi}\int_{-\infty}^{+\infty}\frac{\sin[\beta T_a/2(\omega-\omega_{RF}/a)]}{\beta T_a/2(\omega-\omega_{RF}/a)}e^{j\omega t}d\omega \\
&= \frac{MM_1X}{\beta T_a}\mathrm{rect}(\frac{t}{\beta T_a}) \quad e^{j\frac{\omega_{RF}}{\beta}t}
\end{aligned}
\tag{6.6.7.4}
$$

Using the processor design relation

$$
\sin\theta = \frac{\lambda f_0 d}{aMv_a}, \tag{6.6.7.5}
$$

where f_0 is the scan control frequency producing a beam scan angle θ, the expression for β is:

$$
\beta = \frac{1}{1+f_0/f_{RF}}. \tag{6.6.7.6}
$$

Therefore, the impulse response is given by:

$$
h(t,\theta) = \frac{MM_1X}{T_a}(1+\frac{f_0}{f_{RF}})\mathrm{rect}(\frac{t}{\beta T_a}) \quad e^{j2\pi(f_{RF}+f_0)t} \tag{6.6.7.7}
$$

Thus, the impulse response of the phased array antenna driven by the optical processor corresponds to a pulse of RF energy of frequency $f_{RF} + f_0$ and length βT_a.

The length of the RF pulse decreases when θ is positive (f_0 is positive) and increases when θ is negative (f_0 is negative), agreeing with the physical picture of the plane wave front radiating array. To avoid any smearing of the RF pulse energy, the pulse transmitted by the antenna array must satisfy the condition:

$$T_p \geq \beta T_a. \tag{6.6.7.8}$$

For the proposed optical processors, we have

$$f_0 \ll f_{RF} \quad \Rightarrow \quad \beta \approx 1. \tag{6.6.7.9}$$

Using this approximation, the impulse response of the antenna/optical processor configuration is given by:

$$h(t,\theta) = \frac{MM_1X}{T_a}\text{rect}(\frac{t}{T_a}) \quad e^{j2\pi(f_{RF}+f_0)t}. \tag{6.6.7.10}$$

This gives the maximum instantaneous bandwidth of the processor to be:

$$BW_{max} = \frac{1}{2T_a}, \tag{6.6.7.11}$$

which is also the maximum beam position switching rate. The analytical results show that indeed the beam scanning speed is determined by the array (or AOD) fill time. Also note that the radar range resolution is determined by the minimum pulse width transmitted, and this in turn is limited by the radar impulse response.

6.6.8 System Noise

The key sources of noise in the processor are:

1 . Electrical noise contributed from the AOD driver amplifiers and detector high speed operational amplifiers.

2 . Optical noise resulting from optical misalignment, light scattering, multiple reflections, acoustic apodization in the AOD's, and optical detector noise.

In the case of optical misalignment of the two interfering beams, this processor has the ability to remove the misalignment by introducing a positive or negative frequency offset to the AOD drive signal, steering the misaligned beam into its correct position.

6.6.9 Input/Output Power Requirements

AOD's are power inefficient devices, and therefore the optical power requirements are high for these processors. In the experimental processors, the AOD's operated at less than 10% diffraction efficiencies, requiring around $250mW$ of Argon laser optical power. One approach to reducing optical power requirements is to use infrared light where present optical detectors are more efficient. The glass cells used a drive power of $.56W$, and the detector output was $80mV_{pp}$ at 50 ohms. The tellurium dioxide cells used a drive power of $.16W$, and the detector output was $60mV_{pp}$ at 50 ohms. The diffraction efficiencies of the Bragg cells can be improved $(100\%/RF\ watt)$ if greater AOD RF drive power is used.

6.7 The Optical Radar Signal Processor:Its Applications

6.7.1 Single and Continuous Mode Beam Scanning

This processor can be used to position the phased array antenna beam at discrete angular positions or to scan continuously the antenna beam over a wide angular region. For single mode beam positioning, a specific control frequency is fed to the AOD to give the appropriate scan angle. For continuous beam scanning, a piece-wise linear FM signal is fed to the AOD. The frequency vs. transmission time relationship is shown in Fig.6.7.1.1. For each discrete frequency, the array beam is directed at a certain angle with respect to broadside.

MULTIPLE BEAM FORMATION

Single and Continuous Mode Beam Scanning:

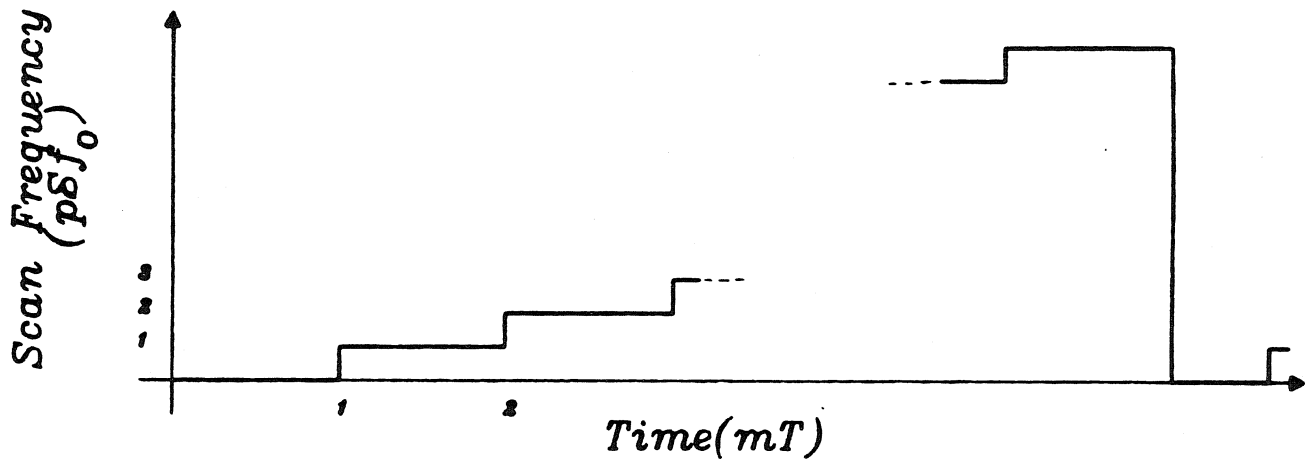

Beam Scan Pattern:

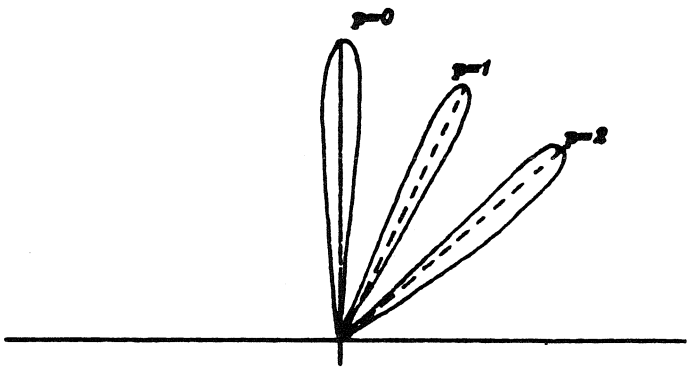

Fig.6.7.1.1 Continuous beam scanning via piece-wise linear FM control frequency signal.

6.7.2 Simultaneous Multiple Beam Formation Capability

The optical radar processor can be used to generate simultaneous multiple beams directed at different angles in space. Also, the processor can be used to produce multiple beams at the same scan angle, although at different RF carrier frequencies.

(a) Triple Beam Formation Feed Network

For a scan control frequency value f_0 corresponding to a beam scan angle θ_0, the drive signals provided by the optical processor can be distributed to the individual antennas such that three independent, simultaneous beams can be generated at positions $\theta = 0°$ (Broadside), $\theta = \theta_0$ and $\theta = -\theta_0$. This particular antenna feed configuration is shown in Fig.6.7.2.1, where the center antenna ($n = 0$) in the array corresponds to the zero phase reference point for the drive signals [17]. Each individual antenna is fed by three signals. For instance, the $n = M$ antenna is driven by signals coming from $n = 0$ (center), $n = M$, and $n = -M$ drivers of the optical processor. Thus, each antenna is fed by a zero phase signal from the center driver of the optical processor, giving the beam at $\theta = 0°$ for all values of the control frequency, plus two conjugate phase signals from the mirror image drivers of the processor, giving the additional two simultaneous beams at $\theta = \theta_0$ and $\theta = -\theta_0$. Thus, by varying the control frequency, the two side beams can be rotated symmetrically around the broadside beam, which stays stationary at all values of the control frequency. The hardware required to implement this feed network could employ an N-way microwave splitter, N-1 microwave 2-way splitters, and N 3-way microwave adders, or could alternately use fiber optic couplers, splitters, and splicing hardware. The 2-way splitter electronic hardware could be eliminated if a 50:50 optical beam splitter is used before the output detector sampling plane of

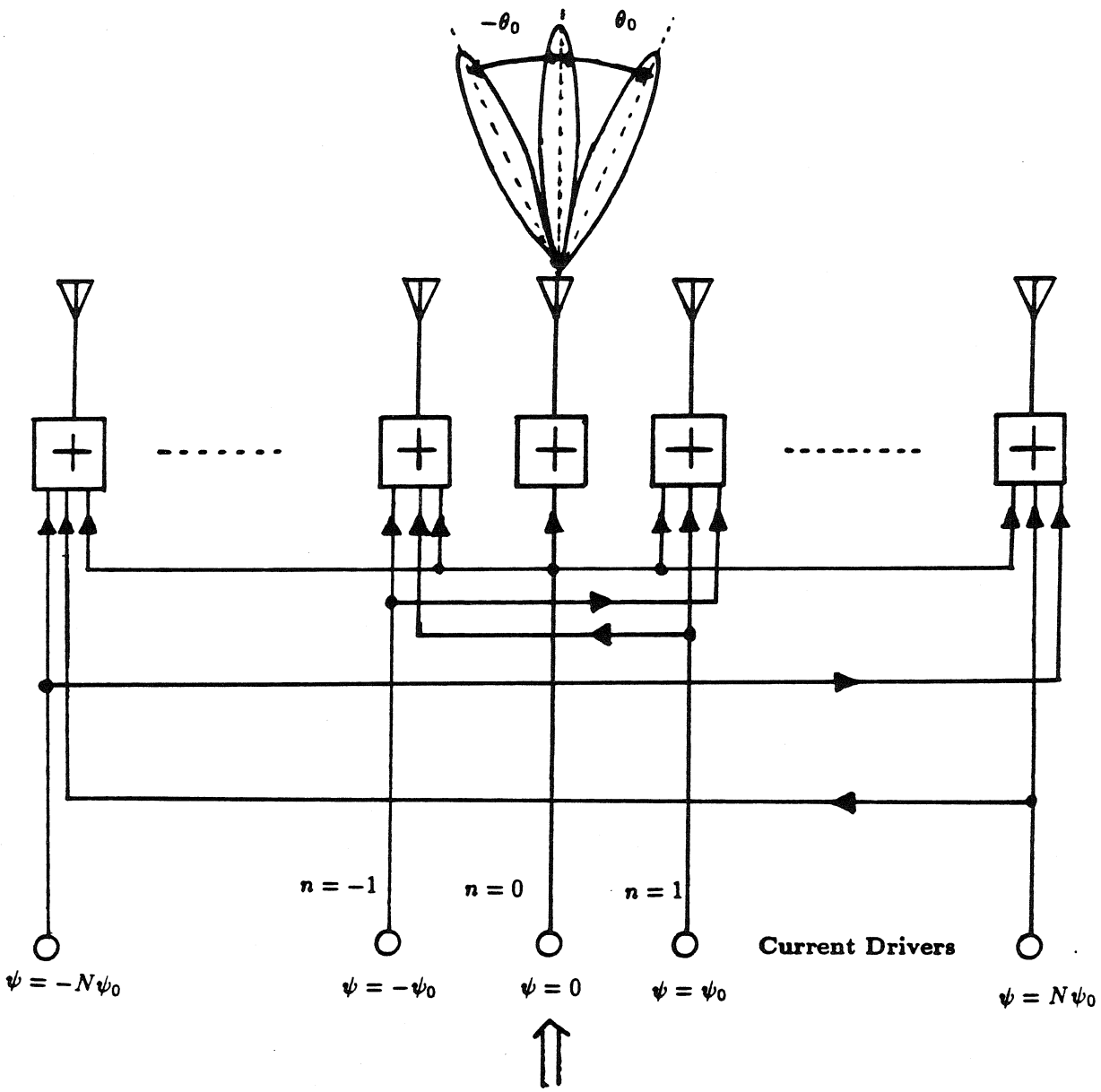

Fig.6.7.2.1 Array antenna triple beam formation feed network.

the processor to cause a coordinate reversal and splitting operation optically. The appropriate signals from the two output ports of the processor are added optically (using fiber couplers) or electronically (using microwave adders) to give the desired three beams. Fig. 6.7.2.2 shows a possible implementation to generate the mirror image beams using fiber couplers and a beam splitter.

(b) Multiple Beam Formation Architecture using a Multichannel AOD

Fig.6.7.2.3 shows the optical system required to form $N+1$ simultaneous arbitrary beams in space. The system is similar to the single beam generation system, except the single laser source is replaced by a laser diode array of $N+1$ mutually incoherent sources, and the second AOD is replaced by an $N+1$ channel AOD corresponding to the $N+1$ beams. The side view of the system shows that light from all the sources interacts with the first single channel AOD, while there is a 1:1 source to channel mapping in the multichannel AOD; i.e., the p^{th} laser diode light interacts only with the p^{th} channel in multichannel AOD. The signal fed to the first AOD is:

$$s_1(t) = a\cos(\omega_c t), \tag{6.7.2.1}$$

while the signal fed to the p^{th} channel of the multichannel AOD is:

$$s_{2p}(t) = a_p\cos[(\omega_c + \omega_p)t], \tag{6.7.2.2}$$

where ω_p is the control frequency required to produce the p^{th} beam at a scan angle θ_p. A combination of spherical and cylindrical lenses at the output of the processor integrates the light from different, spatially multiplexed channels in the AOD on to the 1-D detector array, giving a sum of individual light intensities from each source; i.e., the light from the n^{th} detector in the linear detector array is:

$$\begin{aligned} i_n(t) &= \sum_{p=0}^{N} I_p(n) \quad + \quad Constant \quad Bias \\ &= I_0(n) + I_1(n) + \ldots + I_N(n) \quad + \quad Constant \quad Bias, \end{aligned} \tag{6.7.2.3}$$

FIBER/BEAM SPLITTER IMPLEMENTATION OF THE
BEAM FORMATION NETWORK

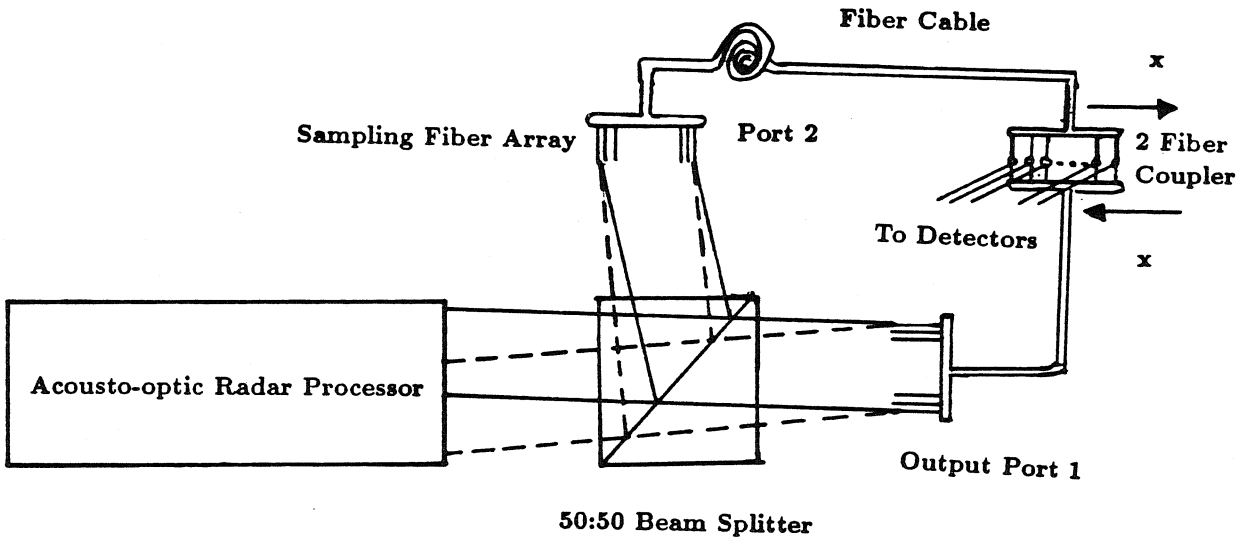

Light at ports 1 and 2 are mutually incoherent

Fig.6.7.2.2 Optical implementation of the triple beam formation network.

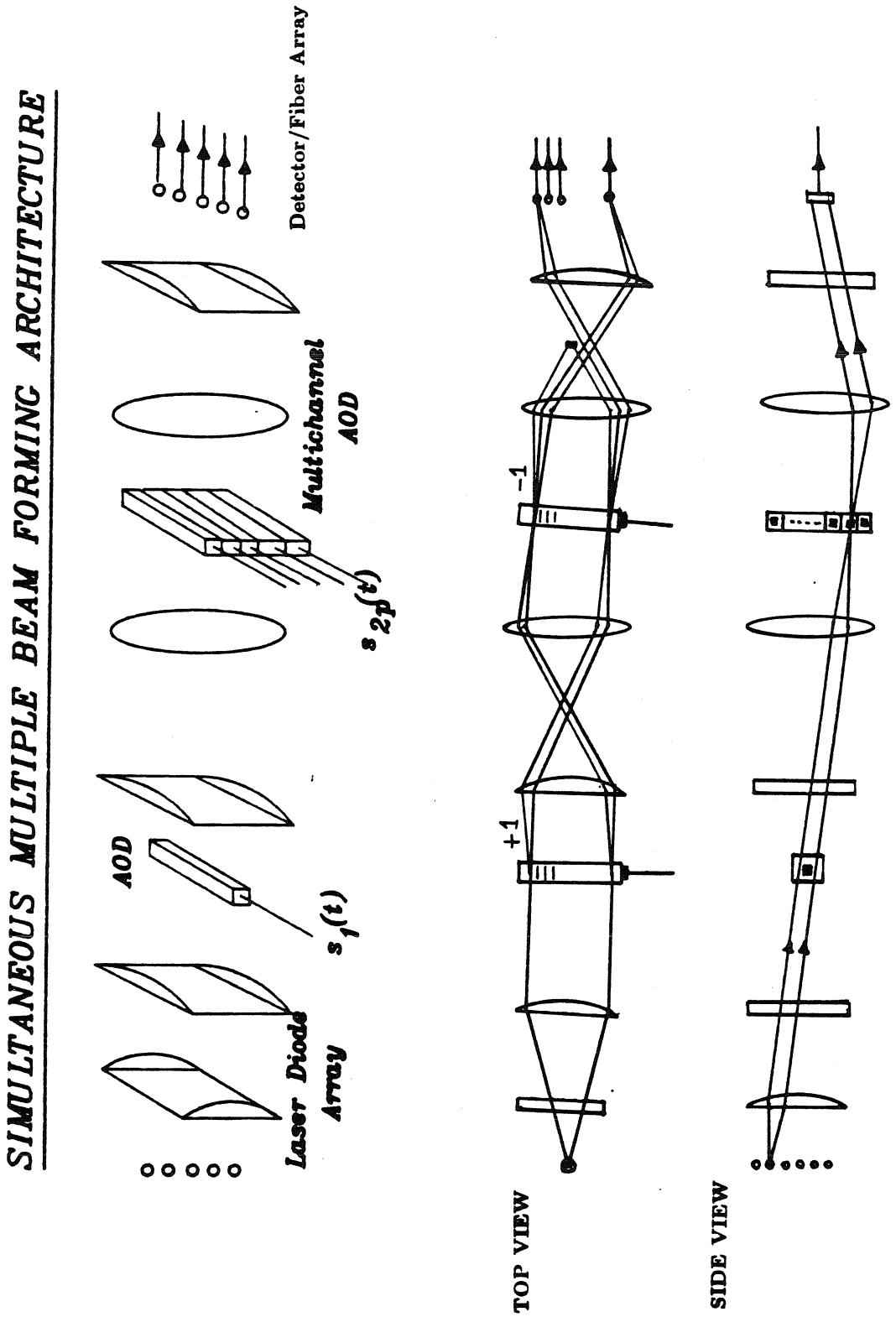

Fig.6.7.2.3 $N+1$ simultaneous beams multi-channel AOD optical beam steerer.

where

$$I_p(n) = G_p \cos[(2\omega_c + \omega_p)t - n\psi_p], \qquad (6.7.2.4)$$

and ψ_p is the required phase shift to position a beam at angle θ_p to broadside. Thus, $i_n(t)$ gives the required $N+1$ signals needed to generate simultaneously $N+1$ beams at scan angles $\theta_0, \theta_1, \ldots, \theta_N$, respectively. Note that each beam position corresponds to a different radar carrier frequency. If we choose $\omega_p = p\delta\omega_0$, where $\delta\omega_0$ is the minimum control frequency required for a beam scan, we can generate the maximum number of beams in space over a certain scan range. Note that the constant bias in the expression for $i_n(t)$ is a sum of all the individual bias contributions from each of the laser diodes. This may lead to saturation of the detectors. A solution to this problem is to replace the 1-D detector array with $N+1$ 1-D detector arrays spatially multiplexed in the direction orthogonal to the linear array, and to replace the last cylindrical lens in the optical processor with a spherical lens. This provides separation in the 2-D detector plane of the light modulated by different channels in the multichannel AOD. The signals from detectors along each of the detector columns are added by electronic means and fed to their respective antennas. Currently available 32 channel AOD's could be used in this system to provide a maximum of 32 simultaneous beams in space.

(c) Coexistent Multiple Multifrequency Beams

Simultaneous beams pointing at the same scan angle but on different radar carrier frequencies can be generated by the multichannel AOD processor. As the phase sampling procedure is periodic with 2π radians, a similar phase increment can be obtained for a periodic increment in the control frequency. This behavior is shown in Fig.6.4.3, where m corresponds to the periodic increment in the control frequency. For instance, control frequencies f_1 and f_2 corresponding to $m = 0, 1$, respectively, give two beams at the same scan angle θ_0. By allowing different frequency beams

to exist at the same scan angle, a high data rate of transmission/reception can be achieved from the particular look direction. In addition, as the beams are on different frequencies, the radar system is less susceptible to jamming, thus making it a more secure system. This added feature of the frequency controlled optical system adds greater overall flexibility to the system. For example, under different weather conditions, different frequencies may be optimum for transmission and reception.

6.7.3 Angular Discrimination Receiver System

So far, the hardware that has been described is an optical processor that generates correctly phased drive signals for a phased array antenna such that a radar beam can be electronically steered to any desired direction in space. This section deals with a receiver system that discriminates the angle, range, and doppler information of targets in the radar search range by processing target return signals from the array antenna elements.

The basis of the postprocessing involves reusing the optically generated array transmit signals to cancel the phase factors associated with the received signals from the individual antenna elements, thus generating in phase signals from all the individual returns. This receiver system is shown in Fig. 6.7.3.1, along with the transmitter part of the system. For target detection at a scan angle θ_0 to broadside, we transmit a pulse $p_T(t)$ of RF energy of duration T on a carrier frequency $2\omega_c+\omega_0$, with appropriate phase ψ_0 set by the optical processor. The current driving the n^{th} antenna in the phased array is:

$$i_n(t) = p_T(t)G\cos[(2\omega_c + \omega_0)t - n\psi_0]. \qquad (6.7.3.1)$$

After transmitting the radar pulse, the antenna is operated in the receive mode. The return signal at the n^{th} antenna from a target at θ_0 to broadside is approximately given by [5]

$$i_n(t') = p_T(t')G_{TR}(n)\cos[(2\omega_c + \omega_0 + \omega_d)t' - n\psi_0], \qquad (6.7.3.2)$$

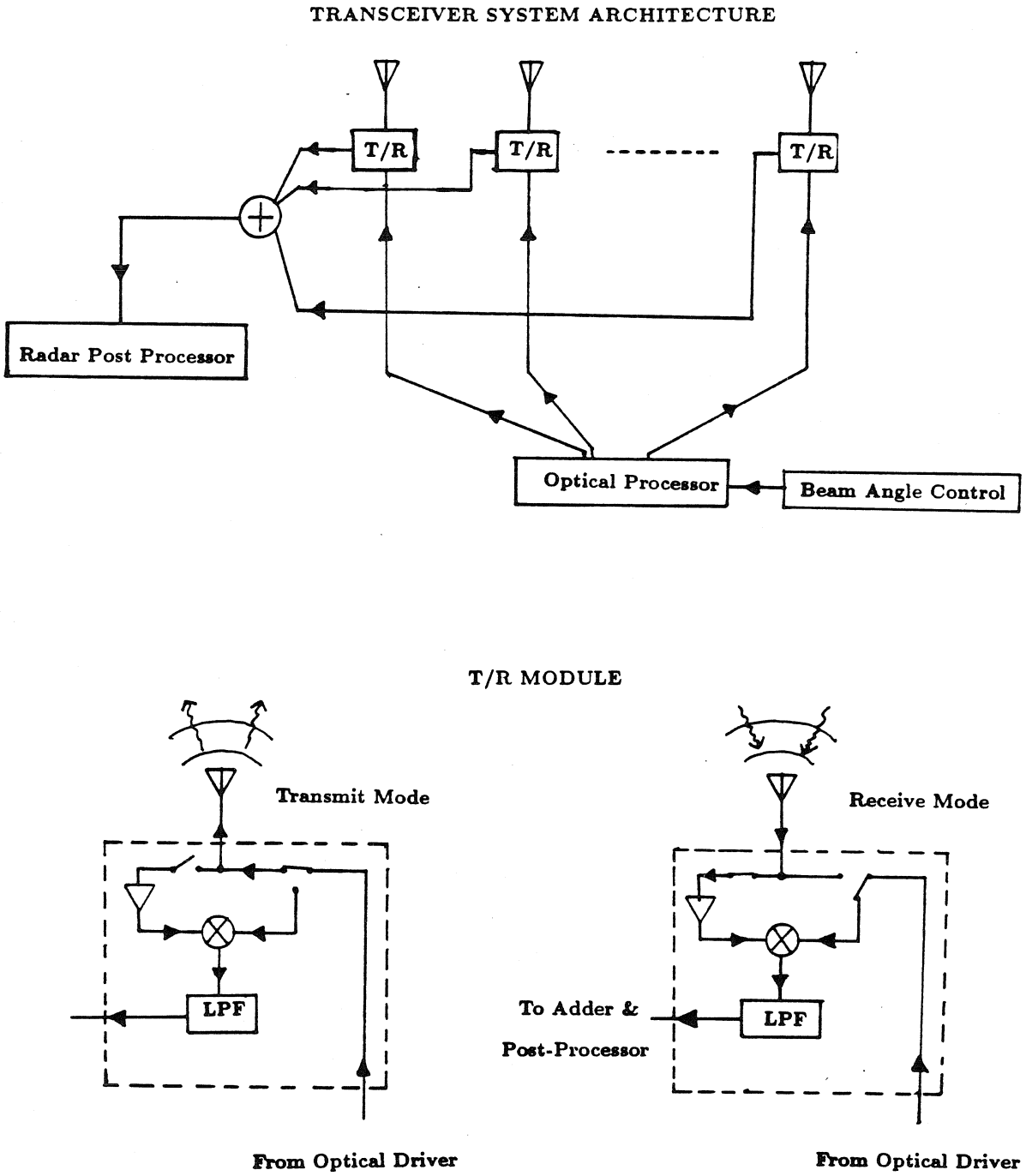

Fig.6.7.3.1 Optical/Electronic phased array radar transceiver system.

where

$$p(t') = rect[t'/T] \tag{6.7.3.3a}$$

$$t' = t - \tau_R \tag{6.7.3.3b}$$

$$\tau_R = Range \quad Delay = 2R/c \tag{6.7.3.3c}$$

$$\omega_d = Doppler \quad Frequency = -2R[dR/dt]\frac{(2\omega_c + \omega_0)}{c}, \tag{6.7.3.3d}$$

where R is the target range for a monostatic system, and $G_{TR}(n)$ is the signal gain dependent on target properties such as radar cross section. The signal in Eqn. 6.7.3.2 is a time delayed, frequency shifted replica of the signal transmitted by the n^{th} antenna in the array. Here we have assumed that the pulse width T is much greater than the maximum interantenna element time delay; i.e.,

$$T \gg Na/c, \tag{6.7.3.4}$$

and the doppler frequency satisfies

$$\omega_d \ll 2\omega_c + \omega_0. \tag{6.7.3.5}$$

The received signals are amplified and then mixed with their corresponding transmitter signals. The output of the mixer consists of a low frequency doppler signal without the phase term $n\psi_0$, and a high frequency signal. The high frequency signal is filtered out by the low pass filter, and the output of the n^{th} T/R module filter is approximately given by

$$i_n(t') = p_T(t')G(n)\cos(\omega_d t'). \tag{6.7.3.6}$$

Note that this signal has a T second time duration with a time delay with respect to the reference transmit time $t = 0$. Also, all the signals from the different T/R

modules are in phase. Next, these in phase signals are added up to maximize the receiver output signal-to-noise ratio, giving the signal:

$$\begin{aligned} i(t') &= \sum_{n=0}^{N} i_n(t') \\ &= (N+1)G\cos(\omega_d t'), \end{aligned} \tag{6.7.3.7}$$

where we assumed constant amplitude G for all the T/R signals. This output signal contains the necessary range and doppler (motion) information of the detected target at the preset scan angle θ_0. This receiver system is also applicable to the system 2 optical processor in Fig. 6.4.3.

6.7.4 Simultaneous Multiple Target Tracking:

The receiver system in Fig. 6.7.3.1 is able to detect multiple targets at the receiver preset scan angle only. In other words, we can track targets at only one scan angle at a time. Modes of operation could include time multiplexed continuous angular tracking, where the receiver tracks different angles in quick time succession. This mode is useful for slowly moving targets.

In the case that targets are moving sufficiently fast to track with a single tracking beam, simultaneous multiple beams in space are required. In this case, we need to use the multichannel AOD optical processor introduced earlier to simultaneously generate the $N+1$ transmit/receive beams in space. The receiver system for this multibeam tracker shown in Fig. 6.7.4.1 consists of $N+1$ receiver channels, each corresponding to a particular beam angle. The basic receiver unit is the same as the single beam tracker in Fig. 6.7.3.1. The hardware required for these T/R modules is readily available in today's high technology, microwave electronics radar industry.

6.7.5 All Optical Transceiver System

The multichannel AOD optical processor (transmitter) based on the single channel AOD beam steerer 2 shown in Fig. 6.4.3 can be combined with a multi-

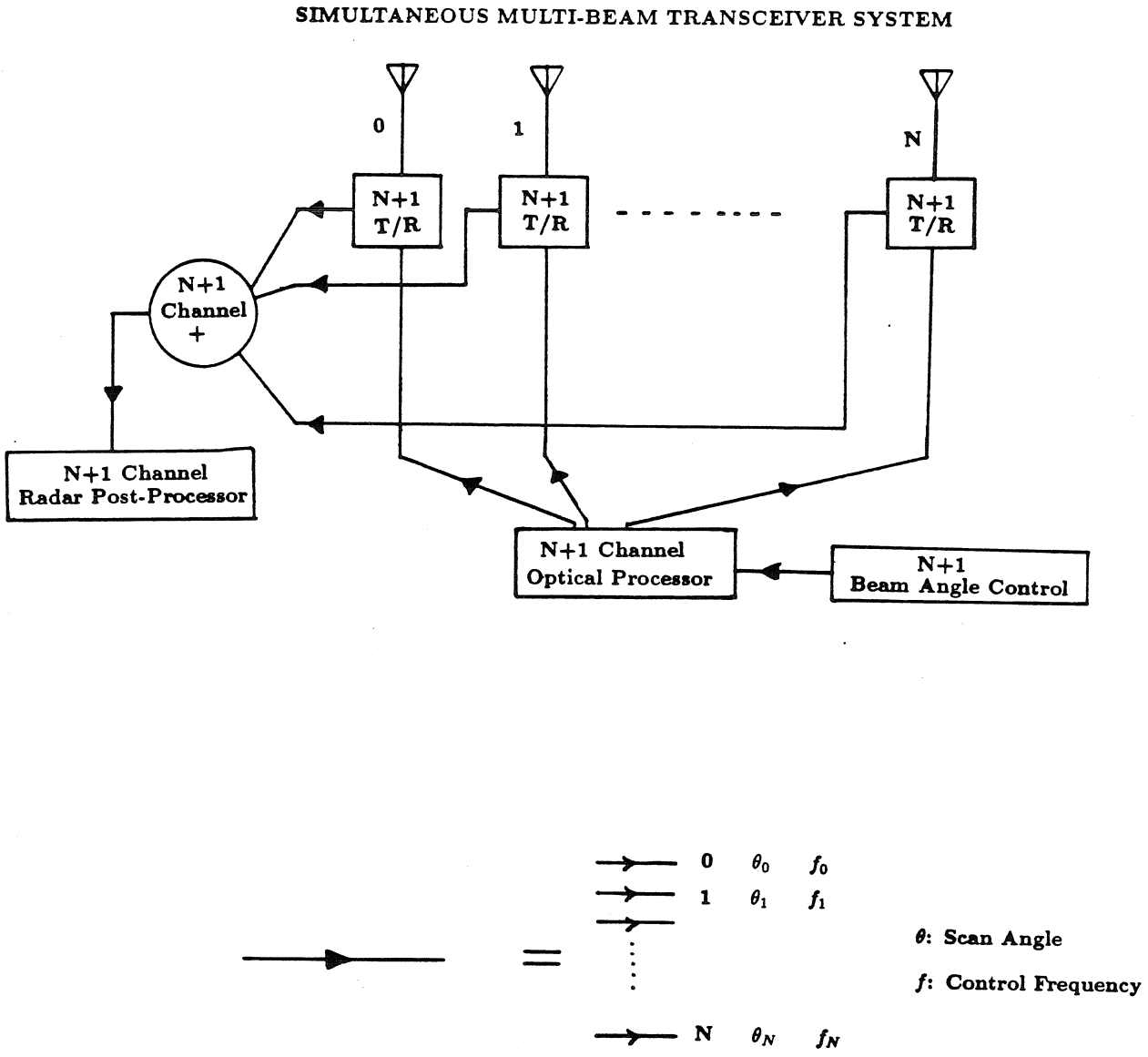

Fig.6.7.4.1 Optical/Electronic phased array radar transceiver system for processing multiple simultaneous beams.

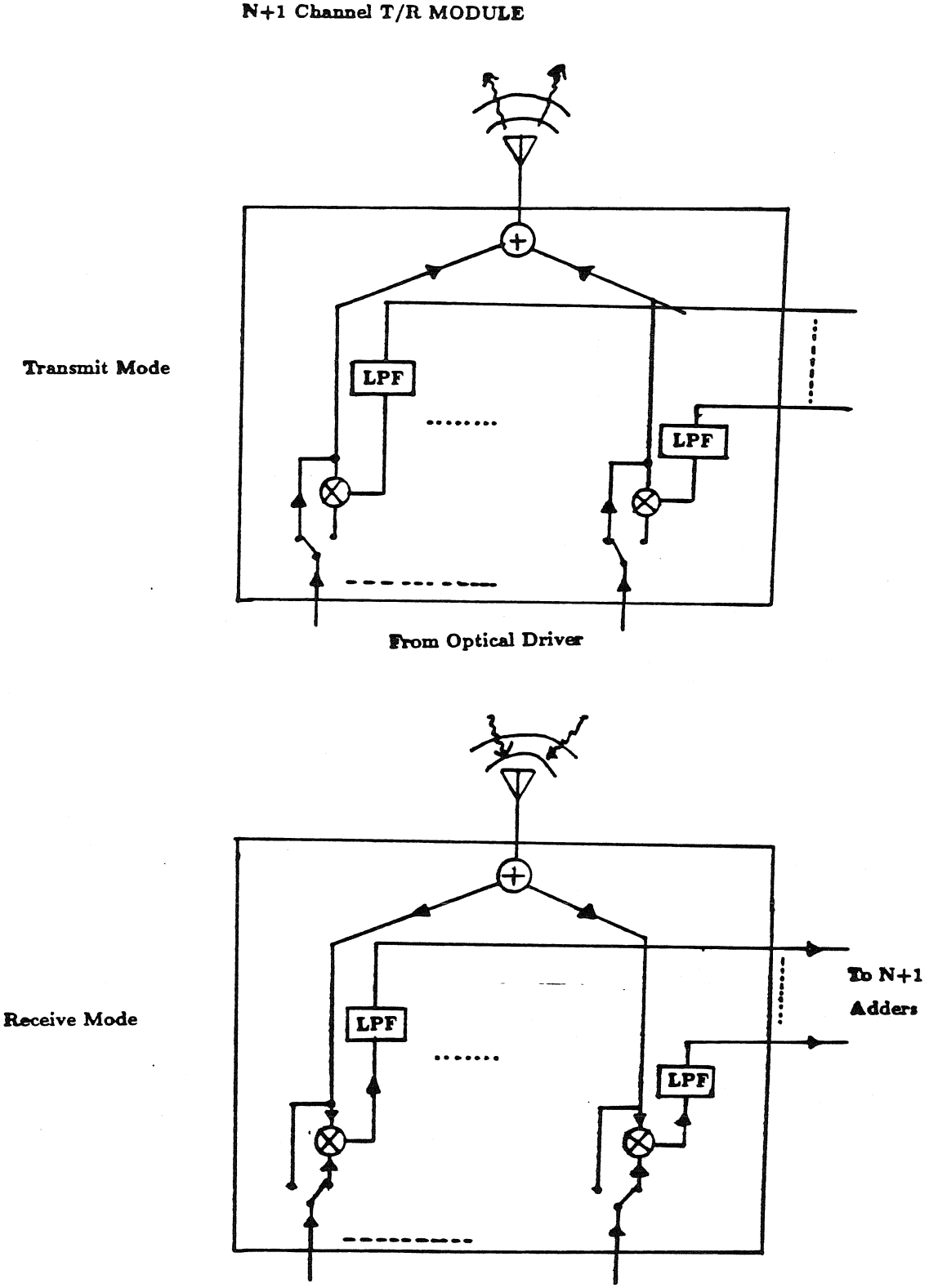

Fig.6.7.4.1 Optical/Electronic phased array radar transceiver system for processing multiple simultaneous beams.

channel AOD space integrating 2-D lens spectrum analyzer (receiver). Originally, the application of the 2-D spectrum analyzer for phased array radar processing was proposed in 1965 by L. Lambert et al. at Columbia University [5]. This Columbia optical receiver system can be combined with the Caltech optical transmitter system to provide an all optical transceiver as shown in Fig. 6.7.5.1. In this receiver, the radar return signals from the antenna array elements are heterodyned to the intermediate frequency (IF) ω_c by mixing each antenna signal return with the transmitter's coherent oscillator $a\cos(\omega_c t)$. The output of the mixer is passed through a bandpass filter centered at ω_c, allowing only the lower sideband to pass through to the channel of the multichannel AOD in the receiver. The light diffracted by the radar returns in all the spatially multiplexed AOD channels is Fourier transformed by a spherical lens, and the output is read by a 2-D CCD array. Like the receiver system in Fig. 6.7.3.1, this receiver system also requires N heterodyners for an N element phased array. The difference is that the system in Fig. 6.7.5.1 can simultaneously track multiple targets as long as crosstalk and sidelobe contributions at the output of the processor do not add up drastically. The receiver architecture in Fig. 6.7.3.1 and Fig. 6.7.4.1, respectively, do not have these light intensity related problems. In effect, the optical receiver hardware replaces the multiple electronic receiver units in Fig. 6.7.4.1 to accomplish the simultaneous target tracking.

The optical design of the multichannel optical receiver is as follows. The field amplitude of the +1 order diffracted light modulated by the complex single sideband signal $\tilde{i}_n(t')$ is approximated as [5]:

$$\tilde{E}(x,y,t') \approx \sum_{n=-N/2}^{N/2} \tilde{i}_n(t' - x/v_a - T_a/2)\text{rect}(x/X)\text{rect}(\frac{y - n\Delta y}{Y}), \qquad (6.7.5.1)$$

where the real signal $i_n(t')$ is given in Eqn. 6.7.3.2 with $\omega = \omega_c + \omega_d$, T_a is the AOD time aperture of spatial width X, Y is the height of the AOD channel, and Δy is the spatial separation between the AOD channels. Substituting the appropriate

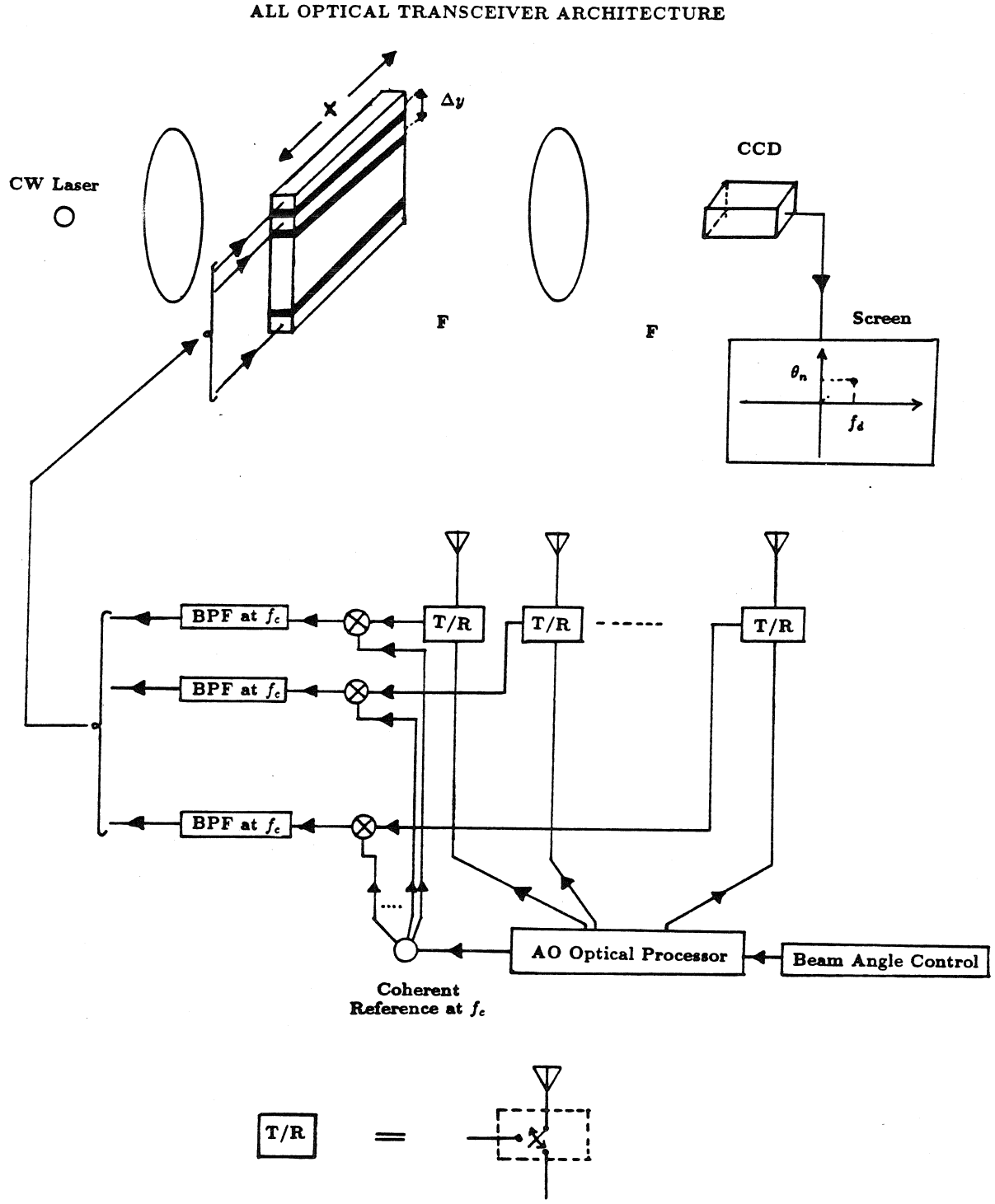

Fig.6.7.5.1 All optical transceiver system with multiple simultaneous beam processing capability.

signal value in Eqn. 6.7.5.1, we get:

$$\tilde{E}(x,y,t') = \sum_{n=-N/2}^{N/2} G_{TR}(n) e^{-j[\omega(t'-x/v_a-T_a/2)-n\psi_0]} \mathrm{rect}(x/X)\mathrm{rect}(\frac{y-n\Delta y}{Y}), \tag{6.7.5.2}$$

where the return pulse width T is greater than the AOD aperture T_a. Assuming a unit signal amplitude for all the AOD channel drive signals, the 2-D spatial Fourier transform of the field distribution in Eqn. 6.7.5.2 is given by:

$$G(u,v,t') = e^{-j\omega(t'-T_a/2)} X\mathrm{sinc}X(u-f/v_a) Y\mathrm{sinc}Yv \frac{\sin\pi(N-1)[v\Delta y - \frac{\psi_0}{2\pi}]}{\sin\pi[v\Delta y - \frac{\psi_0}{2\pi}]}, \tag{6.7.5.3}$$

where $(u,v) = (x',y')/\lambda F$, (x',y') are the output plane coordinates, F is the focal length of the Fourier transforming lens, and λ is the optical wavelength. The intensity distribution on a 2-D time integrating detector for a single target having a doppler f_d at beam direction θ_0 is given by:

$$\begin{aligned} I(u,v) &= \left|G(u,v,t')\right|^2 \\ &= X^2\mathrm{sinc}^2X(u-f/v_a) Y^2\mathrm{sinc}^2Yv \frac{\sin^2\pi(N-1)[v\Delta y - \frac{\psi_0}{2\pi}]}{\sin^2\pi[v\Delta y - \frac{\psi_0}{2\pi}]}. \end{aligned} \tag{6.7.5.4}$$

Note that the temporal doppler variation has been removed by the intensity detection operation. Converting the v spatial dimension into a dimension for antenna space angle, i.e.

$$v\Delta y = \frac{a}{\lambda}\sin\theta, \tag{6.7.5.5}$$

and using Eqn. 6.7.5.5 to evaluate Eqn. 6.7.5.4 at the line $u = f/v_a$, we get the light intensity distribution:

$$I(\theta) = Y^2\mathrm{sinc}^2[\frac{Ya}{\lambda\Delta y}\sin\theta] \frac{\sin^2\Big[\pi(N-1)(a/\lambda)[\sin\theta - \sin\theta_0]\Big]}{\sin^2\Big[\pi(a/\lambda)[\sin\theta - \sin\theta_0]\Big]}. \tag{6.7.5.6}$$

For a typical design of $a = \lambda/2$ and $Y = \Delta y/2$, the sinc^2 weighting function varies from 0 to approximately 0.8 over the $\pm 90°$ variation of beam scan angle θ. In effect,

this weighting function is a slowly varying constant, and therefore does not affect the angular position term in Eqn. 6.7.5.6. The output of the optical processor can be written as:

$$I(u,v) = K\text{sinc}^2[\frac{Ya}{\lambda\Delta y}\sin\theta]\text{sinc}^2 X[u-(f_c+f_d)/v_a] \frac{\sin^2\left[\pi(N-1)\Delta y[v-\frac{a}{\lambda\Delta y}\sin\theta_0]\right]}{\sin^2\left[\pi\Delta y[v-\frac{a}{\lambda\Delta y}\sin\theta_0]\right]}. \quad (6.7.5.7)$$

Note that the 2-D output in Eqn. 6.7.5.7 has a spatial peak whose coordinates are related to the target doppler frequency and angular position. As mentioned before, this processor has the nice feature of simultaneously processing multiple target returns. The processor performance for multitarget scenes is limited mainly by the degree of signal crosstalk and sidelobe contributions of the different target returns in the output frequency plane of the processor. Next, let's look at some of the features of the proposed acousto-optic beam steerers.

6.8 Features of the Optical Beam Steering Technique

6.8.1 Simplicity of Design

The optical and electronic design of the processor is not complex. The components required for this system are available as highly engineered products in the high technology market place. The overall system is less hardware intensive than currently operating phased array radars.

6.8.2 Simplicity of Control

The processor requires a single control parameter, namely, the frequency of a signal to control the radar beam position in space. This control signal being analog in nature allows for a more gradual radar response with changes in the control

parameter. We no longer require the multiple control signals provided by extensive computer hardware and software, as required in digital phase shifters.

6.8.3 Simplicity of Antenna Feed Network

There is a direct parallel feed from the individual current drivers in the optical processor to the respective array antenna elements. Unlike the commonly used corporate feed structure that requires microwave power splitters for signal distribution, this direct parallel feed network is less susceptible to complete system failure, allowing a graceful degradation of beam pattern.

6.8.4 No Phase Shifters

Signal phase shift for the antennas is obtained from a global process of controlled optical beam interference, and not from local phase shifting devices. In this way, we do away with the individual phase shifters and their support hardware required for the antenna elements.

6.8.5 Phase Shift Hardware Independent of Radar Carrier

The optical phase control mechanism (hardware) is independent of the radar carrier frequency. This is unlike most conventional phase shift mechanisms, where a frequency dependent material parameter is used to introduce the phase shift. For instance, in the shuttle imaging radar, digital phase shifters with switched microstrip delay lines are used. Here, for separate L band and C band operation, two different sets of L band and C band phase shifters are used, as the physical size of the stripline for a particular phase shift is different at the two respective frequencies. This frequency independence feature of the optical technique gives a radar operator greater freedom to switch between different radar frequencies, making the complete radar system more attractive to various radar band applications.

6.8.6 Frequency Doubling Effect

Via the doppler effect in the two acousto-optic devices in the optical processor, the input AOD drive frequency is doubled. This feature allows the use of a signal source of half the desired radar carrier frequency. Thus, the oscillator, being lower in frequency (e.g., 2 GHz instead of 4 GHz), is more stable, less expensive, and easier to maintain than a higher frequency signal generator.

6.8.7 Ease of Array Format Change

The linear phased array can easily be changed from a uniform linear array to a non-uniform linear array by simply rearranging the phase sampling detectors (fibers) in the desired format. This readily changes the transmit antenna radiation pattern.

6.8.8 Stable Optics

The optics for the proposed radar processor is highly stable as the system is an in-line additive system. In other words, the two interfering beams in the system travel through almost identical paths, and any system imperfections affect both beams equally and simultaneously. Moreover, this system has the ability to correct for any misalignment by steering one of the beams by electronic frequency control until the beams are aligned.

6.8.9 Lower EMI

As optical signals are less susceptible to electromagnetic interference effects, the optically based radar system performance is more secure to hostile electromagnetic wave jamming. In addition, the use of fibers to carry the phased array signals to the antenna elements will reduce the internally generated electromagnetic fields that could affect the surrounding radar system components [10].

6.9 Potential of the Optical Radar Processor

The proposed optical radar processors have the potential to exist as highly engineered, compact processing units built with existing **bulk** (discrete) devices or in an **integrated** form on a suitable substrate. The existence of an integrated optic radar processor will drastically cut down the large physical size of currently existing systems, allowing highly practical light weight arrays. This miniaturization could lead to greater applications in airborne and space borne systems.

In this processor, the maximum radar carrier frequency is limited by the highest AOD transducer center frequency available in today's market. Current practical limits on the center frequency are in the 3 GHz range, giving a radar carrier of 6 GHz. This allows radar operation up to the C band range (see table 6.9.1). Note that the optical processors could be used with even higher radar carrier frequencies if external frequency multipliers such as simple non-linear diodes are used in the system. The other possibility is the use of magneto-static devices for beam steering, which would allow carrier frequencies into the millimeter wave regime.

Fig. 6.9.1 shows the compact and simple design of the bulk optical radar processor. The optics consists of a laser source, a collimating lens, two acousto-optic devices, a cylindrical lens for 1-D imaging, and a spatially multiplexed array of fibers in the phase sampling output plane. A fiber cable guides the phase sampled optical signals to the array antennas [13]. The detector/amplifier array can exist as a monolithic microwave integrated circuit on a semiconductor substrate such as silicon or gallium arsenide. This allows the bulk processor to be smaller and more robust.

Another alternative for the optical processor is shown in Fig. 6.9.2, which consists of an all integrated opto-electronic processor. Here, almost all the discrete components of the bulk processor are integrated on to a single substrate such as

Table 6.9.1

THE RADAR BANDS FOR THE OPTICAL PROCESSOR

DESIGNATION BY ITU	ASSIGNED FREQUENCIES
VHF	138 - 144 MHz 216 - 225 MHz
UHF	420 - 450 MHz 890 - 942 MHz
L	1.215 - 1.4 GHz
S	2.3 - 2.5 GHz 2.7 - 3.7 GHz
C	5.25 - 5.925 GHz

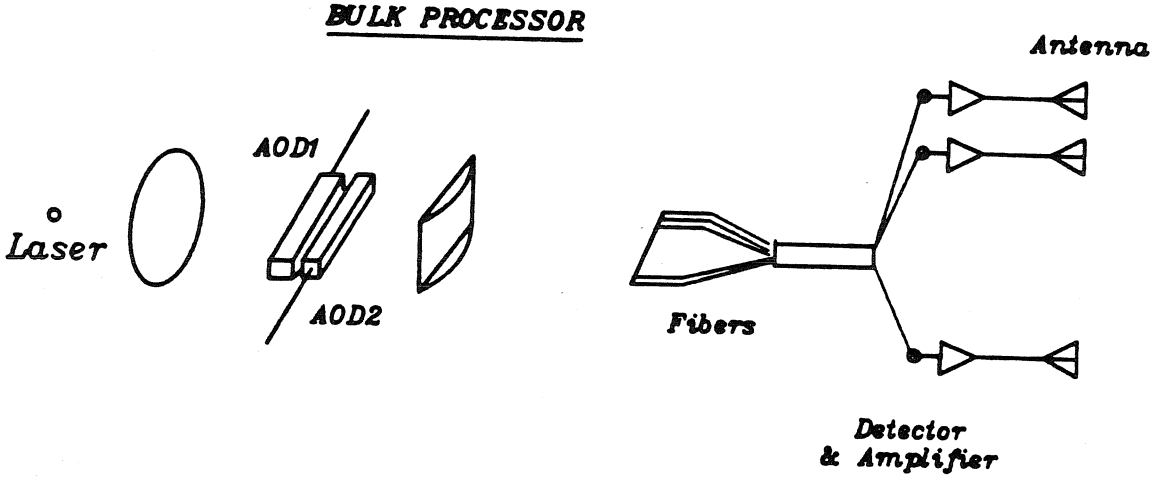

Fig.6.9.1 Compact bulk optical phased array radar processor.

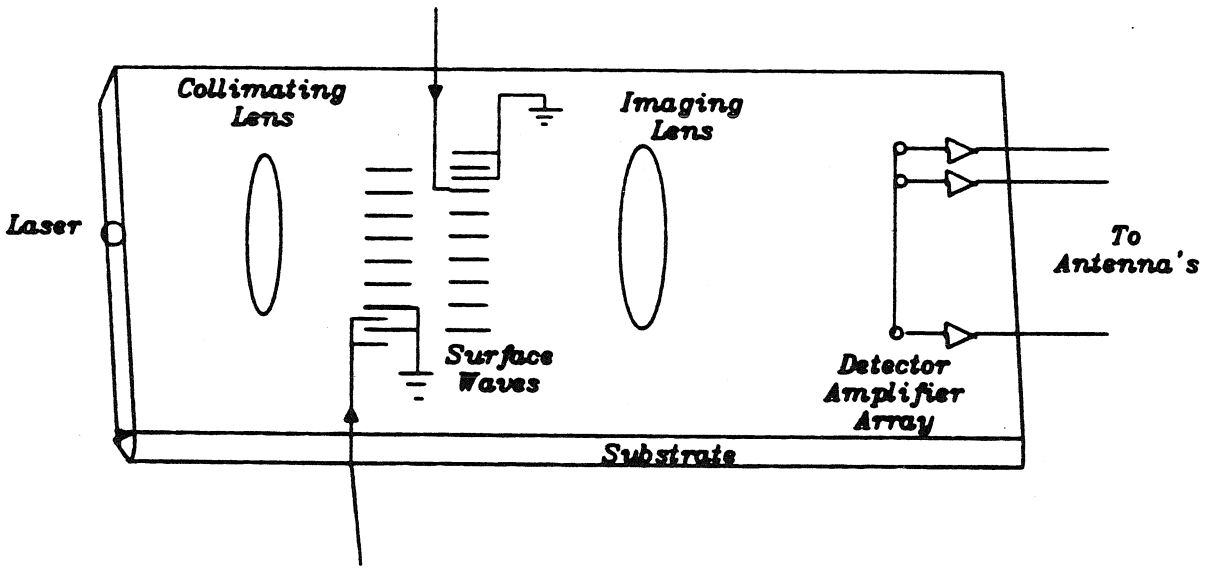

Fig.6.9.2 Integrated optical phased array radar processor.

gallium arsenide, gallium phosphide, or lithium niobate. Depending on the substrate being used, for example, lithium niobate, the laser source has to be externally butt-coupled to the substrate wave-guiding optics. On the other hand, using gallium arsenide could allow the laser diode to be produced on the system base substrate. The collimating, imaging, and guiding optics can be produced by industry standard processes such as the proton-exchange of titanium indiffused lithium niobate [27]. The two surface acoustic wave devices (SAW) can be produced by industry mastered Bragg cell fabrication techniques. For example, SAW devices of nearly 10% per watt diffraction efficiency using Y-cut lithium niobate have been manufactured [28]. The detector/amplifier array of the processor can be integrated on the substrate if we use a III-V semiconductor substrate. Otherwise, a fiber array can be used to sample the light and externally fed to an external detector/amplifier array that has been fabricated by semiconductor based integrated processing.

Next, let's look at some extensions of the proposed optical processor.

6.10 Extensions of the 1-D Optical Linear Phased Array Radar Processor

The 1-D optical linear phased array processor can be modified to provide several applications.

6.10.1 Multiple Linear Array Feeds

Instead of focussing the light as a thin slit on the detector (fiber) sampling array at the output of the optical radar processor for a linear phased array, the light is spread out along the direction orthogonal to the detector array. This allows additional sampling detector (fiber) arrays to be placed at the enlarged light spatial sampling plane. Note that the spatial frequency along the sampling direction is unaffected by the modification, producing identical signals along a particular sampling position. This allows the optical processor to be used to simultaneously feed

multiple linear arrays of antennas without requiring additional electronics such as M-way power splitters. In other words, we could feed a planar array of antennas by this method, producing a narrow pencil beam that is steered in one orthogonal direction (height or azimuth) corresponding to the linear array antennas that sample the spatial phase. Fig. 6.10.1.1 shows the modified feed network for a two element non-sampling array that feeds a $2 \times N$ element planar array.

6.10.2 Non-uniform Phase Sampling

So far, the spatial phase pattern at the output plane of the processor was uniformly sampled along the linear dimension; that is, the samplers (detectors or fibers) were placed equidistant from each other. Another option for phase reading is to use non-uniform sampling by placing the samplers in any required arrangement giving a desired transmit beam shape and direction. This technique is useful when a special beam pattern is desired.

6.10.3 Single Frequency Beam Azimuth/Height Control

A linear phased array optical processor can be used to steer an $N \times M$ element planar array beam in azimuth/height using one control frequency, although the azimuth and height coordinates are not independent of each other. As the control frequency is varied, the beam follows a specific path in azimuth/height coordinates, as shown by the curves in Fig. 6.10.3.1(c). The $N \times M$ sampler locations along the linear slit of light are shown in Fig. 6.10.3.1(a). Note that the sampler located at the linear coordinate $x = nd + m\Delta d$ drives the (m, n) element in the array, where m is the row number and n is the column number, respectively. d is the physical sampler spacing between samplers feeding adjacent elements along a row of the array antennas. Δd is the sampler separation in the N sets of M samplers that feed the column elements of the planar antenna array. Note that the phase shift

MULTIPLE LINEAR ARRAY FEED SYSTEM

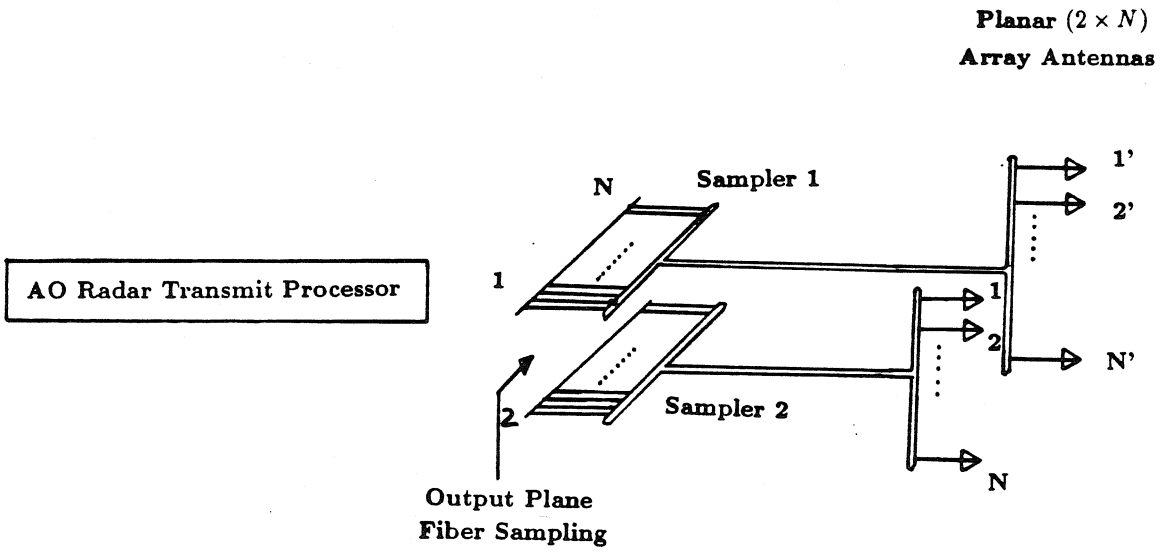

Fig.6.10.1.1 Multiple linear array feed configuration for a $2 \times N$ planar array antenna with 2 linear arrays.

a): Sampler Distribution Along Linear Phase Pattern

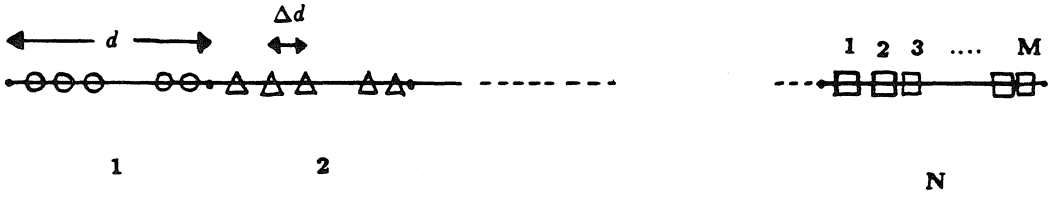

b): Planar $N \times M$ Array Current Feed Configuration

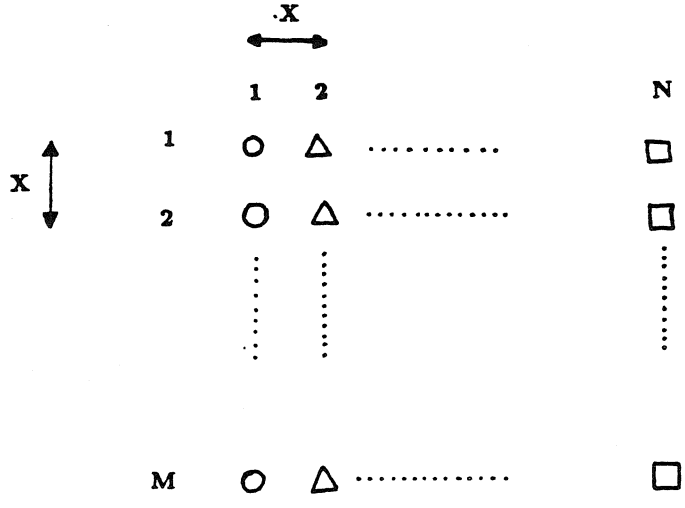

c): Beam Scan Path in Space

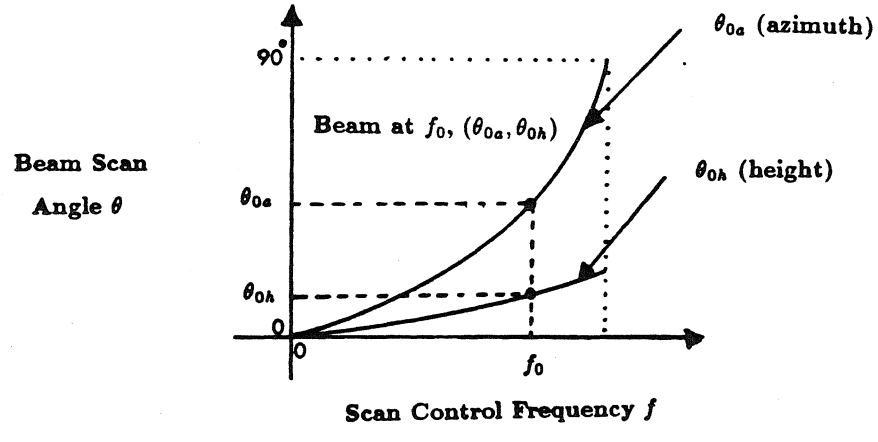

Fig.6.10.3.1(a,b,c) Single control frequency signal beam azimuth/height control configuration for a planar array antenna.

between adjacent elements (m, n) and $(m, n+1)$ is ψ, while for elements (m, n) and $(m+1, n)$ is ψ/M, that is, M times smaller. This leads to a large angular deflection with frequency in one direction (with the large phase change), while a nearly M times smaller angular deflection in the orthogonal direction. This type of array feed format may be useful when a narrow pencil beam with a wide scanning range in one direction and a small scan width in the orthogonal direction is required. For example, this type of feed is useful in the shuttle scanning strip-mode synthetic aperture radar where $\pm 23°$ of azimuth coverage is required compared to $\pm 1°$ for height changes to account for earth curvature effects. Fig. 6.10.3.1(b) shows the current feed configuration on the planar $N \times M$ array antenna.

6.10.4 Independent Beam Azimuth/Height Control Via Two Control Signals

Independent radar beam height and azimuth control for a planar phased array radar may be obtained by using two single element, 2-D acousto-optic laser beam deflectors [29]. The xy diffracted beam's coordinates are controlled by the frequency of the two respective signals fed to their respective orthogonally oriented AO cell transducers. The proposed architecture using the 2-D AO cells is shown in Fig. 6.10.4.1. The laser beam is incident at 2-D Bragg angle at the first 2-D AO cell, producing a DC beam, an x position diffracted beam, a y position diffracted beam, and the desired xy position diffracted beam on an upshifted doppler. The x and y position beams are blocked in the Fourier plane, while the DC beam is 2-D Bragg matched to the second similarly oriented 2-D AO cell producing diffracted beams. Note that the xy diffracted beams from the two 2-D AO cells are almost collinear, and are expanded before being interfered at the 2-D phase sampling plane. In effect, we have two plane waves interfering at the output plane, with the angles θ_a and θ_h between the planes controlled independently by the difference in AOD

INDEPENDENT BEAM AZIMUTH/HEIGHT CONTROL ARCHITECTURE

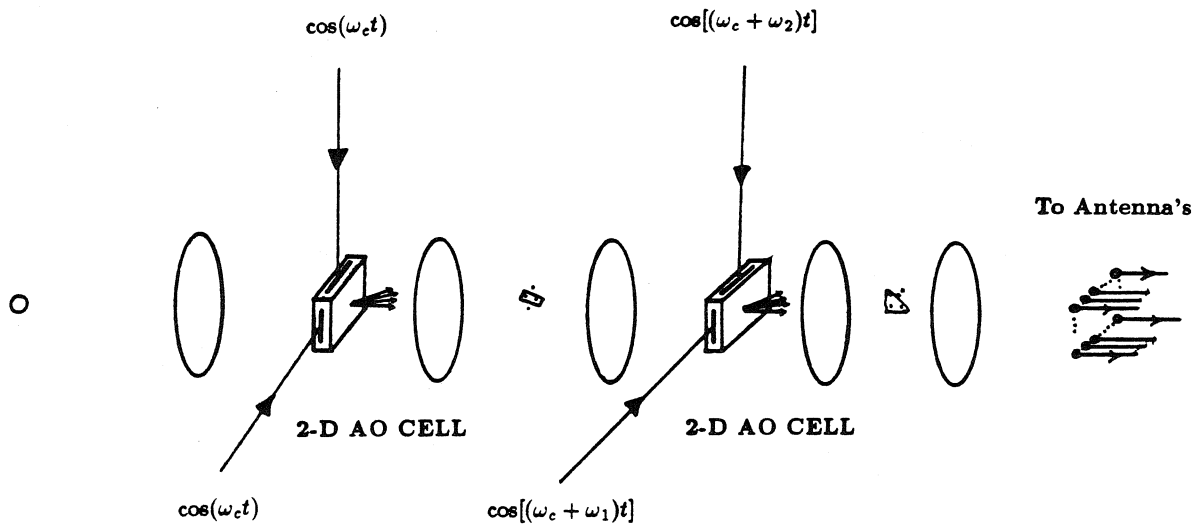

Fig.6.10.4.1 Independent beam azimuth/height control system for a planar array antenna using two control frequency signals.

drive frequencies in the similarly oriented channels in the 2 cells. θ_a and θ_h control the azimuth and height angles of the phased array radar pencil beam.

6.11 Conclusion

This chapter has introduced simple, compact, and powerful optical techniques for control and signal processing in phased array radars. The proposed optical approach eliminates the need for phase shifters that are required in typical electronically controlled phased array radars. Using a single control signal, this technique simultaneously provides the correctly phased signals for transmission and reception in phased array radars. The principles of the optical phased array processor for transmission of radar beams has been demonstrated experimentally in the laboratory. The processor performance is analytically studied, and system issues have been discussed. In addition, there is the possibility of integrating the processor on a substrate, thus leading to smaller and lighter phased array radar systems.

References:

[1] M. I. Skolnik, "50 years of radar," IEEE Proceedings, February, 1985.

[2] R. J. Mailloux, "Phased array theory and technology," *Proc. of the IEEE*, Vol.70, No.3, March, 1982.

[3] R. J. Mailloux, "Antennas and radar," Microwave Journal, March, 1988.

[4] R. Douville and M. G. Stubbs, "Monolithic integrated technology (MIC)for phased arrays," Microwave Journal, March, 1988.

[5] L. B. Lambert, M. Arm, and A. Aimette, "Electro-optical signal processors for phased array antennas," Chapter 38, *Optical and Electo-Optical Information Processing*, edited by J. T. Tippett *et al.*, MIT Press, Cambridge, MA, 1965.

[6] M. King, W. R. Bennett, L. B. Lambert, and M. Arm, "Real-time electro-optical signal processors with coherent detection,"*Applied Optics*, Vol.6, August, 1967.

[7] D. Casacent and F. Casasayas, "Electro-optical processing of phased array antenna data,"*IEEE Trans. on Aerospace and Electronic Systems*, Vol. AES-11, No.1, Jan., 1975.

[8] D. Casasent, "Radar Signal Processing," in *Optical Data Processing: Applications*, ed. by D. Casacent, Topics in Applied Physics (Springer, Berlin, Heidelberg, New York), Section 8.4, November, 1977.

[9] "Opto-electronic Signal Processing for Phased Array Antennas", Edited by K. B. Bhasin and B. M. Hendrickson, *SPIE Conference Proc.*, Vol.886, 12-13 January, Los Angeles, CA, 1988.

[10] M. H. Popek, "Electro-optic system components for phased array radar applications," *SPIE Proc.*, Vol.886-05, Jan., 1988.

[11] L. P. Anderson, F. Boldissar, and D. C. D. Chang, "Antenna beamforming using optical processing," *SPIE Proc.*, Vol.886-27, Jan., 1988.

[12] I. C. Chang, and S. S. Tarng, "Phased array beamforming using acousto-optic techniques," *SPIE Proc.*, Vol.936-18, April, 1988.

[13] J. J. Pan, "Fiber optics for wideband extra high frequency (EHF) phased arrays," *SPIE Proc.*, Vol.886-08, Jan., 1988.

[14] R. R. Kunath and K. B. Bhasin, "Optically controlled phased array technology for space communication systems," *SPIE Proc.*, Vol.886-27, Jan., 1988.

[15] N. A. Riza and D. Psaltis, "An acousto-optic technique for beam scanning and beam formation in phased array radars," *OSA Annual Conf. Digest*, No. 0127, Oct-Nov., Santa Clara, CA, 1988.

[16] G. W. Stimson, *Introduction to Airborne Radar*, p.579, Copyright: Hughes Aircraft Company, El Segundo, CA, 1983.

[17] M. L. Skolnik, *Introduction to Radar Systems*, Chapter 8, Copyright: McGraw-Hill, 1981.

[18] J. W. Goodman, *Introduction to Fourier Optics*, McGraw-Hill Inc., 1968.

[19] J. Browne, "Phase accuracy accents components for signal processing," Microwaves and RF Journal, March, 1988.

[20] E. Caro, Private communication, JPL array design section, Pasadena,CA, March, 1988.

[21] R. Stockton, Private communication, Ball Aerospace Company, Phased array design section, Boulder, Colorado, March, 1988.

[22] E. Miglia, Private communication with Senior Scientist, Active array radar program, Hughes Aircraft Company, El Segundo, CA, March, 1988.

[23] M. R. Stiglitz, "GaAs foundry operations 1988," Microwave Journal, March, 1988.

[24] R. Schneiderman, "GaAs foundries key on custom markets," High Speed Outlook Journal, March, 1988.

[25] C. L. Chen, W. E. Courtney, L. J. Mahoney, M. J. Manfra, A. Chu, and H. A.

Atwater, "A low loss Ku-Band Monolithic Analog Phase Shifter," IEEE Trans. on MTT, Vol. 35, No.3, March, 1987.

[26] I. W. Hammer, "Frequency scanned arrays," Chapter 13, *Radar Handbook*, edited by M. I. Skolnik, McGraw-Hill, New York, 1970.

[27] R. G. Hunsperger, *Integrated Optics: Theory and Technology*, Springer, Berlin, Heidelberg, New York, Tokyo, 2nd Edition, 1985.

[28] R. L. Davis, "Integrated Optic Interferometric Spectrum Analyzer," *SPIE Proc.*, Los Angeles, CA, Jan., 1988.

[29] R. G. Rosemeier, J. I. Soos, and J. Rosenbaum, "A single element 2-D acousto-optic GaP laser beam steerer," *SPIE Proc.*, No. 898-07, Los Angeles, CA, Jan., 1988.